AAAS

Science

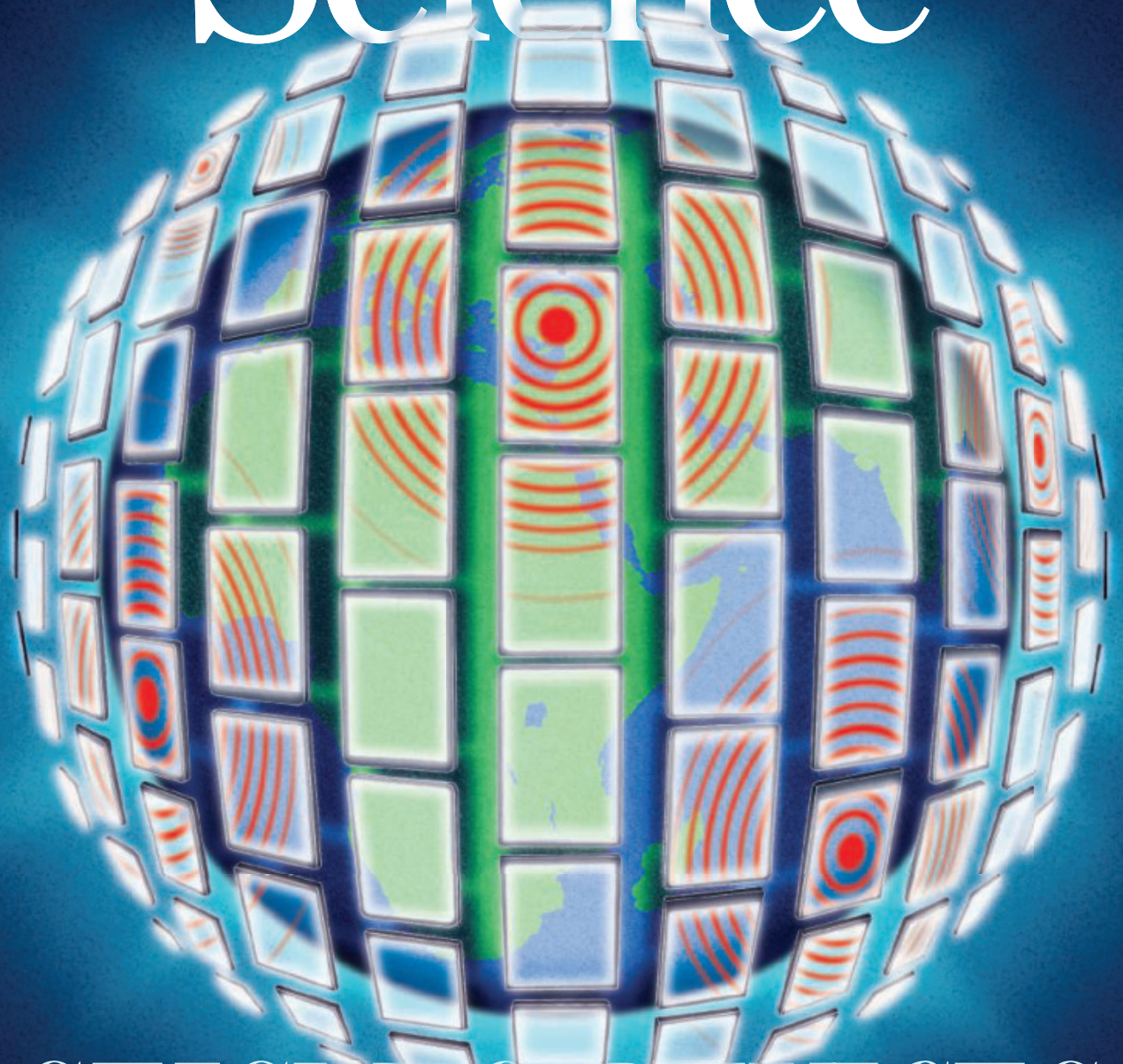

SEISMIC DEVICES

Billions of phones can now sense shaking, and then send warnings p. 254

17 JULY 2025

The sharks attacked. Then came the scientists p. 228

Gut immune cells promote food tolerance pp. 236 & 268

Cellular interactome wins Chen Institute & *Science* Prize p. 244

ASU Science

PRIZE FOR TRANSFORMATIONAL IMPACT

Apply now to the Arizona State University and *Science* Prize for Transformational Impact!

Arizona State University and *Science* have partnered to create the **ASU–*Science* Prize for Transformational Impact**. This prize recognizes transformational research that uses innovative methods and approaches to identify problems and develop solutions with impacts on policy and decision-making.

The grand prize winner will receive a prize of **US$30,000** and their prize-winning essay will be published in *Science* online and print. A runner-up will receive **US$10,000** and have their essay published in *Science* online.

APPLY BY **AUGUST 15, 2025**

www. Science.org/ASU

CONTENTS

17 JULY 2025 | VOLUME 389 | ISSUE 6757

228

Bull sharks terrorized a tropical island.

PHOTO: PETE OXFORD/MINDEN PICTURES

EDITORIAL

219 Science philanthropy faces a new reality
—A. Falk

NEWS

220 Molecular fossils show how life survived Snowball Earth
Overlooked rock samples from 640 million years ago record microbes clinging to life beneath frozen oceans —E. Cutts

222 Astronomers race to study third known interstellar interloper
World's telescopes scrutinize inbound comet for clues on exoplanet formation
—A. Mann

223 NIH suspends alleged 'gain-of-function' studies
Scientists told to stop pathogen work say agency's criteria are mysterious and will stymie needed research
—J. Cohen and J. Kaiser

225 U.S. cancels hunt for signs of cosmic inflation
Downsizing and high ratings did not save effort known as CMB-S4
—A. Cho

226 Fruit fly studies mostly defy concerns about irreproducibility
But large verification attempt finds some "suspicious" papers that fare much worse
—C. O'Grady

FEATURES

228 Haunted by sharks
After a series of deadly shark attacks, the Indian Ocean island of Réunion became a hub of shark attack science —A. Robles-Gil
PODCAST

COMMENTARY

PERSPECTIVES

232 A new age of molecular chirality
Advanced optical approaches reshape the frontiers of chiral sensing —O. Smirnova

234 Polyglycine proteins leave transfer RNAs unglued
Disruption of transfer RNA processing may unite the pathogenesis of CGG repeat expansion disorders
—M. Kapur and S. L. Ackerman
RESEARCH SUMMARY p. 253

235 Disorder meets its match
Designed protein pockets recognize intrinsically disordered protein regions
—A. M. Moses and J. D. Forman-Kay
RESEARCH SUMMARY p. 252

236 RORing for oral tolerance
An antigen-presenting cell subtype tames the immune response to food antigens in early life —C. Johansson
RESEARCH ARTICLE p. 268

POLICY FORUM

238 The pursuit of 1.5°C endures as a legal and ethical imperative in a changing world
As the world nears 1.5°C of global warming, near-term emissions reductions and adequate adaptation become ever more important to ensure a safe and livable planet for present and future generations
—J. Rogelj and L. Rajamani

Science AAAS

CHEN TIANQIAO & CHRISSY INSTITUTE

CO-HOST ETH zürich

AI & MENTAL HEALTH

SEPTEMBER 8–9, 2025 | ZURICH

Mental health is a vast and growing worldwide problem. In addition to the suffering experienced by individuals and their affected family members it also has an enormous economic impact. Because it can affect people at a young age they will often need treatment for many years and during that period they will not be able to participate to their full potential in society.

REGISTER TODAY!

LETTERS

242 US disregards scientific consensus on race
—J. L. Graves Jr. *et al.*

242 US should reject color-blind racial ideology
—T. Russo-Tait *et al.*

243 Combat disinformation about gender research
—A. J. Restar *et al.*

PRIZE ESSAY

244 AI to rewire life's interactome
Structural foundation models help to elucidate and reprogram molecular biology —Z. Qiao

RESEARCH

HIGHLIGHTS

246 From *Science* and other journals

RESEARCH SUMMARIES

249 Molecular biology
Autoinhibition imposed by a large conformational switch of INO80 regulates nucleosome positioning —U. Kaur *et al.*

250 Malaria
Vaccination to mitigate climate-driven disruptions to malaria control in Madagascar —B. L. Rice *et al.*

251 Plant science
Redox-regulated Aux/IAA multimerization modulates auxin responses —D. Roy *et al.*

252 Protein design
Design of intrinsically disordered region binding proteins
—K. Wu *et al.*
PERSPECTIVE p. 235

253 Cellular neuroscience
Polyglycine-mediated aggregation of FAM98B disrupts tRNA processing in GGC repeat disorders
—J. Yang *et al.*
PERSPECTIVE p. 234

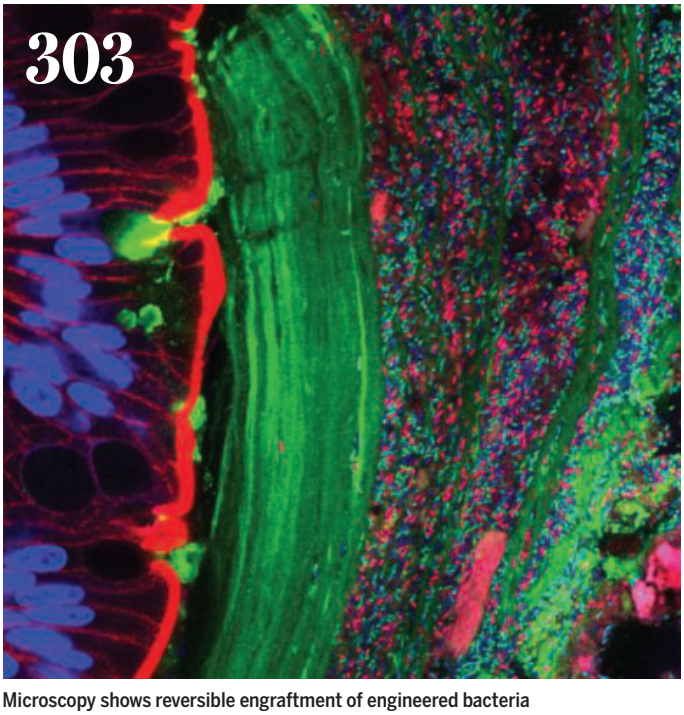

Microscopy shows reversible engraftment of engineered bacteria (red and green stippling) in a mouse gut.

PHOTO: WESTON R. WHITAKER, STANFORD UNIVERSITY

RESEARCH ARTICLES

254 Earthquake alerts
Global earthquake detection and warning using Android phones
—R. M. Allen *et al.*

260 Neuroimmunology
Type 2 cytokines act on enteric sensory neurons to regulate neuropeptide-driven host defense
—R. M. Barilla *et al.*

268 Immunology
A wave of Thetis cells imparts tolerance to food antigens early in life —V. Cabric *et al.*
PERSPECTIVE p. 236

275 Organic chemistry
Skeletal editing of pyrrolidines by nitrogen-atom insertion —J. Li *et al.*
RESEARCH ARTICLE p. 295

282 Neuroscience
Midline assembloids reveal regulators of human axon guidance
—M. M. Onesto *et al.*

290 Materials science
Dome-celled aerogels with ultrahigh-temperature superelasticity over 2273 K
—K. Pang *et al.*

295 Organic chemistry
Bridging the pyridine-pyridazine synthesis gap by skeletal editing
—M. Puriņš et al.
RESEARCH ARTICLE p. 275

299 Electronic materials
Two-dimensional indium selenide wafers for integrated electronics
—B. Qin *et al.*

303 Microbiota
Controlled colonization of the human gut with a genetically engineered microbial therapeutic
—W. R. Whitaker *et al.*
PODCAST

309 Molecular biology
ASB7 is a negative regulator of H3K9me3 homeostasis
—L. Zhou *et al.*

WORKING LIFE

318 Stigma did not kill my dream
—J. C. Cambronero-Heinrichs

218 *Science* Staff
317 *Science* Careers

ON THE COVER

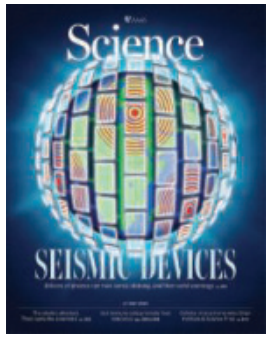

A global network of smartphones is symbolically portrayed working together to help detect earthquakes and provide early warnings to people. The Android Earthquake Alerts system uses the sensors across billions of phones in earthquake-prone regions to characterize earthquakes from the onset of shaking at the epicenter. If the system detects an earthquake, it can alert people in harm's way, helping to save lives.
See page 254. Illustration: Sara Gironi Carnevale

ON THE PODCAST

Studying a shark-haunted island, and upgrading our microbiomes with engineered bacteria

Science **serves as a forum for discussion of important issues related to the advancement of science by publishing material on which a consensus has been reached as well as including the presentation of minority or conflicting points of view. Accordingly, all articles published in *Science*—including editorials, news, commentary, and book reviews—are signed and reflect the individual views of the authors and not official points of view adopted by AAAS or the institutions with which the authors are affiliated.** *Science* (ISSN 0036-8075) is published weekly on Thursday, except last week in December, by the American Association for the Advancement of Science, 1200 New York Avenue, NW, Washington, DC 20005. Periodicals mail postage (publication No. 484460) paid at Washington, DC, and additional mailing offices. Copyright © 2025 by the American Association for the Advancement of Science. The title *Science* is a registered trademark of the AAAS. Domestic individual membership, including subscription (12 months): $165 ($74 allocated to subscription). Domestic institutional subscription (51 issues): $2865; Foreign postage extra: Air assist delivery: $135. First class, airmail, student, and emeritus rates on request. Canadian rates with GST available upon request, GST #125488122. Publications Mail Agreement Number 1069624. **Printed in the U.S.A. Change of address:** Allow 4 weeks, giving old and new addresses and 8-digit account number. **Postmaster:** Send change of address to AAAS, P.O. Box 96178, Washington, DC 20090–6178. **Single-copy sales:** $15 each plus shipping and handling available from backissues.science.org; bulk rate on request. **Authorization to reproduce** material for internal or personal use under circumstances not falling within the fair use provisions of the Copyright Act can be obtained through the Copyright Clearance Center (CCC), www.copyright.com. The identification code for *Science* is 0036-8075. *Science* is indexed in the *Reader's Guide to Periodical Literature* and in several specialized indexes.

Science AAAS

EDITOR-IN-CHIEF **Holden Thorp**, hthorp@aaas.org

EXECUTIVE EDITOR Valda Vinson

EDITORS, RESEARCH Sacha Vignieri, Jake S. Yeston **EDITOR, COMMENTARY** Lisa D. Chong

DEPUTY EXECUTIVE EDITOR Lauren Kmec

DEPUTY EDITORS Stella M. Hurtley (UK), Phillip D. Szuromi **SENIOR EDITORS** Caroline Ash (UK), Michael A. Funk, Angela Hessler, Di Jiang, Priscilla N. Kelly, Marc S. Lavine (Canada), Sarah Lempriere (UK), Mattia Maroso, Yevgeniya Nusinovich, Ian S. Osborne (UK), L. Bryan Ray, H. Jesse Smith, Keith T. Smith (UK), Jelena Stajic, Peter Stern (UK), Yury V. Suleymanov, Valerie B. Thompson, Brad Wible **ASSOCIATE EDITORS** Jack Huang, Sumin Jin, Bianca Lopez, Sarah Ross (UK), Madeleine Seale (UK), Corinne Simonti, Ekeoma Uzogara **SENIOR LETTERS EDITOR** Jennifer Sills **NEWSLETTER EDITOR** Christie Wilcox **NEWSLETTER INTERN** Jasmin Galvan **RESEARCH & DATA ANALYST** Jessica L. Slater **LEAD CONTENT PRODUCTION EDITORS** Chris Filiatreau, Harry Jach Sr. **CONTENT PRODUCTION EDITOR** Amelia Beyna **CONTENT PRODUCTION EDITORS** Anne Abraham, Robert French, Julia Haber-Katris, Nida Masiulis, Abigail Shashikanth, Suzanne M. White **SENIOR PROGRAM ASSOCIATE** Maryrose Madrid **EDITORIAL MANAGER** Joi S. Granger **EDITORIAL ASSOCIATES** Aneera Dobbins, Lisa Johnson, Jerry Richardson, Anita Wynn **SENIOR EDITORIAL COORDINATORS** Alexander Kief, Ronmel Navas, Isabel Schnaidt, Alice Whaley (UK), Brian White **EDITORIAL COORDINATORS** Samuel Bates, Clair Goodhead (UK), Kat Kirkman **ADMINISTRATIVE COORDINATOR** Karalee P. Rogers **ASI DIRECTOR, OPERATIONS** Janet Clements (UK) **ASI OFFICE MANAGER** Carly Hayward (UK) **ASI SR. OFFICE ADMINISTRATORS** Simon Brignell (UK), Jessica Waldock (UK) **COMMUNICATIONS DIRECTOR** Meagan Phelan **DEPUTY DIRECTOR** Matthew Wright **SENIOR WRITERS** Walter Beckwith, Joseph Cariz, Abigail Eisenstadt **WRITER** Mahathi Ramaswamy **SENIOR COMMUNICATIONS ASSOCIATES** Zachary Graber, Sarah Woods **COMMUNICATIONS ASSOCIATES** Kiara Brooks, Haley Riley, Mackenzie Williams

NEWS EDITOR Tim Appenzeller

NEWS MANAGING EDITOR John Travis **INTERNATIONAL EDITOR** David Malakoff **DEPUTY NEWS EDITORS** Rachel Bernstein, Shraddha Chakradhar, Martin Enserink, David Grimm, Eric Hand, Michael Price, Kelly Servick, Matt Warren (Europe) **SENIOR CORRESPONDENTS** Daniel Clery (UK), Jon Cohen, Jeffrey Mervis **ASSOCIATE EDITORS** Jeffrey Brainard, Michael Greshko, Katie Langin **NEWS REPORTERS** Adrian Cho, Jennifer Couzin-Frankel, Phie Jacobs, Jocelyn Kaiser, Rodrigo Pérez Ortega (Mexico City), Robert F. Service, Erik Stokstad, Paul Voosen, Meredith Wadman **CONSULTING EDITOR** Elizabeth Culotta **CONTRIBUTING CORRESPONDENTS** Vaishnavi Chandrashekhar, Dan Charles, Warren Cornwall, Andrew Curry (Berlin), Ann Gibbons, Sam Kean, Kai Kupferschmidt (Berlin), Andrew Lawler, Mitch Leslie, Virginia Morell, Dennis Normile (Tokyo), Cathleen O'Grady, Elisabeth Pain (Careers), Charles Piller, Sara Reardon, Richard Stone (Senior Asia Correspondent), Gretchen Vogel (Berlin), Lizzie Wade (Mexico City) **INTERN** Alexa Robles-Gil **COPY EDITORS** Julia Cole (Senior Copy Editor), Hannah Knighton, Cyra Master (Copy Chief) **ADMINISTRATIVE SUPPORT** Meagan Weiland

CREATIVE DIRECTOR Beth Rakouskas

DESIGN MANAGING EDITOR Chrystal Smith **GRAPHICS MANAGING EDITOR** Chris Bickel **PHOTOGRAPHY MANAGING EDITOR** Emily Petersen **MULTIMEDIA MANAGING PRODUCER** Kevin McLean **DIGITAL DIRECTOR** Kara Estelle-Powers **DESIGN EDITOR** Marcy Atarod **DESIGNER** Noelle Jessup **SENIOR SCIENTIFIC ILLUSTRATOR** Noelle Burgess **SCIENTIFIC ILLUSTRATORS** Austin Fisher, Kellie Holoski, Ashley Mastin **SENIOR GRAPHICS EDITOR** Monica Hersher **GRAPHICS EDITOR** Veronica Penney **SENIOR PHOTO EDITOR** Charles Borst **PHOTO EDITOR** Elizabeth Billman **SENIOR PODCAST PRODUCER** Sarah Crespi **SENIOR VIDEO PRODUCER** Meagan Cantwell **SOCIAL MEDIA STRATEGIST** Jessica Hubbard **SOCIAL MEDIA PRODUCER** Sabrina Jenkins **WEB DESIGNER** Jennie Pajerowski

CHIEF EXECUTIVE OFFICER AND EXECUTIVE PUBLISHER

Sudip Parikh

PUBLISHER, SCIENCE FAMILY OF JOURNALS Bill Moran

DIRECTOR, BUSINESS OPERATIONS & ANALYSIS Eric Knott **MANAGER, BUSINESS OPERATIONS** Jessica Tierney **SENIOR MANAGER, BUSINESS ANALYSIS** Cory Lipman **BUSINESS ANALYSTS** Kurt Ennis, Maggie Clark, Isacco Fusi **BUSINESS OPERATIONS ADMINISTRATOR** Taylor Fisher **DIGITAL SPECIALIST** Marissa Zuckerman **SENIOR PRODUCTION MANAGER** Jason Hillman **SENIOR MANAGER, PUBLISHING AND CONTENT SYSTEMS** Marcus Spiegler **CONTENT OPERATIONS MANAGER** Rebecca Doshi **PUBLISHING PLATFORM MANAGER** Jessica Loayza **PUBLISHING SYSTEMS SPECIALIST, PROJECT COORDINATOR** Jacob Hedrick **SENIOR PRODUCTION SPECIALIST** Kristin Wowk **PRODUCTION SPECIALISTS** Kelsey Cartelli, Audrey Diggs **SPECIAL PROJECTS ASSOCIATE** Shantel Agnew

MARKETING DIRECTOR Sharice Collins **ASSOCIATE DIRECTOR, MARKETING** Justin Sawyers **GLOBAL MARKETING MANAGER** Allison Pritchard **ASSOCIATE DIRECTOR, MARKETING SYSTEMS & STRATEGY** Aimee Aponte **SENIOR MARKETING MANAGER** Shawana Arnold **MARKETING MANAGER** Ashley Evans **MARKETING ASSOCIATES** Hugues Beaulieu, Ashley Hylton, Lorena Chirinos Rodriguez, Jenna Voris **MARKETING ASSISTANT** Courtney Ford **SENIOR DESIGNER** Kim Huynh

DIRECTOR AND SENIOR EDITOR, CUSTOM PUBLISHING Erika Gebel Berg **ADVERTISING PRODUCTION OPERATIONS MANAGER** Deborah Tompkins **DESIGNER, CUSTOM PUBLISHING** Jeremy Huntsinger **SENIOR TRAFFIC ASSOCIATE** Christine Hall

DIRECTOR, PRODUCT MANAGEMENT Kris Bishop **PRODUCT DEVELOPMENT MANAGER** Scott Chernoff **ASSOCIATE DIRECTOR, PUBLISHING INTELLIGENCE** Rasmus Andersen **SR. PRODUCT ASSOCIATE** Robert Koepke **PRODUCT ASSOCIATES** Caroline Breul, Anne Mason

ASSOCIATE DIRECTOR, INSTITUTIONAL LICENSING MARKETING Kess Knight **ASSOCIATE DIRECTOR, INSTITUTIONAL LICENSING SALES** Ryan Rexroth **INSTITUTIONAL LICENSING MANAGER** Nazim Mohammedi, Claudia Paulsen-Young **SENIOR MANAGER, INSTITUTIONAL LICENSING OPERATIONS** Judy Lillibridge **MANAGER, RENEWAL & RETENTION** Lana Guz **SYSTEMS & OPERATIONS ANALYST** Ben Teincuff **FULFILLMENT ANALYST** Aminta Reyes

ASSOCIATE DIRECTOR, INTERNATIONAL Roger Goncalves **ASSOCIATE DIRECTOR, US ADVERTISING** Stephanie O'Connor **US MID WEST, MID ATLANTIC AND SOUTH EAST SALES MANAGER** Chris Hoag **DIRECTOR, OUTREACH AND STRATEGIC PARTNERSHIPS, ASIA** Shoupeng Liu **SALES REP, ROW** Sarah Lelarge **SALES ADMIN ASSISTANT, ROW** Victoria Glasbey **DIRECTOR OF GLOBAL COLLABORATION AND ACADEMIC PUBLISHING RELATIONS, ASIA** Xiaoying Chu **ASSOCIATE DIRECTOR, INTERNATIONAL COLLABORATION** Grace Yao **SALES MANAGER** Danny Zhao **MARKETING MANAGER** Kilo Lan **ASCA CORPORATION, JAPAN** Rie Rambelli (Tokyo), Miyuki Tani (Osaka)

DIRECTOR, COPYRIGHT, LICENSING AND SPECIAL PROJECTS Emilie David **RIGHTS AND PERMISSIONS ASSOCIATE** Elizabeth Sandler **LICENSING ASSOCIATE** Virginia Warren **RIGHTS AND LICENSING COORDINATOR** Dana James **CONTRACT SUPPORT SPECIALIST** Michael Wheeler

EDITORIAL
science_editors@aaas.org

NEWS
science_news@aaas.org

INFORMATION FOR AUTHORS
science.org/authors/
science-information-authors

REPRINTS AND PERMISSIONS
science.org/help/
reprints-and-permissions

MULTIMEDIA CONTACTS
SciencePodcast@aaas.org
ScienceVideo@aaas.org

MEDIA CONTACTS
scipak@aaas.org

PRODUCT ADVERTISING & CUSTOM PUBLISHING
advertising.science.org
science_advertising@aaas.org

CLASSIFIED ADVERTISING
advertising.science.org/
science-careers
advertise@sciencecareers.org

JOB POSTING CUSTOMER SERVICE
employers.sciencecareers.org
support@sciencecareers.org

MEMBERSHIP AND INDIVIDUAL SUBSCRIPTIONS
science.org/subscriptions

MEMBER BENEFITS
aaas.org/membership/
benefits

INSTITUTIONAL SALES AND SITE LICENSES
science.org/librarian

AAAS BOARD OF DIRECTORS

CHAIR Joseph S. Francisco

IMMEDIATE PAST PRESIDENT
Willie E. May

PRESIDENT
Theresa A. Maldonado

PRESIDENT-ELECT
Marina Picciotto

TREASURER Carolyn N. Ainslie

COUNCIL CHAIR
Ichiro Nishimura

CHIEF EXECUTIVE OFFICER
Sudip Parikh

BOARD
Mark Dingfield
Morton Ann Gernsbacher
Kathleen Hall Jamieson
Jane Maienschein
Babak Parviz
Gabriela Popescu
Juan S. Ramírez Lugo
Susan M. Rosenberg
Vassiliki Betty Smocovitis
Roger Wakimoto

BOARD OF REVIEWING EDITORS (Statistics board members indicated with **(S)**)

Erin Adams, *U. of Chicago*
Takuzo Aida, *U. of Tokyo*
Leslie Aiello, *Wenner-Gren Fdn.*
Anastassia Alexandrova, *UCLA*
Mohammed AlQuraishi, *Columbia U.*
James Analytis, *UC Berkeley*
Paola Arlotta, *Harvard U.*
Jennifer Balch, *U. of Colorado*
Nenad Ban, *ETH Zürich*
Carolina Barillas-Mury, *NIH, NIAID*
Christopher Barratt, *U. of Dundee*
François Barthelat, *U. of Colorado Boulder*
Franz Bauer, *Universidad de Tarapacá*
Andreas Baumler, *UC Davis*
Carlo Beenakker, *Leiden U.*
Sarah Bergbreiter, *Carnegie Mellon U.*
Kiros T. Berhane, *Columbia U.*
Aude Bernheim, *Inst. Pasteur*
Joseph J. Berry, *NREL*
Dominique Bonnet, *Francis Crick Inst.*
Chris Bowler, *École Normale Supérieure*
Ian Boyd, *U. of St. Andrews*
Malcolm Brenner, *Baylor Coll. of Med.*
Emily Brodsky, *UC Santa Cruz*
Ron Brookmeyer, *UCLA* **(S)**
Christian Büchel, *UKE Hamburg*
Johannes Buchner, *TUM*
Dennis Burton, *Scripps Res.*
Carter Tribley Butts, *UC Irvine*
György Buzsáki, *NYU School of Med.*
Annmarie Carlton, *UC Irvine*
Jane Carlton, *Johns Hopkins U.*
Simon Cauchemez, *Inst. Pasteur*
Ling-Ling Chen, *SIBCB, CAS*
Hilde Cheroutre, *La Jolla Inst.*
Wendy Cho, *UIUC*
Ib Chorkendorff, *Denmark TU*
Chunaram Choudhary, *Københavns U.*
Karlene Cimprich, *Stanford U.*
Laura Colgin, *UT Austin*
James J. Collins, *MIT*
Robert Cook-Deegan, *Arizona State U.*
Carolyn Coyne, *Duke U.*
Roberta Croce, *VU Amsterdam*
Ismaila Dabo, *Penn State U.*
Jeff L. Dangl, *UNC*
Nicolas Dauphas, *U. of Chicago*
Claude Desplan, *NYU*
Sandra Díaz, *U. Nacional de Córdoba*
Samuel Díaz-Muñoz, *UC Davis*
Ulrike Diebold, *TU Wien*
Stefanie Dimmeler, *Goethe-U. Frankfurt*
Hong Ding, *Inst. of Physics, CAS*
Dennis Discher, *UPenn*
Jennifer A. Doudna, *UC Berkeley*
Ruth Drdla-Schutting, *Med. U. Vienna*
Raissa M. D'Souza, *UC Davis*
Bruce Dunn, *UCLA*
William Dunphy, *Caltech*
Scott Edwards, *Harvard U.*
Todd A. Ehlers, *U. of Glasgow*
Tobias Erb, *MPS, MPI Terrestrial Microbiology*
Beate Escher, *UFZ & U. of Tübingen*
Barry Everitt, *U. of Cambridge*
Vanessa Ezenwa, *U. of Georgia*
Toren Finkel, *U. of Pitt. Med. Ctr.*
Natascha Förster Schreiber, *MPI Extraterrestrial Phys.*
Elaine Fuchs, *Rockefeller U.*
Caixia Gao, *Inst. of Genetics and Developmental Bio., CAS*
Daniel Geschwind, *UCLA*
Lindsey Gillson, *U. of Cape Town*
Alemu Gonsamo Gosa, *McMaster U.*
Simon Greenhill, *U. of Auckland*
Gillian Griffiths, *U. of Cambridge*
Nicolas Gruber, *ETH Zürich*
Hua Guo, *U. of New Mexico*
Taekjip Ha, *Johns Hopkins U.*
Daniel Haber, *Mass. General Hos..*
Hamida Hammad, *VIB IRC*
Brian Hare, *Duke U.*
Wolf-Dietrich Hardt, *ETH Zürich*
Kelley Harris, *U. of Wash*
Carl-Philipp Heisenberg, *IST Austria*
Christoph Hess, *U. of Basel & U. of Cambridge*
Heather Hickman, *NIAID, NIH*
Janneke Hille Ris Lambers, *ETH Zürich*
Kai-Uwe Hinrichs, *U. of Bremen*
Deirdre Hollingsworth, *U. of Oxford*
Pinshane Huang, *UIUC*
Christina Hulbe, *U. of Otago, New Zealand*
Randall Hulet, *Rice U.*
Auke Ijspeert, *EPFL*
Gwyneth Ingram, *ENS Lyon*
Darrell Irvine, *Scripps Res.*
Erich Jarvis, *Rockefeller U.*
Peter Jonas, *IST Austria*
Sheena Josselyn, *U. of Toronto*
Matt Kaeberlein, *U. of Wash.*
Daniel Kammen, *UC Berkeley*
Kisuk Kang, *Seoul Nat. U.*
Vedika Khemani, *Stanford U.*
V. Narry Kim, *Seoul Nat. U.*
Nancy Knowlton, *Smithsonian*
Etienne Koechlin, *École Normale Supérieure*
Alex L. Kolodkin, *Johns Hopkins U.*
LaShanda Korley, *U. of Delaware*
Paul Kubes, *U. of Calgary*
Deborah Kurrasch, *U of Calgary*
Laura Lackner, *Northwestern U.*
Mitchell A. Lazar, *UPenn*
Hedwig Lee, *Duke U.*
Fei Li, *Xi'an Jiaotong U.*
Jianyu Li, *McGill U.*
Ryan Lively, *Georgia Tech*
Luis Liz-Marzán, *CIC biomaGUNE*
Omar Lizardo, *UCLA*
Jonathan Losos, *WUSTL*
Ke Lu, *Inst. of Metal Res., CAS*
Christian Lüscher, *U. of Geneva*
Jean Lynch-Stieglitz, *Georgia Tech*
David Lyons, *U. of Edinburgh*
Fabienne Mackay, *QIMR Berghofer*
Zeynep Madak-Erdogan, *UIUC*
Vidya Madhavan, *UIUC*
Anne Magurran, *U. of St. Andrews*
Asifa Majid, *U. of Oxford*
Oscar Marín, *King's Coll. London*
Matthew Marinella, *Arizona State U.*
Charles Marshall, *UC Berkeley*
Christopher Marx, *U. of Idaho*
Geraldine Masson, *CNRS*
Jennifer McElwain, *Trinity College Dublin*
Scott McIntosh, *NCAR*
Rodrigo Medellín, *U. Nacional Autónoma de México*
Mayank Mehta, *UCLA*
C. Jessica Metcalf, *Princeton U.*
Tom Misteli, *NCI, NIH*
Jeffery Molkentin, *Cincinnati Children's Hospital Medical Center*
Alison Motsinger-Reif, *NIEHS, NIH* **(S)**
Rosa Moysés, *U. of São Paulo School of Medicine*
Carey Nadell, *Dartmouth College*
Daniel Neumark, *UC Berkeley*
Thi Hoang Duong Nguyen, *MRC LMB*
Helga Nowotny, *Vienna Sci. & Tech. Fund*
Pilar Ossorio, *U. of Wisconsin*
Andrew Oswald, *U. of Warwick*
Isabella Pagano, *Istituto Nazionale di Astrofisica*
Giovanni Parmigiani, *Dana-Farber* **(S)**
Zak Page, *UT Austin*
Sergiu Pasca, *Standford U.*
Julie Pfeiffer, *UT Southwestern Med. Ctr.*
Philip Phillips, *UIUC*
Matthieu Piel, *Inst. Curie*
Kathrin Plath, *UCLA*
Martin Plenio, *Ulm U.*
Katherine Pollard, *UCSF*
Elvira Polloczanska, *Alfred-Wegener-Inst.*
Julia Pongratz, *Ludwig Maximilians U.*
Philippe Poulin, *CNRS*
Suzie Pun, *U. of Wash*
Lei Stanley Qi, *Stanford U.*
Simona Radutoiu, *Aarhus U.*
Maanasa Raghavan, *U. of Chicago*
Trevor Robbins, *U. of Cambridge*
Adrienne Roeder, *Cornell U.*
Joeri Rogelj, *Imperial Coll. London*
John Rubenstein, *SickKids*
Yvette Running Horse Collin, *Toulouse U.*
Mike Ryan, *UT Austin*
Alberto Salleo, *Stanford U.*
Miquel Salmeron, *Lawrence Berkeley Nat. Lab*
Nitin Samarth, *Penn State U.*
Erica Ollmann Saphire, *La Jolla Inst.*
Joachim Saur, *U. zu Köln*
Alexander Schier, *Harvard U.*
Wolfram Schlenker, *Columbia U.*
Susannah Scott, *UC Santa Barbara*
Anuj Shah, *U. of Chicago*
Vladimir Shalaev, *Purdue U.*
Jie Shan, *Cornell U.*
Jay Shendure, *U. of Wash.*
Steve Sherwood, *U. of New South Wales*
Ken Shirasu, *RIKEN CSRS*
Brian Shoichet, *UCSF*
Robert Siliciano, *JHU School of Med.*
Emma Slack, *ETH Zürich & U. of Oxford*
Richard Smith, *UNC* **(S)**
Ivan Soltesz, *Stanford U.*
John Speakman, *U. of Aberdeen*
Allan C. Spradling, *Carnegie Institution for Sci.*
V. S. Subrahmanian, *Northwestern U.*
Sandip Sukhtankar, *U. of Virginia*
Naomi Tague, *UC Santa Barbara*
A. Alec Talin, *Sandia Natl. Labs*
Patrick Tan, *Duke-NUS Med. School*
Sarah Teichmann, *Wellcome Sanger Inst.*
Dörthe Tetzlaff, *Leibniz Institute of Freshwater Ecology and Inland Fisheries*
Amanda Thomas, *U. of Oregon*
Rocio Titiunik, *Princeton U.*
Shubha Tole, *Tata Inst. of Fundamental Res.*
Maria-Elena Torres Padilla, *Helmholtz Zentrum München*
Kimani Toussaint, *Brown U.*
Barbara Treutlein, *ETH Zürich*
Li-Huei Tsai, *MIT*
Jason Tylianakis, *U. of Canterbury*
Matthew Vander Heiden, *MIT*
Wim van der Putten, *Netherlands Inst. of Ecology*
Jo Van Ginderachter, *VIB, U. of Ghent*
Ivo Vankelecom, *KU Leuven*
Henrique Veiga-Fernandes, *Champalimaud Fdn.*
Reinhilde Veugelers, *KU Leuven*
Elizabeth Villa, *UC San Diego*
Bert Vogelstein, *Johns Hopkins U.*
Julia Von Blume, *Yale School of Med.*
David Wallach, *Weizmann Inst.*
Jane-Ling Wang, *UC Davis* **(S)**
Jessica Ware, *Amer. Mus. of Natural Hist.*
David Waxman, *Fudan U.*
Alex Webb, *U. of Cambridge*
Chris Wikle, *U. of Missouri* **(S)**
Ian A. Wilson, *Scripps Res.* **(S)**
Sylvia Wirth, *ISC Marc Jeannerod*
Hao Wu, *Harvard U.*
Amir Yacoby, *Harvard U.*
Benjamin Youngblood, *St. Jude*
Yu Xie, *Princeton U.*
Kenneth Zaret, *UPenn School of Med.*
Lidong Zhao, *Beihang U.*
Bing Zhu, *Inst. of Biophysics, CAS*
Xiaowei Zhuang, *Harvard U.*
Maria Zuber, *MIT*

Science philanthropy faces a new reality

Adam Falk

As the ground under American science shifts in troubling and unpredictable ways, questions have arisen as to how philanthropies should respond. Having recently led a private foundation that supports science, I can say unequivocally that philanthropy could not fill a void left by draconian cuts in federal support. It can, however, continue to play a valuable role as a new reality unfolds.

In 2021, basic science funding from the US federal government was almost $50 billion. By contrast, philanthropy provided approximately $5 billion each to universities and to nonprofit research institutes. Of course, all but the largest private donors contributed only a small fraction of this total. For example, the Alfred P. Sloan Foundation (where I recently served as president) gives roughly $25 million annually to the natural sciences. Because of this vast discrepancy in scale, philanthropies must operate in a way that is strategically complementary to the government, opportunistically filling gaps in the funding landscape.

Philanthropies have long funded projects that don't quite fit into the disciplinary silos of the National Science Foundation (NSF) or the disease-oriented focus of the National Institutes of Health (NIH). They may also favor risky projects aimed at pushing technological boundaries, or speculative projects for which the chances of a discovery are slim but the possible consequences profound. Philanthropies might invest in the future of a field by providing unrestricted money to early career investigators, or by concentrating financial support on a problem they see as underfunded.

Philanthropies can pursue such strategies because they are not responsible for the overall structures that support science, from physical assets such as research laboratories, supercomputers, and observatories, to human systems such as graduate programs that train the next generation of scientists. Philanthropies simply do not have the resources to take on that role, even if they wanted to do so. Rather, they rely on a solid base of federal support for science to make their own relatively small contributions impactful.

In May, the Trump administration proposed slashing federal support by nearly $18 billion for the NIH and $5 billion for the NSF. This drastic reduction would certainly cause philanthropies to reconsider how to make investments in this new reality. Perhaps this would mean more support for core research facilities at universities and research institutions, whose existence likely has been taken for granted, or focusing more funds on scholarships, fellowships, and grants for students or investigators who are just embarking on career paths in science and are thus particularly vulnerable. It could mean that philanthropies reduce support for individual projects and instead fund research infrastructure that the government has abandoned, such as shared lab facilities or public repositories for data. What philanthropy cannot do is restore America's research enterprise to what it once was if the proposed cuts to federal funding come to pass.

This drastic reduction would... cause philanthropies to reconsider how to make investments...

While waiting to see what new situations must be confronted, philanthropy cannot abandon its values or its principles. Philanthropies can be flexible and adaptable because, in contrast to federal agencies, their funding decisions are constrained only by their boards and their program staff. This freedom implies that philanthropies should hold themselves to a high ethical standard in using their privileged status. This includes the responsibility to take full account of the effect of their funding on the fields they support, making adequate provision for administrative costs, for example, so as not to starve the institutions at which grantees are located of critical investments. It involves thinking not just about the work that is to be done today, but how that work can help build a healthy future for the field.

To support that goal of a healthy future, it is essential that funders who have worked to broaden participation in science maintain those commitments. This is both a practical and an ethical matter—practical, because the fields that philanthropies support cannot flourish without drawing talent from every part of society; and ethical, because the persistent exclusion of those who have been marginalized historically is a stain on America's scientific community. Philanthropies that care about the future of science must strive to make it a place where everyone with desire and talent can thrive. And whether or not they describe this as "diversity, equity, and inclusion," they should be at least as courageous about pursuing this goal as their grantees are.

For all the change and uncertainty, there is one thing that will not change. Philanthropy will remain a vital part of the science ecosystem, not a force outside of it. But as private funders consider anew how to work within this ecosystem, they must make clear to the science community the roles they can and cannot play. □

Adam Falk is the president and chief executive officer of the Wildlife Conservation Society, New York, NY, USA. afalk@wcs.org

10.1126/science.aea4929

GEOCHEMISTRY

Molecular fossils show how life survived Snowball Earth

Overlooked rock samples from 640 million years ago record microbes clinging to life beneath frozen oceans

ELISE CUTTS

Microbial mats grow below the ice of Lake Vanda in Antarctica. Similar structures may have formed during a Snowball Earth event.

PHOTO: DALE T. ANDERSEN/CARL SAGAN CENTER/SETI INSTITUTE

Several times in Earth's history, the planet froze over. Ice blanketed the world from pole to equator, and temperatures plummeted as low as −50°C. Somehow, life endured. Now, scientists are reporting the first glimpse of this hardscrabble existence during the most recent of these Snowball Earth episodes, which occurred between 651 million and 635 million years ago.

The results, presented last week at the Goldschmidt conference in Prague, come from molecular fossils, chemical biomarkers in seafloor sediments that were buried, turned to stone, and preserved in ancient rocks in a core drilled in Australia.

"Seeing life hanging on through the Snowball Earth is amazing," says Alan Collins, a geologist at the University of Adelaide who attended the presentation. Biomarkers are fragile, so finding rocks that span the entire Snowball episode "and actually getting biomarkers out from that is incredible," he says.

The biomarkers point to a world where microbes clung to life in the dark on the oxygen-starved sea floor, subsisting on whatever organic material drifted down from the ice above. At the top of the core, fine layered structures record what came millions of years later, when the glaciers began to retreat and daylight finally filtered into the shallow seas: mats of photosynthetic bacteria that may have resembled those found today on the floors of ice-covered lakes in Antarctica. Eukaryotes—cells more complex than a microbe—were almost entirely absent, even though they had evolved more than 1 billion years earlier.

Besides offering a peek at life under the ice, the study also bolsters an emerging hypothesis suggesting that eukaryotic green algae did not flourish until after the Snowball episode, when they became the food source that finally allowed the world's first animals to appear. "It will be influential," says geochemist Fred Bowyer of the University of Leeds, who also attended the talk.

One of scientists' favorite places to look for biomarkers from the Cryogenian, the icy period from 720 million to 635 million years ago that saw the two most recent Snowball Earth episodes, is in Oman. But Jochen Brocks, the Australian National University geobiologist who presented the new results, was having trouble getting access to good samples for his biomarker hunt. He tasked his graduate student Caleb Bishop, a sedimentologist, with looking for samples from Australia.

A year later, Bishop came back with a long-forgotten core, drilled decades earlier by the Geological Survey of Western Australia that was just sitting in an archive. When Brocks first saw pieces of the 1700-meter-long core, he thought they looked too light in color to contain biomarkers, which are often dark. "That stuff looks really bad," he recalls telling Bishop. "But prove me wrong."

Proving his adviser wrong took Bishop several years. Like fossils, buried biomolecules can sometimes survive for hundreds of millions of years in rock. But they break down over the ages, losing telling details. Worse, the core was contaminated with petroleum products, perhaps drilling fluid, that had to be carefully removed.

But eventually, using tools that break up molecules and separate the fragments by their

weight, Bishop was able to see signals characteristic of the surviving carbon skeletons of fatty molecules similar to cholesterol. Those molecules vary depending on whether they came from bacteria, animals, or algae. Most abundant in the samples were molecules called hopanes, which are markers for bacteria.

At first, Brocks was skeptical. The biomarkers looked a lot like those found in older cores, from earlier Cryogenian times and even before, and he thought the molecules could have simply come from old material scraped off the continents by the advancing Snowball glaciers. But the core displayed a tidy relationship between sample depth and the degree of "fossilization" the molecules had endured. That, along with the presence of intact microbial mats at the top of the core, convinced Brocks that the core really was sediment laid down gradually on the ocean floor during the Snowball event. He and Bishop hypothesize that the hopanes it preserves represent the residue of a microbe-dominated world: bottom dwellers and drifters in the dark seas feeding on the remains of light-harvesting cyanobacteria. Those microbes would have lived above, in the ice, either in cracks or holes that formed where dark dirt or soot warmed in the Sun and melted through a glacier.

One of the most striking things about the new data is the complete absence of biomarkers for eukaryotic green algae. Biomarkers tend to reflect only the most abundant, important groups, so even though green algae survived Snowball Earth, they must have been relegated to the ecological margins.

Their absence matters, because "the appearance and diversification of algae is directly related to the evolution of complex animal life," says Juliana de Moraes Leme, a paleontologist at the University of São Paulo who attended the talk. For most of Earth's history, the food chain rested on the tiny backs of cyanobacteria. Some researchers believe complex animals couldn't arise until big, nutritious green algae finally dethroned bacteria as the world's foremost photosynthesizers.

This had clearly happened by the middle of the Ediacaran period, immediately after the Cryogenian, when the first large animal fossils—odd creatures resembling ferns and bathmats—suddenly appear in the rock record. It's possible that Snowball Earth glaciations helped set the stage for their rise by scraping nutrients into the sea and fueling a photosynthetic bloom.

But a record from Oman, dating to a warm window between the two Cryogenian Snowball periods, suggested an ecosystem of algae and early animals already existed, according to a landmark 2009 study by University of California, Riverside geochemist Gordon Love and colleagues.

"Now we have so much more data," Brocks says, and he thinks the new data point to a simpler story in which green algae don't proliferate until the Ediacaran. The Oman biomarkers, he suspects, were contaminated by oil that leaked down from younger Ediacaran sediments. Oil is itself fossil organic material, so it contains biomarker molecules. "It looked exactly like petroleum," Brocks says. "Identical."

Love disagrees. The Oman biomarkers came from solid organic material that stays put in the rock where it formed—not from oil, which can move around. The criticism, he says, "is wishful thinking more than any scientific argument."

Taking a second look at the Oman core would help settle the score. But it's owned by Petroleum Development Oman, an oil company, and no one has been granted access for a reanalysis, Bowyer says. "It's a big problem." Next year, researchers will drill for fresh Snowball Earth samples in Oman through the International Continental Scientific Drilling Program. Brocks and Love plan to analyze the resulting samples in parallel.

Although uncertainties remain, Collins says the new work is an exciting step toward understanding a mysterious period in Earth's history that can fairly be described as the beginning of the world as we know it. Between the Cryogenian and the mid-Ediacaran, he points out, the atmosphere became breathable, vibrant animal ecosystems emerged, and the seas might even have changed color as green algae began to flourish.

"I thought the story [Brocks] presented was much more convincing and, in many ways, much more interesting" than the old story about an earlier rise of algae, Collins says. If Brocks is right, he adds, "the rise of green algae is getting much closer to when we first see animals evolving." □

Elise Cutts is a science journalist based in Graz, Austria.

IN OTHER NEWS

PANELS IN CONGRESS DEFY TRUMP'S CALL FOR RESEARCH CUTS The U.S. Congress continues to push back against the drastic cuts to research sought by President Donald Trump. But the 2026 budgets of most agencies would still be below current levels under spending blueprints released this week by the appropriations committee for the House of Representatives.

Some highlights:

- The Department of Energy's Office of Science would receive a 2% boost, to $8.4 billion, rather than the 14% cut Trump has proposed.
- The National Science Foundation (NSF) would receive $7 billion, $2 billion less than its current budget but $3.1 billion more than Trump's request. A Senate panel last week proposed maintaining NSF at its 2025 level.
- NASA science missions would suffer a cut of $1.3 billion, to $6 billion. But that's $2.1 billion more than Trump is seeking. The Senate panel has proposed level funding.
- House and Senate panels are divided on next year's budget for the Food and Drug Administration (FDA). Last week, a Senate panel voted unanimously for a $7 billion budget that would keep FDA's spending roughly at current levels. Last month, a House panel embraced Trump's request for a cut to $6.8 billion.
- The National Institute of Standards and Technology (NIST) would see its budget fall by 12%, to $1 billion, rather than the 30% reduction Trump has requested. But some of that budget is likely to be diverted to legislators' pet projects that agencies have not requested, which would reduce the amount available for research and upgrades to NIST facilities.
- The U.S. Geological Survey is facing a 5.6% cut rather than the 39% reduction Trump wants, and the budget for the U.S. Fish and Wildlife Service, which oversees most of the nation's endangered species, would drop by 6.5% instead of Trump's 32% decrease.

All these figures are preliminary. To avoid a government shutdown, legislators must agree on final numbers before the 1 October start of the 2026 fiscal year or vote to extend current spending levels while negotiations continue.
—*Science* News staff

IN OTHER NEWS

NATIONS MOVE TO FILL HIV/AIDS FUNDING GAP In response to President Donald Trump's cuts to U.S. spending on foreign aid, at least 25 nations expect to increase their outlays on treating and preventing HIV infection and AIDS, according to a 10 July United Nations report. South Africa, which has the highest number of people living with HIV—nearly 8 million—last week also released its own plan to fill the gap. U.S. aid for HIV/AIDS totaled $6.7 billion in 2024, and analysts say the increases won't make up for the cuts. —Jon Cohen

NEW LEADER FOR U.S. SCIENCE ACADEMY Neil Shubin, a biologist best known for discovering an important ancient fish, has been nominated to head the National Academy of Sciences (NAS) next year. Shubin, an associate dean at the University of Chicago, will take over an NAS in turbulent, uncharted waters. The current president, Marcia McNutt (former editor-in-chief of *Science*), has already announced significant job cuts because of the loss of government contracts for advisory activities. Shubin's nomination must be ratified by NAS members later this year. —Erik Stokstad

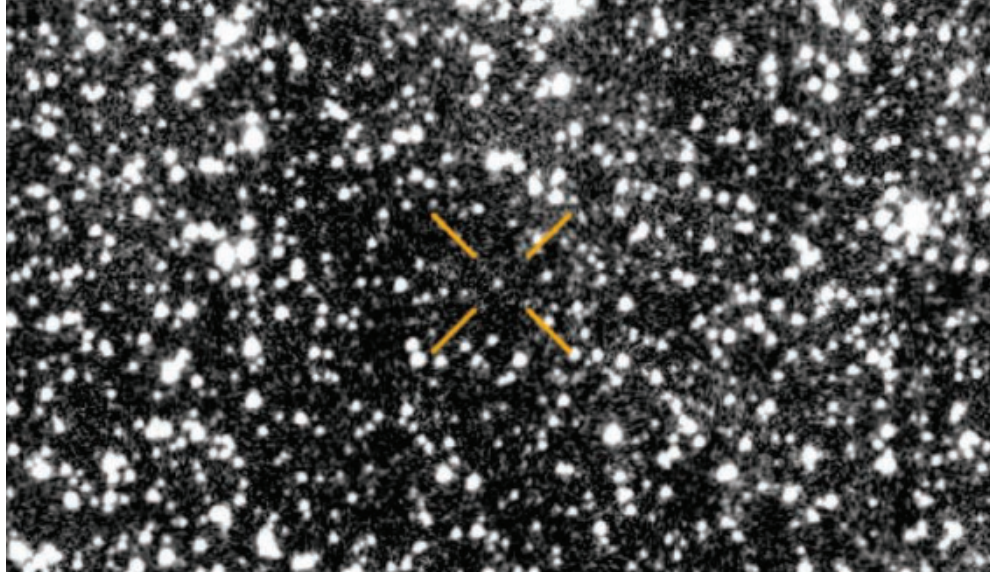

PHOTO: ATLAS/UNIVERSITY OF HAWAII/NASA

SPACE

Astronomers race to study third known interstellar interloper

World's telescopes scrutinize inbound comet for clues on exoplanet formation

ADAM MANN

It all began on 1 July, when an asteroid-hunting telescope in Chile spotted a tiny white dot hurtling against the background stars. The online chatter began almost immediately as astronomers tracked the object in earlier images and amateur observations. Soon it was clear the dot was moving through the Solar System so fast—209,000 kilometers per hour—that it could not be orbiting the Sun. That night, says Michigan State University (MSU) astronomer Darryl Seligman, "I woke up at 1 a.m. [and] saw messages saying, 'Oh, this is for sure interstellar.'" The next day, he and his colleagues began typing up the first paper characterizing the new intruder.

3I/ATLAS, named for the instrument that found it, the Asteroid Terrestrial-impact Last Alert System (ATLAS) survey telescope, is just the third object of its kind ever spotted. Like its predecessors, 1I/'Oumuamua in 2017 and 2I/Borisov in 2019, it is a stray leftover from the formation of exoplanets around other stars and will vanish back into interstellar space within months. As a result, astronomers around the world are swiveling ground- and space-based telescopes toward the object, hoping to catch it while it remains visible, and trying to make sense of early clues. "I couldn't really work on Thursday," says University of Cologne astronomer Susanne Pfalzner, a theoretician specializing in stellar and planetary formation. "I was just jumping about."

Beyond a few basics, ATLAS remains mostly a mystery, but astronomers have already learned enough to intrigue them. For one, the object is conspicuously bright. ATLAS was discovered while it was still 670 million kilometers from the Sun, out near the orbit of Jupiter—more than five times farther than 'Oumuamua was when it was first spotted. This suggests ATLAS might be as large as 20 kilometers across, much larger than 'Oumuamua (thought to be a cigar-shaped chunk 400 meters long) and Borisov (975 meters wide). However, estimates of the object's size come with an asterisk. If ATLAS is outgassing like a comet, it might be surrounded by a haze that makes it appear larger than it really is.

What is certain is ATLAS's unusually wide curve through the Solar System. To describe how much an object's orbit deviates from a perfect circle, astronomers calculate a metric known as eccentricity. All planets, asteroids, and comets within the Solar System have orbits with an eccentricity between zero and one, meaning they trace out an ellipse around the Sun. 'Oumuamua's eccentricity was 1.2—a hyperbolic arc. Borisov's was 3.3. With an eccentricity above six, ATLAS is blowing both out of the water.

According to Auburn University astronomer John Noonan, ATLAS's trajectory could mean the object has been drifting through the Galaxy for longer than 'Oumuamua and Borisov. However, pinning down exactly where ATLAS came from remains challenging, as the gravity of dust clouds or stars that it passed could have bent its path through the Milky Way. At least one team has used high-precision data on the positions of our Galaxy's stars to suggest ATLAS may have originated in the Milky Way's sparse outer disk.

As the object enters the inner Solar System, astronomers are scrambling to get as many eyes on it as possible. "It's about as 'code red' as astronomy can get," says MSU astronomer Adina

This image from the Asteroid Terrestrial-impact Last Alert System telescope in Chile, taken on 1 July, helped reveal the interstellar comet 3I/ATLAS (center).

Feinstein, who studies young stellar systems. Time is short. By the beginning of October, when ATLAS will have entered the inner Solar System and crossed Mars's orbit, it will be too close to the Sun to be observed with ground-based telescopes. At that point scientists hope to enlist spacecraft like NASA's Mars Reconnaissance Orbiter and the European Space Agency's (ESA's) Jupiter Icy Moons Explorer, which is inbound to the gas giant, to study the object. ATLAS then should reappear for Earth observation by early December and remain visible until May 2026.

The main thing scientists want to figure out is ATLAS's composition. Comets and asteroids represent the leftovers of planet formation—meaning ATLAS is a discarded sample of alien worlds, flung out from the dusty disk surrounding a distant star. By comparing its ratios of things such as carbon monoxide, water, ammonia, and salts with those of our local comets and asteroids, researchers hope to learn whether other planetary systems have ingredients like our own. "If we see that this building block looks like all the building blocks in our Solar System, that's good news," says Karen Meech, an astronomer at the University of Hawaii at Manoa. "That's encouraging for the potential for life" elsewhere in the Galaxy.

Already ATLAS appears to have a reddish color, which means its surface probably contains organic materials such as methane, typical for both comets in our Solar System and 'Oumuamua and Borisov. More detail is likely to come as larger instruments such as the Hubble Space Telescope and JWST swing into action. A team of astronomers has submitted a request to target the object with JWST next month. Noonan has sent a similar proposal to Hubble, with the goal of observing ATLAS near the beginning of December.

The pace of interstellar findings is likely to quicken. The powerful Vera C. Rubin Observatory on Cerro Pachón in Chile, which recently began to catalog the entire southern night sky every 3 days, is expected to find between six and 51 additional visitors over the coming decade. Upcoming telescopes designed to find near-Earth asteroids, such as NASA's space-based NEO Surveyor satellite or ESA's Flyeye instruments, should also detect a few interstellar objects once they become operational.

As the field grows, the exhilaration over each individual discovery will probably decrease, but the wonder these fleeting objects evoke won't fade. Astronomers expect they will one day be studying entire populations of interstellar interlopers—yielding insights into the cosmos that were once the stuff of dreams. "We get these tiny memories of solar systems past zipping through," Noonan says. "And we have months to characterize them as best as we can before they're gone again." □

Adam Mann is a journalist based in Oakland, California.

BY THE NUMBERS

23,695

Papers on artificial intelligence produced by China in 2024, topping the combined output of the United States (6378), the United Kingdom (2747), and the European Union (10,055), according to a report by Digital Science.

$51,000,000

Spending by Mexico and the United States on a facility that will, by 2026, produce more than 100 million sterile male screwworms annually in a bid to prevent a resurgence of the pest, which can kill cattle and other livestock.

INFECTIOUS DISEASES

NIH suspends alleged 'gain-of-function' studies

Scientists told to stop pathogen work say agency's criteria are mysterious and will stymie needed research

JON COHEN and **JOCELYN KAISER**

In response to White House concerns about allegedly risky research on viruses, bacteria, and other pathogens, the National Institutes of Health (NIH) has begun a crackdown on dozens of studies it was funding, *Science* has learned.

Citing President Donald Trump's executive order promising greater oversight of "gain-of-function" (GOF) research that's potentially dangerous, the agency has demanded the scientists leading those studies suspend part or all of their work and propose modifications to their experiments that would limit any risk of creating more deadly or transmissible pathogens.

"NIH has identified 40 projects that may meet the definition of dangerous gain-of-function research. … Erring on the side of caution, all projects potentially meeting the definition are being suspended," Matt Memoli, NIH's deputy director, wrote in a 3 July draft letter to the White House describing NIH's "interim response" to the executive order. The letter, obtained by *Science*, indicates an additional 172 projects have been flagged for potential suspension or termination.

The suspended studies cover a wide range of pathogens or their toxins. A handful center on the well-known viruses that cause COVID-19, influenza, dengue, and Zika, but other suspensions cover more obscure pathogens such as alphaviruses, bunyaviruses, and phleboviruses. Most of the suspended projects are taking place at U.S. universities, but nine are being conducted by NIH's in-house scientists, according to a spreadsheet listing the 40 projects. That document also notes that those intramural investigators have already agreed to either stop or modify their research.

NIH's selections have puzzled many infectious disease scientists and dismayed others. Nearly half involve tuberculosis (TB); studies on the mycobacterium that causes the disease have not traditionally sparked GOF concerns because many infections produce no harm, the pathogen depends on prolonged exposure to spread, and TB is curable in most cases.

The studies targeted by NIH include both relatively low-risk, routine work and higher risk experimentation that is essential for developing new drugs and vaccines, several researchers told

Science. JoAnne Flynn, a TB researcher at the University of Pittsburgh who is a co–principal investigator of one of the suspended grants, reviewed NIH's list and called it "crazy" and "ridiculous." Flynn's own project involved using standard techniques to create mutants of *Mycobacterium tuberculosis* (*Mtb*) that are resistant to antibiotics. But she stresses that her work is not using compounds currently recommended for TB treatment so she sees no risk of creating a dangerous strain capable of undermining those therapies. "This will really impede our understanding of *Mtb* infection," Flynn says.

University of Wisconsin–Madison toxicologist Sabine Pellett similarly

Many of the suspended studies have an unexpected subject: the bacterium that causes tuberculosis.

was dismayed and mystified by the suspension of her grant, though she recognizes the risks posed by her lab's work with *Clostridium botulinum*, a bacterium that produces a deadly neurotoxin. "My project is already done under high security conditions and already has undergone review following the processes by NIH," Pellett says. "My lab is the only academic lab in the U.S. that can do what I do. There's no safer place to work with the agent I work with." She says the suspension will impede understanding of the bacterium and slow the development of new treatments for its neurotoxin.

The American Society for Microbiology (ASM) also expressed concern at NIH's choices. "For some of the grants it's hard to see the justification for the pause unless you interpret the executive order very broadly. Other grants are already subjected to a higher level of scrutiny. This is all compounded by the lack of an appeals process," said Allen Segal, an ASM spokesperson.

Concern about GOF research came to the fore in 2011 when two labs modified the deadly H5N1 bird flu virus to determine which mutations might allow it to better transmit between mammals. Federal officials in 2014 paused 18 projects before releasing 2017 guidelines that allowed work to move forward. But the debate flared again during the COVID-19 pandemic, when some scientists and Republican politicians, including Trump, alleged that the coronavirus responsible came from GOF work at a lab in Wuhan, China, that had received NIH funding.

Former President Joe Biden's administration later revamped the U.S. government's GOF policy, but Trump officials jettisoned that work with its executive order on 5 May. Some researchers criticized Trump's order as vague and potentially so broad that it could derail relatively low-risk, promising research. NIH provided some follow-up guidance, but until now many infectious disease scientists were uncertain what work would be stopped by the agency.

NIH began to send out suspension notices last week and more were being issued this week, according to Memoli's letter. NIH staff reviewed more than 71,000 projects, he said.

In the NIH spreadsheet, there is a column noting the rationale for each grant's selection. For 17 projects, that rationale included the phrase "suspended out of an abundance of caution." One such study involves examining protective antibodies to two deadly viruses, but the work does not involve the actual pathogens, raising questions about why the work sparked GOF concerns.

Richard Chaisson, a TB researcher at the Johns Hopkins University Bloomberg School of Public Health, points out that one of NIH's suspended projects studied a *loss* of function to *Mtb*. NIH has also suspended a project to modify a flu virus to treat cancer.

Virologist Andrew Pekosz of Johns Hopkins notes that NIH doesn't provide detailed explanation for its decisions. "There doesn't seem to be a risk-benefit analysis," Pekosz says, or an understanding that many of the pathogen manipulations scientists are doing in the lab also happen naturally.

Debates about what constitutes a GOF experiment that is too risky have raged for years, with many arguments revolving around whether the modifications to the pathogens being studied have the potential to trigger a pandemic or worsen the harm they already cause to humans. David Relman, a microbiologist at Stanford University who has pushed for stronger GOF regulations, worries NIH's ambiguous criteria for unallowed studies could lead some principal investigators (PIs) to stop doing work that does not present high risks to the public. "Ill-considered self-censorship by PIs and the effects of intimidation on PIs might be some of the most damaging and (both figuratively and literally) sickening effects of the current circumstances," Relman wrote in an email.

Harvard University epidemiologist Marc Lipsitch, who has also called for stronger U.S. regulations on high-risk pathogen lab work, questioned why NIH had suspended most of these projects. "Only a handful plausibly meet the standard in the executive order that they 'could result in significant societal consequences,'" Lipsitch says. "While there are a few studies where I would want to learn more about the risks and benefits, I would predict that ending this list of studies, as a whole, will be detrimental to health security and public health."

Paul Friedrichs, who headed the White House Office of Pandemic Preparedness and Response Policy under Biden, says he hopes the government will better explain how it decided to single out these specific projects. "Ambiguous criteria which are applied unilaterally may paradoxically actually increase, not decrease, our vulnerabilities to future biological threats," says Friedrichs, a retired major general who worked at the Pentagon before serving at the White House.

Some of the affected scientists say the way NIH has communicated the suspensions has further confused the situation. Volker Briken, who studies *Mtb* at the University of Maryland, says he received the agency's letter on 27 June "completely out of the blue" and responded within 2 days, as requested. He told NIH his group would not perform the specific experiment it had flagged, which called for studying mutations that help *Mtb* dodge immune attack.

"I have not received a response, not even an acknowledgement of our response," says Briken, noting that he also didn't receive a 1 June funding installment for the now-suspended grant. "I have no idea what is going on," Briken says. "We find ourselves at the mercy of whatever direction the current administration chooses to take. Who knows what will happen next." □

PHOTO: NATIONAL INSTITUTE OF ALLERGY AND INFECTIOUS DISEASES/NATIONAL INSTITUTES OF HEALTH

PHOTO: KEITH VANDERLINDE

The current South Pole Telescope would have been replaced with more sensitive arrays.

COSMOLOGY

U.S. cancels hunt for signs of cosmic inflation

Downsizing and high ratings did not save effort known as CMB-S4 **ADRIAN CHO**

A major effort to study the origins of the cosmos has been felled by earthly budget and logistical realities. Last week the U.S. government canceled CMB-S4, a plan to scrutinize the afterglow of the Big Bang, the cosmic microwave background (CMB), for proof that the newborn universe underwent an exponential growth spurt called cosmic inflation. The project had already faced infrastructure problems at one of its planned locations, the South Pole, and it clashed with the White House's proposed cuts to the budgets of its sponsors, the National Science Foundation (NSF) and the Department of Energy's (DOE's) Office of Science.

Project leaders are disappointed but not surprised. "We didn't know what was coming, but we knew it wasn't going to be, 'Let's go, go, go!'" says John Carlstrom, a cosmologist at the University of Chicago who helped lead CMB-S4 from its inception in 2013. He and his colleagues spent the past 14 months eliminating the new instruments at the South Pole from the plan and cutting the project's estimated $900 million cost roughly in half. But last week they received a three-paragraph, unsigned statement stating simply, "DOE and NSF have decided that they can no longer support the CMB-S4 project."

To detect the telltale patterns expected from inflation, the team's roughly 400 researchers envisioned new arrays of ultrasensitive microwave telescopes at the South Pole and in Chile's Atacama Desert, places where the still, dry air is ideal for CMB studies. NSF's South Pole Telescope (SPT), a 10-meter dish, is already scrutinizing the microwave signal, which forms a kind of cosmic wallpaper behind all the stars and galaxies. Other smaller telescopes have studied the CMB from the same vantage point—including one that in 2014 claimed, incorrectly, to have spotted the prized signal CMB-S4 sought. The Atacama has also hosted multiple CMB telescopes, including the privately funded Simons Observatory, which consists of three 0.5-meter telescopes and one 6-meter one.

CMB-S4 aimed to best them all. At the South Pole, researchers envisioned a new 5-meter telescope and 18 telescopes with mirrors 0.55 meters across. In the Atacama, they planned two 6-meter telescopes. All told, the focal planes of all these telescopes would contain 550,000 microwave detectors, 10 times as many as any other array. CMB-S4's primary goal was to detect extremely faint pinwheel-like swirls in the polarization of the CMB. These swirls would be traces of gravitational waves generated during inflation, when the newborn universe doubled and redoubled in size roughly 100 times over in the tiniest fraction of a nanosecond.

In November 2021, CMB-S4 ranked second among ground-based facilities in U.S. astronomers' decadal survey, the community's list of priorities for projects proposed for the subsequent decade. In December 2023, the Particle Physics Project Prioritization Panel ranked it as the highest priority for new facilities. "I don't think NSF and DOE have not built things of that high a priority," says Eric Isaacs, president of the Research Corporation for Science Advancement.

However, in June 2023 NSF warned physicists that the aging infrastructure at the agency's Amundsen-Scott South Pole Station could not support the additional demands of new projects there. In May 2024, NSF declined to advance CMB-S4 from the development phase to design and told researchers they could put no new instruments at the South Pole.

So, the team came up with a Chile-only plan, Carlstrom says. They revised it to incorporate data from the existing SPT and the smaller BICEP Array, a battery of four 0.55-meter microwave telescopes at the South Pole. They also tempered their ambitions to avoid reproducing the capabilities of the Simons Observatory and aimed instead to work with it, Carlstrom says.

But DOE told CMB-S4 researchers the agency couldn't start any major new projects, Carlstrom says. Even before the proposed budget cuts, DOE's Office of Science was struggling to afford multiple major projects, including a new neutrino experiment that will cost $3.2 billion—twice as much as originally estimated.

CMB-S4 was also undermined by the fact that the project progressed so slowly, Carlstrom notes. If it had been realized quickly, it would have had far better sensitivity than any other instrument. However, with planned upgrades, the Simons Observatory and existing South Pole instruments might be able to get within a factor of two of CMB-S4's sensitivity goal, he says, albeit in a decade's time.

At this point, CMB-S4 wouldn't have been much faster. "It had become obvious that the goals of the CMB-S4 project would be difficult to achieve in a timely, cost-efficient way," says Regina Ramieka, DOE's associate director for high-energy physics. "This was not a purely monetary decision."

The DOE and NSF statement says the agencies see CMB studies as a "priority" and "will continue to partner with the CMB science community to explore potential science that can be achieved with limited upgrades to existing experiments." Suzanne Staggs, a cosmologist at Princeton University and co-director of the Simons Observatory, takes some consolation in the positive comments. "It would have been worse if they hadn't said that," she says.

Given the budget cutting fervor in Washington, D.C., the loss of CMB-S4 is likely only the beginning of the heartache for scientists funded by DOE's Office of Science, notes Bill Madia, former director of two DOE national labs. "This may be one of the first [major projects] you see canceled, but I don't think it'll be the last." □

THEY SAID IT

None of the 19 selected publications derived from [the Tuskegee Study of Untreated Syphilis in the Negro Male] ever received a retraction notice or expression of concern.

Mikyung Kim and the late Christopher Shook of the Seoul National University College of Medicine, in the 8 July issue of *Research Ethics*. Citing the infamous study involving 600 Black men as an example, they call on journals to publicly flag papers now seen to be the product of unethical research.

REPLICATION CRISIS

Fruit fly studies mostly defy concerns about irreproducibility

But large verification attempt finds some "suspicious" papers that fare much worse **CATHLEEN O'GRADY**

Attempts to replicate findings from fields including psychology, economics, and cancer biology have often yielded gloomy results. But findings from fruit fly immunology, a field that has been crucial for our understanding of how innate immunity works, are more encouraging. In a pair of preprints uploaded last week, researchers report the majority of claims from more than 50 years of research have already been replicated.

The findings suggest "the literature is, by and large, pretty good," says Brian Lazzaro, an evolutionary geneticist at Cornell University who was not involved with the work. The field may fare better than others because fly researchers have easy access to large sample sizes, and their experiments rest on strong theory, he says, making for "tighter, more focused hypotheses that are easily verifiable."

The study also found, however, that more than one-quarter of the claims have had no published replication attempts—and when the authors tried to reproduce a handpicked subset of these, they could only confirm a small minority. Those that failed replication often did so for interesting reasons that could inspire future research, Lazzaro adds.

Swiss Federal Institute of Technology Lausanne geneticist Bruno Lemaitre, who led the study, says he had long heard mutterings about puzzling results in fruit fly immunology. He wanted to "clean up the field" by providing an overview of which studies were reliable. He and his colleagues searched the academic database PubMed and found 400 papers published between 1959 and 2011 that made testable claims in fruit fly immunology. When they looked at more recent research that had directly tackled the 1006 scientific claims made in those 400 papers, they found 60% had already been "verified." A further 9% had been partly replicated, and 3% had failed to replicate.

Tim Errington, a metascientist at the Center for Open Science, thinks the true replication rate could be lower. He notes that other labs might have failed to replicate the same findings and never published the results. Errington led the Reproducibility Project: Cancer Biology,

A tasty mushroom turns problematic invader

With a nutty flavor, the golden oyster mushroom (*Pleurotus citrinopileatus*) is popular with cooks in its native range of eastern Russia, northern China, and Japan. But in North America, where farmers grow it, it has become an invasive species—the first known example of a cultivated fungus to have run wild. It could have widespread ecological consequences, researchers reported this week in *Current Biology*. The mushroom grows on dead trees, and when Aishwarya Veerabahu of the University of Wisconsin–Madison and colleagues sampled 26 dead elm trees in Wisconsin, they found those with golden mushrooms supported roughly half as many fungal species as trees without. The reduced diversity could slow decay and harm animals that depend on fungi. And the impact could be broad: Data collected by community scientists indicate golden oyster mushrooms now grow in at least 25 U.S. states and a Canadian province. —Erik Stokstad

which in 2021 reported that only eight of 23 preclinical cancer papers had been independently replicated.

Lemaitre and his team did find a lower rate when they turned to some of the 285 claims that did not have any published replication attempts. They selected 45 claims to follow up on themselves, focusing on "suspicious" claims that had drawn private skepticism from many in the community, as well as those that were straightforward to test.

Rather than directly repeat the original experiments, the researchers tested the claims using different methods, to see whether the original findings held up in new contexts. In some cases, they used updated methods—for instance, in place of RNA interference, which "turns down" the volume on a gene by reducing how much protein it makes, they used CRISPR mutants with that gene entirely knocked out.

Of the 45 claims, 38 could not be verified. Many, the authors say, had been published in high-prestige journals such as *Science* and *Nature* and had senior authors affiliated with high-prestige institutions.

A sizable chunk of the failed replications could be explained by the use of updated techniques, the authors say. For instance, a 2008 paper reported that a gene called *Undertaker* played a critical role in enabling immune cells to engulf bacteria. Lemaitre and his colleagues found that the original study, which used RNA interference, had likely targeted a different but related gene; when they used fruit flies that had a broken version of the *Undertaker* gene, they found it made no difference to the ability to engulf bacteria.

The work is "a paradigm for how these studies should be performed in other scientific fields," says Susan Celniker, a fruit fly geneticist at Lawrence Berkeley National Laboratory. She praises the interactive website set up by the team, where other researchers can comment on the claims and replication attempts.

Errington notes that selecting "suspicious" claims for closer examination means the replication rate was always likely to be low. Still, he says all methods of selecting studies to replicate involve "putting your thumb on the scale" in some way.

Salk Institute for Biological Studies immunologist Janelle Ayres, some of whose work on resistance to infection was challenged by the replication effort, says the new experiments sometimes deviated so far from the original methods—changing the food, injection methods, strains of fly, sex, and even the pathogens used—that it's difficult to draw strong conclusions. David Schneider, a microbiologist at Stanford University whose work was also challenged, agrees. "You can't discuss reproducibility until you actually reproduce an experiment," he says.

But using a different method is a useful way to check on original findings, Celniker says. "Just doing one type of experiment is not as powerful as showing it multiple different ways."

And finding that a study falls short when tested with more modern tools doesn't necessarily mean the original work was flawed, Lazzaro says: "That could have been the best work that was possible at that time under those circumstances." Using better techniques to find its limitations is, he says, "a really valuable contribution to the field." □

PHOTO: DOUG WECHSLER/NPL/MINDEN PICTURES

HAUNTED BY SHARKS

After a series of deadly shark attacks, the Indian Ocean island of Réunion became a hub of shark attack science

ALEXA ROBLES-GIL

IN AN INSTANT, one French surfer's tropical vacation became a nightmare. On a late afternoon in February 2011, Éric Dargent was riding the waves off Réunion, a small island in the Indian Ocean renowned for its world-class waves, when a shark mangled his left leg. Luckily, a nearby surfer quickly fashioned a tourniquet to stem the bleeding and helped him ashore. Surgeons ended up amputating Dargent's leg above the knee.

At the time, the attack was seen as unusual. But it turned out to be the beginning of what would become known on Réunion as "*la crise requins*," or the shark crisis. Over the next 8 years, sharks attacked 30 people around the island, killing 11—accounting for an extraordinary 18.5% of known global shark fatalities over that period. The attacks earned Réunion infamy as a "shark island," prompting officials to close its beaches to swimming and surfing, causing immense damage to its lucrative tourism industry.

Scientists, however, flocked to the island. In an effort to understand the outbreak and prevent future attacks, the French government, which oversees Réunion, poured millions of euros into studying shark ecology and behavior, as well as technologies to deter attacks. Réunion soon became a major center for shark attack research, rivaling long-established programs in Australia and South Africa. The work has resulted in scores of scientific papers in a wide range of fields, from ecology to social science, and produced technology now used in other regions to catch dangerous sharks while sparing less threatening animals. It has also fueled controversy—including debates over

In the waters off Réunion, sensors rigged to a surfboard are part of a test of a shark-deterrent device that relies on electric fields.

CREDITS: (PHOTO) ALANVAN GYSEN; (MAP) M. HERSHER/*SCIENCE*

whether wearable electrical devices designed to repel sharks really work and whether the mass killing of the predators increases beach safety—and exposed deep divides in how people view sharks.

Now, officials on Réunion are hoping what scientists have learned will help them reopen beaches and restore the island's reputation and tourism economy. They also hope to rebuild the relationship many islanders had with the sea. Before the attacks, families would spend their weekends playing in the surf, recalls marine biologist Arnault Gauthier, whose family has called Réunion home for nearly 200 years. But the crisis, he says, "has taken away Réunion's identity."

Although shark attacks get headlines, they are relatively rare. Worldwide, a person is more likely to be killed by mishandling fireworks than by a shark, although the risks vary by region. Still, shark attacks on humans have a long history. Archaeologists have found evidence of shark bites on human bones that are roughly 6000 years old. Since the early 1500s, there have been 6800 recorded attacks, according to a database compiled by the International Shark Attack File at the Florida Museum of Natural History.

On Réunion, the earliest recorded shark attack occurred in 1904, when a 16-year-old ship's apprentice attempted to cool off on a hot day by swimming a lap around his vessel. He was "mutilated by a shark" and later died, according to a local newspaper. But sharks weren't considered a serious problem until 2011, when the French surfer lost his leg and then, just a few months later, a shark killed a local bodyboarder off the island's west coast.

The fatalities unsettled the island, sparking calls for action and highlighting a troubling reality: Researchers knew little about the sharks that cruised offshore. The lack of data spurred the government to put nearly 1 million euros into a program known by the French acronym CHARC. It aimed to study the behavior and ecology of two shark species—the bull shark (*Carcharhinus leucas*) and the tiger shark (*Galeocerdo cuvier*)—known for attacking humans.

One of the first questions CHARC addressed was where the sharks were lurking offshore. To track the predators, scientists had to catch and tag them—a task that could be risky and difficult. Working from a small boat in the middle of the night, for example, shark researcher Antonin Blaison reeled in a 3-meter-long bull shark, but the line became entangled on the propeller. He jumped into the ocean as the fish thrashed nearby to disentangle the line so he could tag and release the animal—highly aware that other sharks might be in the area. "I did something very crazy," recalls Blaison, now at the Réunion Island Marine Observatory. "I won't do that again."

Blaison also faced challenges back on land. "[People] said I was a criminal," he says, because he was releasing captured sharks instead of killing them. Some islanders even accused him of somehow causing sharks to attack people.

Despite such issues, CHARC, which ran from 2011 to 2015, produced useful findings. Data from 46 tagged tiger sharks showed they were seasonal visitors to Réunion and preferred offshore waters, researchers reported in the *African Journal of Marine Science* in 2015. In contrast, tag data from 36 bull sharks showed the presence of males peaked in winter and females stayed year-round. Data also showed bull sharks often cruised close to the shore, especially during the afternoons, when most attacks occurred, and at night.

"For science, these were very good results," Blaison says. "But for security, it was quite bad," because they showed sharks stayed close to shore all year. And many islanders were frustrated the research didn't point to clear solutions. "There is a huge gap," he says, "between what [people] want to know and what research can bring to solve the problem."

That frustration burst into public protests in 2015 when a 13-year-old surfing champion named Elio Canestri died after being dragged out to sea by a shark. Some residents called for greater efforts to kill sharks, such as by using drumlines, baited hooks hanging from buoys that were developed in Australia in the 1960s to protect beaches. Hooked sharks and other animals are either killed or released. But others opposed such methods. They worried that drumlines, for instance, would indiscriminately kill harmless shark species and other marine creatures.

Driving much of the fear and anger was the big question that haunted Réunion: Why did shark attacks increase so suddenly?

Nearly 15 years of research have shown there's no single answer. But scientists have identified a number of possible contributors.

One is Réunion's rapid human population growth, a team from the University of Réunion reported in *Scientific Reports* in 2018. From 1980 to 2016, the population grew by 67% to nearly 1 million. The arrival of surfing in the 1960s also made Réunion a top recreation destination. More people on the island and in the water increased the risks of surfers and swimmers encountering dangerous sharks.

The boom also catalyzed changes in urban development and agriculture that altered runoff patterns and made some coastal waters more attractive to certain sharks. In the early 2000s, engineers built an irrigation system that moves water from east to west across the island to support new farms. The resulting runoff lowered salinity off of Réunion's west coast, creating an attractive habitat for bull sharks, which prefer lower saline waters and can even survive in freshwater. "We are living in a world where there is a huge degradation of the marine environment," says marine ecologist Sébastien Jaquemet of the University of Réunion.

Bull sharks, which can grow to 3.5 meters long and weigh more than 200 kilograms, were involved in many of the roughly 30 attacks on surfers and swimmers that occurred off Réunion from 2011 to 2019.

A ban on selling shark meat was another possible factor. In the mid-1990s, nearly 100 people died on nearby Madagascar after eating shark meat carrying ciguatoxin, a neurotoxin produced by algae that accumulate in the food chain. In response, officials on Réunion banned the sale of shark meat, which reduced fishing for the animals and potentially allowed their populations to increase. Some islanders have also blamed a marine reserve created in 2007 off western Réunion, saying

PHOTO: PETE OXFORD/MINDEN PICTURES

it protected schools of forage fish that attracted hungry sharks. There are few hard data to support either theory, however.

To some, the lack of clarity is disappointing. But, "If anyone tells you they know the reason for [the crisis]," Gauthier says, "they're lying to you."

The uncertainty hasn't prevented scientists from searching for ways to prevent attacks. In 2016, the government created the Shark Security Centre on Réunion to bring together scientists, risk managers, and policymakers. It has since made the island a testing ground for a wide range of deterrence tools and strategies. One project, for example, tested the effectiveness of drones, which have been used successfully in California to spot white sharks and help develop forecasting tools that predict when sharks are more likely to show up. On Réunion, however, the researchers discovered that sharks were difficult to spot because of the island's black sand beaches and coastal waters often muddied by cyclones.

Another major effort has tested electric deterrents, devices made by a number of companies that emit electric fields claimed to repel sharks. Sharks have sensory organs in their heads called the ampullae of Lorenzini that detect electrical fields and help them navigate and hunt. Electric deterrents are designed to essentially blind a shark, like a bright light blinding a person, says Gauthier, who has spent years studying these devices.

On Réunion, surfers are now required to wear one of the devices in secured surfing areas, commonly attached to their ankle or surfboard. But the surfing community has long questioned the efficacy of electric deterrents. To test whether they could deter bull sharks, the center's team traveled to New Caledonia, a French territory in the South Pacific Ocean known for its abundance of the species. They spent 21 days testing how the sharks responded to baits accompanied by five different electric deterrents. Initially, one type protected baits 43% of the time, they found, two others 16% of the time, whereas the remaining two did not work at all. Even the deterrents that worked initially became less effective over time, with sharks eventually showing no hesitation in attacking the static baits, the team reported in *Scientific Reports* in 2020. (The researchers believe this kind of habituation is unlikely to occur with surfers or swimmers wearing the devices.) Though disappointing to some people, Gauthier says the findings were "still a good result," because they could prevent surfers from trusting devices that may not work.

The Réunion research push did yield one product that has had worldwide impact: a drumline that

Keeping sharks at bay

Researchers who study shark attacks on humans have experimented with a variety of methods for preventing harmful encounters. There is no single solution, but layered defenses can help keep swimmers and surfers safe.

Graphic by **NOELLE BURGESS**

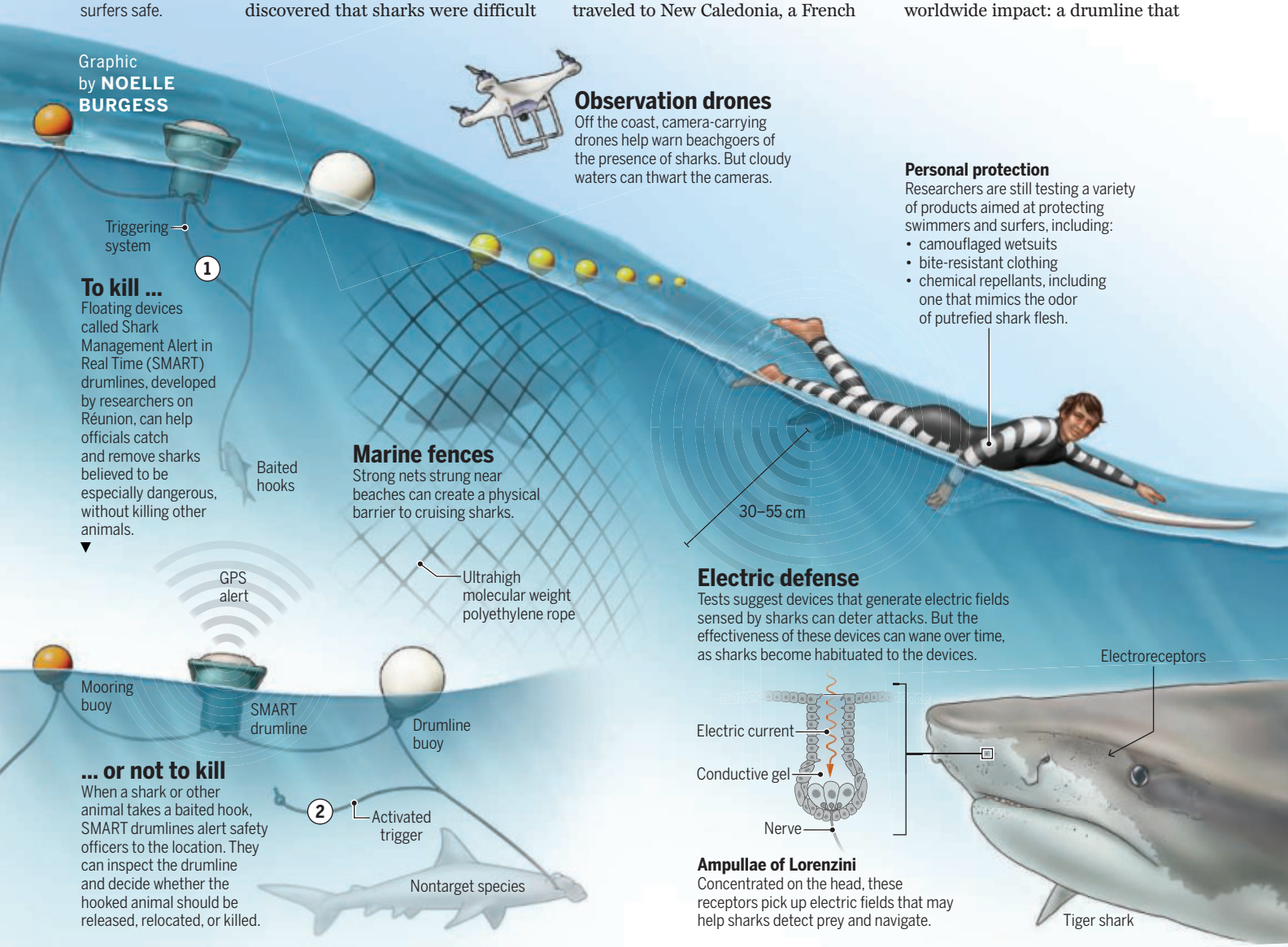

automatically texts its location to observers via satellite when an animal is hooked. Sharks caught on conventional drumlines often die before anyone can reach them, which results in the deaths of many harmless animals. But the signal enables officials to quickly visit the buoy and decide whether to kill, relocate, or release the animal. Fisheries engineer David Guyomard worked with a local fisherman to develop the device, called the Shark Management Alert in Real Time (SMART) drumline. A 3-year trial of 20 SMART drumlines deployed off Réunion found that 87% of 269 caught animals were recovered alive, a far higher survival rate than seen with conventional drumlines, Guyomard and colleagues reported in *Fisheries Research* in 2019.

Now used in Australia, the SMART drumline is "a world first" and "a huge deserver of accolades," says Geremy Cliff, a retired marine biologist in South Africa who's led efforts to prevent shark attacks for the past 4 decades. It's often used in programs aimed at killing larger sharks, which are believed to be more dangerous. On Réunion, the devices have also helped researchers study the genetics, diet, ecology, and growth of sharks. The catch data have suggested, for example, that the local population of bull sharks, which appear to have been responsible for most of the Réunion attacks, has decreased, Jaquemet says.

Drumlines also make it possible to systematically kill sharks, which has fed controversy. Since 2018, a "preventive fishing program" on Réunion has used SMART drumlines to catch and kill 68 bull sharks and 543 tiger sharks. Many islanders support the program, but animal rights and conservation groups have gone to court to try to stop it, arguing that sharks are important to the marine ecosystem and that there's no proof the culling prevents attacks.

The Shark Security Centre's director of operations, Michaël Hoarau, says the culling program tries to walk a fine line between protecting biodiversity and preventing attacks. "It's difficult," he says. "We're trying to find a balance." He notes the 802 sharks caught off Réunion over 11 years pales in comparison with the tens of millions killed by commercial fisheries each year. And even scientists who are not thrilled by culling concede it would take a carefully designed study to prove it's not effective. "You can't argue that a shark that's been fished is a shark that's not going to bite someone down the line," Gauthier says. "There's literally no argument against it."

Researchers on Réunion developed the Shark Management Alert in Real Time drumline, which sends an alert when it has hooked a shark, enabling safety officials to decide whether to release or kill it.

Still, after years of discussion, the center recently decided to alter its culling program, by releasing juvenile tiger sharks instead of killing them, with a goal of tagging and tracking some of these animals. Late last year, it also handed the data collected by the program to a group of independent scientists for review. Among other things, they'll try to evaluate the fishing program's impact on local marine biodiversity and its effectiveness at reducing shark attack risks.

It's now been 6 years since the last known fatal attack off Réunion, which took the life of surfer Kim Mahbouli in 2019. Since then, officials have been slowly reopening some surfing spots and experimenting with layered defenses, including exclusion nets, boat patrols, underwater freedivers who spot sharks, and automated cameras that use artificial intelligence to detect sharks. Earlier this year, the French government also amended the islandwide swimming and surfing ban, relaxing some restrictions on swimming.

There's no guarantee these measures will prevent another shark attack, Hoarau says. But when a dozen of the field's leading researchers gathered on the island earlier this year to review its efforts, they found few faults. "I don't know why they needed us. They're doing everything correctly already," says Gavin Naylor, a researcher at the Florida Museum of Natural History. "Réunion has addressed the issue in a very state-of-the-art approach," adds André Afonso, a marine ecologist at the University of Coimbra who has led efforts to prevent shark attacks in Brazil, though he hopes the island will ultimately be able to replace its fishing program with nonlethal alternatives.

The researchers, who include shark risk specialists from Australia, South Africa, the United States, and other nations, are now working on a paper reviewing shark deterrence efforts on Réunion and around the world. Hoarau hopes others will be able to learn from the island's painful experience. "We can't copy-paste what's happened in Réunion to another area, but at least some lessons can be learned from what our region went through," he says.

One thing researchers have learned, Gauthier says, is that steps to prevent shark attacks will be shaped not just by science, but also by how people view sharks. "Either they're innocent puppies that haven't harmed anyone … or they are bloodthirsty monsters," he says. The reality, he adds, is that sharks are neither. "They are wild animals and can be very dangerous," he says. "But they aren't going to hunt every human in the water." □

PHOTO: ALAN VAN GYSEN

PHYSICS

A new age of molecular chirality

Advanced optical approaches reshape the frontiers of chiral sensing

Olga Smirnova[1,2,3]

In Lewis Carroll's novel *Through the Looking-Glass, and What Alice Found There*, the characters Tweedledum and Tweedledee are nonsuperimposable mirror images of each other. A geometrical property that distinguishes this asymmetry is chirality, which also describes the distinct handedness of a molecule. Enantiomers—a pair of left-handed and right-handed versions of the same molecule—are ubiquitous in living organisms, often with enantiomeric excess (one handedness prevails over the other). This dominance ensures uniform chirality across the amino acids, which stabilizes proteins, as well as stereospecific interactions among proteins that support metabolic processes. However, abnormal enantiomeric excess of common medium-sized chiral molecules in living organisms, such as carbohydrates and amino acids, is linked to conditions such as cancer, brain disorders, and kidney diseases (*1*). Thus, new optical methods that distinguish the handedness of enantiomers could be transformative in research and development, from neuroscience and medicine to the pharmaceutical industry.

Although differentiating chirality of a large object may be easy, probing chirality with both precision and speed is challenging in the microscopic world (*1*). Chemical methods such as chromatography can precisely detect and separate enantiomers. However, speed is inherently limited because separation at practical scales occurs on timescales of tens of seconds. By contrast, optical techniques exploit attosecond (10^{-18} s)–to–picosecond (10^{-12} s) light-matter interactions, potentially enabling rapid chirality analysis. Traditional optical methods, such as absorption circular dichroism, use circularly polarized light—in which the electric field vector rotates in a circle while the light propagates through space, tracing a helical path (see the figure)—to identify the handedness of a molecule. However, when the wavelength of light far surpasses the size of a molecule, the electric field that surrounds the molecule becomes effectively homogeneous in space, losing its helical shape. Consequently, the fraction of signal arising from chirality relative to the total signal decreases substantially. Thus, resolving chiral molecular biomarkers, which can be thousands of times smaller than the wavelength of visible light, using traditional optical methods is very challenging (*1*).

Next-generation optical methods use local interactions between a molecule and light to determine chirality (*2*). These new methods are several orders of magnitude more effcient than traditional optical methods (*3*). Among these approaches, photoelectron circular dichroism (*3*) differentiates chirality by analyzing the asymmetric distribution of electrons that are ejected from a randomly oriented molecule upon local interactions with circularly polarized light. Molecules of opposite handedness preferentially emit electrons in opposite directions with respect to the light propagation axis. This method can detect chirality at a high speed with subpercent (<1%) precision (*4*, *5*). Because of its high enantio-sensitivity, photoelectron circular dichroism provides new perspectives on the origins of homochirality (the dominance of a single chirality) in biological molecules on Earth. For example, it is proposed that circularly polarized light in the cosmos can break the balance between left and right enantiomers by selectively destroying or forming one enantiomer over the other through absorption circular dichroism. However, photoelectron circular dichroism—enantio-sensitive direction of electron ejection by circularly polarized light—is orders of magnitude stronger, causing opposing recoil of left and right chiral molecular ions. This recoil could spatially separate molecular enantiomers in the cosmos, thereby influencing chiral bias on Earth (*6*).

Molecular chirality can be encoded in a... three-dimensional chiral trajectory...

Molecular chirality can be encoded in a time-dependent three-dimensional chiral trajectory of an electric field vector, which is associated with the charge current excited by a light field in a molecule (*7*). Such a trajectory is local because its chirality is expressed in time and not in space. A pump-probe method excites a molecule with a light beam, then probes its nonequilibrium chiral dynamics (electronic, vibrational, or rotational) by applying a subsequent light beam. This technique can discriminate the chirality of a molecule through time-resolved measurements of the directional changes of the charge current associated with nonequilibrium dynamics excited by circularly polarized light (*7*). The ability to discern the chirality of molecular structure in this manner is due to opposite temporal chirality of charge currents in opposite enantiomers.

The concept of temporal chirality is applicable to any vector, such as the electric field vector of light, as long as its trajectory is three-dimensional and handed (*2*). Combining multiple light beams of different wavelengths propagating at an angle to each other (tight focusing or noncollinear light) makes light locally chiral at every point in space (*8*). The shape of such a three-dimensional chiral trajectory can be adjusted by controlling the relative delays between oscillations of electric fields of light at different wavelengths. Locally chiral light can distinguish molecular chirality by matching the handedness of temporal trajectories of locally chiral light and locally chiral charge currents induced in the molecule. When they compare favorably, new frequencies of light are emitted by the molecule. By contrast, the emission is suppressed when the trajectories do not match.

Probing chirality with light

Optical techniques exploit the interaction between light waves and a molecule to determine an enantiomer, which is a left-handed or right-handed version of the same molecule. Locally chiral light may improve the speed and precision of chiral measurements compared with traditional methods that use circularly polarized light.

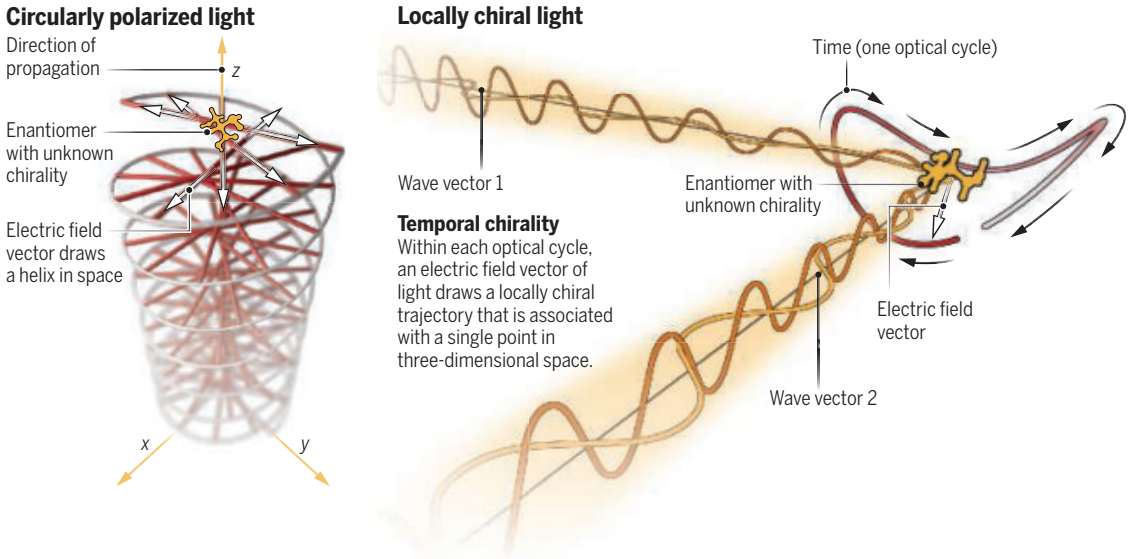

Resolving temporal chiral trajectories of light polarization or charge currents involves nonlinear processes. The lowest-order nonlinear process is sum frequency generation, in which two photons of different frequencies combine to generate a third photon with a frequency equal to the sum of the two. Locally chiral light induces interference of conventional nonlinear optical response with a sum-frequency emission that is specific to a chiral molecule (*2*). This interference can make one enantiomer dark and the other bright. Using this scheme at free-electron lasers could allow localized excitation of electrons in chiral molecules, enabling efficient detection of molecular handedness at specific atomic sites.

Interactions between matter and locally chiral light bring opportunities for separating enantiomers by optical forces (*9*) and enantiosensitive population transfer in rotational (*10*), vibrational (*11*), or electronic states of a molecule. Efficient control over excitations in various degrees of freedom could allow the observation of exotic phenomena such as parity violation energy splitting, a tiny energy difference between enantiomers arising from weak nuclear forces that violate mirror symmetry (*12*). It can also reduce molecular motion of chiral molecules (cooling) to isolate and study specific quantum states of enantiomers. Furthermore, locally chiral light can imprint chirality on achiral matter by creating chiral superpositions (a quantum state combining two components with a defined phase relation) of highly excited states of atoms (*2*). Such atoms can be used for studying many-body chiral interactions or act as a chiral sensor of its environment at varying distances. These distances are controlled by the principal quantum number of the chiral superposition, which is excited by the locally chiral field.

An unusual opportunity for chiral discrimination may arise at the interface of chirality and topology. The time-dependent chiral trajectory of charge currents in a molecule depends on the relative orientations of the molecule to the polarization plane of the light that drives these currents. Different molecular orientations give rise to various temporal chiral shapes that contribute to the chiral signal. A collection of several temporal chiral shapes gives rise to an object with a specific topology within the abstract space of molecular orientations. Topology encompasses geometric properties that remain unchanged through continuous shape deformations. Such robust properties can often be expressed as a single number called a topological invariant. If an enantio-sensitive observable, such as a change in molecular excitations, is proportional to the topological invariant, it also becomes robust. For example, external factors such as the fluctuation of a laser, variation in detector response, dilution of samples, and small fluctuations in enantiomeric excess would not affect the measurement.

Identifying geometric quantities that characterize the manifold (collection) of chiral temporal shapes, such as curvature, in the electronic and optical response of gas-phase molecules is one way to link topology and local chirality. This yields new curvature-driven observables such as enantio-sensitive molecular orientation (*13*). Another option for exploring the interface between topology and chirality in gas-phase molecules (*14*) is to combine locally chiral light with so-called vortex beams (light beams shaped like a tornado with a dark spot in the middle) or by modulating frequencies of locally chiral light (*15*). These could enable topologically robust detection of small fluctuating values of enantiomeric excess (*14*) and enantio-sensitive quantized rates of frequency conversion (*15*), respectively.

Chirality emerges as a key aspect in new technologies developing in fields as diverse as nanotechnology and material and life sciences. Beyond sensing chirality, the nonlinear interaction between locally chiral light and matter could allow for imprinting and manipulating properties (such as electron and spin transport) of handed molecules and materials. This could open a pathway to chiral information processing that is faster than conventional spintronic devices and operates at ambient conditions. However, careful examination of the underlying physics is needed by combining experiments and theoretical models. □

REFERENCES AND NOTES

1. Y. Liu, Z. Wu, D. W. Armstrong, H. Wolosker, Y. Zheng, *Nat. Rev. Chem.* **7**, 355 (2023).
2. D. Ayuso, A. F. Ordonez, O. Smirnova, *Phys. Chem. Chem. Phys.* **24**, 26962 (2022).
3. L. Nahon, G. Garcia, I. Powis, *J. Electron Spectrosc. Relat. Phenom.* **204**, 322 (2015).
4. A. Kastner *et al.*, *ChemPhysChem* **17**, 1119 (2016).
5. A. Comby *et al.*, *Phys. Chem. Chem. Phys.* **25**, 16246 (2023).
6. R. Hadidi *et al.*, *Commun. Chem.* **4**, 72 (2021).
7. S. Beaulieu *et al.*, *Nat. Phys.* **14**, 484 (2018).
8. P. Král, M. Shapiro, *Phys. Rev. Lett.* **87**, 183002 (2001).
9. R. P. Cameron, D. McArthur, A. M. Yao, *New J. Phys.* **25**, 083006 (2023).
10. J. Lee *et al.*, *Phys. Rev. Lett.* **128**, 173001 (2022).
11. D. S. Tikhonov *et al.*, *Sci. Adv.* **8**, eade0311 (2022).
12. I. Erez, E. R. Wallach, Y. Shagam, *Phys. Rev. X* **13**, 041025 (2023).
13. A. F. Ordonez *et al.*, arXiv:2409.02500 (2025).
14. N. Mayer *et al.*, *Nat. Photonics* **18**, 1155 (2024).
15. K. Schwennicke, J. Yuen-Zhou, *J. Phys. Chem. Lett.* **13**, 2434 (2022).

ACKNOWLEDGMENTS

The author acknowledges funding from the European Union (ERC, ULISSES, 101054696). The author gratefully acknowledges helpful discussions with L. Nahon, Y. Mairesse, and J. Riedel. The author holds a related US Patent Application (No. 17/562,691).

10.1126/science.adn0905

[1]Theory Department, Max-Born Institut, Berlin, Germany. [2]Fakultät II–Mathematik und Naturwissenschaften,, Technische Universität Berlin, Berlin, Germany. [3]Department of Physics, Technion–Israel Institute of Technology, Haifa, Israel. Email: olga.smirnova@mbi-berlin.de

GRAPHIC: A. FISHER/*SCIENCE*

CELL BIOLOGY

Polyglycine proteins leave transfer RNAs unglued

Disruption of transfer RNA processing may unite the pathogenesis of CGG repeat expansion disorders

Mridu Kapur[1,2] and **Susan L. Ackerman**[1,2]

Microsatellites or short tandem repeats (STRs) account for about 3% of the human genome. These segments of DNA sequence (typically 1 to 6 base pairs) are repeated multiple times in a row and are highly unstable in a length-dependent manner because of slippage during genome duplication. Slippage can add repeat units over cycles of cell division, and such expansion of these repeats over a threshold size has been linked to more than 50 genetic disorders (*1*). Notably, CGG/GGC repeat expansion in different genes causes neurodegenerative diseases with overlapping clinical and histopathological features, suggesting that these disorders have a common pathophysiology (*2*). However, a shared molecular pathway has remained elusive (*3*–*5*). On page 253 of this issue, Yang *et al.* (*6*) report that disruption of transfer RNA (tRNA) processing by polyglycine proteins produced from CGG/GGC repeats unites these diseases.

One of the best-characterized repeat expansions is in the 5′-untranslated region (UTR) of the gene encoding fragile X messenger ribonucleoprotein 1 (*FMR1*). Expansion of *FMR1* CGG repeats beyond 200 copies prevents transcription of the gene, causing fragile X syndrome. This is a neurodevelopmental disorder characterized by intellectual disabilities and autistic-like behaviors. Expansion between 55 and 200 repeats does not silence *FMR1* transcription but increases risk for fragile X–associated tremor/ataxia syndrome (FXTAS), a neurodegenerative disease characterized by gait ataxia, parkinsonism (tremors, muscle stiffness), and protein aggregates in cell nuclei (nuclear inclusions) (*4*). The FXTAS-associated *FMR1* CGG repeats are translated from a noncanonical start codon to produce a polyglycine protein flanked by locus-specific amino acids (*4*, *7*). Similarly, neuronal intranuclear inclusion disease (NIID), which is clinically indistinguishable from FXTAS, is caused by expansion to more than 60 GGC repeats in the 5′-UTR of the gene encoding Notch 2 N-terminal like C (*NOTCH2NLC*). These repeats are translated from an upstream start codon to generate a toxic polyglycine-containing protein (*5*). Although the translation of repeats into polyglycine underlies pathogenesis, the relative contribution of polyglycine versus flanking amino acid sequences and the exact mechanism of toxicity are controversial (*2*–*5*, *7*).

To separate the effects of the polyglycine repeats from the endogenous genomic context, Yang *et al.* expressed either a benign or pathogenic number of GGC repeats fused to green fluorescent protein in a human cell line. Consistent with previous studies, the authors observed repeat number–dependent formation of insoluble polyglycine protein aggregates. Mass spectrometry revealed that the aggregates also incorporated other proteins with glycine-rich domains, including family with sequence similarity 98 member B (FAM98B).

FAM98B is a member of the five-subunit tRNA ligase complex (tRNA-LC). tRNAs are small noncoding RNAs that are essential for protein synthesis. A subset of tRNA-encoding genes contains an intron, a short sequence that must be removed from precursor RNAs to generate functional tRNAs. tRNA introns are excised by the tRNA splicing endonuclease (TSEN) complex and the cleavage factor polyribonucleotide kinase subunit 1 (CLP1). The resulting tRNA halves (exons) are then ligated by the tRNA-LC to generate mature tRNAs (*8*). Yang *et al.* found that the recruitment of FAM98B to polyglycine aggregates results in sequestration of the other four components of the tRNA-LC as well. This caused a depletion of the tRNA-LC from the soluble proteins in the cell and thus likely reduced the amounts of functional tRNA-LC. Indeed, expression of pathogenic polyglycine repeats led to an accumulation of unligated exons of intron-containing tRNA genes. To address whether these defects in tRNA splicing were relevant to human CGG/GGC repeat expansion disorders, the authors investigated patient tissues. tRNA-LC subunits were present in nuclear inclusions in both FXTAS and NIID patients. They also identified a substantial increase in tRNA halves from intron-containing tRNAs in FXTAS patients. In mice, depletion of *Fam98B* impaired motor coordination and caused reactive gliosis. Studies that investigate whether prevention of FAM98B recruitment to aggregates can rescue polyglycine disease in animal models should help to confirm the role of the tRNA-LC in pathogenesis.

How depletion of the tRNA-LC leads to cellular dysfunction is unclear. Mutations in the TSEN complex and CLP1 cause pontocerebellar hypoplasia, a neurodegenerative disorder that shares characteristics with FXTAS and NIID, supporting the conclusion that disruption of tRNA splicing is involved in the pathogenesis induced by polyglycine protein aggregates (*8*). However, the identity and toxicity of tRNA intermediates generated by impaired splicing remain controversial (*9*, *10*). Further, although changes in the amount of mature tRNA have been associated with disease, the studies that identified these links have involved either complete loss of multiple tRNA-encoding genes, or additional mutations in genetically interacting genes (*11*, *12*). Although Yang *et al.* observed that polyglycine expression or *Fam98B* depletion causes substantial accumulation of tRNA fragments, only subtle changes were observed in the amount of the corresponding mature tRNAs, suggesting an alternative mechanism to produce mature tRNAs. Indeed, a recent study determined that RNA 5′-phosphate and 3′-OH ligase 1 (RLIG1) can function as a tRNA ligase, which could enable completion of tRNA splicing when the tRNA-LC is depleted or compromised (*13*).

Yang *et al.* provide compelling evidence that disruption of the tRNA-LC may play a critical role in polyglycine-associated neurodegenerative diseases. Previous studies have identified thousands of polymorphic CGG repeats in the human genome, many of which are associated with genes involved in neurodevelopment, suggesting that this pathology may play an even broader role in neurological disease (*14*, *15*). □

REFERENCES AND NOTES

1. C. Depienne, J.-L. Mandel, *Am. J. Hum. Genet.* **108**, 764 (2021).
2. Z.-D. Zhou, J. Jankovic, T. Ashizawa, E.-K. Tan, *Nat. Rev. Neurol.* **18**, 145 (2022).
3. J. Yu *et al.*, *Proc. Natl. Acad. Sci. U.S.A.* **119**, e2208649119 (2022).
4. C. Sellier *et al.*, *Neuron* **93**, 331 (2017).
5. M. Boivin *et al.*, *Neuron* **109**, 1825 (2021).
6. J. Yang *et al.*, *Science* **389**, eado2403 (2025).
7. P. K. Todd *et al.*, *Neuron* **78**, 440 (2013).
8. C. K. Hayne, T. A. Lewis, R. E. Stanley, *Wiley Interdiscip. Rev. RNA* **13**, e1717 (2022).
9. C. E. Monaghan *et al.*, *Proc. Natl. Acad. Sci. U.S.A.* **118**, e2110730118 (2021).
10. A. E. Schaffer *et al.*, *Cell* **157**, 651 (2014).
11. L. A. Hughes *et al.*, *Nat. Commun.* **14**, 2210 (2023).
12. R. Ishimura *et al.*, *Science* **345**, 455 (2014).
13. Y. Hu *et al.*, *Proc. Natl. Acad. Sci. U.S.A.* **121**, e2408249121 (2024).
14. B. Trost *et al.*, *Nature* **586**, 80 (2020).
15. D. J. Annear *et al.*, *Sci. Rep.* **11**, 2515 (2021).

ACKNOWLEDGMENTS

S.L.A. is an investigator of the Howard Hughes Medical Institute and a scientific advisory board member of Tevard Biosciences.

10.1126/science.adz2236

[1]University of California San Diego, La Jolla, CA, USA. [2]Howard Hughes Medical Institute, La Jolla, CA, USA. Email: sackerman@health.ucsd.edu

COMPUTATIONAL BIOLOGY

Disorder meets its match

Designed protein pockets recognize intrinsically disordered protein regions

Alan M. Moses[1,2] *and* **Julie D. Forman-Kay**[3,4]

Most proteins encoded in the human genome work in groups to carry out specific functions (*1*). For example, mitochondrial complex I, which is responsible for the cell's energy production, has a defined number of subunits that are largely bound by stable interactions (*2*). By contrast, certain tasks such as cellular information processing (or "signaling") require dynamic interactions. Proteins bind to each other only briefly to transmit information, then separate. Such transient complexes often include proteins bearing intrinsically disordered regions that do not adopt a stable folded structure. This structural variability makes targeting disordered regions challenging. On page 252 of this issue, Wu *et al.* (*3*) report a powerful tool to design small, folded protein domains that interact tightly with intrinsically disordered protein regions. This enables an efficient means for generating direct binders of disordered regions of proteins that are involved in key biological functions and diseases.

Customized binding pockets

Existing computational methods tailor a peptide or a small molecule that targets a folded binding pocket of a protein. Designing a binding pocket that can fit the target disordered region sequence provides a general solution to recognition of intrinsically disordered proteins, which lack folded domains.

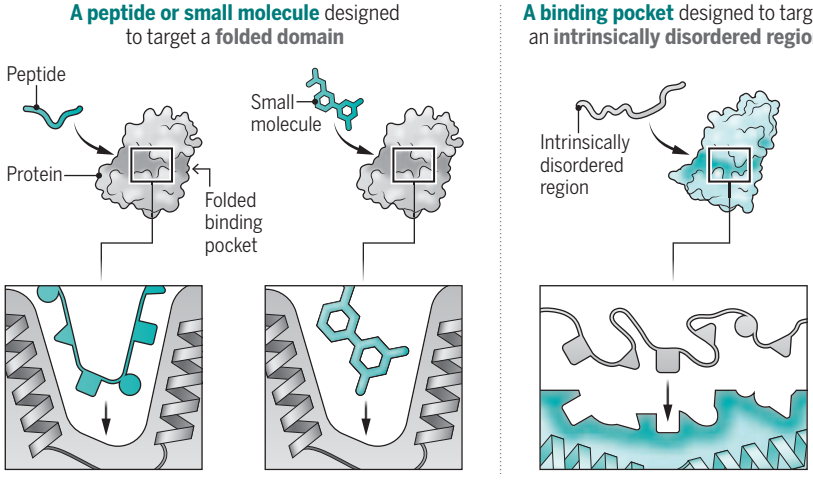

Intrinsically disordered regions make up approximately one-third of the amino acids in the human proteome—the entire set of proteins encoded by all human genes (*4*). These exist as ensembles of rapidly interconverting states instead of more static tertiary, folded structures. Multiple interacting elements of a disordered region can underlie dynamic complexes, such as short motifs that are recognized by peptide-recognition domains, which regulate protein-protein interactions by binding to short peptide sequences. For example, the Src homology 2 protein domain recognizes phosphorylated tyrosine-containing peptide motifs, as part of regulating cellular processes (*5*). The proteome allows for millions of potential similar interactions (*6*) that are responsible for dynamic functions. Computational methods have previously been applied to design interactions of peptide-recognition domains. For example, a tight binder for the folded Src homology 3 domain of a signaling protein called growth factor receptor–bound protein 2 was produced using a deep learning approach (*7*). However, previous strategies mainly focused on targeting binding pockets within folded domains by optimizing physicochemical interactions with small proteins, peptides, or small molecules (*7*–*9*). Because intrinsically disordered regions lack folded binding pockets, it is generally impossible to use existing structure-based machine learning design methods for disordered targets.

Instead of finding a binder to a specific structure (*7*), Wu *et al.* created a folded binding pocket that can fit the peptide sequence of the target disordered region (see the figure). These designed peptide recognition domains can bind to certain arbitrary peptide sequences with nanomolar affinity. The authors generated template libraries of pockets that form intermolecular interactions with target peptide backbones (without side-chain groups). Optimal matches of binder pockets to a specific peptide sequence of an intrinsically disordered region, including amino acid side chains, were identified by searching the template library. Candidate binder pocket matches were further refined by testing various combinations of the target and the matched binders. Wu *et al.* also demonstrated specificity of designed binder domains by using binding assays and in cells. Colocalization of a fluorescent protein that is fused to the binders with their targets indicated that the produced binder domains function in cells.

The approach of Wu *et al.* does not rely on inducing a folded state of the disordered target by the binder pocket. In addition, the demonstrated high-affinity interactions between binders and targets are beyond what is observed in nature. These were clearly demonstrated by the designed binder for the intrinsically disordered neuropeptide dynorphin A, which plays an important role in pain perception. Structural characterization of the binder-target complex confirmed that the bound intrinsically disordered segment is in an extended conformation and does not adopt secondary or tertiary structure to gain high affinity. The observed structural features were different from the known complexes of dynorphin A bound to its native binding proteins. The designed binders displayed much stronger affinity to the target than the native complexes of dynorphin A. This implies that highly favorable interactions can be made with many residues along an extended peptide chain.

Given the increasing recognition of intrinsically disordered proteins in disease states, molecules that bind to and modulate the activity of these proteins could have great therapeutic potential. However, only a few small molecules with nanomolar affinity to disordered regions have been identified, such as ralaniten, which binds to the disordered N-terminal region of the androgen receptor (*10*). Thus, the designed binder pockets could represent new classes of medicines. In particular, intrinsically disordered regions are critical for biomolecular condensates (dynamic compartments without bounding lipid membranes), which regulate cellular processes in

GRAPHIC: N. BURGESS/*SCIENCE*

both normal and disease states (*11*). Therapeutics to modulate such condensates are under development (*12*), and the custom-tailored peptide recognition domains could be an important component. These binders could also be used as antibody-like drugs to compete with or replace specific binding of endogenous proteins in disease states. In addition, such binders could also be valuable as research reagents—for example, to investigate biophysics and functions of disordered protein regions.

Perhaps one of the most intriguing applications for designed peptide recognition domains could arise when they are combined with synthetic disordered regions (*13*). The number of possible disordered protein sequences is astronomical but relatively easy to explore computationally (*14*). The approach of Wu *et al*. could be used to engineer interactions between synthetic disordered proteins and customized peptide recognition domains that are orthogonal to any endogenous interactions. These "fully customized" protein interaction networks could help build dynamic assemblies within a cell—for example, new condensates or readouts of natural signaling activity. This can facilitate a wide range of experimental and translational applications that were not previously accessible. □

REFERENCES AND NOTES

1. L. H. Hartwell, J. J. Hopfield, S. Leibler, A. W. Murray, *Nature* **402**, 47 (1999).
2. K. Fiedorczuk *et al*., *Nature* **538**, 406 (2016).
3. K. Wu *et al*., *Science* **389**, eadr8063 (2025).
4. A. S. Holehouse, B. B. Kragelund, *Nat. Rev. Mol. Cell Biol*. **25**, 187 (2024).
5. T. Pawson, G. D. Gish, P. Nash, *Trends Cell Biol*. **11**, 504 (2001).
6. P. Tompa, N. E. Davey, T. J. Gibson, M. M. Babu, *Mol. Cell* **55**, 161 (2014).
7. J. Dauparas *et al*., *Science* **378**, 49 (2022).
8. S. Bhat *et al*., *Sci. Adv*. **11**, eadr8638 (2025).
9. K. Rezaee, H. Eslami, *Artif. Intell. Rev*. **58**, 156 (2025).
10. M. D. Sadar, *Expert Opin. Drug Discov*. **15**, 551 (2020).
11. S. F. Banani, H. O. Lee, A. A. Hyman, M. K. Rosen, *Nat. Rev. Mol. Cell Biol*. **18**, 285 (2017).
12. N. N. Foressi, L. C. Rodríguez, M. S. Celej, *Biophys. Rev*. **17**, 491 (2024).
13. A. Garg, N. S. González-Foutel, M. B. Gielnik, M. Kjaergaard, *Protein Eng. Des. Sel*. **37**, gzae004 (2024).
14. B. Strome, K. Elemam, I. Pritisanac, J. D. Forman-Kay, A. Moses, bioRxiv 2023.04.28.538739 (2023).

ACKNOWLEDGMENTS

The authors thank Z. H. Liu for discussions. The authors acknowledge support from the Canadian Institutes of Health Research (PJT-148532). A.M.M. acknowledges the Canada Foundation for Innovation . J.D.F.-K. acknowledges funding from the National Institutes of Health (R01GM127627). J.D.F.-K. holds a Canada Research Chair in Intrinsically Disordered Proteins.

10.1126/science.adz5035

[1]Department of Cell and Systems Biology, University of Toronto, Toronto, ON, Canada. [2]Department of Computer Science, University of Toronto, Toronto, ON, Canada. [3]Program in Molecular Medicine, The Hospital for Sick Children, Toronto, ON, Canada. [4]Department of Biochemistry, University of Toronto, Toronto, ON, Canada. Email: alan.moses@utoronto.ca; forman@sickkids.ca

IMMUNOLOGY

RORing for oral tolerance

An antigen-presenting cell subtype tames the immune response to food antigens in early life

Cecilia Johansson

Throughout life, everyone is exposed to foreign antigens that enter the body through the skin, lungs, and gut. In particular, early life sees the ingestion of many new types of food and encounters with microbes that colonize mucosal tissues. How immune systems learn to "tolerate" foreign antigens, yet remain quickly responsive to other threats such as pathogenic viruses and bacteria, remains an unsolved problem in immunology. On page 268 of this issue, Cabric *et al*. (*1*) describe a key piece of the puzzle. The authors identify a subtype of antigen-presenting cells (APCs) in the mesenteric lymph nodes in mice that help train regulatory T cells (T_{reg} cells) to suppress inflammatory responses to food antigens in the period around weaning. The identification of this APC subtype potentially opens the door to the development of therapies for food-associated allergies and inflammatory diseases.

Oral tolerance of ingested, nonharmful foreign antigens is key to avoiding overreactive immune responses that result in intestinal inflammation, food allergies, or celiac disease (an intestinal autoimmune response to dietary gluten) (*2*). T_{reg} cells are important mediators of oral tolerance. They differentiate from naïve T cells (those that express CD4) that are specific for food and commensal antigens in the lymph nodes that drain the gut. These antigen-specific T_{reg} cells then migrate back to the gut where they prevent other immune cells from launching destructive responses to those antigens. How naïve $CD4^+$ T cells are instructed to become food-specific T_{reg} cells has long been unclear, although recent studies (*3*–*7*) are beginning to point to candidate APCs.

The findings... challenge the dogma that dendritic cells...are key for prompting oral tolerance.

Intestinal APCs that induce the differentiation of T_{reg} cells and tolerance to microbial constituents of the gut were recently discovered (*2*). Their hallmark is the expression of an isoform of the retinoic acid receptor–related orphan receptor gamma transcription factor (RORγt), which is important for the differentiation and function of multiple immune cell types (*8*). In the context of oral tolerance, these APCs have been identified using diverse criteria and given different names, including $ROR\gamma t^+$ APCs (*6*), $ROR\gamma t^+$ dendritic cells (*4*, *9*), extrathymic AIRE-expressing cells (*7*), and tolerizing dendritic cells that express PR domain containing 16 (*5*). Although most of these studies have focused on laboratory mice, seemingly equivalent APCs can be found in human gut–draining lymph nodes (*5*, *10*, *11*). However, the degree to which various APC types identified in mice and humans overlap remains to be determined, as does agreement on their nomenclature.

Referring to them as Thetis cells (TCs), Cabric *et al*. provide a comprehensive analysis of $ROR\gamma t^+$ APCs in mice, implicating some of them in the differentiation not only of commensal-specific T_{reg} cells but also those that recognize food antigens. There are several types of TCs, and the authors show that the $ROR\gamma t^+$ TC IV subset, which is exclusively found in the gut and gut-draining lymph nodes,

Serving up food antigens

Food antigens sampled by cells in the small intestine are taken up by RORγt⁺ Thetis cell subtype IV (TC IV). These cells present the antigens, on MHC-II, to naïve CD4⁺ T cells in mesenteric lymph nodes. Actived TGF-β then drives their differentiation into T_{reg} cells. These cells migrate back to the intestine and suppress immune responses to food antigens, limiting inflammation and food allergies.

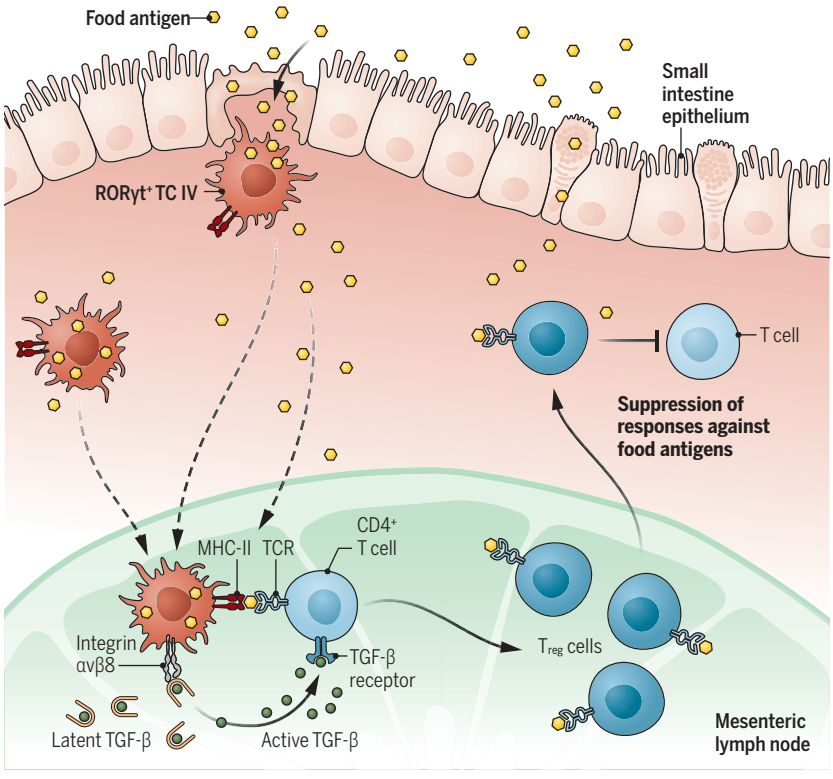

MHC-II, major histocompatibility complex class II; RORγt, retinoic acid receptor-related orphan receptor gamma transcription factor; TCR, T cell receptor; TGF-β, transforming growth factor–β; T_{reg} cell, regulatory T cell.

GRAPHIC: K. HOLOSKI/*SCIENCE*

is critical for the development of food-specific T_{reg} cells. They found that the subtype TC IV express integrin alpha V beta 8 heterodimer protein (αvβ8), major histocompatibility complex class II (MHC-II), retinaldehyde dehydrogenase 2, and interferon regulatory factor 8 (*11*). The authors also observed that TC IV readily take up the antigen ovalbumin delivered to mice by oral gavage. By following OVA-specific CD4⁺ T cells that were infused into ovalbumin-gavaged animals, Cabric *et al.* noted that conversion into T_{reg} cells in mesenteric lymph nodes was absent when RORγt⁺ cells were deficient in MHC-II. This resulted in intestinal inflammation when mice were given a second exposure to ovalbumin. This response was attributed to uncontrolled T helper cell responses to the antigen, including the release of cytokines that activate other immune cells to combat threats. Furthermore, mice tolerized to ovalbumin by oral gavage were also protected from developing lung inflammation upon subsequent intranasal administration of the antigen.

Notably, Cabric *et al.* found that the number of TC IV in mice was greatest during the periweaning phase, when the immune system displays a higher threshold for immune activation (*12*). This constitutes a window of opportunity (*13*) for inducing oral tolerance to reducing food allergies. One explanation may be that TC IV can also attenuate responses to intestinal pathogens. As such, their decline in number after early life may represent a strategy to bolster protection to infection later in life while meeting the need to develop tolerance to food and commensals during the important postnatal period.

How do these TC IV instruct naïve CD4⁺ T cells to preferentially differentiate into T_{reg} cells? Cabric *et al.* show that TC IV express integrin αvβ8, which is key for converting latent transforming growth factor–β (TGF-β) into its active form. By using bone marrow chimeric mice (bone marrow has been replaced with that from a different mouse), the authors found that both antigen presentation and conversion of latent TGF-β are needed for RORγt⁺ cells to stimulate T_{reg} cell development in the mesenteric lymph nodes (see the figure). It is unclear whether additional features of TC IV contribute to triggering T_{reg} cell production.

The findings of Cabric *et al.* challenge the dogma that dendritic cells, the main APCs involved in instruction of most CD4⁺ T cell responses, are key for prompting oral tolerance. The authors report that dendritic cells are dispensable for stimulating the development of T_{reg} cells specific to oral antigens yet seem to have a role in sustaining early antigen-experienced CD4⁺ T cells that are differentiating toward the T_{reg} cell fate under instruction from TC IV.

Future studies will be needed to assess how long food-specific T_{reg} cells and tolerogenic responses are maintained and whether established tolerance can be broken. Furthermore, it will be interesting to determine how and where TC IV access antigens and how their responses might differ between exposure to small amounts of food antigens that are ingested frequently and exposure to a few high-doses of antigen (as with experimental ovalbumin). It will also be fascinating to explore how food-specific T_{reg} cells could be generated when there are already primed inflammatory T helper cells specific for the same antigens or in scenarios in which exposure to new food antigens occurs concomitantly with infection or antibiotic treatment. It is possible that in this situation, a balance of APCs that induce T_{reg} cell production versus APCs that prime proinflammatory T helper cells determines whether tolerance is maintained or broken (*3*). It will be important to explore whether T_{reg} cell–promoting APCs in the gut function in humans as they do in mice and whethers oral tolerance can be leveraged clinically to ameliorate autoimmunity, transplant rejection, and neuroinflammation. □

REFERENCES AND NOTES

1. V. Cabric *et al.*, *Science* **389**, 268 (2025).
2. V. Cerovic, O. Pabst, A. M. Mowat, *Nat. Rev. Immunol.* **25**, 42 (2025).
3. M. C. C. Canesso *et al.*, *Science* **387**, eado5088 (2024).
4. P. F. Rodrigues *et al.*, *Cell* **188**, 2720 (2025).
5. X. Fu *et al.*, *Nature* **637**, 965 (2025).
6. A. Rudnitsky *et al.*, *Nature* (2025).
7. I.-H. Sun *et al.*, *J. Exp. Med.* **222**, e20250573 (2025).
8. G. Eberl, *Mucosal Immunol.* **10**, 27 (2017).
9. H. Narasimhan *et al.*, *Proc. Natl. Acad. Sci. U.S.A.* **122**, e2417308122 (2025).
10. A. U. Antonova *et al.*, *Proc. Natl. Acad. Sci. U.S.A.* **120**, e2318710120 (2023).
11. B. Akagbosu *et al.*, *Nature* **610**, 752 (2022).
12. V. Verhasselt, *Immunol. Rev.* **326**, 117 (2024).
13. Y. A. P. Iza, C. C. Brown, *Immunol. Rev.* **323**, 303 (2024).

ACKNOWLEDGMENTS

C.J. acknowledges suport from the Medical Research Council (MR/V000659/1, MR/X001075/1, and MR/Y004450/1).

10.1126/science.adz5931

National Heart and Lung Institute, Imperial College London, London, UK.
Email: c.johansson@imperial.ac.uk

CLIMATE CHANGE

The pursuit of 1.5°C endures as a legal and ethical imperative in a changing world

As the world nears 1.5°C of global warming, near-term emissions reductions and adequate adaptation become ever more important to ensure a safe and livable planet for present and future generations

Joeri Rogelj[1,2,3] and **Lavanya Rajamani**[4,5]

Since the 2015 adoption of the Paris Agreement (PA; see table S1), the planet has all but reached 1.5°C of global warming—a limit included under the PA to protect vulnerable populations from the most severe impacts of climate change. With global warming approaching 1.5°C, some scientists have argued that recognizing the precise year when 1.5°C is reached is of utmost urgency (*1*). Their reasoning is that reaching 1.5°C of global warming will trigger questions on what needs to be done to meet the PA's goal. We explain that although approaching 1.5°C is deeply worrying, a robust response requires no such precision. Legal and policy implications do not abruptly emerge but gradually strengthen in importance before, at, and after crossing 1.5°C (see the figure). The pursuit of efforts to limit warming to 1.5°C is, and remains, a critical part of the PA, directing efforts in mitigation, adaptation, and broader climate governance.

Our planet's climate is in a dire state, and 2024 was the hottest year on record, with global average temperatures 1.6°C higher than during the preindustrial period (*2*). This 1.6°C figure consists of the underlying long-term global warming trend, which stood at 1.3° to 1.4°C in 2024 (*3*), combined with short-term natural variability that can make individual years slightly warmer or cooler than the long-term average. The PA's global warming limit of 1.5°C refers to this underlying long-term trend (*4*). At present, global warming is increasing by around 0.26°C per decade (*3*), and climate policies slow down but do not yet curb this trend. Policies presently on the books suggest central estimates of about 2°C of warming by 2050 and almost 3°C by the end of the century (*5*). Even the most optimistic projections, assuming all announced greenhouse gas (GHG) emissions reduction targets are diligently implemented, see median warming estimates peaking at 1.7°C with a 1-in-10 chance of exceeding 2.3°C (*5*).

These projections are not definitive. Countries can submit more ambitious pledges to the PA, called nationally determined contributions (NDCs), over the course of this year or overachieve pledges already made. However, recent geopolitical developments—including President Trump's executive orders that withdraw the US from the PA, roll back low-carbon policies, set up trade barriers, support fossil fuels, and undercut governance and research—add to, rather than reduce, uncertainties around this projection and increase the estimates of the lowest levels of global warming that can be avoided.

Fundamentally, the chances of keeping warming to 1.5°C are small. Global warming might already be at 1.5°C today (*3*), and our central estimate is that it will exceed 1.5°C over the next decade, with ambitious near-term emission reductions instrumental in limiting the estimated likelihood and magnitude of overshoot but unable to categorically avoid it. This sobering realization begs the question of how the scientific, policy, and legal communities can respond to the world's failure to keep global warming to levels that limit climate risks within acceptable bounds. We argue that most of the consequences are already applicable today, in a world approaching 1.5°C of global warming.

ENDURING TEMPERATURE GOAL

The 1.5°C warming limit is key in international climate law and policy, and its underpinning rationale does not change when 1.5°C of warming is reached. The 1992 United Nations Framework Convention on Climate Change (UNFCCC; see table S1) identified the objective of the climate regime as "stabilization of GHG concentrations in the atmosphere at a level that would prevent dangerous anthropogenic interference with the climate system" (UNFCCC, article 2). The understanding of what was considered dangerous, left undetermined at the time, was concretized in the PA (see table S2). In response to scientific advances and increasing political will, the level was set as one that would hold global warming to "well below 2°C" while pursuing efforts toward limiting it to 1.5°C. Parties to the PA chose this level because they recognized that "this would significantly reduce the risks and impacts of climate change" [PA, article 2.1(a)]. As more compelling evidence emerged of the discernible differences in risks and impacts between 2° and 1.5°C (*6*) and scientific assessments showed that high climate risks can already be expected at lower levels of warming (*7*), the emphasis in the PA goal shifted to 1.5°C (see table S3).

Although the emphasis, rightly, in response to the science, is on 1.5°C, the PA temperature goal covers a range from "well below 2°C" to 1.5°C (*8*). Article 2 does not exclude temporary exceedance of 1.5°C. Meanwhile, the PA's aim to reach net-zero GHG emissions in the second half of the century (PA, article 4.1) implies that warming should peak well before the end of the century but does not provide a precise timing. Exceeding 1.5°C therefore does not render the goal irrelevant.

The nature of the precise goal that is being frustrated matters. Frustration of a goal might render that goal irrelevant in a context

where the goal is no longer achievable, for instance, if the goal is to protect a species but the species becomes extinct. This is not the case, however, where the goal remains within reach, albeit through a different path, as in the case of the goal to limit global warming to 1.5°C. Indeed, exceedance of 1.5°C, rather than rendering the goal irrelevant, is a wake-up call alerting Parties to redouble their efforts to bring emissions down and thereby halt or even reverse the increase in global warming. The anchoring of the temperature goal, from the UNFCCC to the PA, to the levels of unacceptable risks and impacts of climate change is a testament to its enduring salience. Just as climate risks and impacts increase as temperatures rise, so, too, does the salience of pursuing efforts to return warming to 1.5°C.

CONTINUING OPERATIONAL RELEVANCE

Moreover, the PA's temperature goal has continuing operational relevance, whether its limits are breached or not. The temperature goal informs requirements relating to the setting, tracking, and strengthening of Parties' NDCs (PA, articles 3, 4, and 14), all of which remain in place and indeed assume greater importance as global warming approaches, reaches, and exceeds 1.5°C. The temperature goal, and, in particular, the consensus on 1.5°C, has been underscored in numerous judicial decisions in national courts (e.g., in the Belgian Klimaatzaak) and has been relied on by States before the International Court of Justice in relation to its Advisory Opinion on Climate Change (see table S1). The driving force of the PA's temperature goal, especially as 1.5°C is exceeded, tightens expectations of States and underscores the urgency of a commensurate response.

The PA's temperature goal also informs the standard of due diligence expected of States in relation to climate harm. The customary principle of harm prevention reflected in the Rio Declaration on Environment and Development (principle 2; see table S1) generates a stringent standard of due diligence for States in relation to climate harm. This standard of due diligence is informed by, among other things, the temperature goal and the nature and extent of harms that would occur in the absence of due diligence (*9*). Every 0.1°C increase in peak temperature increases loss and damage (*6*, *7*) as well as the risk of key tipping points being triggered in the Greenland and West Antarctic Ice Sheets, Atlantic Meridional Overturning Circulation, and Amazon rainforest (*10*). Overshoot pathways for 1.5°C have a markedly higher risk of triggering these tipping points, as compared with scenarios in which warming remains below 1.5°C (*11*). The extent by which 1.5°C is exceeded therefore increases climate harm substantially (*6*, *7*, *12*) and presents evidence that States have not exercised the due diligence required of them. Due diligence would then require States to take actions to limit the magnitude and length of overshoot, in order to limit harm and avoid triggering even more catastrophic impacts.

SHIFTING MITIGATION PERSPECTIVES

Exceeding 1.5°C strengthens rather than weakens States' obligations to develop and communicate NDCs that reflect their highest possible ambition (PA, article 4.3). These expectations do not suddenly emerge when 1.5°C is reached (see the figure). They apply at any point before, at, or after 1.5°C and are therefore not hampered by imprecision around the exact timing of when 1.5°C would be reached.

Note that even in a world that has exceeded 1.5°C of global warming, States can continue to pursue 1.5°C-aligned pathways. Though this may seem counterintuitive, such pathways would reflect each State's equitable contribution to limiting warming to 1.5°C from a year-2015 perspective, the year the PA was adopted.

Meanwhile, reaching and exceeding 1.5°C makes clear that some States have failed to do their fair share. Their disproportionate consumption of the global carbon budget in line with 1.5°C needs to be addressed through continued action to lower emissions, both domestically and by supporting others, and through plans to reach net negative emissions that reverse the excess (*13*). Also, this represents a gradual shift of society's long-term focus: from reaching global net-zero GHG emissions as already indicated under the PA to achieving and managing a sustainable net-negative emissions economy to limit overshoot of 1.5°C as much as possible in both magnitude and duration (*12*). In the near-term, however, mitigation expectations before, at, or after crossing 1.5°C remain the same. They need to represent a country's highest possible ambition.

Exceeding 1.5°C of global warming also has implications for developing States that have not yet exhausted their equitable share of the global carbon budget. Beyond 1.5°C, scientific evidence shows (and governments have acknowledged) that additional GHG emissions will expose poor and vulnerable populations, particularly in developing countries, to potentially existentially dangerous harm (*6*, *7*). This reality creates a tension between these States' claims to emit an equitable share of the GHGs within a global PA-aligned carbon budget—their equitable access to atmospheric space—and their obligations to take all feasible measures to mitigate and adapt to climate change in order to protect their citizens from breaches of a range of human rights.

MOUNTING ADAPTATION RISKS

Risk management dictates that adaptation plans should focus on levels of warming that cannot yet be excluded rather than the temperature limits that the world aspires to avoid. The realization that 1.5°C is crossed reemphasizes

Legal and climate policy implications of approaching 1.5°C of global warming

Implications and expectations do not suddenly emerge when 1.5°C is reached. They are already fully applicable well before warming reaches 1.5°C and gradually strengthen in importance before, at, and after crossing 1.5°C, not hampered by imprecision around the exact timing of when 1.5°C would be reached.

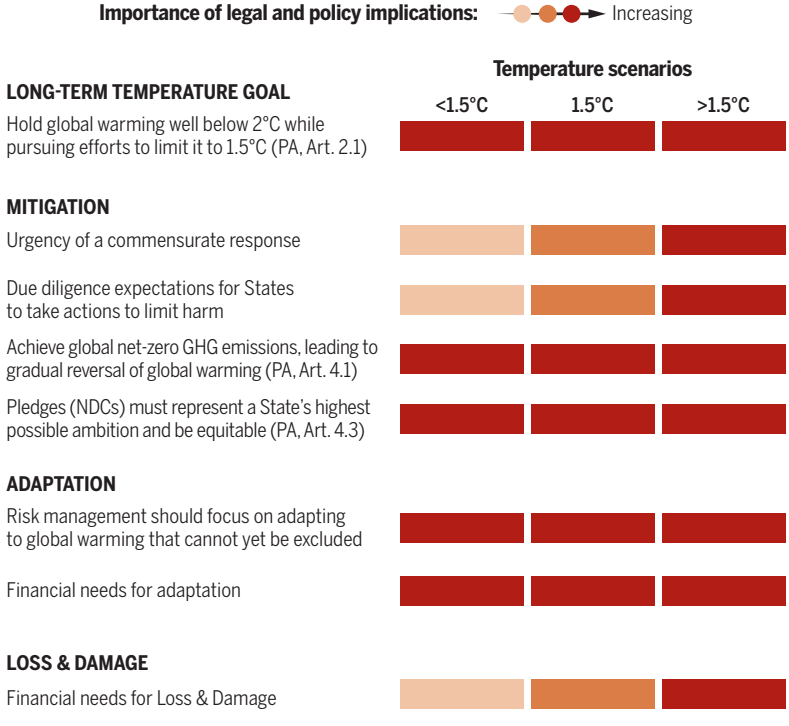

PA, Paris Agreement; Art., Article; GHG, greenhouse gas; NDCs, Nationally Determined Contributions

GRAPHIC: V. PENNEY/*SCIENCE*

An activist highlights the 1.5°C goal during a demonstration in Berlin in October 2021.

but doesn't change this position. As indicated above, present policy estimates point to warming close to 2°C by mid-century and 3°C by the end of it (*5*). Children alive today risk experiencing global warming crossing 4°C over the course of their lifetime (*5*). These daunting levels of climate change should remain at the front and center of adaptation and resilience efforts as long as global GHG emissions are not curbed. Even if an overshoot of 1.5°C can be limited in extent and magnitude, the possibility of warming being reversed toward the end of the century provides no respite for adaptation planners (*12*). Although integral to achieving the mitigation aim of the PA, reversal of global warming depends first on achieving net-zero carbon dioxide (CO_2) emissions and sustained aggregate CO_2 removal thereafter—a formidable challenge at present and one that will require appropriate legal and governance frameworks to be put in place.

INCREASING CLIMATE COSTS

As we exceed 1.5°C of global warming, climate risks and impacts escalate. Adaptation needs will become more pressing, and financial needs to compensate for climate-related loss and damage will increase. One study estimates the global costs of extreme weather attributable to climate change in the past 20 years at US$143 billion per year (*14*). Although costs of Loss and Damage are estimated in the hundreds of billions of US dollars, the United Nations Fund for responding to Loss and Damage has thus far attracted pledges that are about three orders of magnitude smaller (see table S1).

ENDURING SALIENCE

The prospect of global warming reaching 1.5°C is deeply concerning and demands sustained attention and decisive action. Approaching, reaching, and surpassing 1.5°C will have profound implications, disproportionally affecting the poor and vulnerable. In response, global climate governance needs to veer toward better and tighter mechanisms of accountability to achieve near-term emissions reductions and a commensurate focus on adaptation, loss and damage, and support.

Critical observers might question whether the goals under the PA matter in a context where the world's largest economy has decided to leave the agreement. We argue that it does and will continue to do so. First, analysis suggests that despite its shortcomings, the PA has contributed to raising ambition and lowering GHG emissions. A review of the first 5 years of the PA's operation found that it is effective in the production of shared norms that raise ambition (*15*). For example, before the PA, estimates put the world on track for a 4°C temperature rise over the course of this century. Presently, this estimate stands about 1°C lower as a result of climate policies that have been adopted since (*5*). Second, the PA is located in a wider multilateral rules-based environment that has evolved over centuries and can withstand and adapt to, as it has in the past, temporary geopolitical shifts and shocks. Finally, the inescapable nature of the consequences of climate change and the need for a globally effective response to this challenge mean that a collective solution must be found. The framework offered by the PA provides the only globally inclusive forum at present.

Despite the challenges posed by today's geopolitical landscape, the PA's goal to pursue efforts to limit global warming to 1.5°C therefore endures as the legal and ethical imperative to secure a safe and livable planet for present and future generations. □

REFERENCES AND NOTES

1. R. A. Betts *et al.*, *Nature* **624**, 33 (2023).
2. World Meteorological Organization (WMO), "WMO confirms 2024 as warmest year on record at about 1.55°C above pre-industrial level" (WMO, 2025).
3. P. M. Forster *et al.*, *Earth Syst. Sci. Data* **16**, 2625 (2024).
4. J. Rogelj, C.-F. Schleussner, W. Hare, *Geophys. Res. Lett.* **44**, 10662 (2017).
5. J. Rogelj, M. G. J. Den Elzen, J. Portugal Pereira, in *Emissions Gap Report 2024: No More Hot Air…Please! With a Massive Gap Between Rhetoric and Reality, Countries Draft New Climate Commitments* (United Nations Environment Programme, 2024), pp. 26–34.
6. Intergovernmental Panel on Climate Change (IPCC), *Global Warming of 1.5°C: An IPCC Special Report on the Impacts of Global Warming of 1.5 °C above Pre-Industrial Levels and Related Global Greenhouse Gas Emission Pathways, in the Context of Strengthening the Global Response to the Threat of Climate Change, Sustainable Development, and Efforts to Eradicate Poverty*, V. Masson-Delmotte *et al.*, Eds. (Cambridge Univ. Press, 2018), pp. 3–24.
7. IPCC, "Summary for policymakers" in *Climate Change 2023: Synthesis Report. Contribution of Working Groups I, II and III to the Sixth Assessment Report of the Intergovernmental Panel on Climate Change*, Core Writing Team *et al.*, Eds. (IPCC, 2023), pp. 1–34.
8. L. Rajamani, J. Werksman, *Philos. Trans. A Math. Phys. Eng. Sci.* **376**, 20160458 (2018).
9. L. Rajamani, *Curr. Leg. Probl.* **77**, 167 (2024).
10. T. Möller *et al.*, *Nat. Commun.* **15**, 6192 (2024).
11. N. Wunderling *et al.*, *Nat. Clim. Change* **13**, 75 (2023).
12. C.-F. Schleussner *et al.*, *Nature* **634**, 366 (2024).
13. S. Pelz *et al.*, *Proc. Natl. Acad. Sci. U.S.A.* **122**, e2409316122 (2025).
14. R. Newman, I. Noy, *Nat. Commun.* **14**, 6103 (2023).
15. K. Raiser, U. Kornek, C. Flachsland, W. F. Lamb, *Environ. Res. Lett.* **15**, 083006 (2020).

SUPPLEMENTARY MATERIALS

science.org/doi/10.1126/science.ady1186

Published online 19 June 2025
10.1126/science.ady1186

[1]Centre for Environmental Policy, Imperial College London, London, UK. [2]Grantham Institute for Climate Change and Environment, Imperial College London, London, UK. [3]Energy, Climate and Environment Program, International Institute for Applied Systems Analysis, Laxenburg, Austria. [4]Faculty of Law, University of Oxford, Oxford, UK. [5]St Peter's College, University of Oxford, Oxford, UK. Email: j.rogelj@imperial.ac.uk

PHOTO: NA FASSBENDER/GETTY IMAGES

CALL FOR PAPERS

SPJ
SCIENCE PARTNER JOURNALS

北京理工大學
BEIJING INSTITUTE OF TECHNOLOGY

中国航天 中国空间技术研究院
China Academy of Space Technology

Space: Science & Technology

Space: Science & Technology is an online-only, Open Access journal published in affiliation with **Beijing Institute of Technology (BIT)** and distributed by the **American Association for the Advancement of Science (AAAS)**. BIT cooperates with China Academy of Space Technology (CAST) in managing the journal. The journal promotes the exploration and research of space worldwide, to lead the rapid integration and technological breakthroughs of interdisciplinary sciences in the space field, and to build a high-level academic platform for discussion, cooperation, technological progress and information dissemination among professional researchers, engineers, scientists and scholars.

Submit your research to *Space: Science & Technology* today!

Learn more at **spj.science.org/space**

The Science Partner Journal (SPJ) program was established by the American Association for the Advancement of Science (AAAS), the nonprofit publisher of the *Science* family of journals. The SPJ program features high-quality, online-only, Open Access publications produced in collaboration with international research institutions, foundations, funders and societies. Through these collaborations, AAAS furthers its mission to communicate science broadly and for the benefit of all people by providing top-tier international research organizations with the technology, visibility, and publishing expertise that AAAS is uniquely positioned to offer as the world's largest general science membership society.

Visit us at **spj.science.org**

@SPJournals **@SPJournals and @SpaceSciTech** **@SPJournals**

OPEN ACCESS

ARTICLE PROCESSING CHARGES CURRENTLY WAIVED FOR ALL ACCEPTED ARTICLES

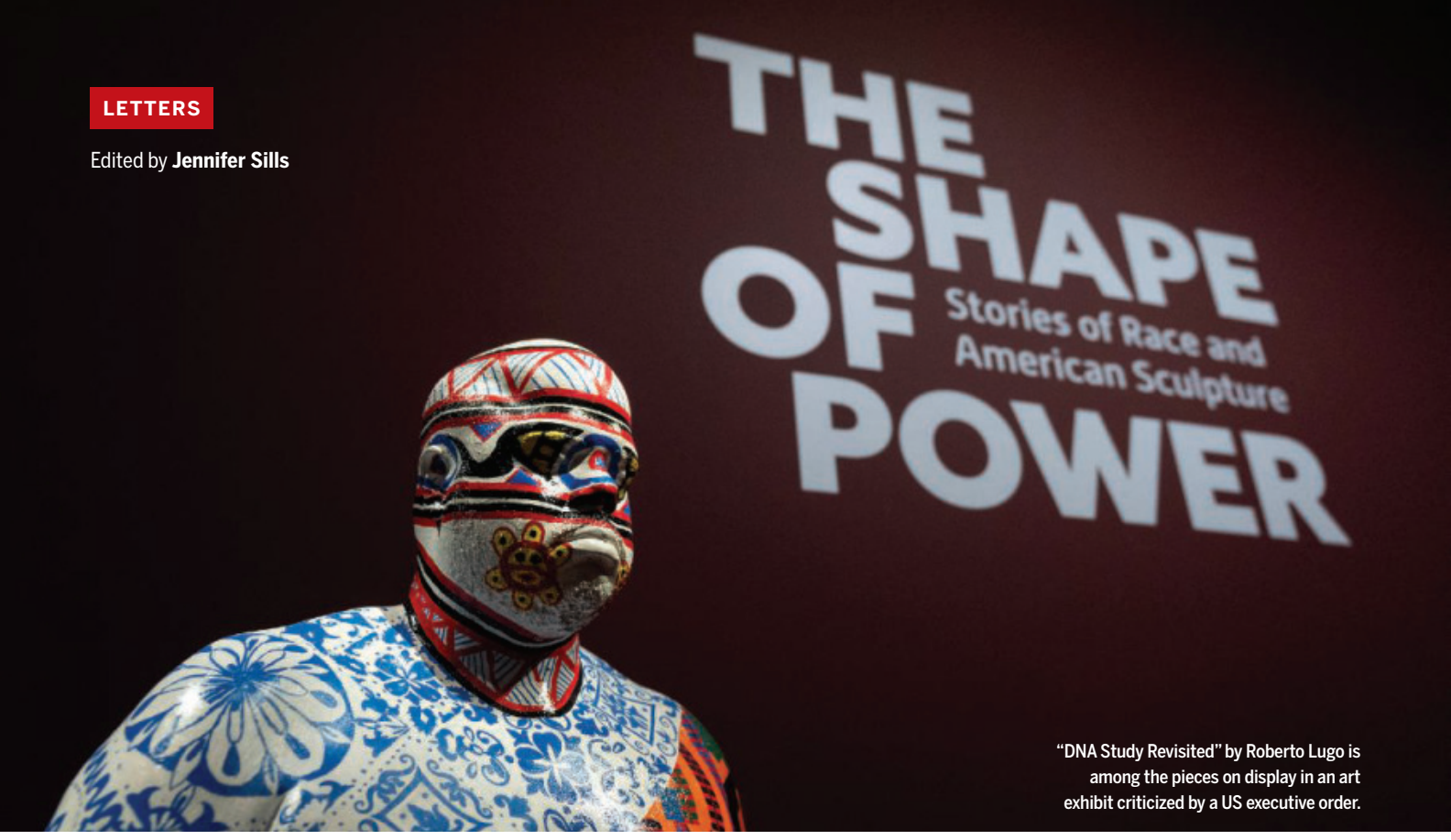

"DNA Study Revisited" by Roberto Lugo is among the pieces on display in an art exhibit criticized by a US executive order.

PHOTO: MARK SCHIEFELBEIN/AP

US disregards scientific consensus on race

The Trump administration's executive order 14253 of 27 March 2025 aims to prevent "replacing objective facts with a distorted narrative driven by ideology rather than truth" and criticizes an art exhibit that defines race as a social construct rather than a biological reality (*1*). This understanding of race, which the Trump administration considers a "divisive, race-centered ideology" (*1*), is supported by decades of research in social and biological sciences that have resulted in the consensus that the modern human species does not contain biological races (*2*–*4*). It is imperative that scientists publicly refute the president's false claim. It is not divisive to illustrate examples of how scientific racism has harmed US society.

The biological definition of race has been applied to nonhuman species of organisms on the basis of physical, geographic, genetic, and phylogenetic similarities (*5*–*7*). However, no biological definition of race can be accurately applied to subgroups of humans, especially not subgroups based on social definitions of race (*3*, *8*), which arbitrarily use physical, geographic, cultural, and linguistic criteria. This consensus is based upon many lines of genetic and evolutionary evidence, particularly data showing that the amount of genetic variation that occurs within human populations is much greater than genetic variation between populations, and that human populations cannot be considered evolutionarily unique lineages (*6*, *9*). Human genetic variation is continuous and cannot be unambiguously divided into biological races. Two recent blue-ribbon panels initiated by the National Academy of Sciences, Medicine, and Engineering have underscored the lack of concordance between social definitions of race and human biological variation (*10*, *11*).

The administration's attempts to resuscitate scientifically disproven schemes serve a political agenda. Scientific racism has been associated with US social institutions since the country's founding and has caused great harm to millions of Americans (*12*). The artists, historians, scientists, and sociologists who have detailed the dynamics of this ideology are not the ones distorting the truth. It is the US president, in attempting to silence these scholars by executive fiat, who is perpetrating a "divisive, race-centered ideology."

Joseph L. Graves Jr.[1], Alan Goodman[2], Stacy Farina[3], Yolanda Moses[4]

[1]Department of Biology, North Carolina A&T State University, Greensboro, NC, USA. [2]Department of Anthropology, Hampshire College, Amherst, MA, USA. [3]Department of Biology, Howard University, Washington, DC, USA. [4]Department of Anthropology, University of California, Riverside, Riverside, CA, USA. Email: gravesjl@ncat.edu

REFERENCES AND NOTES

1. US Office of the President, "Restoring truth and sanity to American history" (Executive Order 14253, 27 March 2025).
2. American Anthropological Association, "AAA statement on race" (AAA, 1998); https://americananthro.org/about/policies/statement-on-race/.
3. A. Fuentes *et al.*, *Am. J. Phys. Anthropol.* **169**, 400 (2019).
4. J. L. Graves, Jr., *Cold Spring Harb. Perspect. Biol.* **15**, a041454 (2023).
5. T. Dobzhansky, *Genetics and the Origin of Species* (Columbia Univ. Press, ed. 3, 1969).
6. A. R. Templeton, *Evolution* **61**, 1507 (2007).
7. J. L. Graves, A. Goodman, *Racism Not, Race: Answers to Frequently Asked Questions* (Columbia Univ. Press, 2022).
8. A. Montagu, *Mankind's Most Dangerous Myth: The Fallacy of Race* (Harper & Brothers, 1942).
9. G. Coop, arXiv 10.48550/arXiv.2207.11595 [Preprint] (2022).
10. National Academies of Sciences, Engineering, and Medicine, *Using Population Descriptors in Genetics and Genomics Research: A New Framework for an Evolving Field* (National Academies Press, 2023).
11. National Academies of Sciences, Engineering, and Medicine, *Rethinking Race and Ethnicity in Biomedical Research: A New Framework for an Evolving Field* (National Academies Press, 2025)
12. C. Brace Loring, *Race is a Four-Letter Word: The Genesis of the Concept* (Oxford Univ. Press, 2005).

10.1126/science.ady2266

US should reject color-blind racial ideology

The Trump administration's executive orders (EOs) 14281 (*1*), 14173 (*2*), and 14151 (*3*) suggest that diversity, equity, inclusion, and accessibility (DEIA) initiatives give jobs and other opportunities to unqualified women and people of color. These EOs use "color-blind"

language and ideology (*4*)—unfounded claims that structural racism no longer exists (*4*, *5*)—to attempt to create a false narrative that ongoing "preferential treatment" for people in protected categories leads to favoritism that must be eliminated in the name of fairness. To provide a clearer understanding of who benefits and suffers from racism in the US, and how inequities can be addressed, politicians, scientists, and the public must recognize that color-blind language perpetuates structural racism and avoid its use (*4*).

Research shows that women and people of color are presumed to be less competent, are under more scrutiny, and must possess more impressive credentials than those of white men to attain equivalent employment and advancement opportunities across job sectors. By contrast, white men are often deemed competent, given the benefit of the doubt, and judged for their potential (*5*–*7*). Whether pilots, scientists, or engineers, people of color are underrepresented because of exclusionary and discriminatory practices in education and the workforce (*4*–*8*), not because they are less qualified.

EOs 14281 and 14173 appear to value fairness by citing the US principle that all citizens should be treated equally. However, the use of color-blind language such as "equality of opportunity" (*1, 2*), "individual merit, aptitude, hard work" (*2*), and "meritocracy" (*1*) serves to justify ongoing racial discrimination by blaming individuals for inequities of outcomes and dismissing the existence of well-documented structural racism in sectors such as education, health, housing, and the labor market (*4*, *5*). Meanwhile, by directing agencies to stop applying "disparate-impact liability," the legal basis of much of the workforce antidiscrimination legislation, EO 14281 openly resists concrete solutions that mitigate racial injustice (*4*). EO 14151 (*3*) also uses color-blind ideology and establishes similarly counterproductive policies.

DEIA and civil rights law are not favoritism or reverse discrimination; they are a strategy to establish a just context in which a meritocracy might be possible. The racialized systemic barriers faced by some but not by others create uneven access and opportunities, an injustice that the policies and practices dismantled by the EOs attempt to address. Scientific research about and by people of color, women, and persons with disabilities has been disproportionally affected by grant terminations and federal agencies' priority changes triggered by the EOs (*9*), providing more evidence that antidiscrimination policies remain necessary.

Underrepresented scientists play a crucial role in research funded by the National Science Foundation, the National Institutes of Health, and other government agencies (*9*). These researchers often focus on important issues such as health and educational disparities and offer diverse perspectives and ideas that contribute to scientific innovation and solutions to long-standing problems (*10*, *11*). If the EOs are not overturned, these researchers and their projects—and as a result, scientific progress and society—will suffer (*10*, *11*).

Tatiane Russo-Tait[1], Summer Blanco[2], Eduardo Bonilla-Silva[3]

[1]Department of Cellular Biology, University of Georgia, Athens, GA, USA. [2]Department of Plant Biology, University of Georgia, Athens, GA, USA. [3]Department of Sociology, Duke University, Durham, NC, USA. Email: tati@uga.edu

REFERENCES AND NOTES

1. US Office of the President, "Restoring equality of opportunity and meritocracy" (Executive Order 14281, 28 April 2025).
2. US Office of the President, "Ending illegal discrimination and restoring merit-based opportunity" (Executive Order 14173, 31 January 2025).
3. US Office of the President, "Ending radical and wasteful government DEI programs and preferencing" (Executive Order 14151, 29 January 2025).
4. E. Bonilla-Silva, *Racism without Racists: Color-Blind Racism and the Persistence of Racial Inequality in America* (Rowman & Littlefield, ed. 6, 2022).
5. National Academies of Sciences, Engineering, Medicine, *Advancing Antiracism, Diversity, Equity, and Inclusion in STEMM Organizations: Beyond Broadening Participation* (National Academies Press, 2023); https://www.nap.edu/catalog/26803.
6. M. Blair-Loy, E. A. Cech, *Misconceiving Merit: Paradoxes of Excellence and Devotion in Academic Science and Engineering* (Univ. Chicago Press, 2022).
7. C. L. Ridgeway, *Am. Sociol. Rev.*, **79**, 1 (2014).
8. National Academies of Sciences, Engineering, Medicine, *Barriers and Opportunities for 2-Year and 4-Year Stem Degrees: Systemic Change to Support Students' Diverse Pathways* (National Academies Press, 2016).
9. J. Mervis, "NSF's grant cuts fall heaviest on scientists from underrepresented groups," *Science*, 16 May 2025.
10. E. O. McGee, *Black, Brown, Bruised: How Racialized STEM Education Stifles Innovation* (Harvard Education Press, 2021).
11. B. Hofstra *et al.*, *Proc. Natl. Acad. Sci. U.S.A.* **117**, 9284 (2020).

10.1126/science.ady7950

Combat disinformation about gender research

US executive order 14168 of 20 January 2025 terminated federal funding for research that examines gender as a scientific and social construct beyond the so-called "immutable biological classification as either male or female" (*1*). The policy is an example of disinformation: the spread of falsehoods with the intention to mislead (*2*). By mischaracterizing rigorous, peer-reviewed gender-affirmation research as ideological, this directive undermines scientific integrity and threatens public health. Scientists must speak out against disinformation efforts that delegitimize this important line of research.

Gender affirmation research is a legitimate interdisciplinary domain of scientific inquiry. Studies explore the medical, psychological, legal, and policy-related dimensions through which individuals affirm their gender, and span fields including epidemiology, medicine, psychology, biology, and economics. This body of work is grounded in established scientific standards using rigorous methodologies, validated measures, careful analysis, and community-engaged approaches that reduce bias (*3*).

This research is not fringe science. A robust and reproducible body of evidence demonstrates that gender-affirming care is associated with reduced suicidality, reduced psychological distress, and improved quality of life (*4*, *5*). These findings have been replicated across populations and settings (*4*, *5*), meeting the gold standards of scientific credibility.

Labeling this work "ideology" reflects a fundamental epistemological error and misunderstanding of science on gender affirmation. Science is defined not by subject matter but by its methodology: empirical observation, testable hypotheses, and openness to revision in the face of new evidence. Ideology, by contrast, rests on fixed and nonfalsifiable beliefs. Gender affirmation research engages the biology of sex, including chromosomal and hormonal diversity, alongside the empirically observable fact that trans and gender-diverse people exist across history, cultures, and societies (*6*).

To combat this pattern of disinformation, scientists must be unequivocal: Gender affirmation research is science. It is grounded in the empirical, testable, and essential accumulation of knowledge aiming to improve health outcomes in a diverse society where trans people exist and matter.

Arjee J. Restar[1], Kristi E. Gamarel[2,3], Don Operario[4]

[1]Department of Social and Behavioral Science, Yale University School of Public Health, New Haven, CT, USA. [2]Department of Health Behavior and Health Equity, University of Michigan School of Public Health, Ann Arbor, MI, USA. [3]Population Studies Center, University of Michigan Institute for Social Research, Ann Arbor, MI, USA. [4]Department of Behavioral, Social, and Health Education Sciences, Emory University Rollins School of Public Health, Atlanta, GA, USA. Email: don.operario@emory.edu

REFERENCES AND NOTES

1. US Office of the President, "Defending women from gender ideology extremism and restoring biological truth to the federal government" (Executive Order 14168, 20 January 2025).
2. American Psychological Association, "Using psychological science to understand and fight health misinformation: An APA consensus statement" (APA, 2023); https://www.apa.org/pubs/reports/misinformation-consensus-statement.pdf.
3. A. I. Scheim *et al.*, *PLOS One* **19**, e0299373 (2024).
4. S. L. Reisner *et al.*, *JAMA Netw. Open* **8**, e250955-e (2025).
5. D. M. Doyle, T. O. G. Lewis, M. Barreto, *Nat. Hum. Behav.* **7**, 1320 (2023).
6. A. J. Restar *et al.*, *Am. J. Epidemiol.* **193**, 1861 (2024).

10.1126/science.adz1709

PRIZE ESSAY

ARTIFICIAL INTELLIGENCE

AI to rewire life's interactome

Structural foundation models help to elucidate and reprogram molecular biology **Zhuoran Qiao**

Biomolecular interactions gained through evolution enable living systems to transduce signals and energies across diverse spatial and temporal scales. The ability to harness patterns from these extensive interactions will unlock vast molecular design and therapeutic development opportunities. My colleagues and I transformed this mission into computable tasks by creating a "computational microscope" of the structural interactome, by leveraging tools from artificial intelligence (AI) and accelerated computing.

The interactions among biomolecules, such as proteins and smaller molecules, define larger biological organizations and orchestrate the fundamental processes of life. To identify these interactions and understand how they take place, we must develop a "microscope" to decode the three-dimensional structures—coordinates of atoms—that form these interactions from zoomed-in snapshots of molecular compartments. Experimental methods to determine molecular structures, such as x-ray crystallography and cryo–electron microscopy, are incredibly powerful but constrained by the slow pace of laboratory research and the months of laborious work to isolate molecular snapshots into analyzable samples. A computational microscope would overcome this bottleneck by directly synthesizing views of structures from the identity of those molecules.

This idea remained a moonshot for half a century until recent breakthroughs in AI-driven protein structure prediction (*1*). Unlike traditional simulation approaches that involve enumerating an astronomical number of hypotheses, AlphaFold2 and related AI-based structure predictors harness traces from millions of years of molecular evolution and patterns learned from experimentally determined structures. Specifically, models of evolutionary constraints—such as multiple sequence alignments (*2*) or protein language models (*3*)—are digested by specialized neural networks to enable reasoning about the three-dimensional constellation of amino acids (building blocks of proteins) with unprecedented accuracy. We have advanced this vision by developing generative machine-learning approaches to address two critical aspects beyond proteins in isolation: protein-ligand interactions and their conformational landscapes.

Biomolecules are highly dynamic and require numerous snapshots to fully capture their behaviors. Protein shapes are modulated by a vast array of small-molecule ligands and posttranslational modifications (*4*), which drive dynamical conformational changes crucial to the regulation of biological functions and provide key opportunities for drug discovery. These complexities challenge traditional lock-and-key computational protein-ligand interaction prediction strategies, which often assume that the protein is a rigid body. Although methods such as molecular dynamics can model binding and conformational changes, they are limited by the prohibitive cost of overcoming the barriers of slow transitions between low-lying conformational states.

We present a generative AI strategy, NeuralPLexer, to resolve this conundrum (*5*) (see the figure). NeuralPLexer models the landscape of protein-ligand binding with generative diffusion (*6*): It starts from an initial sketch of the entire molecular complex and progressively refines the finer-grained details of the reasoned structures. The AI model generates an ensemble of conformational snapshots, based on multiple simultaneous guesses of the initial sketch, to cover the thermodynamic landscape of the biomolecule. Such a "one-shot" generation provides a pathway to bypass the sampling barriers and quickly obtain the full picture of molecular interactions with atomistic details. NeuralPLexer uses a neural network that mirrors the multiscale hierarchical organization of biomolecular complexes. It initializes predictions by leveraging inferred protein-ligand contacts and subsequently generates detailed geometric representations, all while maintaining the essential physical symmetries.

As an initial validation, we applied NeuralPLexer to predict the formation of cryptic pockets—binding sites induced by ligand binding that are absent in unbound structures. We used a dataset where small-molecule binding considerably alters protein conformations, and NeuralPLexer successfully generated conformational distributions consistent with structural experiments. On a diverse collection of enzymatic systems, the sampled conformational ensembles showed strong agreement with experimental protein conformations, as quantified by metrics such as TM-score (*7*) and Q-factors (*8*), effectively overcoming the limitations of static protein-folding models. Additionally, by assigning confidence levels to its conformational predictions, NeuralPLexer demonstrated the ability to distinguish strong bind-

AI shows potential to unify biomolecular structure prediction and design across diverse modalities

(**A**) Schematics of generative structure prediction for protein-ligand complexes. (**B**) Generative modeling enables fast sampling from molecular conformational landscapes. (**C**) Structural insights revealed by NeuralPLexer predictions, as exemplified by the prediction of the human KRAS G12C ligand-bound state. (**D**) New opportunities for structure prediction foundation models and de novo molecular design approaches.

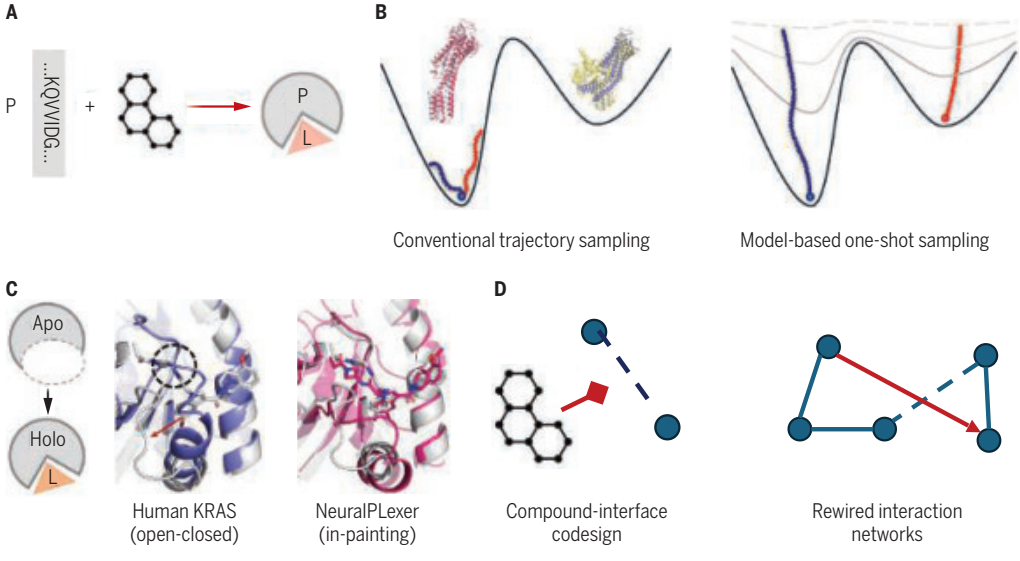

KQVVIDG, Lys-Gln-Val-Val-Ile-Asp-Gly; L, ligand; P, protein

GRAPHIC: ADAPTED FROM (5) BY A. FISHER/*SCIENCE*

ers from weak ones across a wide array of targets, despite never having been trained on affinity measurements.

We further used this strategy to gain mechanistic insight into protein functions. For example, in a ketol-acid reductoisomerase, whose catalytic mechanism was recently characterized, the model accurately captured the closure motion of the N-subdomain upon cofactor and inhibitor binding while providing hints about target self-assembly. Additionally, NeuralPLexer predictions can assist in identifying structural elements crucial for protein activation and deactivation. In the case of a G protein–coupled receptor, the model generated a conformational hypothesis that explained the receptor's constitutive activity in the absence of ligands. These capabilities highlight NeuralPLexer's potential as a powerful tool to unravel various molecular mechanisms underlying allosteric regulation and enzyme catalysis.

Beyond atomistic conformations, we developed a geometric deep-learning approach named OrbNet-Equi (*9*) to study the energetics of molecular interactions with accuracy comparable to full-precision quantum mechanical methods across main-group chemistry while being about 1000-fold faster. By combining these tools, we can resolve variations in protonation states and electronic charge and spin configurations at greater resolution to provide a comprehensive strategy to interpret and devise proton or electron transfer pathways.

Beyond structure predictions for known protein–small-molecule interactions, we enhanced NeuralPLexer with an inpainting-based approach to discover new pockets. This capability could enable us to design ligands for previously uncharacterized binding sites. Similar to AI image editing tools that paint and restyle a selected region based on its surrounding context, our method simultaneously infers ligand structure, protein sequence, and pocket-shape variations using only the backbone of the target protein. This strategy led to accurate predictions on challenging targets such as KRAS-G12C, where it achieved a markedly higher design success rate than traditional conformational search and docking algorithms.

As structural prediction foundation models achieve greater accuracy (*10*), future research will be extending these capabilities to encompass more sophisticated interactions and arbitrary bioassembly stoichiometry. This includes protein-protein interaction interfaces stabilized by chemical modulators—a phenomenon known as induced proximity (*11*). Such advancements pave the way for the rational design of ligands to reprogram protein interaction networks and ultimately restore healthy cellular states. Unified interaction prediction models, together with de novo binder design frameworks, will become a powerful platform to design stabilizers of protein-protein interfaces, modulating the subcellular localization of pathogenic proteins (*12*) and biasing the formation of specific assembly states. This approach to rewiring cellular signaling not only holds promise for therapeutic precision but also enhances the therapeutic window by selectively targeting oligomeric states of proteins, sparing monomeric forms essential for normal cellular functions (*13*). These emerging capabilities will help translate the structural foundation model we have developed into versatile tools for advancing chemical biology and expediting drug discovery. □

REFERENCES AND NOTES

1. J. Jumper *et al.*, *Nature* **596**, 583 (2021).
2. S. Ovchinnikov *et al.*, *Science* **355**, 294 (2017).
3. Z. Lin *et al.*, *Science* **379**, 1123 (2023).
4. R. Nussinov, C. J. Tsai, *Cell* **153**, 293 (2013).
5. Z. Qiao, W. Nie, A. Vahdat, T. F. Miller III, A. Anandkumar, *Nat. Mach. Intell.* **6**, 195 (2024).
6. Y. Song *et al.*, arXiv:2011.13456 (2020).
7. Y. Zhang, J. Skolnick, *Nucleic Acids Res.* **33**, 2302 (2005).
8. R. B. Best, G. Hummer, *Proc. Natl. Acad. Sci. U.S.A.* **102**, 6732 (2005).
9. Z. Qiao *et al.*, *Proc. Natl. Acad. Sci. U.S.A.* **119**, e2205221119 (2022).
10. J. Abramson *et al.*, *Nature* **630**, 493 (2024).
11. B. Z. Stanton, E. J. Chory, G. R. Crabtree, *Science* **359**, eaao5902 (2018).
12. C. S. C. Ng, A. Liu, B. Cui, S. M. Banik, *Nature* **633**, 941 (2024).
13. R. C. Sarott *et al.*, *Science* **386**, eadl5361 (2024).

10.1126/science.adx7802

Chai Discovery, San Francisco, CA, USA. Email: zrqiao0@gmail.com

GRAND PRIZE WINNER

Zhuoran Qiao received an undergraduate degree from Peking University and a PhD from the California Institute of Technology. He then served as a senior machine-learning scientist at Iambic Therapeutics during 2023–2024 and started at Chai Discovery as a scientist and founding team member in 2025. His research centers around physics-driven machine-learning approaches to address problems in chemistry and structural biology involving complex molecular systems. **www.science.org/doi/10.1126/science.adx7802**

FINALISTS

Aditya Nair received an undergraduate degree from the National University of Singapore and a PhD from the California Institute of Technology in Computation and Neural Systems. He is an incoming Nanyang Assistant Professor at Nanyang Technological University, Singapore, and an incoming principal investigator at the Institute of Molecular and Cellular Blology, A*STAR Singapore. His research sits at the intersection of neuroscience and artificial intelligence, examining how brains and machines process affect and emotion to ultimately deepen our understanding of mental health disorders.**www.science.org/doi/10.1126/science.adx7811**

Alizée Roobaert received both her master's degree and PhD from the Université Libre de Bruxelles (ULB). After a postdoctoral fellowship in the BGeoSys research group at ULB, partly in collaboration with Princeton University, she joined the Flanders Marine Institute (VLIZ) in 2023. There, she is part of the Past, Present and Future Marine Climate Change research group, where her research focuses on marine biogeochemistry and the ocean carbon cycle, using machine-learning approaches to investigate air-sea carbon dioxide fluxes, particularly in coastal seas, and their spatiotemporal variability, with the aim of improving our understanding of the ocean's role in the global carbon cycle. **www.science.org/doi/10.1126/science.adx7826**

Chen Institute & Science Prize for AI Accelerated Research

PHOTOS: (TOP TO BOTTOM) COURTESY OF ZHUORAN QIAO; JULIA ANN EHLERT NAIR; COURTESY OF ALIZÉE ROOBAERT

RESEARCH

IN *SCIENCE* JOURNALS

Edited by Michael Funk

SICKLE CELL DISEASE

Underhanded complement

Acute chest syndrome (ACS) is the most severe complication that individuals with sickle cell disease may experience. A form of acute lung injury, ACS currently lacks any treatment options. Chonat *et al.* found that the complement pathway is activated in individuals with sickle cell disease during ACS and in a mouse model of ACS. Genetic deletion or pharmacological inhibition of complement components 3 or 5, respectively, alleviated disease severity in mice. These data suggest that complement inhibitors, which are already being used in the clinical setting, could be used as a preventative or therapeutic for ACS caused by sickle cell disease. —Courtney Malo

Sci. Transl. Med. (2025) 10.1126/scitranslmed.adl4922

Distorted red blood cells, pictured here in a microscopy image, can lead to severe complications in the lungs of people with sickle cell disease.

EARTHQUAKE ALERTS

Getting shake warnings into more hands

Earthquake early warning systems depend on real-time analysis of waves detected at nearby seismic stations or by smartphone accelerometers. The latter approach, although less sensitive, is a promising way to offer alerts in areas without seismic stations. In a major step forward, Allen *et al*. describe the outcomes of an alert system rolled out to Android phones in 98 countries, which increased total warning system access 10-fold to 2.5 billion people over 3 years. Issuing more than 1200 alerts over that period, the system recorded low-magnitude errors and provided preshake warnings consistent with other detection systems but on a much larger scale. —Angela Hessler

Science p. 254, 10.1126/science.ads4779

ELECTRONIC MATERIALS

Growing phase-pure InSe wafers

The electronic properties of indium selenide (InSe) can surpass silicon, but films of InSe are often inferior in performance because the material grows nonstoichiometrically. Qin *et al*. now report a solid–liquid–solid growth method to produce highly-crystallinity InSe wafers. The authors used a liquid indium seal around the wafer to create an indium-rich liquid interface that drives the transformation of amorphous InSe into crystalline InSe. Transistor array devices had extremely high mobility and a near Boltzmann-limit subthreshold swing, with an average value as low as 67 millivolts per decade. —Phil Szuromi

Science p. 299, 10.1126/science.adu3803

MOLECULAR BIOLOGY

Reining in heterochromatin

Heterochromatin, marked by histone H3 lysine 9 trimethylation (H3K9me3), is crucial for genome stability and gene repression. However, how cells prevent excessive H3K9me3 accumulation has been unclear. Zhou *et al*. discovered that the protein ASB7, which is recruited to heterochromatin by heterochromatin protein 1, acts as a negative regulator by promoting the degradation of the H3K9 methyltransferase SUV39H1. During cell division, phosphorylation of ASB7 temporarily prevents this degradation, allowing H3K9me3 restoration. These findings reveal a dynamic feedback circuit that maintains H3K9me3 balance, ensuring proper epigenetic inheritance and preventing harmful over-heterochromatinization. —Di Jiang

Science p. 309, 10.1126/science.adq7408

IMAGE: SCIENCE SOURCE

NEUROIMMUNOLOGY

Enteric neurons support gut immunity

The enteric nervous system (ENS) has been shown to modulate the immune response during infection. However, the mechanisms responsible for sensing inflammatory cues and modulating the ENS response remain to be fully elucidated. Barilla *et al*. identified a subset of enteric neurons that upregulate the production of the neuropeptides neuromedin U and calcitonin gene–related peptide beta after sensing the infection-induced type 2 cytokines interleukin-4 and -13. The upregulation of the neuropeptides was critical for triggering host defense to intestinal helminths, suggesting that bidirectional ENS-immune communication in the gut is critical for regulating intestinal immunity. —Mattia Maroso

Science p. 260, 10.1126/science.adn9850

ORGANIC CHEMISTRY

Rings with an extra nitrogen

Six-membered rings with five carbons and one nitrogen are very common motifs in pharmaceuticals. By contrast, analogs with two adjacent nitrogens and four carbons are seen much less often in drug research, notwithstanding their appealing properties. The discrepancy likely stems from the comparative synthetic challenge of incorporating the extra nitrogen. Two groups now report complementary approaches to conveniently access these compounds. Puriņš *et al.* used photochemistry to slice into six-membered pyridine, add in a nitrogen, and expel the carbon. Li *et al*. started with five-membered pyrrolidine and introduced the nitrogen through ring expansion. —Jake S. Yeston

Science p. 295, 10.1126/science.adx4762, p. 275, 10.1126/science.adl4755

MATERIALS SCIENCE

A library of robust aerogels

Aerogels, which are typically made using a sol-gel process, consist of a group of materials with high porosity, near transparency, and ultralow density, as they can be up to 99% empty space. Pang *et al*. developed a two-dimensional channel–confined method to make dome-celled aerogels from a wide range of oxides, carbides, metals, and even high-entropy mixtures. The dome shape imbues the aerogels with mechanical and thermal robustness, allowing them to undergo thousands of compressive cycles up to 99% strain and wide-temperature-change thermal shock. Many of the carbides also have very low thermal conductivity even at high temperatures. —Marc S. Lavine

Science p. 290, 10.1126/science.adw5777

MICROBIOTA

Developing microbiota therapeutics

The gut microbiota has long been an aspirational target for clinical delivery of therapeutics. Successful therapy by this route depends on ensuring engraftment of the therapeutic organisms and their clearance after treatment. Whitaker *et al*. have engineered a strain of *Bacteroides vulgatus*, which is commonly found in the gut of healthy humans, with two genetic modules. One is therapeutic to rectify oxalate metabolism for preventing kidney stone formation, and the second adds multiple biosafety promoters that make the organism reliant on an essential nutrient, in this case porphyrin. Although the approach is very promising therapeutically, so far it is still encountering problems with horizontal gene transfer creating "biosafety escape" mutants. —Caroline Ash

Science p. 303, 10.1126/science.adu8000

IN OTHER JOURNALS

Edited by **Corinne Simonti** and **Jesse Smith**

ANIMAL WELFARE

Quantifying pain can lead to reduction

Research has increasingly shown that animals from across the taxonomic spectrum experience pain and suffering, leading to efforts to reduce these in food animals. One such recent approach, the Welfare Footprint Framework (WFF), facilitates calculation of the cumulative amount of time an animal spends in positive and negative affective states. Schuck-Paim *et al.* used this metric to quantify the welfare impact of asphyxiation in farmed rainbow trout. They found that it leads to an average of 10 minutes of moderate to intense pain per fish, an experience that could be greatly reduced through effective—and cost-effective—stunning. Given the similar processes that occur in the more than one trillion fish harvested annually, substantial opportunities exist to improve fish welfare. —Sacha Vignieri *Sci. Rep.* (2025) 10.1038/s41598-025-04272-1

Measuring suffering reveals simple, cost-effective ways to improve the welfare of food animals like the rainbow trout (*Oncorhynchus mykiss*).

PHOTO: BRUNO MATHIEU/MINDEN PICTURES

SEXUAL FUNCTION

Sexual health in menopause

After age 40, changes in hormone levels, particularly estrogen, trigger symptoms related to perimenopause and menopause called genitourinary syndrome of menopause (GSM). These can include reduced sexual interest, skin changes, poor lubrication, and vaginal pain and itching. To better understand this condition, Sato *et al*. studied more than 900 women 40 to 79 years of age in Japan who were divided based on whether they were regularly

TRANSCRIPTOMICS

Sequencing senescence in plants

Single-nucleus RNA sequencing (snRNA-seq) can spatially and temporally resolve transcriptomic information in a wide range of plant cell types. However, senescing cells do not typically respond well to removing the cell wall, which is required for snRNA-seq. By capturing a time course of senescing plant tissues across different organs, Guo *et al.* mapped the single-nucleus transcriptome. The authors found that senescing cells have substantial shared transcriptomes across different tissue types. Additionally, by mapping the expression of sugar and nitrate transporters, the authors established the detailed timing of nutrient allocation during senescence and identified networks of genes that may contribute to nutrient movement and plant growth. —Madeleine Seale *Cell* (2025) 10.1016/j.cell.2025.03.024

Senescing cells in *Arabidopsis thaliana* show similar gene expression despite coming from different tissues.

or infrequently sexually active. Although the frequency of sexual activity declined with age, sexual satisfaction did not, and women who maintained more regular sexual activity had fewer GSM symptoms. It is unclear whether sexual activity helps to reduce symptoms or if women with fewer symptoms engage in more sexual activity. —Ekeoma Uzogara

Menopause (2025)
10.1097/GME.0000000000002539

PAIN

Don't sleep on your pain

Individuals with chronic pain often report impairments in sleep quality, which eventually lead to fatigue and deterioration of life quality. However, whether and how chronic pain alters the sleep architecture remains to be fully elucidated. Burek *et al.* performed a detailed analysis of sleep architecture in a mouse model of chronic inflammatory pain and showed that chronic pain increased sleep duration during the active phase of the animals and increased sleep fragmentation during the sleep phase. The effects were remarkably consistent and similar between sexes, suggesting that sleep analysis might represent a potential biomarker that could be used for pain management. —Mattia Maroso

Neuropsychopharmacology (2025)
10.1038/s41386-025-02152-w

CHEMISTRY

Recovering a pot of gold

Many methods of extracting gold from ore and electronic waste exist, but some of these approaches are limited because of low throughput and high cost and complexity. Mann *et al.* used trichloroisocyanuric acid, which is often used for disinfecting water, with a halide catalyst to leach gold from ore and waste. Sulfur-derived polymer sorbents recovered gold from the leachate with high affinity. Postrecovery thermal depolymerization achieved 98% yield of gold, and more than half of polymers were recycled into monomers. Although proper management of waste stream and tailing is needed, this method has promise for use in a closed-loop system of gold recycling. —Sumin Jin

Nat. Sustain. (2025)
10.1038/s41893-025-01586-w

ORGANIC CHEMISTRY

Choosing the crowded product

Compounds containing carbon-carbon double bonds can adopt two different geometries, which are called *Z* or *E* depending on whether the largest substituents on each carbon lie on the same sides or opposite sides of the bond axis, respectively. Because the *Z* isomer is more crowded, it tends to be less stable and so more difficult to access. Hou *et al.* took advantage of the faster reactivity of *Z* intermediates to favor *Z* products in an iridium-catalyzed allylic substitution. By also photochemically scrambling an *E* reactant into a *Z*/*E* mixture, the authors were able to funnel nearly all of the product to *Z*. —Jake S. Yeston

J. Am. Chem. Soc. (2025)
10.1021/jacs.5c05792

EARTHQUAKES

Complex faults cause jerky shaking

Two earthquakes of the same magnitude can have very different ground-shake patterns. Strong, high-frequency shaking raises certain risks, motivating a deeper look at the causes. Lee *et al.* found that the complexity of the fault network near a main slip surface is generally correlated with complex, high-frequency rupture energy at both the regional and global scales. Their study stresses the need for high-resolution mapping of the networks of smaller faults adjacent to primary earthquake-producing faults because these can affect how energy propagates to Earth's surface. —Angela Hessler

Geophys. Res. Lett. (2025)
10.1029/2025GL115592

PHOTO: NIGEL CATTLIN/MINDEN PICTURES

RESEARCH ARTICLE SUMMARY

MOLECULAR BIOLOGY

Autoinhibition imposed by a large conformational switch of INO80 regulates nucleosome positioning

Upneet Kaur†, Hao Wu†, Yifan Cheng*, Geeta J. Narlikar*

Full article and list of author affiliations: https://doi.org/10.1126/science.adr3831

INTRODUCTION: The packaging of eukaryotic DNA into nucleosomes occludes access to the underlying DNA. A primary mechanism for regulating access to DNA is through the rearrangement of nucleosomes by adenosine 5′-triphosphate (ATP)–dependent chromatin remodelers. There are several classes of remodelers, with each class catalyzing a specific set of nucleosome rearrangements. The chromatin remodeler INO80 is critical for precisely positioning nucleosomes near sites of transcription initiation and origins of DNA replication. In vitro, INO80 displays a switch-like response to the length of DNA flanking a nucleosome such that increasing the length from 40 to 80 base pairs (bp) results in ~100-fold faster nucleosome sliding. This property helps explain INO80's ability to precisely position nucleosomes in vivo. However, the mechanistic basis for the tight regulation of INO80's activity by flanking DNA length remains elusive.

RATIONALE: INO80 is a multisubunit complex, within which groups of subunits are organized as biochemically separable modules. Existing cryo-EM structures of INO80 on nucleosomes with long flanking DNA show one of these modules, the Arp8 module together with the helicase-SANT–associated (HSA) region of the Ino80 adenosine triphosphatase (ATPase) bound to flanking DNA. Such observations have led to the model that the Arp8 module stimulates INO80 remodeling by helping the HSA region act as a ruler to sense flanking DNA length. To test this role of the Arp8 module, we used cryo–electron microscopy (cryo-EM) to compare the structures of INO80 bound to nucleosomes with 40 bp of flanking DNA (0/40) with those of INO80 bound to nucleosomes with 80 bp of flanking DNA (0/80). We further tested the functional effects of the Arp8 module by either deleting the entire Arp8 module or by targeted mutations in the N-terminal region of the Arp8 subunit. The combination of these structural and biochemical approaches has allowed us to uncover a new role for the Arp8 module in the flanking DNA length sensitivity displayed by INO80.

RESULTS: Our cryo-EM structure of INO80 bound to 0/40 nucleosomes revealed that the Arp8 module adopts a distinct autoinhibited conformation, rotating 180° away from flanking DNA. This conformation occludes the HSA from interacting with the flanking DNA, providing an explanation for slower nucleosome sliding. When the flanking DNA length is increased to 80 bp, the Arp8 module gets released from the inhibited conformation, allowing the HSA to interact with flanking DNA. Deletion of the entire Arp8 module or just mutation of the negatively charged N terminus of Arp8 enables rapid sliding of 0/40 nucleosomes, effectively equalizing sliding rates of 0/40 and 0/80 nucleosomes. These results reveal that the Arp8 module does not enable a ruler-like mechanism but rather acts as a brake to inhibit INO80's sliding activity when the flanking DNA is short. We also uncovered an additional conformational state on 0/80 nucleosomes in which the Arp8 module is conformationally dynamic. Our biochemical data suggest that this additional state represents an activated intermediate that is on path for rapid remodeling.

CONCLUSION: Our results highlight how a multisubunit chromatin remodeler utilizes its subunits to impose autoinhibition in a manner that is regulated by nucleosomal cues. We speculate that the tunability of INO80's flanking DNA length dependence allows for rapid decrowding of nucleosomes during DNA damage. This property also explains how INO80 precisely positions nucleosomes during replication and transcription. □

*Corresponding author. Email: yifan.cheng@ucsf.edu (Y.C.); geeta.narlikar@ucsf.edu (G.J.N.) †These authors contributed equally to this work. **Cite this article as U. Kaur *et al.*, *Science* 389, eadr3831 (2025). DOI: 10.1126/science.adr3831**

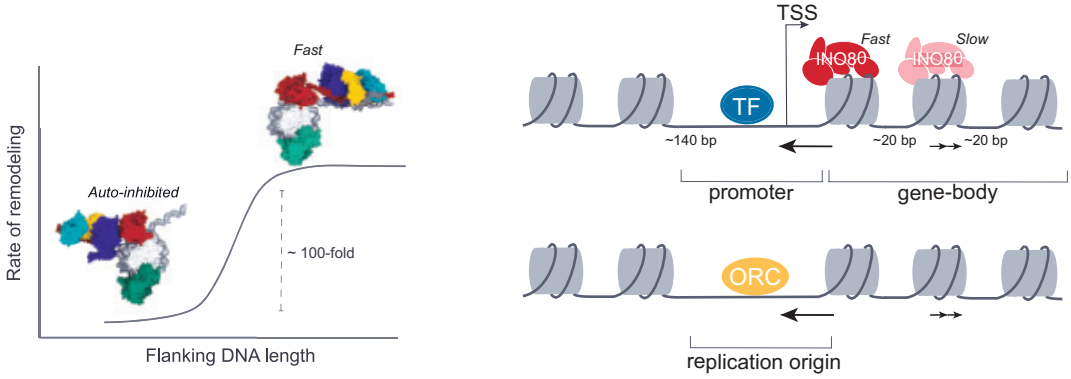

INO80's switch-like response to flanking DNA is gated by conformational switching of the Arp8 module. This conformational rearrangement sheds light (left panel) on how INO80 spaces nucleosomes in collaboration with transcription factors (TFs) at transcription start sites (TSS) and the origin recognition complex (ORC) at replication origins (right panel).

RESEARCH ARTICLE SUMMARY

MALARIA

Vaccination to mitigate climate-driven disruptions to malaria control in Madagascar

Benjamin L. Rice*, Estelle Raobson, Sylviane Miharisoa, Mahery Rebaliha, Joseph Lewinski, Hanitriniaina Raharinirina, Christopher D. Golden, Gabriel A. Vecchi, Amy Wesolowski, Bryan Grenfell, C. Jessica E. Metcalf

Full article and list of author affiliations: https://doi.org/10.1126/science.adp5365

INTRODUCTION: Extreme weather events, such as tropical cyclones, interrupt public health activities, threatening global progress toward malaria control. The increasing intensity of tropical cyclones makes this a growing challenge, as malaria-endemic countries include large cyclone-vulnerable populations. Limited data, however, are available to assess the impacts of these disruptions on disease burden.

RATIONALE: Using data from a prospective cohort study in southeast Madagascar with malaria infection observations before and after major tropical cyclones in 2022 and 2023 (n = 20,718), we derived estimates of the force of infection in the aftermath of these storms across localities reflecting a range of infection intensity. We then used mathematical models parameterized with estimates of the duration and efficacy of the range of available malaria control tools (e.g., mass drug administration or seasonal malaria chemoprophylaxis) to quantify the potential for applying additional prevention strategies, including vaccination, to mitigate climate-mediated disruptions.

RESULTS: Because of their shorter half-life, we find that brief (i.e., <1 month) discontinuities in standard intervention activities such as chemoprophylaxis result in rapid rebounds in infection, an outcome that is robust to sources of uncertainty in estimates of infection rate. Among intervention options, vaccination—newly available for malaria—can be particularly effective at mitigating the impacts of temporal gaps in the coverage of other prevention interventions. By modeling the deployment of antimalarial vaccination in a cyclone-vulnerable setting, we identified an approximate halving of the number of symptomatic infections expected in the wake of a disruption when sufficient coverage (e.g., >70%) is attained for a vaccine with efficacy similar to that reported for the recently approved R21 malaria vaccine.

CONCLUSION: Our results demonstrate the benefit of considering disruptions to malaria control measures when evaluating intervention recommendations in high malaria burden, climate-vulnerable geographies. We quantified the effects of a range of available interventions for malaria and identified newly available malaria vaccines as having considerable potential in mitigating these risks. Our data suggest that the effects of climate on disease burden via disruption of health care will be an important element of how climate change shapes global health and emphasize the importance of discontinuities as a challenge to global health progress generally. □

*Corresponding author. Email: b.rice@princeton.edu Cite this article as B. L. Rice *et al.*, *Science* **389**, eadp5365 (2025). DOI: 10.1126/science.adp5365

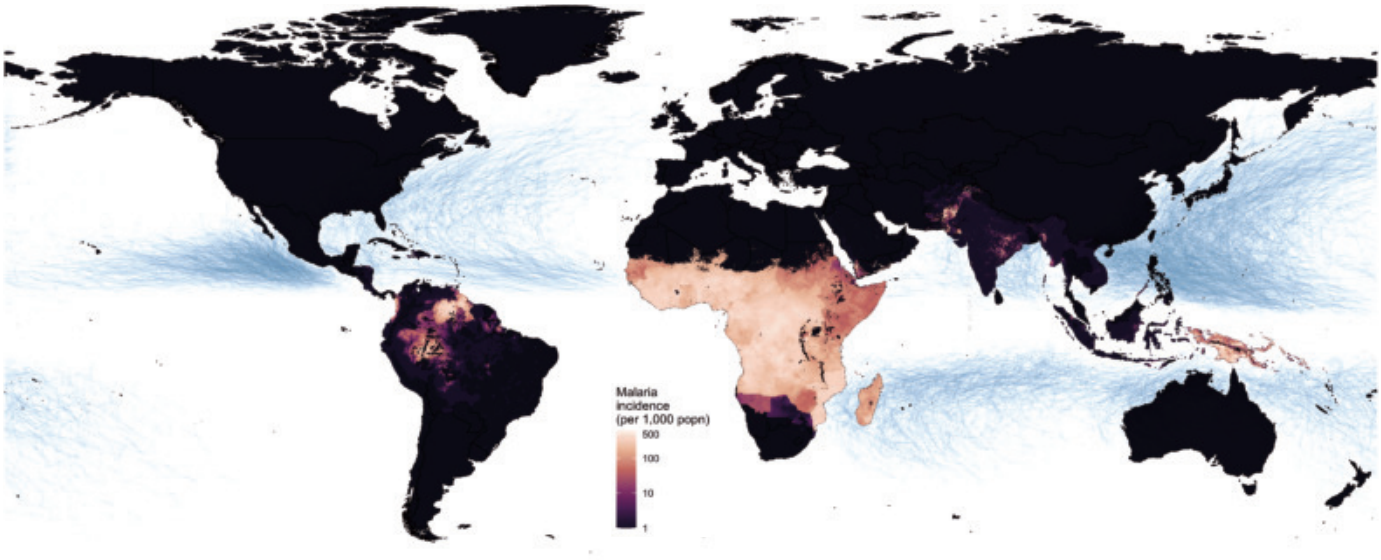

Cyclone and malaria co-occurrence. The intersection of tropical cyclone activity and malaria. Blue lines show cyclone tracks for cyclones since 1980, and land surface is colored by estimated malaria incidence. popn, population.

RESEARCH ARTICLE SUMMARY

PLANT SCIENCE

Redox-regulated Aux/IAA multimerization modulates auxin responses

Dipan Roy*†, Poonam Mehra*†, Lisa Clark, Vaishnavi Mukkawar, Kevin Bellande, Raquel Martin-Arevalillo, Srayan Ghosh, Kishor D. Ingole, Prakash Kumar Bhagat, Adrian Brown, Kawinnat Sue-ob, Andrew Jones, Joop E. M. Vermeer, Teva Vernoux, Kathryn Lilley, Phil Mullineaux, Ulrike Bechtold, Malcolm J. Bennett, Ari Sadanandom*

Full article and list of author affiliations: https://doi.org/10.1126/science.adu1470

INTRODUCTION: Plasticity in branching patterns is a critical determinant of the foraging capacity of roots because water and nutrients are often heterogeneously distributed in their surrounding soil environment. When growing root tips lose contact with moist soil (e.g., in an air gap), roots temporarily cease branching until they reestablish contact with moist soil (called a xerobranching response). Hence, xerobranching is an acclimative response that enables roots to respond to spatial variation in soil water availability. Insights into the molecular mechanisms that govern xerobranching are relevant to approaches to mitigate the effects of climate change and water scarcity on plants.

RATIONALE: Despite growing appreciation for the role of reactive oxygen species (ROS) during stress responses in plants, the precise mechanism by which these signals function in root tissues during abiotic stress remains poorly understood. The phytohormone auxin integrates multiple endogenous and environmental signals to maintain phenotypic plasticity in plants. Given that both ROS and auxin play crucial roles in regulating various plastic developmental responses, their intersection represents a key nexus of biological importance. A deeper understanding of this cross-talk will help us understand how different developmental responses such as xerobranching are coordinated in accordance with the dynamic changes in their environment.

RESULTS: Respiratory burst oxidase homolog (RBOH) proteins are the major producers of ROS in plants. We therefore screened *rboh* mutants for xerobranching defects. Selected *rboh* mutants exhibited strong xerobranching defects. ROS biosensors revealed that exposure to air-gap conditions stimulates a rapid nuclear burst of hydrogen peroxide (H_2O_2) within root apical tissues. Biochemical approaches revealed that the Aux/IAA transcriptional repressor protein IAA3 forms redox-dependent multimers through sulfhydryl bridges via four specific cysteines residues. Notably, redox responsiveness of IAA3 can be directly modulated by RBOHs. By generating a quadruple cysteine-to-serine substitution mutant of IAA3 (4C/S-IAA3), we demonstrated that multimerization through these specific cysteine residues is critical for IAA3 repressor function. At the molecular level, combinatorial cysteine-to-serine substitutions abrogated IAA3's capacity to form multimers and abolished its interaction with the co-repressor TOPLESS (TPL). TPL is an evolutionarily conserved protein that inhibits transcription by recruiting histone deacetylases (HDACs) that deacetylate histones, causing a more compact, less accessible chromatin structure inhibitory for transcription. In the context of auxin signaling, the effectiveness of Aux/IAAs as transcriptional repressors is determined by their capacity to interact with TPL and recruit it to the target loci. Thus, the disruption of the 4C/S-IAA3–TPL interaction led to the de-repression of downstream auxin-responsive target genes. At the phenotypic level, attenuation of the gene repression capacity of the redox-insensitive 4C/S-IAA3 mutant led to inherently higher lateral root density and a failure to suppress lateral root formation in air gaps (xerobranching).

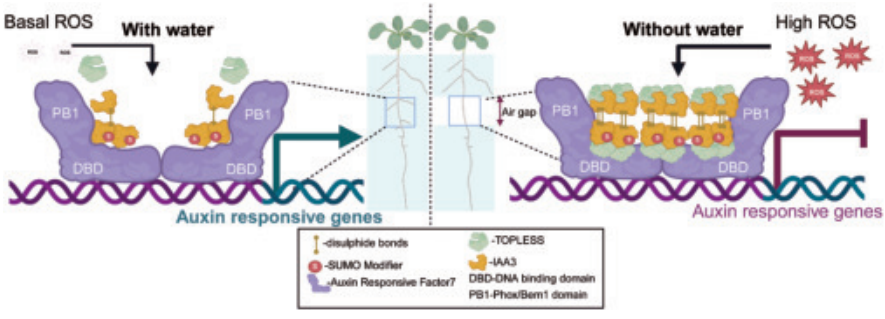

Model of the proposed mechanism for ROS-modulated IAA3 multimerization in mediating the repression of lateral root development during xerobranching. Low-water stress, such as in the air gap, triggers an increase in the ROS levels that promotes redox-dependent multimerization of wild-type IAA3 (WT-IAA3) to form a specific pattern of higher-order multimers. These multimers are recruited at target promoter sites, such as *LBD16*, through their interaction with auxin response factor (ARF) proteins, such as ARF7, via the SUMO-SIM interaction. WT-IAA3 higher-order multimers provide an increased interface for interaction with TOPLESS (TPL), leading to robust repression of auxin-dependent gene expression during xerobranching in the air gap (double-headed red arrow), curtailing lateral root development. In the presence of water, such as moist agar, ROS is reduced to basal levels. Consequently WT-IAA3 does not form higher-order multimers. Hence, the recruitment of TPL to target loci is substantially reduced, which leads to de-repression of gene expression promoting lateral root development.

CONCLUSION: Taken together, our study reveals how IAA3 multimerization can decode elevated ROS triggered by environmental changes (low-water stress) through auxin-mediated plant developmental regulation (inhibition of lateral root development). Multimerization of transcriptional repressors can confer additional layers of regulation of target gene expression in a context-driven manner. The phenomenon of redox-dependent multimerization of IAA3 reveals how the ROS signaling mechanism has been adapted by plants during the course of evolution to fine-tune plastic responses according to cellular redox status. This research helps us understand how plants respond to low water, which is relevant because water scarcity exacerbated by global climate change is becoming a widespread problem that negatively affects plant growth and development. □

*Corresponding author. Email: ari.sadanandom@durham.ac.uk (A.S.); dipan.roy@durham.ac.uk (D.R.); p.mehra@nottingham.ac.uk (P.M.) †These authors contributed equally to this work. Cite this article as D. Roy *et al.*, *Science* **389**, eadu1470 (2025). DOI: 10.1126/science.adu1470

RESEARCH ARTICLE SUMMARY

PROTEIN DESIGN

Design of intrinsically disordered region binding proteins

Kejia Wu*†, Hanlun Jiang†, Derrick R. Hicks†, David Baker*, *et al.*

Full article and list of author affiliations:
https://doi.org/10.1126/science.adr8063

INTRODUCTION: Intrinsically disordered proteins and peptides play key roles in biology, but the lack of defined structures and high variability in sequence and conformational preferences has made targeting such systems challenging. Peptide-specific antibodies have been obtained by immunization or library selection, but these methods require considerable effort and disordered antigens are susceptible to degradation following injection. In silico design of proteins that can recognize unfolded peptides based on their sequence is thus an important challenge.

RATIONALE: We sought to develop a method for achieving specific recognition of an intrinsically disordered region sequence of interest that would be broadly useful for applications in proteomics, targeting, sensing, and sequencing. We reasoned that a general solution to the intrinsically disordered region binding problem could employ an induced fit–based binding strategy, taking advantage of the fact that disordered protein regions should be flexible and lacking in preferred secondary structure. We set out to generate a set of designed binding proteins in complex with peptide backbones in a variety of conformations, with sufficient diversity to accommodate any target disordered amino acid sequence. We aimed to do this by combining physical-based and deep learning–based design methods. Using classical design methods, we first generated extended repeating protein scaffolds with pockets specialized for repeating peptide sequences. We then recombined the pockets and generalized them to a wide range of sequences using the deep learning RFdiffusion approach. Given such a set of designed binder-target peptide templates, we reasoned we could achieve general recognition of disordered protein regions by threading them through each of the templates to search of the optimal binding modes. For the most favorable matches, we used machine learning–based sequence design and backbone refinement methods to optimize binder affinity.

RESULTS: We tested our approach by designing binders for 18 synthetic peptide sequences and 21 broadly diverse, therapeutically relevant, intrinsically disordered regions. The designs were expressed and purified, and binding to the targeted disordered regions was measured by biolayer interferometry, with most designs showing picomolar to nanomolar dissociation constants. We obtained binders for 39 of 43 targets from this one-shot design process, testing 22 designs per target, on average. All-by-all binding experiments showed that each design only binds tightly to the target it was designed to bind. We showed that the binders can enrich low abundance proteins from cellular lysates for proteomics analyses, target disordered regions of extracellular receptors implicated in cancer, antagonize G protein coupled receptor signaling, and drive protein localization inside cells.

CONCLUSION: Our computational design pipeline enables the design of binding proteins to arbitrary disordered peptides and proteins. Although targeting disordered proteins has been a considerable challenge for traditional methods, we show that the disorder is an advantage: The designed binding protein drives the target sequence into a privileged binding-competent conformation, with, for example, the hydrophobic residues primarily on one face and the polar residues in customized binding modes. For each target, we sampled a wide variety of conformations and identified those compatible with high affinity binding. This approach contrasts with folded targets, whose fixed structures may admit few optimal binding solutions. Our approach should be broadly useful for designing binders for arbitrary disordered protein regions of interest. □

*Corresponding author. Email: kejiawu@uw.edu (K.W.); dabaker@uw.edu (D.B.) †These authors contributed equally to this work. **Cite this article as K. Wu *et al.*, *Science* 389, eadr8063 (2025). DOI: 10.1126/science.adr8063**

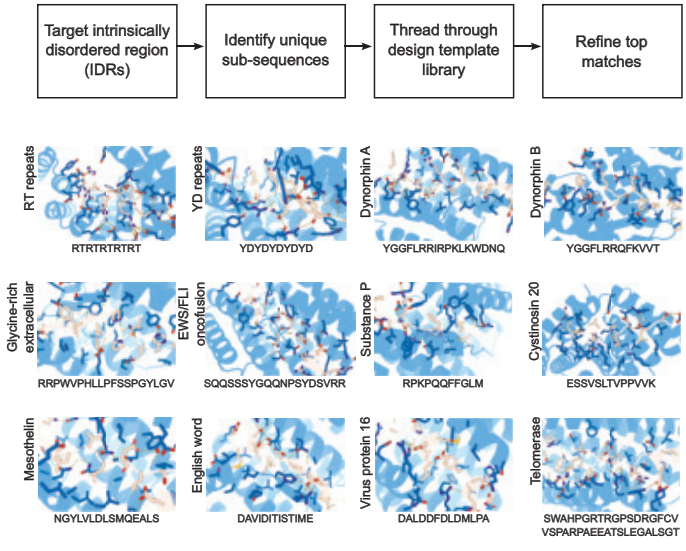

Design of IDR binding proteins. Design pipeline and 12 representative examples of active designs (for each panel, the target name is at left and the target sequence is at the bottom; targets are tan and binders are blue in the structure models. Interface residues are shown as sticks).

RESEARCH ARTICLE SUMMARY

CELLULAR NEUROSCIENCE

Polyglycine-mediated aggregation of FAM98B disrupts tRNA processing in GGC repeat disorders

Jason Yang, Yunhan Xu, David R. Ziehr, Martin S. Taylor, Max L. Valenstein, Evgeni M. Frenkel, Jack R. Bush, Kate Rutter, Igor Stevanovski, Charlie Y. Shi, Maheswaran Kesavan, Ricardo Mouro Pinto, Ira Deveson, David P. Bartel, David M. Sabatini, Raghu R. Chivukula*

Full article and list of author affiliations: https://doi.org/10.1126/science.ado2403

INTRODUCTION: Although protein aggregates are a hallmark of neurodegenerative diseases, their roles in pathogenesis remain controversial. Recent work has revealed that various GGC repeat expansions underlie a family of neurodegenerative disorders characterized by intranuclear protein aggregates in neurons as well as other cell types. Although initially thought to reside in noncoding regions of the genome, several expanded GGC repeats are now known to be translated into proteins containing aggregation-prone polyglycine (polyGly) tracts. These polyGly-containing proteins are present within intranuclear inclusions of patients with GGC repeat diseases and are toxic when expressed in animal models, suggesting that their production may contribute to neurodegeneration.

RATIONALE: The two best-characterized GGC repeat diseases are fragile X-associated tremor/ataxia syndrome (FXTAS) and neuronal intranuclear inclusion disease (NIID), which are nearly indistinguishable clinically. Given their striking similarity despite their causal loci sharing only GGC repeats in common, we reasoned that the contributions of polyGly-containing proteins to neurodegeneration in these two diseases might be attributable to their polyGly tracts per se rather than any flanking host locus sequence. We therefore developed a system to express artificial expanded polyGly proteins, purify the resulting protein aggregates, and profile their composition.

RESULTS: We found that polyGly aggregates preferentially recruit endogenous proteins containing glycine-rich intrinsically disordered regions (IDRs). Notably, among the most highly enriched of such endogenous proteins was family with sequence similarity 98 member B (FAM98B), which harbors the single most glycine-rich sequence in the entire human proteome. FAM98B is a component of the transfer RNA (tRNA) ligase complex (tRNA-LC), which catalyzes a key step in the biogenesis of intron-containing tRNAs. Through the glycine-rich IDR of FAM98B, polyGly aggregation sequesters and depletes the tRNA-LC from the soluble nucleoplasm, resulting in impaired ligation of tRNA exons.

To explore whether this process might represent a unifying pathogenic mechanism across different GGC repeat diseases, we examined tissue samples from individuals with FXTAS or NIID. In both diseases, tRNA-LC components were recruited to intranuclear inclusions and depleted from the soluble nucleoplasm. Lastly, to directly test whether impairment of tRNA ligation could contribute to neuropathology, we depleted Fam98b from the brains of adult mice. These animals developed severe motor coordination defects and widespread gliosis, which are key signs and symptoms of neurodegenerative GGC repeat diseases in humans.

CONCLUSION: These data suggest a pathogenic mechanism wherein polyGly-containing proteins produced from expanded GGC repeats interact with the glycine-rich IDR of FAM98B to sequester and deplete the tRNA-LC. Loss of tRNA ligase activity could contribute to cellular toxicity through insufficient production of mature spliced tRNAs or accumulation of tRNA splicing intermediates, ultimately resulting in neurodegeneration. Consistent with this model, mutations in other tRNA splicing pathway components cause a group of severe prenatal-onset neurodegenerative diseases exhibiting substantial phenotypic overlap with GGC repeat disorders. Our work thus suggests a mechanistic link between protein aggregation in GGC repeat disorders and inherited defects in tRNA processing machinery previously known to cause neurodegeneration. Notably, these findings raise the possibility that restoration of tRNA ligation might represent a therapeutic strategy applicable across GGC repeat diseases caused by expansions at different loci. □

*Corresponding author. Email: rchivukula@mgh.harvard.edu Cite this article as J. Yang *et al.*, *Science* **389**, eado2403 (2025). DOI: 10.1126/science.ado2403

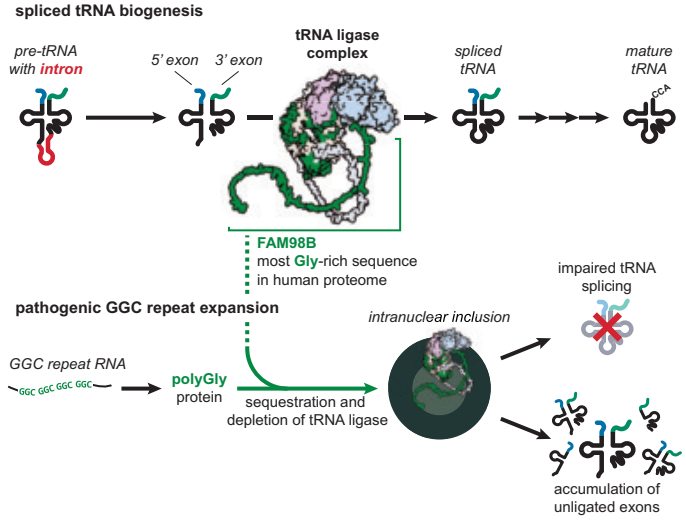

Neurodegenerative GGC repeat expansions disrupt tRNA processing through aggregation of a singularly glycine-rich disordered region in FAM98B. In normal tRNA splicing, exons are ligated by the tRNA ligase complex, a heteropentameric complex containing FAM98B. PolyGly proteins produced in GGC repeat disorders interact with FAM98B, which harbors the single most glycine-rich sequence in the human proteome, resulting in sequestration and depletion of the tRNA ligase complex.

EARTHQUAKE ALERTS

Global earthquake detection and warning using Android phones

Richard M. Allen[1,2]*, Alexei Barski[1], Micah Berman[1], Robert Bosch[1], Youngmin Cho[1], Xia Summer Jiang[1], Yun-Ling Lee[1], Steve Malkos[1], S. Mostafa Mousavi[1,3], Patrick Robertson[4], Boone Spooner[1], Marc Stogaitis[1], Nivetha Thiruverahan[1], Greg Wimpey[1]

Earthquake early-warning systems are increasingly being deployed as a strategy to reduce losses in earthquakes, but the regional seismic networks they require do not exist in many earthquake-prone countries. We use the global Android smartphone network to develop an earthquake detection capability, an alert delivery system, and a user feedback framework. Over 3 years of operation, the system detected an average of 312 earthquakes per month with magnitudes from *M* 1.9 to *M* 7.8 in Türkiye. Alerts were delivered in 98 countries for earthquakes with *M* ≥4.5, corresponding to ~60 events and 18 million alerts per month. User feedback shows that 85% of people receiving an alert felt shaking, and 36, 28, and 23% received the alert before, during, and after shaking, respectively. We show how smartphone-based earthquake detection algorithms can be implemented at scale and improved through postevent analysis.

Earthquakes remain a constant challenge for many communities around the world. Our global understanding of where seismic events will occur is excellent (*1*), and we know how to engineer structures that can withstand shaking. However, we still face catastrophic earthquakes. Some kill and injure thousands of people such as in Türkiye and Morocco in 2023; many more injure hundreds, thereby disrupting many lives. Access to the knowledge and necessary resources to construct safe buildings remains a limiting factor in many parts of the world. Even with the resources, it would still take many decades to replace vulnerable buildings. Once earthquake-resilient buildings are in place, there remain hazards from falling objects inside buildings that can cause many injuries and some fatalities. We must therefore continue to look for additional strategies to reduce the impact of future earthquakes globally. Earthquake early-warning (EEW) alerts are one such strategy.

The global adoption of smartphone technology places sophisticated sensing and alerting capabilities in people's hands, in both the wealthy and less-wealthy portions of the planet. Although the accelerometers in these phones are less sensitive than the permanent instrumentation used in traditional seismic networks, they can still detect the ground motions and building response in hazardous earthquakes (*2*–*9*). Traditional seismic networks have been used to develop EEW systems that rapidly detect an earthquake close to the epicenter and issue a warning across the affected region (*10*). EEW was first implemented in Mexico and Japan. The success of these systems led to implementation in Taiwan, South Korea, the United States, Israel, Costa Rica, and Canada (*11*–*17*). All these systems use permanent seismic stations deployed as part of regional or national seismic networks.

We present the methodology and performance of an algorithm that uses the existing network of Android smartphones to detect earthquakes globally and deliver early-warning alerts to smartphone owners ahead of hazardous shaking. The goal of the system is to deliver useful and timely alerts in as many earthquake-prone regions around the globe as possible. The system is supplementary to any existing national warning systems and includes the collection of uniform user feedback. We compare the accuracy of our early warnings against the global catalog of postshaking evaluations, and we also measured the utility of the alerts using surveys completed by more than a million alert recipients. We discuss the successes and challenges of this global sensing and alerting network called Android Earthquake Alerts (AEA) system.

Earthquake detection with smartphones

AEA uses the same principles of seismic wave propagation as traditional earthquake detection systems. When an Android smartphone is stationary, it uses the output of its accelerometer to detect a sudden increase in acceleration as would be generated by *P* and *S* waves in an earthquake. When an individual phone triggers, it sends a message to Google servers with acceleration information and an approximate location (location coarsened to preserve privacy). The servers then search for candidate seismic sources that are consistent with the time-space trigger distribution. When a candidate earthquake source satisfies the observed data with a high enough confidence, an earthquake is declared and its magnitude, hypocenter, and origin time (OT) are estimated on the basis of the arrival time and amplitude of the *P* and *S* waves. This detection capability is deployed as part of Google Play Services core system software, meaning it is on by default for most Android smartphones. As Android phones represent an estimated 70% of all smartphones globally (*18*), this system largely provides an earthquake detection capability wherever there are people, in both wealthy and less-wealthy nations.

From 1 April 2021 to 31 March 2024, AEA detected a total of 11,231 earthquakes (Fig. 1, fig. S1, and movie S1). Of these, 85% match an earthquake listed in a traditional earthquake catalog that our system was able to automatically ingest for detection validation (materials and methods). All nonmatching events were reviewed to verify whether they were earthquakes or not on the basis of user survey feedback, felt-shaking reports collected through Google Search (*19*), manual review of additional earthquake catalogs, and review of waveforms and triggers. For matching events, the traditional network magnitude estimates range from *M* 1.9 to *M* 7.8 (corresponding to an event in Japan and Türkiye, respectively). The ability of the system to detect earthquakes depends on the distribution of phones and other sources of cultural noise at the time of the earthquake. AEA does not detect earthquakes on most mid-ocean ridges but does detect subduction zone events that are tens to hundreds of kilometers offshore. Global Android detections and alerts are shown in Fig. 1 and fig. S1.

Figures S2 and S3 show waveform envelope record sections for two *M* 5.0 earthquakes illustrating *P*-wave sensitivity out to 100 to 200 km and *S* waves out beyond 350 km. To understand the detection sensitivity as a function of the distance of the earthquake from phones, we considered all detected earthquakes that were offshore and calculate the distance of the epicenter from the nearest coastline. Figure S4 shows that *M* 4.5 earthquakes were detected up to ~100 km offshore. A review of all AEA detections shows that the system has detected earthquakes within 30 km of 40% of all major onshore faults (fig. S5). The magnitude of completeness (M_c) is a standard measure of network detection sensitivity characterizing the minimum magnitude above which we are reliably detecting earthquakes. Using the maximum curvature method to determine M_c (*20*), we found a global M_c of 4.9 (fig. S6). In North America, M_c is 4.1; in South America, 4.9; and in Europe, 4.6.

The most challenging earthquake source parameter for EEW is rapid determination of the magnitude. Any delay in estimating the magnitude is also a delay in the warning provided to users. Figure 2 shows the improvement in the accuracy of the magnitude estimates generated by

[1]Google LLC, Mountain View, CA, USA. [2]Seismological Laboratory, University of California, Berkeley, Berkeley, CA, USA. [3]Department of Earth and Planetary Sciences, Harvard University, Cambridge, MA, USA. [4]Google Germany GmbH, Munich, Germany. ***Corresponding author. Email: rallen@berkeley.edu**

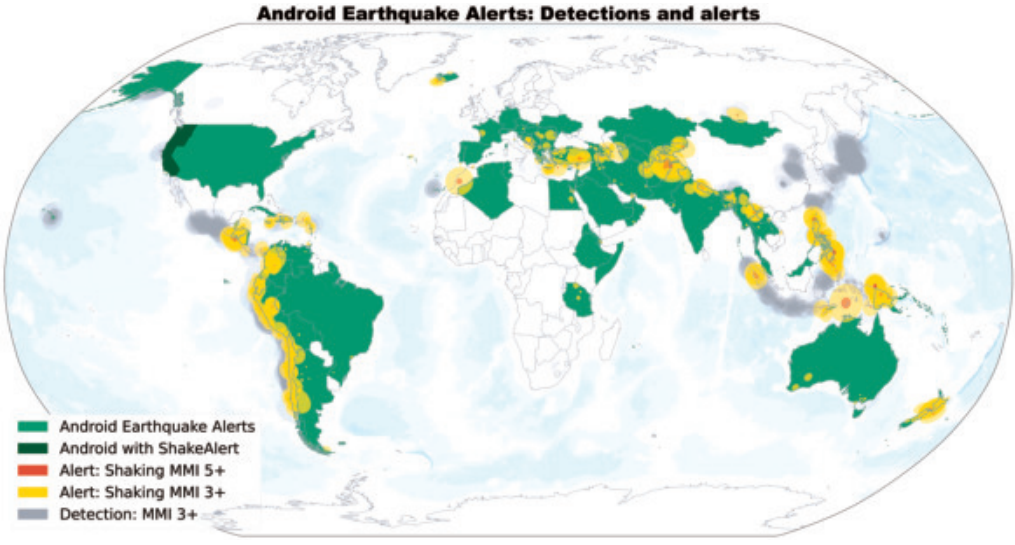

Fig. 1. Global distribution of earthquakes detected and alerted. Light-green areas show the countries where AEA is currently detecting and delivering alerts. Android also delivers alerts generated by ShakeAlert in California, Oregon, and Washington (dark green). Yellow and red circles show the areas alerted on the basis of Android detections (data S1), and gray circles indicate other detections in regions where alerts were not issued. The size of the circles indicates the approximate estimated shaking region with MMI 3+ (yellow and gray) or MMI 5+ (red).

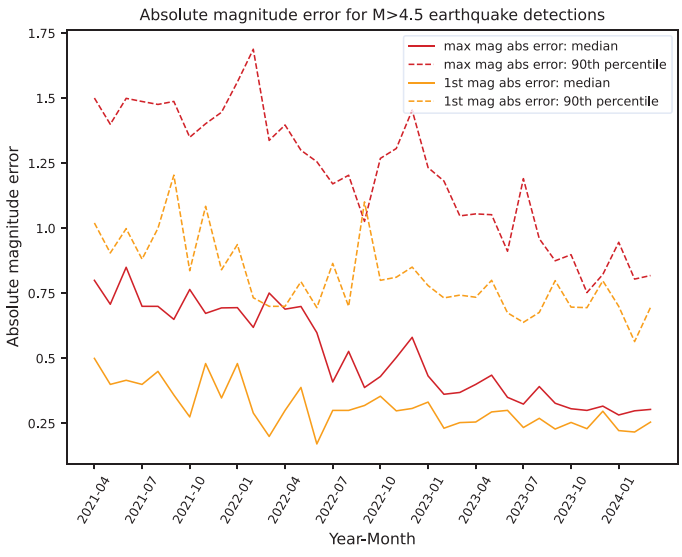

Fig. 2. Evolution of AEA earthquake magnitude error over the past 3 years (data S2). Plotted are the median and 90th percentile absolute magnitude errors for detected earthquakes each month with $M \geq 4.5$. We plot the error of the first magnitude estimate and the maximum magnitude estimate. Both magnitude metrics have improved over the 3 years of development of AEA. The median absolute magnitude errors of the first alert and the maximum magnitude are currently 0.25 and 0.30 magnitude units, respectively.

AEA over the past 3 years as the detection system has been improved. During an earthquake, source parameters are updated approximately every second as ground shaking evolves and more phone-based observations become available to centralized detection servers.

Figure 2 shows the accuracy of the first magnitude estimate and the maximum magnitude over the 3-year period. The first estimate is important because it provides the maximum warning time, whereas the maximum magnitude estimate generates an alert for the largest area. Over the past 3 years, the median absolute error of the first magnitude estimate has improved from 0.50 to 0.25, and the 90th percentile has dropped from 1.02 to 0.70. The most important source of long-term improvement has been the development of regional detection models. These models account for the different tectonic settings and attenuation characteristics as well as differences in how varying models of phones sample ground motion because of regional variations in building type. They provide a data-driven regional scaling between parameters such as the number of phones triggering and the estimated magnitude. The result is an effective correction to the magnitude estimate, which ranges from +0.6 to −1.4 magnitude units (fig. S7).

Alert performance

As of May 2024, AEA delivered alerts to Android phones in 98 countries. In most countries, the alerts were generated from Android event detections (light green in Fig. 1). In the United States, AEA also delivered alerts generated by ShakeAlert, which is the national EEW system using traditional regional seismic networks (*17*, *21*). The priority of AEA, as with other EEW systems, is moderate- to large-magnitude earthquakes that represent a hazard to people living in the region. Alerts were therefore issued for earthquakes with an estimated $M \geq 4.5$ and delivered to the region expected to experience shaking of Modified Mercalli intensity (MMI) 3 or larger. Although an earthquake has a single magnitude estimate, the shaking intensity (MMI) varies as a function of distance from the earthquake fault rupture. The expected distance to which MMI 3+ occurs increases with increasing magnitude. Figure 1 shows the estimated MMI 3 regions for all Android-detected earthquakes with estimated $M \geq 4.5$. Events for which Android alerts were issued are shown in yellow or red; detections in countries where alerting was not activated are shown in gray.

The rollout of AEA started with the delivery of alerts generated by ShakeAlert in California on 11 August 2020. Alerts generated by Android detections started 28 April 2021 in New Zealand and Greece and then expanded to Türkiye, the Philippines, and central Asia on 15 June 21. In 2022, the system was rolled out to remaining high-hazard countries where alerting is allowed; AEA was delivering alerts in 93 countries by the end of 2022 and 98 countries by the end of 2023 (see data S1).

Figure 3 shows the number of people with access to EEW alerts globally from all sources. Alerting started in 1991 in Mexico City and then Japan in 2007. With the addition of Taiwan, South Korea, and the United States, 250 million people had access to EEW in 2019. Today, with the addition of AEA, 2.5 billion people have access to alerts. The EQN smartphone EEW system also provides alerts to an estimated 2 million users globally (*22*).

AEA has issued alerts to Android phones for a total of 1279 events detected by the Android phone network [as of 31 March 2024 (data S1)]. Of these, three were false alerts. Two were due to thunderstorms. The system detects many non-earthquake seismic events every day owing to various sources of acceleration detected by the phones. Most thunderstorms are correctly identified as such, but these two instances were outside the classifier range. Learning from these events, we expanded the range of parameters for a sonic source and increased the confidence required before an alert is used (materials and methods). Replays showed that these two events would no longer produce

an alert. The third false alert was due to a mass notification event vibrating many phones. In this case, improvements to the detection algorithm's recognition of other events causing phone vibrations were made, and similar mass notifications have not triggered an alert since.

The alert region for each earthquake was determined by the rapid magnitude estimate. We compared the accuracy of the AEA magnitudes with those of EEW systems using traditional seismic networks. Table 1 compares the mean, median, and 90th percentile absolute error in the magnitude estimates for AEA, the US ShakeAlert, and the Japanese JMA EEW systems. We calculated the error in both the first magnitude estimate and the maximum magnitude estimate compared with final catalog magnitude determined after the event using traditional seismic networks. The errors are very similar for the three systems. AEA and ShakeAlert use the same M 4.5 threshold for alerts and have lower errors. JMA errors are slightly higher, but they also only issue alerts for larger earthquakes. AEA has the lowest errors and issues an order of magnitude more alerts than the other two systems (Table 1).

Two types of alert messages are delivered by AEA. When the estimated magnitude is ≥4.5, a "TakeAction" alert is delivered to the region expected to experience MMI ≥5, and a "BeAware" alert is delivered to the region expected to experience MMI 3 or 4. The alerts are delivered to octagonal regions centered on the estimated epicentral location to approximate the expected circular shape of the shaking region. The distance of the octagon vertices from the epicenter is determined on the basis of the estimated magnitude and the depth of the event. AEA currently uses the same alert distance contours as ShakeAlert (*23*, *24*), but with a correction for event depth. For an event with an estimated magnitude of 5.5 and depth of 20 km, the TakeAction alert would extend to 8 km, and the BeAware alert to 197 km. For a M 6.5, the alert regions extend to 78 and 442 km for TakeAction and BeAware, respectively. The same alert distance contours are currently used for all regions. Alerting performance can be improved in the future by accounting for regional seismic attenuation differences.

The TakeAction and BeAware alerts (fig. S8 and audios S1 and S2) were designed on the basis of best practices for alerts (*25*–*28*) and through focus groups. The goal is to deliver on the user's desire for alerts whenever they feel shaking while also indicating urgency when stronger shaking is expected. The TakeAction alert breaks through all do-not-disturb settings, takes over the whole screen, and plays a loud and characteristic sound. It is designed to immediately draw the user's attention and prompt them to take the recommended protective action, which in most countries is "Drop, cover and hold on" (DCHO) (fig. S8). In countries where this is not the recommended action, the screen displays "Protect yourself." The BeAware alert appears on the phone in a similar way to other standard Android notifications but has a characteristic sound. It does not break through do-not-disturb settings. If an alert reaches a phone after the expected period of shaking, then an "earthquake occurred at…" notification is shown (fig. S8). Tapping on any of the alerts takes the user to an earthquake safety page with tips for what to do after the earthquake, more information about the quake provided by Google Search, and a link to a user survey that collects information about the user's experience with the alert and shaking.

We illustrate typical AEA system behavior and warning times with two example earthquakes. The first is the 17 November 2023 earthquake in the Philippines with a magnitude of 6.7 and a hypocenter 40 km offshore at a depth of 52 km according to the US Geological Survey (USGS) global catalog. It took about 12 s for the P wave to reach the closest cluster of phones, and the first alert was generated 18.3 s after the OT with an estimated magnitude of 5.5. The magnitude estimate grew over time to a maximum of 6.5, 28.6 s after OT (table S1). Figure 4A shows the warning time for users receiving a BeAware alert that ranged from a few seconds for those closest to the epicenter experiencing the strongest shaking, up to ~90 s for those at 400 km experiencing light shaking. Warning times for the strongest shaking (MMI 7 or 8, very strong to severe) ranged up to ~15 s. For the moderate shaking, which also causes damage (MMI 5 or 6, moderate to strong), warning times ranged from seconds up to a minute (Fig. 4A). Almost 2.5 million phones were alerted for this event, and more than 100,000 received TakeAction alerts. The TakeAction alerts (Fig. 4B) arrived at most phones a few seconds before the S-wave arrival and ~2 to 8 s before peak shaking of MMI 6, 7, and 8.

The second example is the 3 November 2023 shallow crustal earthquake in Nepal with a USGS catalog magnitude of 5.7 and a depth of 12 km. The first AEA alert was 15.6 s after the USGS OT with an estimated magnitude of 5.5. This was updated to 5.7 and then 5.9 at 28.2 s (table S2). The population was sparse near the epicenter, which delayed the detection and meant there was no warning time within ~50 km of the epicenter and no TakeAction alerts ahead of ground shaking. The BeAware alert extended beyond 300 km from where the intensity reported to USGS Did You Feel It (DYFI) ranged from 2 to 6 (weak to strong). Similar to the Philippines example, the large number of people experiencing MMI 5 and 6 received from a 10- to 60-s warning. More than 10 million BeAware alerts were delivered in this earthquake.

The most challenging events for all EEW systems are the largest ones, M>7.5 (*29*, *30*). The most impactful earthquakes since AEA became operational were the 6 February 2023 M 7.8 Pazarcik and M 7.5 Elbistan earthquakes in Türkiye. AEA was operational at the time

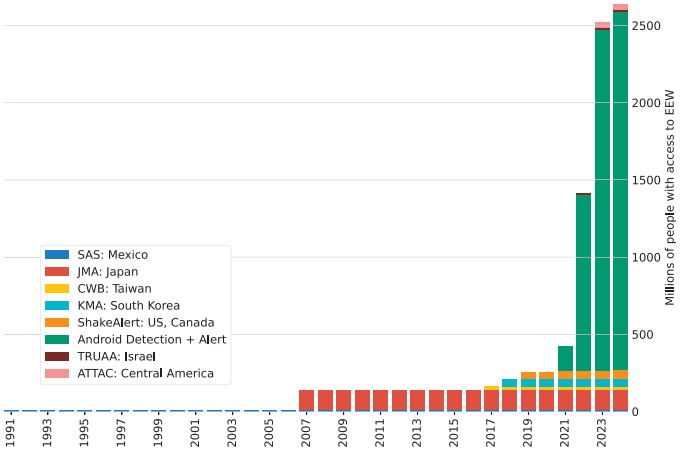

Fig. 3. Growth in the number of people with access to EEW alerts globally. The number of people with access to EEW alerts is estimated for each system on the basis of the delivery mechanism, smartphone penetration, and types (data S3).

Table 1. Comparison of magnitude errors for alerts issued by various EEW systems. Bold numbers indicate the lowest errors in each column.

EEW system	Number of events	1st magnitude absolute error median	1st magnitude absolute error 90th percentile	1st magnitude absolute error mean	Max magnitude absolute error median	Max magnitude absolute error 90th percentile	Max magnitude absolute error mean
Android*	1005†	**0.3**	**0.8**	**0.39**	**0.3**	**0.8**	**0.38**
ShakeAlert‡	107	0.4	0.9	0.45	**0.3**	0.9	0.47
JMA§	102	0.4	1.1	0.54	0.40	1.0	0.47

*All public alerts through March 2024 (estimated magnitude ≥4.5, 18 September 2020 to 31 March 2024). †Of the 1279 alert events, 1005 have matching events in the traditional network ground truth catalogs for error estimation (materials and methods). ‡All public alerts through March 2024 (estimated magnitude ≥4.5, 17 October 2019 to 31 March 2024). §All public alerts 1 January 2018 through 31 March 2024.

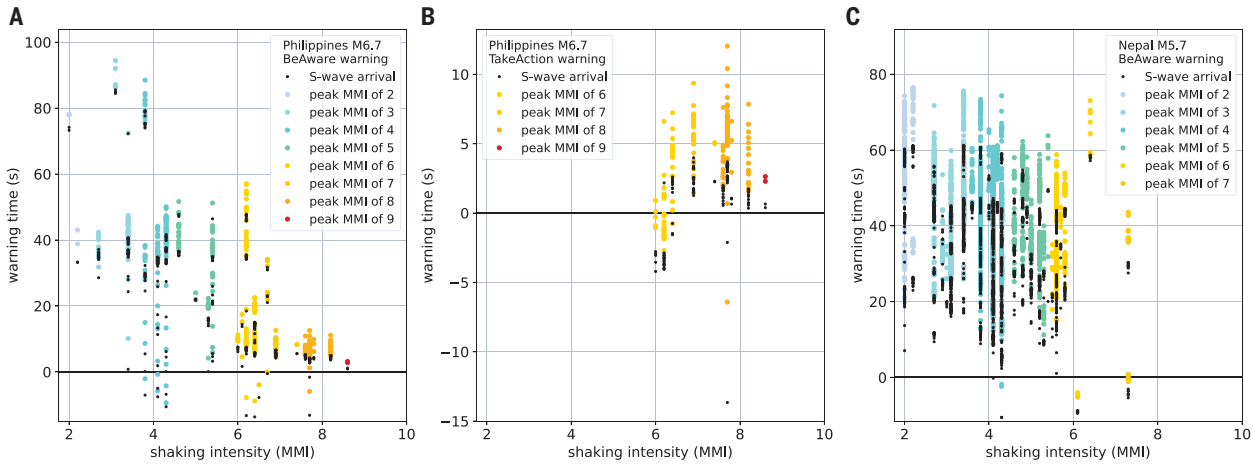

Fig. 4. Warning time versus shaking intensity. (**A**) BeAware alert warning times for the *M* 6.7, 17 November 2023 earthquake in the Philippines. (**B**) TakeAction alert warning times for the same Philippines event. (**C**) BeAware alert warning times for the *M* 5.7, 3 November 2023 earthquake in Nepal. In all three panels, the warning time is plotted as a function of the observed shaking intensity. The shaking intensity comes from the nearest USGS DYFI report of MMI shaking (within 5 km). Two warning times are plotted. Black dots show the time from alert delivery on a phone until the *S*-wave arrival. Colored dots show the time until peak shaking observed on the phone and are colored on the basis of shaking intensity (ShakeMap color scale). As peak shaking typically follows *S*-wave onset, warning times until peak shaking are a few seconds longer. Figure S9 shows the same data plotted versus epicentral distance. See data S4.

in Türkiye and detected both events. For the first event, the initial magnitude estimate was 4.5 at 7.1 s after OT, and the maximum magnitude estimate was 4.9 at 18.7 s. A total of 512,411 BeAware alerts were issued out to a distance of 64 km. In the second event ~9 hours later, the initial magnitude estimate was 6.1, at 24.4 s after OT, which increased to magnitude 6.3 5.2 s later. A BeAware alert was delivered to 3,944,909 phones in this event, with warning times ranging from a few seconds to more than a minute.

In addition to AEA, the EQN app-based warning system was also operational in the region at the time. They report detecting the *M* 7.8 Pazarcik event 12.1 s after OT and delivering alerts to 63,539 users, with 62,419 of those users receiving mild shaking alerts out to a distance of 3506 km. EQN did not detect the *M* 7.5 Elbistan quake (*22*).

Postevent analysis revealed several limitations to the detection algorithms that have since been improved. First, the duration of monitoring has increased. At the time of the event, the algorithm only allowed updates to earthquake parameters for 10 s after first detection. The number of allowed updates was limited because there was a trade-off between more updates providing additional information for larger earthquakes and more updates introducing outlying single-epic data causing a large overalert. We now allow updates for 30 s and use other checks on the rate of variation in earthquake parameters before updating an alert. Second, there were a large number of noisy phones in the monitoring pool at the time of the Türkiye earthquakes. These high-noise phones triggered late, particularly after the *P* wave for the *M* 7.8 event, which had a slow start and complex rupture (*31*–*34*). The AEA system is now more selective about which phones are included in the monitoring pool. Individual phones determine their noise level when they become available for monitoring, and this noise level is factored into the detection algorithm. Third, many phones were receiving a BeAware alert and vibrating, which prevented them from triggering on the earthquake ground motion. The alerts now issued by Android EEW no longer cause phones that are detecting to vibrate.

Using our evaluation system, we ran the new algorithms on the data collected for the Türkiye earthquakes in simulated real time. The algorithm in production today generated an initial magnitude of 4.6, 6.3 s after OT. The magnitude then climbed to a maximum magnitude of 7.4 over a period of 24 s. This generated TakeAction alerts out to 158 km that would have been received by 10 million Android phones, providing up to a 35-s warning, and BeAware alerts to a distance of 604 km that would have been received by 67 million users, providing a 2.5-min warning before the first *S* wave (figs. S13 and S14). For context, the "heavy" MMI 8 shaking in places such as Antakya, Türkiye, did not occur until more than a minute after OT (*32*) (for more detail on both events, see materials and methods and figs. S10 to S14). Work continues to improve the algorithm for large ruptures, when the finite fault effect becomes important.

User response to alerts

The purpose of AEA is to deliver useful and actionable alerts to people. We therefore request information and feedback from users to determine their opinions of the alerts that they receive and actions that they take after the alerts. We accomplish this using Google's standard in-product user surveys (*35*). When a user clicks on any AEA alert, they are presented with a page of additional information including safety tips and information about the earthquake. At the bottom of this page is another link inviting them to take a user feedback survey after an informed consent message (figs. S15 and S16). The survey consists of six questions as detailed in the materials and methods section and is currently delivered in 24 languages. This is not a randomized sample; rather, users choose to complete the survey. As far as we are aware, this is true of all surveys about EEW to date [e.g., (*36*–*39*)].

How helpful was the alert?

Over the period 5 February 2023 to 30 April 2024, $N = 1{,}555{,}006$ people responded to the survey after having received alerts generated from an Android detection—i.e., alerts in all countries except the US. Over the same period and region, 412 million alerts were delivered, giving a response rate of 0.38%. Of those responding, 3900 received TakeAction alerts, and the rest received BeAware alerts. The first question asked was "How helpful or unhelpful was the earthquake alert?" The users selected a score from 1 ("Not helpful at all") to 5 ("Very helpful"). The average score was 4.7 with 85% of respondents reporting it was "very helpful" (Fig. 5). If we consider just those receiving TakeAction alerts, the average score was also 4.7. This positive response to EEW alerts (for both BeAware and TakeAction) is consistent with previous studies that ask whether an EEW alert is useful or not. For example, in the United States (one earthquake, $N = 2490$, *36*) and Japan (two earthquakes, $N = 449$, *37*), recent studies found that 67

and 75%, respectively, of people surveyed found the alerts useful. In an independent study of AEA alerts for two earthquakes ($N = 3150$) in New Zealand, 84 and 83% of respondents reported the alerts were useful (*38*). These studies were also based on responses to surveys.

Did you feel shaking?

Of the respondents (all of whom received alerts), 85% felt shaking, with 53% classifying it as "strong" and 32% as "weak." Of the users reporting they felt "strong" and "weak" shaking, 87 and 85%, respectively, rated the alert as "very helpful" (Fig. 5). Of those reporting no shaking, still 79% rated the alert as very helpful. The fact that people are positive about receiving the alert, despite not feeling shaking, is likely due to one of several factors: (i) The alert plays a key educational role making the user aware of the system and demonstrating that it is functional (*36*, *38*). (ii) There is a strong desire for immediate information after an earthquake (*40*), and the alert provides some of that information along with links to more. (iii) In almost every case there was an earthquake, and friends and neighbors likely felt it. Therefore, it is considered an effective alert and keeps people aware of what is happening in their community.

How strong was the shaking?

We separated responses according to whether they received BeAware or TakeAction alerts. As expected, a larger percentage of those receiving TakeAction alerts ($N = 2219$) classified the shaking as "strong" (92%), compared with 53% of those receiving BeAware alerts ($N = 1{,}116{,}395$; Fig. 5). There were very few users who received a TakeAction alert and then reported not feeling shaking (2%), compared with 14% of people receiving a BeAware. The very low fraction of people receiving the more intrusive and disruptive TakeAction alert who then did not feel shaking likely contributed to the overall forgiving response of users who do not feel shaking.

When did you receive the alert?

Of all the respondents ($N = 1{,}487{,}182$; the number of responses drops with each successive question), 36% said they received the alert before shaking, 28% during, 23% after, and 13% did not know (Fig. 5). BeAware alerts always extend farther from the epicenter than the TakeAction alerts, leading to longer BeAware warning times. This resulted in a larger fraction of BeAware alerts ($N = 1{,}082{,}495$) being received before shaking (44%) than TakeAction (14%, $N = 2136$; Fig. 5). There was a positive correlation between when the alert arrived and helpfulness score. Of those receiving the alert before, during, and after shaking, 93, 86, and 75%, respectively, rated the alert as "very helpful" (Fig. 5).

What action did you take?

Recommended actions when receiving an alert (or experiencing shaking) are mostly DCHO or flee and evacuate outside (*41*). Previous studies of what people actually do have found that the most common responses to receiving an EEW alert are to mentally prepare, tell others, look for more information, stop and wait, or do nothing (*36*–*39*). We confirm these conclusions, finding that 30% of all respondents shared the alert with others, 25% waited to see whether shaking started, 20% searched for more information online, and 19% did nothing.

The recommended protective action when feeling shaking or getting an alert in most countries is DCHO (*41*). This is the fifth most common response of our users receiving a BeAware alert, with 14% reporting taking DCHO action. Encouragingly, for users receiving a TakeAction alert, the most common response was DCHO with 28% of users reporting taking that action, whereas fewer shared the alert or waited (Fig. 5).

Will you trust future alerts?

For AEA to continue to be effective, and to be more effective in the future, users should trust the system and the alerts. The final question asked users about their trust in the system given their experience with the alert they just received. Of those responding, 84% said they would trust the system more next time, 13% said it did not affect their trust, and 3% said they will trust it less in future (fig. S10). Users also have the option to opt out of the system if they do not want future alerts. Three years into operation, only 0.1% of users have disabled alerts.

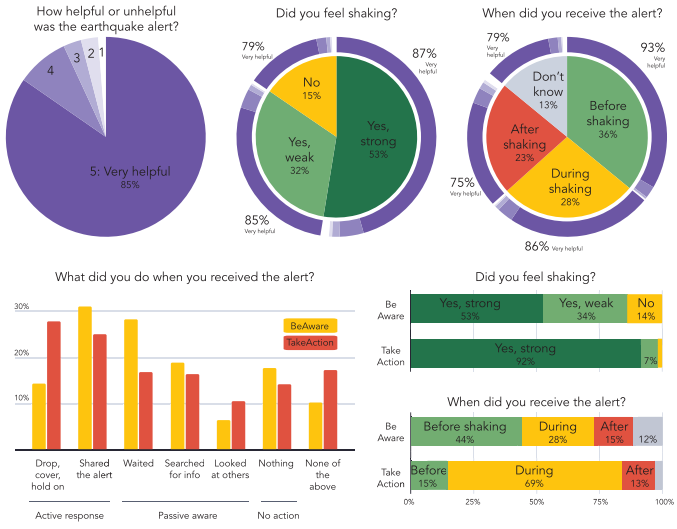

Fig. 5. Feedback from users who received an alert. A total of 1,555,006 responses to the user survey were collected over the period from 5 February 2023 to 30 April 2024. During this time, alerts were issued for 1042 earthquakes detected by AEA. Response data are included in tables S3 to S11.

Implications for EEW systems

The proliferation of low-cost sensors in consumer products provides opportunities for new observations of our physical environment that are both dense and global in scale (*42*). AEA makes it possible to make global observations of earthquakes through smartphones by turning that information into useful alerts. Maximizing the effectiveness of EEW systems, including AEA, requires synergizing (i) our understanding of earthquake physics, (ii) the technical limitations of sensor networks and alert delivery, and (iii) user-informed social science about alert delivery. The physics of the earthquake process limit prediction of strong (MMI > 5) shaking to a few seconds ahead of onset (*43*). The TakeAction alerts were designed to prompt users to take protective actions, but by delivering them only when we have predicted strong shaking, we are only able to provide a few seconds' warning. The BeAware alerts are less intrusive and more informational and often delivered with a warning of many tens of seconds.

Most recipients of both alert types do respond. Goltz and colleagues (*36*) categorized user responses to EEW as "active," "passive aware," and "no action." Although an active response such as DCHO is preferable, the more common passive aware responses will also likely reduce the number of injuries. Having been alerted to the pending hazard, and assuming the user has some basic knowledge of how to protect themselves, they are less likely to be injured when the shaking starts.

The BeAware alerts provide some of this education to users. Most users will receive a BeAware alert before they receive a TakeAction alert. This makes them aware of the system, provides simple information about what to do when they receive an alert, and has a very high helpfulness rating (86% rate it as "very helpful"). The very high helpfulness rating by users who did not feel shaking and those receiving the alert after shaking (Fig. 5) also demonstrates the educational and informational value of the alerts. Users also expect and want alerts for

low-intensity shaking (*36*, *39*), making the BeAware-type alerts a critical element of an EEW system.

It is encouraging that 28% of recipients who received a TakeAction warning reported following the recommended DCHO action. This is higher than in previous surveys. Only 6% reported following DCHO when receiving an alert for an earthquake in southern California (*36*), similar to the 8% who reported doing DCHO in the last earthquake they felt before EEW being operational in the United States (*44*). Users are also tolerant of overalerting (*39*), i.e., receiving an alert despite not feeling shaking during an earthquake (Fig. 5). One possibility for EEW systems might therefore be to deliver intrusive TakeAction-like alerts at lower shaking thresholds for larger earthquakes. This could improve warning times for TakeAction alerts and mitigate some of the alerting challenges in the largest earthquakes.

Central to the future success of AEA is the result that 84% of users responding report that they will trust the AEA system more next time, and only 3% say less. Trust in an alert is one of the key factors promoting compliance with the recommended actions (*25*), and it also supports the application of phone-derived data to this work.

AEA demonstrates that globally distributed smartphones can be used to detect earthquakes and issue warnings at scale with an effectiveness comparable to established national systems. Large earthquakes remain the most important and challenging for all EEW systems, and the global implementation of AEA supports efforts to improve detection with rapid, large-scale data collection and feedback to algorithms. In the future, the AEA detection system could also provide additional information and products that could reduce hazards. Small earthquake detections in regions without seismic networks could help characterize faults and associated hazards beneath urban environments. The dense, local, and real-time ground motion observations could provide rapid post-earthquake maps of shaking intensity similar to ShakeMap, which are critical to emergency response (*33*, *35*). Aggregated observations of shaking over multiple earthquakes could support improved regional hazard models globally. Delivering these products, with the support and trust of users, will help build community awareness of earthquake hazards and strategies to reduce them.

REFERENCES AND NOTES

1. K. Johnson *et al.*, Global Earthquake Model (GEM) Seismic Hazard Map (version 2023.1 - June 2023); https://doi.org/10.5281/zenodo.8409647 (2023).
2. S. Dashti *et al.*, *Earthq. Spectra* **30**, 721–742 (2014).
3. L. R. Evans *et al.*, *Seismol. Res. Lett.* **85**, 147–158 (2014).
4. Q. Kong, R. M. Allen, L. Schreier, Y.-W. Kwon, *Sci. Adv.* **2**, e1501055 (2016).
5. F. Finazzi, *Bull. Seismol. Soc. Am.* **106**, 1088–1099 (2016).
6. Q. Kong, S. Patel, A. Inbal, R. M. Allen, *Seismol. Res. Lett.* **90**, 1937–1949 (2019).
7. R. M. Allen, Q. Kong, R. Martin-Short, *Pure Appl. Geophys.* **177**, 1699–1712 (2020).
8. S. C. Patel *et al.*, *Sensors* **23**, 8668 (2023).
9. S. Marcou, R. M. Allen, N. A. Abrahamson, C.-S. Sung, *Bull. Seismol. Soc. Am.* **115**, 86–105 (2024).
10. R. M. Allen, D. Melgar, *Annu. Rev. Earth Planet. Sci.* **47**, 361–388 (2019).
11. A. Cuéllar, G. Suárez, J. M. Espinosa-Aranda, *Bull. Seismol. Soc. Am.* **107**, 1451–1463 (2017).
12. D. H. Sheen *et al.*, *Seismol. Res. Lett.* **88**, 1491–1498 (2017).
13. Y. Kodera *et al.*, *Front. Earth Sci.* **9**, 726045 (2021).
14. R. N. Nof, I. Lior, I. Kurzon, *Front. Earth Sci.* **9**, 684421 (2021).
15. J. Porras *et al.*, *Front. Earth Sci.* **9**, 700843 (2021).
16. Y. M. Wu, H. Mittal, D.-Y. Chen, T.-Y. Hsu, P.-Y. Lin, *J. Geol. Soc. India* **97**, 1525–1532 (2021).
17. A. I. Lux *et al.*, *Bull. Seismol. Soc. Am.* **114**, 3041–3062 (2024).
18. Recent (2024 and 2025) public domain analyses of Android smartphone market share globally range from 70 to 72%. See https://backlinko.com/iphone-vs-android-statistics, https://prioridata.com/data/smartphone-stats/, and https://www.demandsage.com/android-statistics/.
19. Google Search collects data from people searching for information about an earthquake. When a user types a search such as "earthquake near me" and AEA has detected a likely earthquake, the user is asked whether they felt shaking. These counts of the number of people reporting felt shaking are used to help verify when an earthquake has occurred.
20. S. Wiemer, M. Wyss, *Bull. Seismol. Soc. Am.* **90**, 859–869 (2000).
21. D. D. Given *et al.*, "Revised technical implementation plan for the ShakeAlert system—An earthquake early warning system for the West Coast of the United States" (US Geological Survey Open-File Report 2018–1155, 2018); https://doi.org/10.3133/ofr20181155
22. F. Finazzi, R. Bossu, F. Cotton, *Sci. Rep.* **14**, 4878 (2024).
23. K. Thakoor, J. Andrews, E. Hauksson, T. Heaton, *Seismol. Res. Lett.* **90**, 1243–1257 (2019).
24. J. K. Saunders, A. S. Baltay, S. E. Minson, M. Böse, *Seismic Rec.* **4**, 121–130 (2024).
25. D. S. Mileti, J. H. Sorensen, *Communication of Emergency Public Warnings: A Social Science Perspective and State-of-the-Art Assessment. No. ORNL-6609* (Oak Ridge National Lab, 1990); https://doi.org/10.2172/6137387.
26. M. M. Wood *et al.*, *Environ. Behav.* **50**, 535–566 (2018).
27. J. Sutton, L. Fischer, L. E. James, S. E. Sheff, *Int. J. Disaster Risk Reduct.* **49**, 101664 (2020).
28. J. Sutton, M. M. Wood, D. O. Huntsman, N. Waugh, S. Crouch, *Nat. Hazards Rev.* **24**, 04023035 (2023).
29. M. Hoshiba, in *Earthquake Hazard, Risk, and Disasters*, J. F. Shroder, M. Wyss, Eds. (Academic Press, 2014), pp. 505–529.
30. A. I. Chung *et al.*, *Bull. Seismol. Soc. Am.* **110**, 1904–1923 (2020).
31. D. Melgar *et al.*, *Seismica* **2**, (2023).
32. P. M. Mai *et al.*, *Seismic Rec.* **3**, 105–115 (2023).
33. D. E. Goldberg *et al.*, *The Seismic Record* **3**, 156–167 (2023).
34. C. Ren *et al.*, *Science* **383**, 305–311 (2024).
35. H. Müller, A. Sedley, in *OzCHI '14: Proceedings of the 26th Australian Computer-Human Interaction Conference on Designing Futures: The Future of Design*, T. Leong, Ed. (Association for Computing Machinery, 2014), pp. 308–315.
36. J. D. Goltz *et al.*, *Seismol. Res. Lett.* **95**, 2745–2760 (2024).
37. K. Nakayachi, J. S. Becker, S. H. Potter, M. Dixon, *Risk Anal.* **39**, 1723–1740 (2019).
38. L. J. Vinnell, M. L. Tan, R. Prasanna, J. S. Becker, *Front. Commun.* **8**, 1229247 (2023).
39. B. Orihuela *et al.*, *Int. J. Disaster Risk Reduct.* **97**, 103982 (2023).
40. S. K. McBride *et al.*, *Int. J. Disaster Risk Reduct.* **50**, 101713 (2020).
41. S. K. McBride *et al.*, *Geophysics* **87**, WA77–WA102 (2022).
42. R. M. Allen, M. Stogaitis, *Science* **375**, 717–718 (2022).
43. S. E. Minson, M.-A. Meier, A. S. Baltay, T. C. Hanks, E. S. Cochran, *Sci. Adv.* **4**, eaaq0504 (2018).
44. A. Bostrom *et al.*, *Int. J. Disaster Risk Reduct.* **82**, 103296 (2022).
45. R. Bossu, M. Böse, R. Steed, D. J. Wald, *Seismol. Res. Lett.* **95**, 2058–2070 (2024).
46. A. Barski, M. Stogaitis, S. Malkos, R. Bosch, "Earthquake Early Warning System" (Technical Disclosure Commons, 2018), https://www.tdcommons.org/dpubs_series/1620
47. R. M. Allen *et al.*, Global earthquake detection and warning using Android phones - Data repository, Zenodo, (2025); https://doi.org/10.5281/zenodo.15498729

ACKNOWLEDGMENTS

The authors thank B. Williams, R. Want, and three anonymous reviewers for providing thoughtful reviews. We appreciate the assistance of the staff at the International Seismological Center and the US Geological Survey National Earthquake Information Center for providing assistance with their catalogs. The authors followed Google's internal review processes while completing this research. Early development of AEA is documented in (*46*). **Funding:** This work was funded by Google LLC. **Author contributions:** Conceptualization: R.M.A., A.B., M.B., R.B., Y.C., S.M., S.M.M., P.R., B.S., M.S., N.T., and G.W. Methodology: R.M.A., A.B., M.B., R.B., Y.C., X.S.J., Y.-L.L., S.M., S.M.M., P.R., B.S., M.S., N.T., and G.W. Investigation: R.M.A., A.B., M.B., R.B., Y.C., X.S.J., Y.L.L., S.M., S.M.M., P.R., B.S., M.S., N.T., and G.W. Visualization: R.M.A., A.B., S.M.M., P.R., B.S., M.S., and N.T. Project administration: M.B., S.M., P.R., B.S., and M.S. Supervision: M.B., S.M., P.R., B.S., and M.S. Writing – original draft: R.M.A. and S.M.M. Writing – review & editing: R.M.A., A.B., Y.C., S.M.M., P.R., B.S., M.S., and N.T. **Competing interests:** R.M.A. is the UC Berkeley PI on the USGS ShakeAlert project and the California Earthquake Early Warning System (CEEWS) project and sits on various advisory committees related to both. R.M.A. is also a coinventor on the smartphone-based earthquake early-warning patent US10887748. **Data and materials availability:** The online repository at Zenodo (*47*) contains data and code used in this analysis including a list of all AEA alerts used in this study. The response counts for the user surveys (Fig. 5 and fig. S16) are all available in tables S7 to S13 in the supplement. Countries where AEA alerts are available are listed in the Android Help Center https://support.google.com/android/answer/9319337. Information about ShakeAlert warnings is available at the USGS NEIC website https://earthquake.usgs.gov/data/shakealert/. Information about the JMA EEW alerts is available on the JMA website https://www.data.jma.go.jp/eew/data/nc/pub_hist/index.html. The USGS collect reports of shaking intensity through a web based questionnaire. These are referred to as the "Did you feel it?" (DYFI) reports and are available online: https://earthquake.usgs.gov/data/dyfi/.

License information: Copyright © 2025 the authors, some rights reserved; exclusive licensee American Association for the Advancement of Science. No claim to original US government works. https://www.science.org/about/science-licenses-journal-article-reuse

SUPPLEMENTARY MATERIALS

science.org/doi/10.1126/science.ads4779
Materials and Methods; Figs. S1 to S17; Tables S1 to S13; References (*48*–*52*); Movie S1; Audio S1 and S2

Submitted 16 August 2024; resubmitted 31 March 2025; accepted 30 May 2025

10.1126/science.ads4779

NEUROIMMUNOLOGY

Type 2 cytokines act on enteric sensory neurons to regulate neuropeptide-driven host defense

Rocky M. Barilla[1,2], Clara Berard[1], Linyu Sun[1], Sumiti Sandhu[1], Sarah Zaghouani[2,3], Krishna S. Iyer[1,4], Gizem Altun[1,5], Chien-Wen Su[6], Jacques Deguine[7], Vasundhara Singh[7], Yu Hou[8], Kanupriya Kusumakar[1,2], Michael L. Rutlin[9], Meenakshi Rao[9], Habib Zaghouani[10], Hai Ning Shi[6], Ramnik J. Xavier[1,7,11]*, Vijay K. Kuchroo[1,7]*

Enteric nervous system (ENS)–derived neuropeptides modulate immune cell function, yet our understanding of how inflammatory cues directly influence enteric neuron responses during infection is considerably lacking. Here, we characterized a primary enteric sensory neuron (PSN) subset producing the neuropeptides neuromedin U (NMU) and calcitonin gene–related peptide β (CGRPβ) and coexpressing receptors for the type 2 cytokines interleukin-4 (IL-4) and IL-13. Type 2 cytokines amplified NMU and CGRPβ expression in PSNs both in vitro and in vivo, and this was abrogated by PSN-specific *Il13ra1* deletion. Deletion of *Il13ra1* in PSNs impaired host defense to the gastrointestinal helminth *Heligmosomoides polygyrus* and blunted muscularis immune responses. Co-administration of NMU23 and CGRPβ rescued helminth clearance deficits and restored anti-helminth immunity, highlighting the essential bidirectional neuroimmune cross-talk regulating intestinal type 2 inflammation.

Although the enteric nervous system (ENS) is best known for coordinating essential physiologic functions such as digestion and gut motility, recent evidence suggests that it is also a critical mediator in gut neuroimmune communication. We and others have demonstrated that ENS neuropeptides, such as neuromedin U (NMU), calcitonin gene–related peptide (CGRP), and vasoactive intestinal peptide (VIP), profoundly influence barrier immune responses and host defense against pathogens (*1*–*4*). For instance, NMU acts on type 2 innate lymphoid cells (ILC2s) that express NMUR1, amplifying their production of the type 2 cytokines interleukin-13 (IL-13) and IL-5 and promoting allergic inflammation in the lung and gut (*1*–*3*). Likewise, CGRP can have both pro- and anti-inflammatory effects depending on the tissue, cell type, and context (*5*–*8*). Regardless, studies investigating the role of neuroimmune communication in barrier defense have primarily focused on neuron-derived factors influencing immune cell function, leaving a considerable gap in our understanding of how enteric neurons respond to inflammatory stimuli, especially cytokines from local immune responses. Furthermore, enteric neurons embedded within the gut wall are uniquely susceptible to microbial exposure, inflammatory damage, and physical perturbations. This is illustrated in the context of infection with tissue-invading helminths such as *Heligmosomoides polygyrus*, which invade the gut wall, promoting local inflammation (*9*). Here, we found that enteric sensory neurons directly respond to type 2 cytokines during a tissue-invasive gastrointestinal helminth infection, consequently shaping the anti-helminth immune response.

Primary enteric sensory neurons directly sense type 2 cytokines to amplify gut NMU and CGRPβ gene expression

To identify cytokine receptors expressed by enteric neurons, we reanalyzed three publicly available single-cell RNA sequencing (scRNA-seq) datasets sampling mouse small intestine (SI) enteric neurons (*10*–*12*) and one dataset sampling human colon enteric neurons (*10*) (fig. S1, A and B). After integrating the mouse SI datasets, we observed 13 distinct clusters resembling the 12 to 13 annotated clusters from each individual dataset (Fig. 1A and fig. S1C). *Nmu* and *Calcb*, encoding the immunomodulatory neuropeptides NMU and CGRPβ, respectively, were exclusively coexpressed by a single cluster of putative primary enteric sensory neurons (PSNs), also known as intrinsic primary afferent neurons (IPANs) (Fig. 1B and fig. S1, C and D). Moreover, we found that *Nmu*$^+$ PSNs were enriched in immune-associated genes such as *Il13ra1*, *Il4ra*, *Jak1*, and *Stat6*, encoding the IL-4/IL-13 heterodimeric receptor and its essential signaling components, and *Il7*, encoding a critical ILC2 and memory T cell survival factor (Fig. 1B and fig. S1, D to F). Consistently, human colonic *NMU*$^+$*CALCB*$^+$ enteric sensory neurons also showed enrichment of *IL13RA1* and *IL4R* (Fig. 1C). In immune cells, IL-4 signals through a distinct heterodimeric receptor composed of IL-4 receptor α (IL-4Rα) and the IL-2 common γ-chain (γ_c). However, we did not observe substantial expression of *Il2rg* in enteric neurons (fig. S1F).

To assess the functional responses of PSN cytokine receptor activation, we first used neural crest progenitor–derived enteric neuron cultures, which display IL-13Rα1 expression localized to enteric neuron cell bodies (Fig. 1D and fig. S2A). Both IL-4 and IL-13, but not interferon-γ (IFNγ), amplified the expression of the PSN-associated neuropeptide genes *Nmu, Calcb,* and *Grp* by an average of ~20- to 200-fold compared with controls (Fig. 1, D and E, and fig. S2B). This up-regulation was STAT6 dependent and was not comparably observed in dorsal root ganglia (DRG) neuron cultures (fig. S2, C to I). Consistent with our in vitro data, administering three daily doses of recombinant IL-4:anti-IL-4 complex to wild-type mice sufficiently augmented gastrointestinal NMU and CGRPβ gene and peptide expression in vivo (Fig. 1, F and G, and fig. S3, A and B). IL-13 complex treatment similarly amplified SI *Nmu* and *Calcb* expression (fig. S3, C and D), although the *Calcb* induction was lower than that observed in IL-4 complex–treated mice (fig. S3D). Type 2 cytokine–induced neuropeptide expression was not observed in other digestive, mucosal, or nervous tissues sampled, including liver, lung, DRG, and brainstem (fig. S3, C and D). Moreover, type 2 cytokine neuropeptide induction was not directly caused by enteric neuron proliferation (fig. S3, E to J).

To determine whether this effect was caused by direct enteric neuron cytokine sensing, we used *Calb2*-cre mice to target neurons expressing calretinin/*Calb2*, including *Nmu*$^+$ and *Sst*$^+$ PSNs and several subsets of excitatory motor neurons (figs. S1C and S4, A and B). We also developed tamoxifen-inducible *Calcb*-ERT-cre (iCGRPβ-ERT-cre) mice to more specifically target PSNs and to circumvent possible effects on ENS development. To validate the specificity of these models, we crossed nuclear green fluorescent protein (GFP) reporter mice (*R26-LSL-Sun1-sfGFP*) to both the *Calb2*-cre and the iCGRPβ-ERT-cre models, observing selective and robust nuclear GFP expression in enteric neurons from the duodenal, ileal, and colonic myenteric and submucosal plexi of both cre lines, with little to no GFP expression in

[1]Gene Lay Institute of Immunology and Inflammation, Brigham and Women's Hospital, Massachusetts General Hospital and Harvard Medical School, Boston, MA, USA. [2]Division of Medical Sciences, Harvard Medical School, Boston, MA, USA. [3]University of Minnesota Medical School, Minneapolis, MN, USA. [4]Department of Experimental Neuroimmunology, Technical University of Munich School of Medicine, Munich, Germany. [5]German Cancer Research Center (DKFZ), Heidelberg, Germany. [6]Mucosal Immunology and Biology Research Center, Massachusetts General Hospital, Harvard Medical School, Charlestown, MA, USA. [7]Broad Institute of MIT and Harvard, Cambridge, MA, USA. [8]Liangzhu Laboratory, Zhejiang University, Hangzhou, China. [9]Department of Pediatrics, Boston Children's Hospital, Harvard Medical School, Boston, MA, USA. [10]University of Missouri School of Medicine, Columbia, MO, USA. [11]Department of Molecular Biology, Massachusetts General Hospital, Harvard Medical School, Boston, MA, USA. ***Corresponding author. Email: xavier@molbio.mgh.harvard.edu (R.J.X.); vkuchroo@rics.bwh.harvard.edu (V.K.K.)**

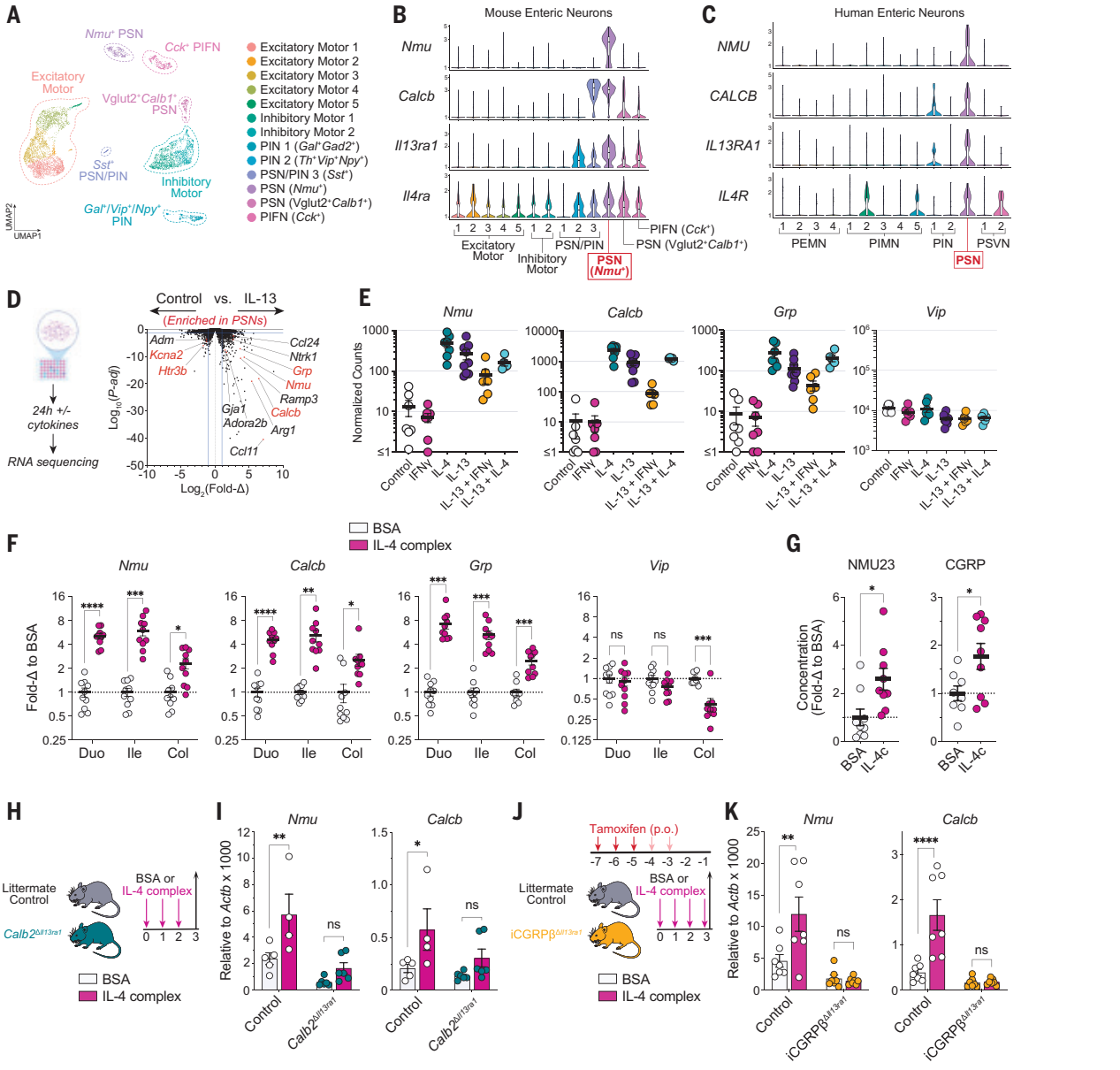

Fig. 1. Type 2 cytokines directly amplify PSN neuropeptide expression. (**A** and **B**) scRNA-seq reanalysis of mouse SI enteric neurons integrated from three independent studies (*10*–*12*). (A) Uniform manifold approximation and projection (UMAP) and (B) violin plots showing indicated gene expression. (**C**) scRNA-seq of human colon enteric neurons from Drokhlyansky *et al*. (*10*). (**D** and **E**) Bulk RNA-seq analysis of in vitro enteric neuroglial cultures treated for 24 hours with indicated cytokines (50 ng ml^{-1} per cytokine). (D) Schematic and volcano plot. (E) DESeq2-normalized gene counts; lower cutoff was set to 1 for log-scale visualization ($n = 5$ to 9 mice). (**F** and **G**) C57Bl/6J mice were administered IL-4 complex intraperitoneally for 3 days (F) or 4 (G) days. (F) Duodenal (Duo), ileal (Ile), and colonic (Col) qPCR gene expression ($n = 10$ mice). (G) NMU23 and CGRP enzyme immunoassay (EIA) concentrations in ileal lysates. Shown is the fold change to bovine serum albumin (BSA) average per experiment ($n = 8$ to 9). (**H** and **I**) *Calb2*$^{\Delta Il13ra1}$ cKO mice and littermate controls administered IL-4 complex. (H) Schematic. (I) Duodenal qPCR ($n = 4$ to 6 mice). (**J** and **K**) iCGRPβ$^{\Delta Il13ra1}$ cKO mice and littermate controls gavaged with three or five consecutive doses of tamoxifen and administered IL-4 complex for 4 days. (J) Schematic. (K) Duodenal qPCR ($n = 7$ mice). Data were pooled from two independent experiments [(F), (G), (I), and (K)] or are representative of three independent experiments (E). Data points represent single mice [(F), (G), (I), and (K)] or distinct in vitro cultures derived from single neonatal mice [(D) and (E)]. qPCR gene expression is relative to *Actb*, represented as $2^{-\Delta Ct} \times 1000$ [(I) and (K)] or fold change to the BSA group per experiment (F). Each graph indicates the mean ± SEM of replicates. ns, not significant; $^{*}P < 0.05$; $^{**}P < 0.01$; $^{***}P < 0.001$; $^{****}P < 0.0001$, two-way ANOVA with Sidak's correction [(F), (I), and (K)] or two-tailed Welch's *t* test (G). PIN, putative interneuron; PIFN, putative intestinofugal neuron; PEMN, putative excitatory motor neuron; PIMN, putative inhibitory motor neuron; PSVN, putative secretomotor/vasodilator neuron.

the gut epithelia and lamina propria (LP) (fig. S4, C to M). Morphological analysis showed that iCGRPβ-ERT-cre–labeled GFP$^+$ neurons had larger cell bodies than GFP$^-$ neurons (fig. S4, I and J), in agreement with previous reports showing that CGRP$^+$ enteric sensory neurons have larger cell bodies (*13*). We next generated PSN-targeting *Il13ra1* conditional knockout (cKO) mice by crossing *Il13ra1*$^{flox/flox}$ mice into either *Calb2*-cre (*Calb2*$^{\Delta Il13ra1}$ cKO) or iCGRPβ-ERT-cre (iCGRPβ$^{\Delta Il13ra1}$ cKO) mice. The administration of IL-4 complex failed to induce signature *Nmu* and *Calcb* expression in the duodena of either *Calb2*$^{\Delta Il13ra1}$ cKO or iCGRPβ$^{\Delta Il13ra1}$ cKO mice (Fig. 1, H and I), indicating that enteric neurons recognize IL-4 directly and specifically through the IL-4Rα/IL-13Rα1 heterodimeric receptor. Furthermore, we found no changes to duodenal CGRPα/*Calca* and *Vip* expression or intestinal size after IL-4 complex treatment in either control or iCGRPβ$^{\Delta Il13ra1}$ cKO mice (fig. S5, A and B), and no differences in general IL-4 complex–induced inflammatory phenotypes such as splenomegaly, immune cell *Chil3* up-regulation, and epithelial cell *Retnlb* up-regulation between IL-4 complex–treated *Calb2*$^{\Delta Il13ra1}$ cKO, iCGRPβ$^{\Delta Il13ra1}$ cKO, and control mice (fig. S5, F to H).

PSN *Il13ra1* ablation impairs host defense to gastrointestinal helminths

To investigate the roles of PSN type 2 cytokine receptor signaling during intestinal inflammation, we used the *H. polygyrus* gastrointestinal helminth infection model, which elicits strong type 2 immune responses in the gut. We observed *IL-13Rα1* immunoreactivity in the soma of *Calb2*-cre–labeled enteric neurons from the myenteric plexi of *H. polygyrus*–infected mice (fig. S6, A and B). *H. polygyrus* displays a complex, multistep life cycle within the host, including a tissue-dwelling phase at ~0 to 7 days postinfection (d.p.i.), when larvae burrow into the muscularis to grow and molt, and a luminal phase (8 to 14+ d.p.i.), when mature worms re-emerge in the lumen to mate and lay eggs. During the tissue-dwelling phase, muscularis-implanted *H. polygyrus* larvae were situated near myenteric plexus neurons,

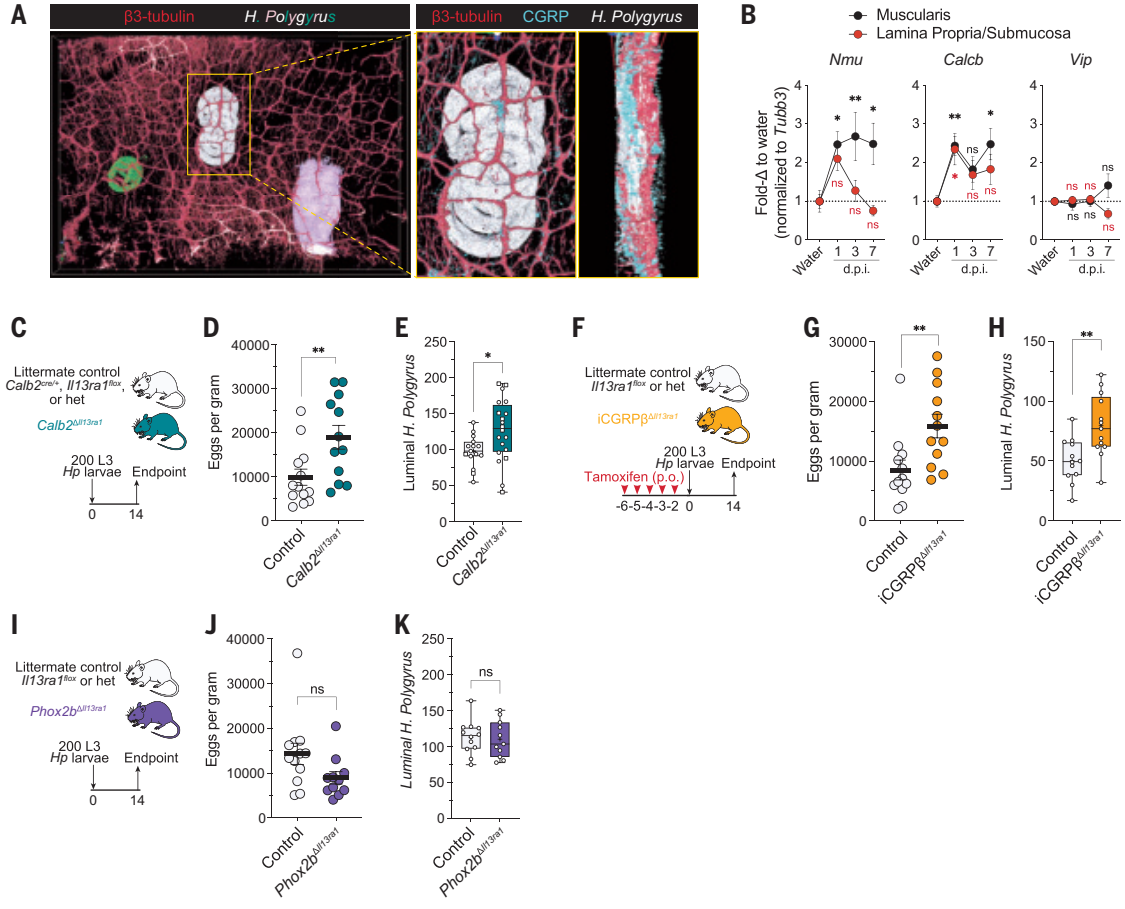

Fig. 2. PSN-specific *Il13ra1* ablation impairs host defense to *H. polygyrus*. (**A**) Confocal imaging and three-dimensional rendering (Aivia) of Ce3D-cleared duodenal muscularis at 6 d.p.i. Autofluorescent *H. polygyrus* larvae are pseudocolored green, white, and pink; enteric neurons/β3-tubulin are shown in red; and CGRP is shown in cyan. Insets (yellow boxes) show magnified white larvae from the top (left inset) and the side (right inset). (**B**) Duodenal qPCR of muscularis (black) and lamina propria/submucosa (red) at the indicated d.p.i. Gene expression is relative to *Tubb3*, represented as fold change to the water group per organ. Statistics compare indicated d.p.i. against the water group per organ. Data were pooled from four independent time points ($n = 3$ to 4 mice per time point). (**C** to **E**) *H. polygyrus*–infected *Calb2*$^{\Delta Il13ra1}$ cKO and littermate control (*Calb2*$^{cre/+}$, *Il13ra1*^{flox}, or heterozygous) mice at 14 d.p.i. (C) Schematic. (D) Fecundity ($n = 12$ to 13 mice). (E) Worm count ($n = 15$ to 20 mice). Squares indicate mice that received daily PBS. (**F** to **H**) *H. polygyrus*–infected tamoxifen-induced iCGRPβ$^{\Delta Il13ra1}$ cKO and littermate control mice. (F) Schematic. (G) Fecundity ($n = 12$ mice). (H) Worm count ($n = 12$ to 13 mice). (**I** to **K**) *H. polygyrus*-infected *Phox2b*$^{\Delta Il13ra1}$ cKO and littermate control mice at 14 d.p.i. (I) Schematic. (J) Fecundity ($n = 11$ to 12 mice). (K) Worm count ($n = 11$ to 12 mice). Data were pooled from two [(D), (H), (J), and (K)], three (G), or four (E) independent experiments. Each data point represents a single mouse [(C) to (K)], and each bar and scatter plot indicate the mean ± SEM of replicates. ns, not significant; $*P < 0.05$; $**P < 0.01$, two-tailed Welch's *t* test [(E), (H), and (K)], two-tailed Mann-Whitney test [(D), (G), and (J)], or two-way ANOVA with Dunnett's correction (B).

including CGRP$^+$ neuronal fibers (Fig. 2A and movie S1), eliciting increased *Nmu* and *Calcb*, but not *Vip*, expression in the duodenal muscularis as early as 1 d.p.i. (Fig. 2B and fig. S6C). Furthermore, at 7 d.p.i., individually implanted larvae in the duodenal wall of *Calb2*$^{\Delta Il13ra1}$ cKO mice occupied ~20% greater areas than those of littermate controls, with no difference in total number (fig. S6, D to F). During the luminal phase of infection, both *Calb2*$^{\Delta Il13ra1}$ cKO and iCGRPβ$^{\Delta Il13ra1}$ cKO mice failed to effectively control the helminth infection, displaying greater *H. polygyrus* fecundity and luminal worm burdens compared with their respective littermate controls (Fig. 2, C to H, and fig. S6, G and H). Moreover, these differences in worm burden and fecundity could not be explained by differences in gastrointestinal motility (fig. S6, I to K).

To exclude the possibility of extrinsic neuronal involvement in our observed phenotypes, we examined cre expression in gut-extrinsic ganglia by crossing *R26-LSL-Sun1-sfGFP* mice to *Calb2*-cre, iCGRPβ-ERT-cre, and *Phox2b*-cre BAC transgenic mice (hereafter, *Phox2b*-cre), which have been reported to express cre primarily in the hindbrain and nodose ganglia but not in the ENS and peripheral ganglia (*14*). Whereas *Calb2*-cre and *Phox2b*-cre reporter–crossed mice showed virtually no sensory neuron GFP labeling in DRG of the thoracic splanchnic nerve, iCGRPβ-ERT-cre reporter mice showed substantial GFP labeling in DRG neurons, in addition to enteric sensory neurons (fig. S7, A to C). Conversely, *Phox2b*-cre mice displayed extensive cre-mediated recombination in the autonomic nervous system, having more GFP$^+$ neurons in the vagal sensory nodose-petrosal-jugular ganglia (N-JG) and the sympathetic celiac ganglia–superior mesenteric ganglia (CG-SMG) than both *Calb2*-cre and iCGRPβ-ERT-cre reporter–crossed mice (fig. S7, D to F). Contrary to previous reports (*14*), we detected sparse (<10%) *Phox2b*-cre recombination in the myenteric plexus (fig. S7, G and H). However, the labeled neurons were calretinin$^-$ and were not larger than GFP$^-$ neurons (fig. S7, I to K), suggesting that *Phox2b*-cre mice do not target PSNs. When *Phox2b*-cre mice were crossed to *Il13ra1* floxed mice (*Phox2b*$^{\Delta Il13ra1}$ cKO) and infected with *H. polygyrus*, we observed no differences in luminal worm burden or helminth fecundity at 14 d.p.i. (Fig. 2, I to K), suggesting that *Il13ra1* ablation in enteric neurons, but not in gut-extrinsic autonomic neurons, impairs host control of *H. polygyrus* infection.

PSN neuropeptides rescue impaired *H. polygyrus* clearance of PSN *Il13ra1* cKO mice

We next investigated how PSN *Il13ra1* ablation influences gut neuropeptide expression. Although steady-state *Nmu* expression was diminished specifically in the duodena of *Calb2*$^{\Delta Il13ra1}$ cKO mice and iCGRPβ$^{\Delta Il13ra1}$ cKO mice (Fig. 3A and fig. S8, A and B), there were no differences in baseline duodenal *Calcb* expression among *Calb2*$^{\Delta Il13ra1}$ cKO mice, iCGRPβ$^{\Delta Il13ra1}$ cKO mice, and littermate controls (Fig. 3A and fig. S8, A and B). However, in the helminth-infected gut, expression of *Nmu* and *Calcb*, but not of other typical ENS neuropeptides, was diminished in all sampled SI regions of *Calb2*$^{\Delta Il13ra1}$ and iCGRPβ$^{\Delta Il13ra1}$ cKO mice (Fig. 3, A and B, and fig. S8, C to H) but was not altered in *Phox2b*$^{\Delta Il13ra1}$ cKO mice (Fig. 3C).

We noticed a strong negative correlation between *H. polygyrus* fecundity and both duodenal *Nmu* and *Calcb* expression at 14 d.p.i. across mice from all linked experimental litters (Fig. 3D) as well as across the littermate control mice only (fig. S8I), suggesting that natural duodenal *Nmu* and *Calcb* variation may influence *H. polygyrus* fecundity in wild-type mice. This PSN neuropeptide anticorrelation was also observed for implanted larval size at 7 d.p.i. (fig. S8J). Furthermore, duodenal *Nmu* and *Calcb* expression exhibited a robust positive correlation with each other ($R^2 = 0.89$ to 0.92, $P < 0.0001$) at steady state and during helminth infection (Fig. 3E and fig. S8K), suggesting that their expression is tightly co-regulated. Therefore, we tested whether PSN neuropeptide co-administration could rescue the helminth clearance deficits of *Calb2*$^{\Delta Il13ra1}$ cKO mice, finding that daily co-administration of equimolar NMU23 and CGRPβ, but not administration of CGRPβ alone, reduced both *H. polygyrus* fecundity and worm burden to values similar to those of phosphate-buffered saline (PBS)–administered littermate control mice (Fig. 3, F and G, and fig. S8L). However, NMU23 and CGRPβ co-administration did not restore the impaired duodenal *Nmu* and *Calcb* expression of *Calb2*$^{\Delta Il13ra1}$ cKO mice (fig. S8M).

We next investigated whether enteric neuron *Il13ra1* ablation influences PSN villus innervation and abundance. *H. polygyrus*–infected *Calb2*$^{\Delta Il13ra1}$ cKO mice displayed lower CGRP$^+$ and calretinin$^+$ fiber densities per villus and per mouse compared with controls at 7 d.p.i. (Fig. 3, H to K). However, there were no differences in calretinin$^+$ fiber density per mouse in the absence of infection (Fig. 3K). Furthermore, *Calb2*$^{\Delta Il13ra1}$ cKO mice displayed fewer calretinin$^+$p75NTR$^+$ neurons than did littermate controls at 7 d.p.i. (Fig. 3L, and fig. S9, A to E), suggesting a loss of *Nmu*$^+$ PSNs coexpressing calretinin and p75NTR/*Ngfr* after infection (fig. S4, A and B).

Because iCGRPβ-ERT-cre reporter–labeled GFP$^+$ neurons were larger than GFP$^-$ neurons (fig. S4I) and because large (above the third quartile in soma size per experiment) calretinin$^+$ neurons displayed greater p75NTR expression than small calretinin$^+$ and calretinin$^-$ enteric neurons (fig. S9F), we used large calretinin$^+$ neurons to discriminate PSNs. Consistently, *Calb2*$^{\Delta Il13ra1}$ cKO mice had lower percentages and total numbers of PSNs in the myenteric plexus compared with littermate controls at 7 d.p.i., but there were no differences in uninfected mice (Fig. 3, M to O, and fig. S9, G to I), suggesting that enteric neuron *Il13ra1* ablation selectively depletes PSNs in the helminth-infected myenteric plexus, leading to diminished NMU and CGRPβ gene expression and loss of intrinsic sensory neuron fibers to the mucosal villi.

PSN neuropeptide expression influences muscularis-specific type 2 immune responses

Assessing the effects of PSN *Il13ra1* ablation on anti-helminthic immunity, we found that *Calb2*$^{\Delta Il13ra1}$ cKO mice displayed blunted duodenal *Il4* and *Il5* expression at 14 d.p.i. (Fig. 4A), which was independent of T cell–priming differences in the mesenteric lymph nodes (fig. S10, A to F). These impairments could be rescued with co-administration of NMU23 and CGRPβ (Fig. 4B). Conversely, *Phox2b*$^{\Delta Il13ra1}$ cKO mice displayed enhanced duodenal *Il4* and *Il13* expression compared with controls at 14 d.p.i. (fig. S10G), suggesting that IL-13Rα1 signaling in intrinsic and extrinsic neurons has distinct effects on gastrointestinal type 2 immune responses.

Because ILC2s are a predominant source of IL-5 in the helminth-infected gut (*15*) and respond to NMU and CGRP (*1*–*3*, *5*, *16*, *17*), we performed bulk RNA-seq on purified ILC2s from the muscularis and LP of *Calb2*$^{\Delta Il13ra1}$ cKO and littermate control mice at 7 d.p.i. (fig. S11A). Comparing control ILC2s from each compartment, muscularis ILC2s were enriched in *Calca* and CGRP receptor genes (*Calcrl*, *Ramp1*, and *Ramp3*) (fig. S12A), whereas LP ILC2s showed greater NMU and VIP receptor gene expression (fig. S12A). Accordingly, muscularis ILC2s expressed genes up-regulated by or downstream of CGRP receptor signaling and genes associated with ST2$^+$ "natural" nILC2s (*5*), whereas LP ILC2s were enriched in genes associated with IL-25R$^+$ "inflammatory" iILC2s (*5*, *17*, *18*) (fig. S12B). Furthermore, muscularis *Calb2*$^{\Delta Il13ra1}$ cKO ILC2s displayed lower expression of *Calcrl*, whereas LP *Calb2*$^{\Delta Il13ra1}$ cKO ILC2s showed lower expression of *Nmur1* compared with their respective control ILC2s (fig. S12C), suggesting that *Calb2*$^{\Delta Il13ra1}$ cKO neuropeptide deficits may influence immunity in a site-specific manner. Confirming this, *Calb2*$^{\Delta Il13ra1}$ cKO ILC2s from the muscularis, but not the LP, displayed greater cell cycle gene expression compared with ILC2s from littermate controls at 7 d.p.i. (fig. S12D). These results are consistent with CGRP's function as a potent inhibitor of ILC2 proliferation (*5*, *16*, *17*) and are in agreement with the CGRPβ gene expression deficits shown in *Calb2*$^{\Delta Il13ra1}$ cKO mice. Nevertheless, we saw no

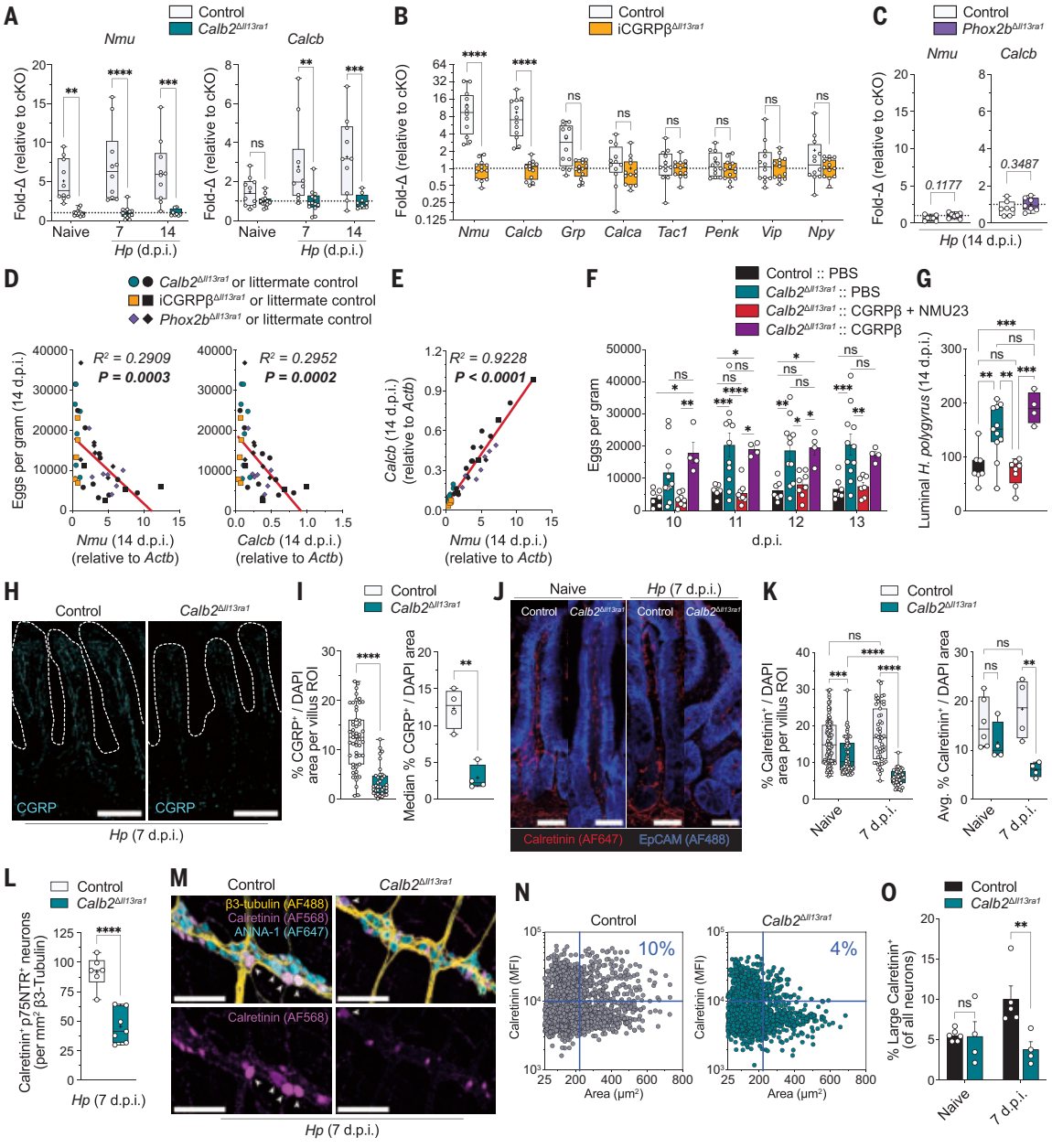

Fig. 3. Type 2 cytokines maintain PSN population and neuropeptide expression. (**A** to **C**) Duodenal qPCR data from the indicated *Calb2*$^{\Delta Il13ra1}$ cKO mice ($n = 8$ to 14 mice) (A), 14 d.p.i. tamoxifen-induced iCGRPβ$^{\Delta Il13ra1}$ cKO mice ($n = 12$ to 13 mice) (B), and 14 d.p.i. *Phox2b*$^{\Delta Il13ra1}$ cKO mice ($n = 7$ mice) (C) and respective littermate controls. (**D** and **E**) Scatter plots correlating 14 d.p.i. duodenal qPCR gene expression (*x* axes) and fecundity (*y* axes) (D) or duodenal qPCR expression of indicated genes from matched experiments (E) ($n = 41$ mice). (**F** and **G**) *Calb2*$^{\Delta Il13ra1}$ cKO mice administered the indicated neuropeptides intraperitoneally (2 nmoles each per injection) or PBS daily. (F) Fecundity on indicated d.p.i. (G) 14 d.p.i. worm count ($n = 4$ to 11 mice). (**H** to **K**) Confocal microscopy of duodenal cross-sections. (H) Representative villi at 7 d.p.i. (I) Percentage CGRP$^+$ area of total 4′,6-diamidino-2-phenylindole (DAPI) area per villus (left) and per mouse (right) ($n = 4$ mice). (J) Representative villi. (K) Percentage calretinin$^+$ area of total DAPI area per villus (left) and per mouse (right) ($n = 4$ to 6 mice). (**L** to **O**) Whole-mount confocal imaging of 7 d.p.i. duodenal myenteric plexi. (L) Calretinin$^+$p75NTR$^+$ neurons per square millimeter of β3-tubulin$^+$ area ($n = 6$ to 7 mice). (M) Representative 7 d.p.i. myenteric plexi immunostained for β3-tubulin (yellow), calretinin (magenta), and ANNA-1 (neuronal nuclei/cell body marker; cyan). Arrows indicate large calretinin$^+$ PSNs. (N) Scatter plot of pooled segmented neurons at 7 d.p.i. from littermate control ($n = 5$) and *Calb2*$^{\Delta Il13ra1}$ cKO ($n = 4$) mice. (O) Percentage of large calretinin$^+$ neurons ($n = 4$ to 6 mice). Data were pooled from two [(B), (K), (O)], three [(D) to (G)], or six (A) independent experiments or are representative of two or more independent experiments [(C), (I), and (L)]. Data points represent single mice or individual villi [(I), left; (K), left]. Scale bars, 100 μm [(H), (J), and (M)]. qPCR gene expression is relative to *Actb*, represented as $2^{-\Delta Ct} \times 1000$ [(D) and (E)] or fold change to the cKO group per experiment [(A) to (C)]. Each bar graph indicates the mean ± SEM of replicates. ns, not significant; *$P < 0.05$; **$P < 0.01$; ***$P < 0.001$; ****$P < 0.0001$, two-way ANOVA with Sidak's correction [(A), (B), and (O)] or Tukey's correction (K), mixed-effects analysis with Tukey's correction (F), one-way ANOVA with Tukey's correction (G), two-tailed *t* test [(C), (I), and (L)], or simple linear regression [(D) and (E)].

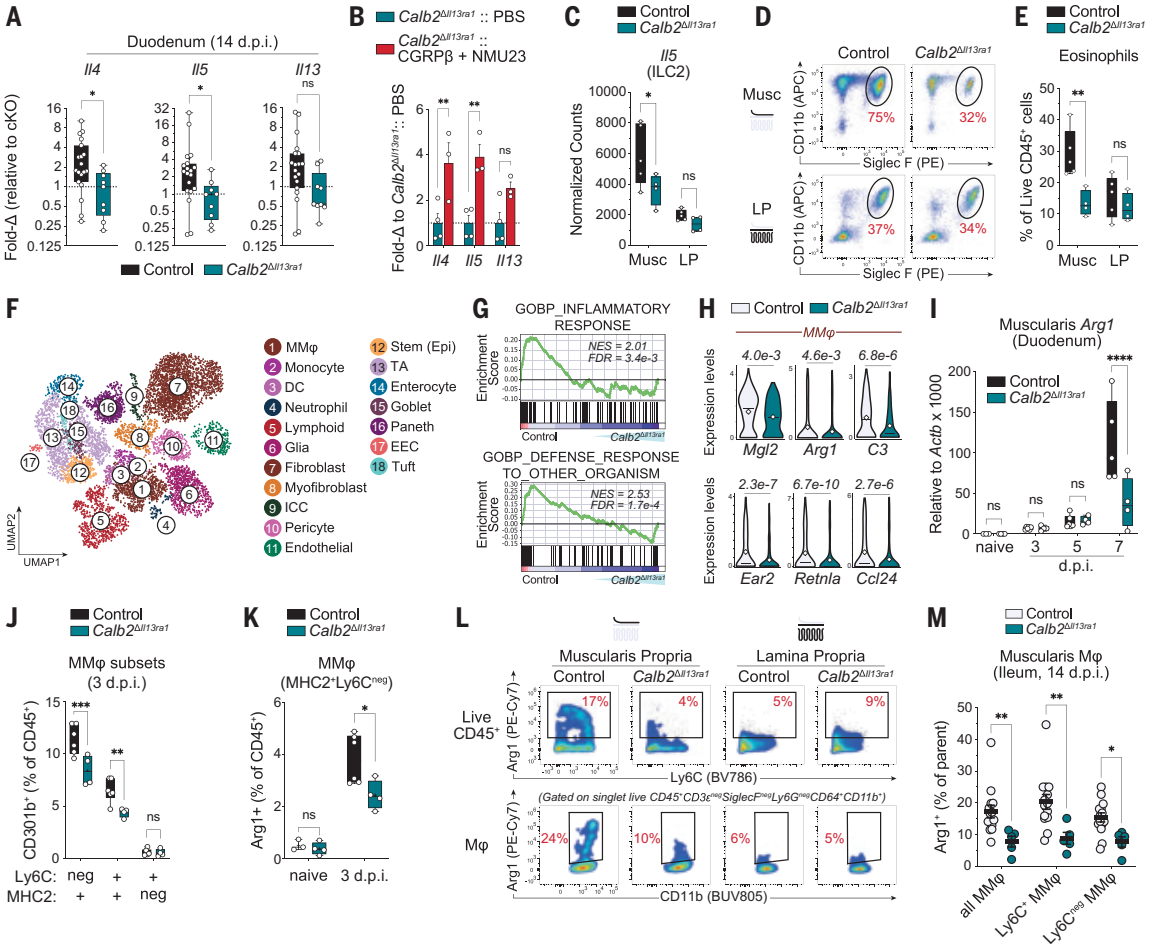

Fig. 4. PSN IL-4/IL-13 sensing promotes muscularis-specific type 2 immune responses. (**A**) Duodenal qPCR gene expression at 14 d.p.i. ($n = 9$ to 19 mice). (**B**) Duodenal qPCR gene expression in mice with daily CGRPβ and NMU23 co-administration as in Fig. 3, F and G ($n = 3$ to 4 mice). (**C**) DESeq2-normalized bulk RNA-seq counts of ileal muscularis and LP ILC2s at 7 d.p.i. as gated in fig. S11A ($n = 4$ to 5 mice). (**D** and **E**) Flow cytometric analysis of ileal muscularis and LP immune cells at 7 d.p.i. (D) Representative flow plots gated on single live CD45$^+$ CD90.2$^-$Lineage(Ter-119, NK1.1, CD19, B220)$^-$ cells. (E) Percentage of muscularis and LP eosinophils (as gated in fig. S11A) of all CD45$^+$ cells ($n = 4$ to 5 mice). (**F** to **H**) scRNA-seq of ileal muscularis (input 50% enriched for stroma or glia as in fig. S13A) and duodenal epithelium at 7 d.p.i. (F) UMAP embedding of 8270 individual cells pooled from two mice per group using general-level cluster annotation. (G) Gene set enrichment analysis (GSEA) plots of general MMφ cluster, depicting Gene Ontology gene sets from MSigDB. (H) Violin plots of general MMφ clusters. (**I**) Duodenal muscularis qPCR gene expression at indicated d.p.i. ($n = 3$ to 6 mice per time point). (**J** and **K**) Flow cytometry of duodenal MMφ (as gated in fig. S11C) at 3 d.p.i. (J) Percentage CD301b$^+$ of CD45$^+$ cells in indicated MMφ subsets at 3 d.p.i. ($n = 4$ to 6 mice). (K) Percentage Arg1$^+$ MMφ (MHC2$^+$Ly6C$^-$) of CD45$^+$ immune cells ($n = 3$ to 6 mice per time point). (**L** and **M**) Flow cytometry of ileal muscularis and LP immune cells at 14 d.p.i. (L) Representative flow plots; shown are total immune cells (top) and macrophages (bottom). (M) Frequency of Arg1$^+$ cells in indicated MMφ subsets ($n = 5$ to 14 mice). Data were pooled from two [(A), (K), and (M)] or four (I) independent experiments or are representative of two or more independent experiments [(B) and (E)]. Each data point represents a single mouse. qPCR gene expression is relative to *Actb*, represented as $2^{-\Delta Ct} \times 1000$ (I) or fold change to the cKO group (A) or PBS-treated cKO group (B) per experiment. Each bar graph indicates the mean ± SEM of replicates. ns, not significant; *$P < 0.05$; **$P < 0.01$; ***$P < 0.001$; ****$P < 0.0001$, two-tailed *t* test (A), two-way ANOVA with Sidak's correction [(B), (C), (E), (I) to (K), and (M)], or Wilcoxon rank-sum test adjusted *P* value (H).

differences in duodenal muscularis ILC2 abundance at steady state or at 5 d.p.i. (figs. S11B and S12, E and F).

Il5 was the most highly expressed ILC2 cytokine in muscularis ILC2s, and its expression was reduced in muscularis, but not LP, *Calb2*$^{\Delta Il13ra1}$ cKO ILC2s compared with control ILC2s (Fig. 4C and fig. S12, G and H). IL-5 is a well-studied differentiation and maturation factor for eosinophils, which are a major source of IL-4 during intestinal helminth infection (*19*) and play a role in killing entrapped *H. polygyrus* larvae (*20*). Eosinophils were most heavily recruited to the duodenal muscularis during the late tissue-dwelling phase and expressed greater *Il4* and *Prg2* than those recruited to the LP (figs. S11C and S12, I to K). Furthermore, the abundance and proportion of eosinophils recruited to the muscularis, but not the LP, were reduced in the proximal and distal SI of *Calb2*$^{\Delta Il13ra1}$ cKO mice compared with littermate controls at 7 d.p.i. (Fig. 4, D and E, and fig. S12L).

CGRPβ synergizes with IL-4 to induce muscularis macrophage arginase-1 expression

To more extensively characterize the helminth-infected muscularis, we performed scRNA-seq on *Calb2*$^{\Delta Il13ra1}$ cKO and littermate control mice at 7 d.p.i. (Fig. 4F and fig. S13, A to F), sampling muscularis cell populations as well as epithelial cell populations, which also displayed impaired type 2 effector responses (fig. S14, A to D). Muscularis macrophages (MMφ) exhibited the most differentially expressed genes, with control MMφ enriched in gene sets involved in host defense (Fig. 4G and fig. S14, G to K), including genes encoding critical type 2

mediators and alternatively activated macrophage (AAMφ) markers with roles in anti-helminth immunity and tissue repair (*Arg1*, *Mgl2*, *Ear2*, and *Retnla*) (*21*, *22*), eosinophil chemotaxis (*Ccl24*), and macrophage adhesion to *H. polygyrus* larvae (*C3*) (*23*, *24*) (Fig. 4H and fig. S14K). *Arg1* gene expression was reduced at 7 d.p.i. in the duodenal muscularis of *Calb2*$^{\Delta Il13ra1}$ cKO mice (Fig. 4I), which also had lower percentages of CD301b/*Mgl2*$^{+}$ and arginase-1–positive (Arg1^{+}) MMφ compared with controls at 3 d.p.i. (Fig. 4, J and K, and fig. S15A). Additionally, *Calb2*$^{\Delta Il13ra1}$ cKO mice displayed reduced duodenal *Arg1* during the luminal phase of infection, with lower percentages of Arg1–expressing MMφ and total immune cells in the ileal muscularis, but not LP, compared with controls (Fig. 4, L and M, and fig. S15, B to D).

Although *Calb2*$^{\Delta Il13ra1}$ cKO CGRP peptide concentrations were diminished in both gut compartments at steady state and at 7 d.p.i., CGRP concentrations were 2- to 2.5-fold greater in the muscularis compared with the LP (Fig. 5A). Furthermore, MMφ had the most *Calcrl* and *Ramp1* gene expression across immune cell clusters, with control MMφ sharing gene signatures with recently reported CGRP-treated macrophages (*8*), and *Calb2*$^{\Delta Il13ra1}$ cKO MMφ sharing signatures with gut macrophages from ILC2-deficient mice (*25*) (Fig. 5B and fig. S15, E to G). This suggests that CGRP may influence MMφ AAMφ programs. Indeed, both CGRPβ and activation of its downstream receptor signaling pathway were sufficient to induce *Arg1* expression in primary cultured SI macrophages (SI-Mφ) and bone marrow–derived macrophages (BMDMs) (Fig. 5, C and D, and fig. S15H). Moreover, CGRPβ synergized with lower doses of IL-4, amplifying BMDM *Arg1* expression to levels equivalent to those observed after treatment with 10× the dose of IL-4 alone (Fig. 5E and fig. S15I).

Consistently, daily CGRPβ and NMU23 in vivo co-administration completely restored *Calb2*$^{\Delta Il13ra1}$ cKO MMφ Arg1 expression deficits at 14 d.p.i. (Fig. 5, F and G; fig. S15J), and the percentage of muscularis Arg1^{+} immune cells was negatively correlated with *H. polygyrus* fecundity and burden (Fig. 5H; fig. S15K). Lastly, we infected mice globally deficient in *Ramp1* (*Ramp1* KO), finding that *Ramp1* KO mice had greater fecal egg burdens than heterozygous littermate controls at 14 d.p.i. (Fig. 5I), which suggests that CGRP receptor signaling is necessary for efficient *H. polygyrus* expulsion and works in synergy with IL-4 to promote AAMφ gene expression.

Discussion

In this work, we uncovered the functional role of type 2 cytokine receptor signaling in PSNs during infection with the gastrointestinal helminth *H. polygyrus*. We demonstrated that direct PSN sensing of IL-4 and IL-13 is sufficient to induce robust expression of the immunomodulatory neuropeptides NMU and CGRPβ in vitro and in vivo, thereby completing a previously described neuropeptide-ILC2 neuroimmune feedback loop (*1*–*3*) (fig. S16, A to C). PSN-dependent helminth control is due in part to the action of NMU on ILC2s, because ILC2 NMUR1 expression is required for effective helminth control (*2*). Additionally, ILC2 CGRP receptor signaling limits proliferation while promoting IL-5 production (*5*, *16*, *17*) and muscularis IL-4^{+} eosinophil recruitment. Therefore, the highly correlated NMU and CGRPβ expression in PSNs may serve to promote appropriate muscularis-specific anti-helminth immunity while buffering the tissue-damaging effects of unrestrained type 2 inflammation in the muscularis. Furthermore, we showed that CGRPβ acts in synergy with IL-4 to induce macrophage

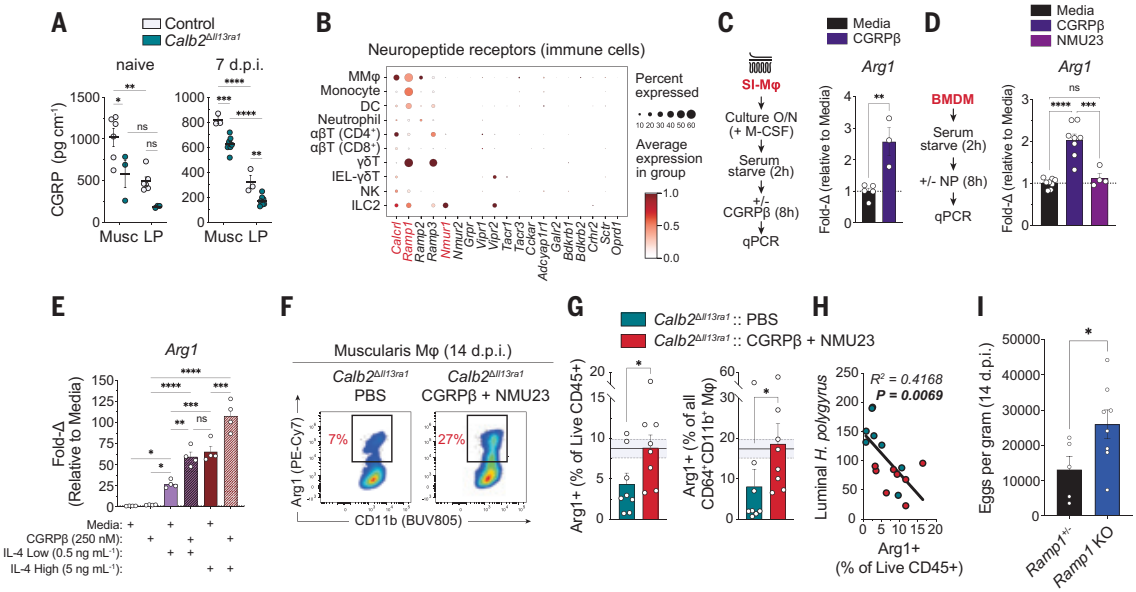

Fig. 5. CGRPβ synergizes with type 2 cytokines to drive MMφ Arg1. (**A**) CGRP EIA peptide concentration ($n = 3$ to 8 mice). (**B**) scRNA-seq dot plot across general immune cell clusters (including lymphoid cell subclusters) from the dataset shown in Fig. 4F. (**C** to **E**) qPCR gene expression in duodenal SI-Mφ cultures ($n = 3$ to 5 wells) (C) or BMDM cultures ($n = 4$ to 8 wells) (D and E) treated for 8 hours with or without indicated neuropeptides (250 nM each) or IL-4 concentrations. (**F** to **H**) Flow cytometry of 14 d.p.i. ileal muscularis immune cells. (F) Representative flow plots depicting percentage Arg1^{+} MMφ (single live CD45^{+} CD3ε^{-}Ly6G^{-}Siglec-F^{-}CD64^{+} CD11b^{+}). (G) Percentage Arg1^{+} muscularis immune cells (left) and MMφ (right) ($n = 8$ mice). Solid and dotted lines with grayed area represent the mean ± SEM of control mice at 14 d.p.i. pooled from four independent experiments ($n = 16$ mice). (H) Scatter plot correlating 14 d.p.i percentage Arg1^{+} muscularis immune cells (*x* axis) with worm count (*y* axis) ($n = 16$ mice). (**I**) The 14 d.p.i. fecundity of *Ramp1* KO and littermate control (*Ramp1*$^{+/-}$) mice ($n = 5$ to 8 mice). Data were pooled from two independent experiments [(G) to (I)] or are representative of two or more independent experiments [(A), (C), (D), and (E)]. Data points represent individual mice [(A) and (G) to (I)] or culture wells pooled from two to five mice per experiment [(C) to (E)]. qPCR gene expression is relative to *Actb*, represented as fold change to media control group per experiment [(C) to (E)]. Each graph indicates the mean ± SEM of replicates. ns, not significant; *$P < 0.05$; **$P < 0.01$; ***$P < 0.001$; ****$P < 0.0001$ using two-way ANOVA with Tukey's correction (A), one-way ANOVA with Tukey's correction [(D) and (E)], two-tailed unpaired *t* test (C), two-tailed Mann-Whitney test (G), two-tailed Welch's *t* test (I), or simple linear regression (H).

Arg1 expression in vitro, and that PSN neuropeptide co-administration promotes Arg1 expression in MMφ, which are essential to *H. polygyrus* host defense and tissue protection (*21*, *23*, *26*). This work demonstrates how PSN cytokine sensing dictates this delicate neuropeptide balance and influences site-specific immunity.

REFERENCES AND NOTES

1. C. S. N. Klose *et al.*, *Nature* **549**, 282–286 (2017).
2. V. Cardoso *et al.*, *Nature* **549**, 277–281 (2017).
3. A. Wallrapp *et al.*, *Nature* **549**, 351–356 (2017).
4. J. Talbot *et al.*, *Nature* **579**, 575–580 (2020).
5. A. Wallrapp *et al.*, *Immunity* **51**, 709–723.e6 (2019).
6. P. Hanč *et al.*, *Science* **379**, eabm5658 (2023).
7. M. Balood *et al.*, *Nature* **611**, 405–412 (2022).
8. F. A. Pinho-Ribeiro *et al.*, *Nature* **615**, 472–481 (2023).
9. R. M. Maizels *et al.*, *Exp. Parasitol.* **132**, 76–89 (2012).
10. E. Drokhlyansky *et al.*, *Cell* **182**, 1606–1622.e23 (2020).
11. K. Morarach *et al.*, *Nat. Neurosci.* **24**, 34–46 (2021).
12. A. Zeisel *et al.*, *Cell* **174**, 999–1014.e22 (2018).
13. T. J. Hibberd *et al.*, *J. Comp. Neurol.* **530**, 3209–3225 (2022).
14. M. M. Scott, K. W. Williams, J. Rossi, C. E. Lee, J. K. Elmquist, *J. Clin. Invest.* **121**, 2413–2421 (2011).
15. J. C. Nussbaum *et al.*, *Nature* **502**, 245–248 (2013).
16. H. Xu *et al.*, *Immunity* **51**, 696–708.e9 (2019).
17. H. Nagashima *et al.*, *Immunity* **51**, 682–695.e6 (2019).
18. Y. Huang *et al.*, *Science* **359**, 114–119 (2018).
19. T. Ahrends *et al.*, *Cell* **184**, 5715–5727.e12 (2021).
20. J. P. Hewitson *et al.*, *PLOS Pathog.* **11**, e1004676 (2015).
21. J. Esser-von Bieren *et al.*, *PLOS Pathog.* **9**, e1003771 (2013).
22. F. Chen *et al.*, *Cell Rep.* **38**, 110215 (2022).
23. J. Esser-von Bieren *et al.*, *J. Immunol.* **194**, 1154–1163 (2015).
24. G. Coakley, N. L. Harris, *Parasite Immunol.* **42**, e12717 (2020).
25. K. J. Jarick *et al.*, *Nature* **611**, 794–800 (2022).
26. R. M. Anthony *et al.*, *Nat. Med.* **12**, 955–960 (2006).
27. N. G. Copeland, N. A. Jenkins, D. L. Court, *Nat. Rev. Genet.* **2**, 769–779 (2001).
28. S. Warming, N. Costantino, D. L. Court, N. A. Jenkins, N. G. Copeland, *Nucleic Acids Res.* **33**, e36 (2005).
29. C. Perner, C. L. Sokol, *STAR Protoc.* **2**, 100333 (2021).
30. G. Toda, T. Yamauchi, T. Kadowaki, K. Ueki, *STAR Protoc.* **2**, 100246 (2020).
31. C. J. C. Johnston *et al.*, *J. Vis. Exp.* **98**, e52412 (2015).
32. F. D. Finkelman *et al.*, *J. Immunol.* **151**, 1235–1244 (1993).
33. X. Zhu *et al.*, *Proc. Natl. Acad. Sci. U.S.A.* **116**, 11480–11489 (2019).
34. W. Li, R. N. Germain, M. Y. Gerner, *Nat. Protoc.* **14**, 1708–1733 (2019).
35. M. Häring, M. Fatt, J. Kupari, *STAR Protoc.* **1**, 100030 (2020).
36. D. Esterházy *et al.*, *Nature* **569**, 126–130 (2019).
37. C.-C. Chen, S. Louie, B. McCormick, W. A. Walker, H. N. Shi, *Infect. Immun.* **73**, 5468–5481 (2005).
38. S. Picelli *et al.*, *Nat. Protoc.* **9**, 171–181 (2014).
39. B. Li *et al.*, *Nat. Methods* **17**, 793–798 (2020).
40. A. Dobin *et al.*, *Bioinformatics* **29**, 15–21 (2013).
41. B. Li, C. N. Dewey, *BMC Bioinformatics* **12**, 323 (2011).
42. M. I. Love, W. Huber, S. Anders, *Genome Biol.* **15**, 550 (2014).
43. F. A. Wolf, P. Angerer, F. J. Theis, *Genome Biol.* **19**, 15 (2018).
44. S. L. Wolock, R. Lopez, A. M. Klein, *Cell Syst.* **8**, 281–291.e9 (2019).
45. P.-L. Germain, A. Lun, C. Garcia Meixide, W. Macnair, M. D. Robinson, *F1000 Res.* **10**, 979 (2021).
46. L. McInnes, J. Healy, J. Melville, UMAP: Uniform Manifold Approximation and Projection for Dimension Reduction. arXiv:1802.03426 [stat.ML] (2018).
47. V. A. Traag, L. Waltman, N. J. van Eck, *Sci. Rep.* **9**, 5233 (2019).
48. C. Domínguez Conde *et al.*, *Science* **376**, eabl5197 (2022).
49. C. Xu *et al.*, *Cell* **186**, 5876–5891.e20 (2023).
50. I. Tirosh *et al.*, *Science* **352**, 189–196 (2016).
51. Y. Hao *et al.*, *Nat. Biotechnol.* **42**, 293–304 (2024).
52. G. Korotkevich *et al.*, Fast gene set enrichment analysis, bioRxiv 060012 [Preprint] (2016); https://doi.org/10.1101/060012.
53. C. Hafemeister, R. Satija, *Genome Biol.* **20**, 296 (2019).
54. C. Ahlmann-Eltze, W. Huber, *Bioinformatics* **36**, 5701–5702 (2021).
55. T. Stuart *et al.*, *Cell* **177**, 1888–1902.e21 (2019).
56. Data for: R. Barilla *et al.*, Type 2 cytokines act on enteric sensory neurons to regulate neuropeptide-driven host defense, Figshare (2025); https://doi.org/10.6084/m9.figshare.c.7716548.

ACKNOWLEDGMENTS

We thank all Kuchroo lab members and Brigham and Women's employees for their support, assistance, and valuable discussions; J. Xia for genotyping mice; L. Ding and BWH Neurotechnology Studio for assistance with image acquisition and analysis; R. Krishnan for managing cell sorting and the BWH flow cytometry core; V. Lennon (Mayo Clinic, MN) for providing the anti–ANNA-1 antibody; I. Chiu (HMS), D. Mathis (HMS), M. Rao (BCH), M. L. Rutlin (BCH), M. Musser (BCH), H. Zaghouani (University of Missouri), H. N. Shi (MGH), and C. W. Su (MGH) for generously sharing resources and valuable advice; J. Deguine (Broad), C. Giem (Broad), and the Broad Institute Genomics Platform for assistance and preparation of scRNA-seq and bulk RNA-seq samples; Y. Han (BWH) and K. Tooley (BWH) for kind assistance with data management and administration; M. Collins for critical feedback and invaluable edits to this manuscript; A. Walker, E. Aw, and other members the Neuro-immune Focus Group (NIFG) for valuable input and discussion; A. Schnell, L. Bod, J. Choi, and Y.-C. Kye for valuable discussion and encouragement; members of the Gut Alliance for help with tissue processing; and S. Zaghouani for the indispensable support. CGRPβ-ERT-cre mice are available from M.R. under a materials transfer agreement with Boston Children's Hospital. The anti–ANNA-1 antibody is available from V. Lennon under a materials transfer agreement with Mayo Clinic. The schematics in Fig. 1C; fig. S7, A and D;, and fig. S16, A to C, were created with BioRender.com. **Funding:** This work was supported by the Food Allergy Science Initiative (FASI) (grants 2021-NEURO-218978113 and 2024-FASI-NEURO-BW24315 to V.K.K.), the National Institutes of Health (grants R01 AG080992 and R01 AI139536 to V.K.K.; grant RC2 DK114784 to R.J.X.; grant DK135707 to M.R.; grant T32 AI118692 to R.M.B.), the Department of Defense (Discovery Award PR170625 to M.R.), the National Science Foundation (fellowships DGE 2140743 and DGE 1745303 to R.M.B.), and the Cancer Research Institute (Irvington fellowship CRI4604 to L.S.). **Author contributions:** Conceptualization: R.M.B., V.K.K.; Data curation: R.M.B., S.S., J.D.; Formal analysis: R.M.B., C.B., L.S., S.S., K.S.I., G.A., Y.H.; Funding acquisition: R.M.B., L.S., M.R., R.J.X., V.K.K.; Investigation: R.M.B., C.B., L.S., S.Z., K.S.I., G.A., C.-W.S., J.D., V.S., Y.H., K.K.; Project administration: R.M.B., V.K.K.; Resources: C.W.S., J.D., M.L.R., M.R., H.Z., H.N.S., R.J.X.; Supervision: R.M.B., V.K.K.; Validation: R.M.B., C.B., L.S., S.Z., K.S.I., G.A., K.K.; Visualization: R.M.B., S.S.; Writing – original draft: R.M.B.; Writing –review and editing: R.M.B., S.Z., S.S., R.J.X., V.K.K., and M. Collins, with input from all authors. **Competing interests:** M.L.R. is currently an employee of Novo Nordisk. V.K.K. has an ownership interest in Tizona Therapeutics, Trishula, Celsius Therapeutics, Bicara Therapeutics, Larkspur Therapeutics, and Werewolf Therapeutics. V.K.K. has financial interests in Biocon Biologic, Compass, Elpiscience Biopharmaceutical Ltd, Equilium Inc, PerkinElmer, and Syngene Intl. V.K.K. is a member of SABs for Cell Signaling Technology, Elpiscience Biopharmaceutical Ltd, Larkspur, Tizona Therapeutics, Tr1X, and Werewolf. V.K.K.'s interests were reviewed and managed by Mass General Brigham in accordance with their conflict-of-interest policies. The remaining authors declare no compting interests. **Data and materials availability:** All data needed to evaluate the conclusions in the paper are available in the main text or supplementary materials. Sequencing datasets are publicly available on Gene Expression Omnibus under accession numbers GSE292613 (scRNA-seq), GSE292633 (bulk RNA-seq, sorted ILC2), and GSE292634 (bulk RNA-seq, ENS cultures). Supporting data generated after publication will be available on Figshare (*56*).

License information: Copyright © 2025 the authors, some rights reserved; exclusive licensee American Association for the Advancement of Science. No claim to original US government works. https://www.science.org/about/science-licenses-journal-article-reuse

SUPPLEMENTARY MATERIALS

science.org/doi/10.1126/science.adn9850
Materials and Methods; Figs. S1 to S16; References (*27*–*55*); MDAR Reproducibility Checklist; Table S1; Data S1 to S5; Movie S1

Submitted 14 January 2024; resubmitted 22 January 2025; accepted 10 May 2025; published online 22 May 2025

10.1126/science.adn9850

IMMUNOLOGY

A wave of Thetis cells imparts tolerance to food antigens early in life

Vanja Cabric[1,2]†, Yollanda Franco Parisotto[1]†, Tyler Park[3], Blossom Akagbosu[1], Zihan Zhao[1], Yun Lo[1,4], Gayathri Shibu[1,4], Logan Fisher[1,4], Yoselin A. Paucar Iza[1,4], Christina Leslie[3], Chrysothemis C. Brown[1,2,4]*

In the intestine, peripherally induced regulatory T (pT_{reg}) cells play an essential role in suppressing inflammatory responses to food proteins. However, the identity of the antigen-presenting cells that instruct food-specific pT_{reg} cells is poorly understood. We found that a subset of Thetis cells, TC IV, is required for food-specific pT_{reg} cell differentiation. TC IV were almost exclusively present within mesenteric lymph nodes, suggesting that their presence underlies the phenomenon of oral tolerance. A wave of TC IV differentiation in the periweaning period was associated with a window of opportunity for enhanced pT_{reg} cell generation in response to food antigens. Our findings indicate that TC IV may represent a therapeutic target for the treatment of food-associated allergic and inflammatory diseases.

The immune system must establish and maintain tolerance to harmless orally ingested food proteins to prevent onset of inflammatory diseases such as food allergy or celiac disease. Antigen-presenting cells (APCs) play a role in determining the nature of the immune response to intestinal antigens by promoting the differentiation of naïve $CD4^+$ T cells into diverse proinflammatory T helper (T_H) cell subsets, which mediate distinct types of inflammation, or peripherally induced $Foxp3^+$ regulatory T (pT_{reg}) cells, which suppress inflammatory responses to harmless microbiota or food antigens (*1*–*6*). Type 1 classical dendritic cells (cDC1s) have been linked to food-specific pT_{reg} (*7*–*9*) and intestinal T_H1 cell differentiation (*10*, *11*) at homeostasis, yet it remains unclear how cDC1s would simultaneously promote inflammatory and tolerogenic immune responses upon antigen presentation.

Although oral tolerance has been widely studied in adult mice, dysregulated responses to food antigens, including immunoglobulin E (IgE)–mediated food allergy, food protein–induced inflammatory enterocolitis, and pediatric celiac disease, present almost exclusively in infancy or childhood, when food antigens are first encountered. Commensurate with a developmental window for oral tolerance, early introduction of allergenic foods, earlier than the World Health Organization–recommended age of 6 months, is associated with reduced incidence of food allergy (*12*–*15*). Moreover, oral immunotherapy trials in food-allergic children have highlighted a window of opportunity for therapeutic benefit (*16*). However, the cellular and molecular mechanisms underpinning the increased propensity for oral tolerance in early life are not known.

We recently identified a lineage of retinoic acid receptor–related orphan receptor gamma t positive ($ROR\gamma t^+$) APCs—Thetis cells (TCs)—enriched in gut lymph nodes during early life (*17*). These cells included a subset of integrin $\alpha v\beta 8^+$ cells (TC IV) that induce pT_{reg} cell differentiation and tolerance to the gut microbiota (*17*–*20*). Given their role in microbiota tolerance, we wondered whether TC IV contributed to tolerance toward food proteins.

TCs induce food-specific pT_{reg} cells and oral tolerance

To establish the full spectrum of APCs that presented food antigens during the weaning period, we administered ovalbumin (OVA) conjugated to AF647 by intragastric gavage (i.g.) to postnatal day 14 (P14) mice and analyzed antigen uptake by major histocompatibility complex class II positive ($MHCII^+$) cells in mesenteric lymph nodes (mLNs) at 8, 24, and 48 hours after gavage. Four APC types could take up antigen: $CCR7^+$ (migratory) type 1 dendritic cells (cDC1s), $CCR7^+$ cDC2s, $MHCII^+$ monocytes or macrophages, and TC IV (Fig. 1, A and B, and fig. S1).

The small intestine and associated lymph nodes represent the major sites of dietary antigen encounter and tolerance induction (*3*, *21*). Thus, to determine whether TCs regulate food-induced pT_{reg} cell generation, we examined individual small intestine lymph nodes (siLNs) and small intestine lamina propria (SI) in mice deficient in MHCII-restricted antigen presentation by $ROR\gamma t^+$ cells ($MHCII^{\Delta ROR\gamma t}$) at 4 weeks of age, to allow for accumulation of pT_{reg} cells in response to dietary and microbiota antigens. We observed a marked reduction in $ROR\gamma t^+Foxp3^+$ cells in all lymph nodes examined as well as in Peyer's patches (PPs) and SI (fig. S2A). Serial analysis of $CD4^+$ T_H cells from 3 to 5 weeks of age revealed evidence of inflammatory responses within the SI of 5-week-old mice with increased T_H17 cells (fig. S2B). At 12 weeks of age, we observed severe small intestinal inflammation with marked inflammatory cell infiltrate, epithelial hyperplasia, and goblet cell loss with epithelial erosions (fig. S2, C and D), confirming a role for $ROR\gamma t^+$ APCs in preventing dysregulated immune responses within the small intestine.

Because loss of small intestinal pT_{reg} cells in $MHCII^{\Delta ROR\gamma t}$ mice could also reflect loss of microbiota-specific pT_{reg} cells, we tested the specific role of $ROR\gamma t^+$ APCs in tolerance to food antigens by adoptive transfer of OVA-specific naïve OT-II $CD4^+$ T cells into $MHCII^{\Delta ROR\gamma t}$ mice at P14 followed by oral administration of OVA (Fig. 1C). Administration of oral antigen in this time window coincides with first encounter with a host of dietary antigens upon weaning from breast milk to solid food and reflects the physiological window for establishing tolerance to dietary proteins in mice. Seven days after transfer, ~60% of OT-II cells in siLNs and SI of wild-type $H2\text{-}Ab1(MHCII)^{fl/fl}$ mice expressed Foxp3 with equal proportions of $ROR\gamma t^+$ and $ROR\gamma t^-$ $Foxp3^+$ cells (Fig. 1, D and E, and fig. S2, E and F). In $MHCII^{\Delta ROR\gamma t}$ mice, OT-II pT_{reg} cell differentiation was almost completely abolished, and absence of OT-II pT_{reg} cells was associated with enhanced OT-II $Tbet^+$ T_H1 cell differentiation (Fig. 1, F and G, and fig. S2G).

$ROR\gamma t^+$ APCs encompass two distinct cell types—TCs and $MHCII^+$ type 3 innate lymphoid cells (ILC3s), also known as lymphoid tissue inducer (LTi) cells. Although we did not observe uptake of OVA in $MHCII^+$ ILC3s (Fig. 1B), to exclude a role for ILC3s in food-specific pT_{reg} cell differentiation, we analyzed OT-II T_{reg} cell conversion in $Rora^{cre}H2\text{-}Ab1^{fl/fl}$ mice, which specifically lack MHCII expression on ILC3s (*17*). In contrast to $MHCII^{\Delta ROR\gamma t}$ mice, OVA-fed $MHCII^{\Delta ROR\alpha}$ mice exhibited normal proportions and numbers of OT-II T_{reg} cells (fig. S2, H and I), excluding a role for ILC3s in food-specific pT_{reg} cell generation.

To determine the impact of impaired food-specific pT_{reg} cell differentiation on oral tolerance and T_H2 allergic responses, $MHCII^{\Delta ROR\gamma t}$ or control mice were immunized with OVA-alum 7 and 14 days after the final exposure to oral OVA and challenged intranasally with OVA on three occasions, 3 or 4 days apart (Fig. 1H). Eosinophilia in the bronchoalveolar lavage (BAL) fluid and serum OVA-specific IgG1 and IgE responses were suppressed in OVA-fed wild-type mice relative to

[1]Immuno-Oncology, Human Oncology and Pathogenesis Program, Memorial Sloan Kettering Cancer Center, New York, NY, USA. [2]Department of Pediatrics, Memorial Sloan Kettering Cancer Center, New York, NY, USA. [3]Computational and Systems Biology Program, Memorial Sloan Kettering Cancer Center, New York, NY, USA. [4]Immunology and Microbial Pathogenesis Program, Weill Cornell Medicine Graduate School of Medical Sciences, New York, NY, USA. ***Corresponding author. Email: brownc10@mskcc.org** †These authors contributed equally to this work.

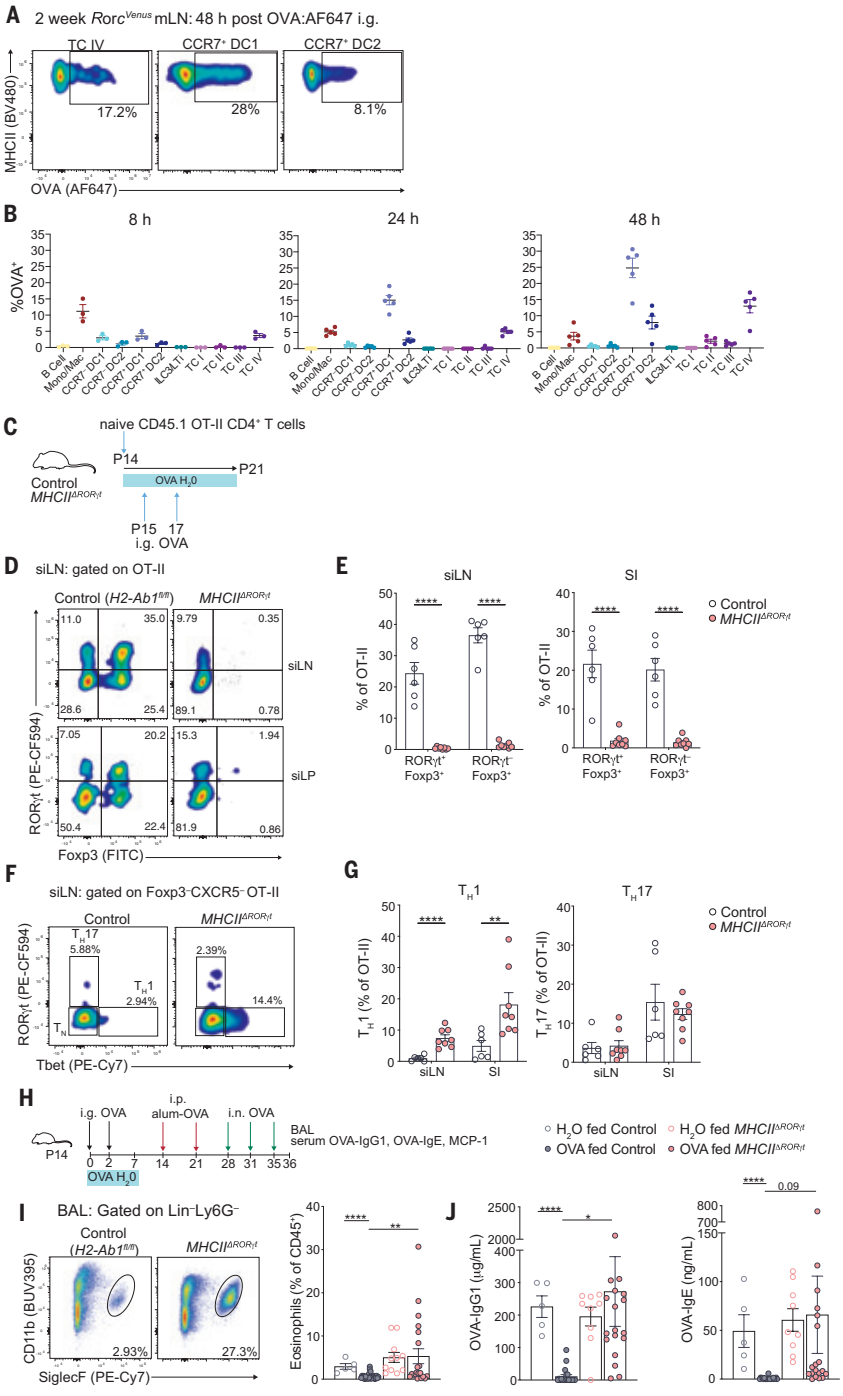

Fig. 1. RORγt$^+$ TCs promote food-specific pT$_{reg}$ cell differentiation and oral tolerance. (**A**) Representative flow cytometry showing percentage of labeled TC IV, CCR7$^+$ cDC1, and CCR7$^+$ cDC2 in the mLNs of *Rorc*$^{Venus\text{-}creERT2}$ mice, 48 hours after i.g. administration of OVA-AF647 at P14. (**B**) Summary graph of frequency of OVA-AF647$^+$ cells among indicated APCs in the mLNs at 8, 24, and 48 hours after OVA-AF647 administration ($n = 3$ to 5 mice per group). (**C** to **G**) *MHCII*$^{\Delta RORγt}$ ($n = 8$) and *H2-Ab1*$^{fl/fl}$ ($n = 6$) littermate control mice were adoptively transferred with 20×10^3 naïve CD45.1 CD4$^+$ OT-II T cells before OVA administration and analyzed 7 days later for frequencies and numbers of RORγt$^+$Foxp3$^+$, RORγt$^-$Foxp3$^+$ pT$_{reg}$, T$_H$1 (Foxp3$^-$Tbet$^+$), and T$_H$17 (Foxp3$^-$RORγt$^+$) cells among OT-II cells in siLNs and SI. (C) Experimental schematic: Mice were adoptively transferred with OT-II cells on P14, received two doses of i.g. OVA on P15 and P17, and were maintained on OVA-supplemented drinking water throughout the duration of the experiment. (D) Flow cytometry of RORγt and Foxp3-expressing OT-II cell subsets and (E) summary graphs for frequencies of OT-II pT$_{reg}$ cells in siLNs and SI. (F) Representative flow cytometry of T$_H$17 and T$_H$1 OT-II subsets. (G) Summary graphs for frequencies of T$_H$1 and T$_H$17 cells among OT-II cells. (**H**) Schematic of oral tolerance induction to alum-induced OVA immunity. (**I**) Representative flow cytometry of eosinophils in bronchoalveolar lavage (BAL) fluid of *H2-Ab1*$^{fl/fl}$ control or littermate *MHCII*$^{\Delta RORγt}$ OVA-tolerized mice (left) and summary graph (right) of eosinophil frequencies among CD45$^+$ cells in BAL fluid, with or without OVA feeding ($n = 5$ to 25 mice per group) as described in (H). (**J**) Serum OVA-IgG1 and OVA-IgE in control or littermate *MHCII*$^{\Delta RORγt}$ mice ($n = 5$ to 21 per group) described in (H). Data in (A) and (B) are representative of three independent experiments. Data in (E) and (G) are pooled from two independent experiments. Data in (I) and (J) are pooled from six independent experiments. Error bars: means ± SEM. Each symbol represents an individual mouse. *P* values were calculated by two-way analysis of variance (ANOVA) in (E) and (G) and by two-tailed unpaired *t* test in (I) and (J). $*P < 0.05$, $**P < 0.01$, $***P < 0.001$, $****P < 0.0001$.

mice that received H_2O gavages and regular drinking water (Fig. 1, I and J). *MHCII*$^{\Delta RORγt}$ mice exhibited levels of OVA-specific IgG1 similar to those of nontolerized mice as well as variable increases in OVA-specific IgE and BAL eosinophils. Both tolerized and nontolerized *MHCII*$^{\Delta RORγt}$ mice had increased serum levels of mast cell protease-1 (MCP-1), a mast cell protease released upon allergen-dependent cross-linking of IgE (fig. S2J), indicating enhanced mast cell activation relative to their wild-type counterparts. Overall, these results indicate that food-specific T$_{reg}$ cells generated in early life comprise both RORγt$^+$ and RORγt$^-$ pT$_{reg}$ cells and that MHCII antigen presentation by TCs is critical for food-specific pT$_{reg}$ cell generation and oral tolerance.

αvβ8$^+$ TC IV are enriched at sites of pT$_{reg}$ cell generation in early life

Expression of the transforming growth factor–β (TGF-β)–activating integrin αvβ8 is required by TCs to induce pT$_{reg}$ cells within colonic lymph nodes in response to microbiota (*17*). Among TCs profiled from mLNs, TC IV express the highest levels of integrin subunit beta 8 (ITGB8) (*17*). To determine whether subset-specific expression of αvβ8 was conserved across TCs from different tissue-draining lymph nodes, we performed single-cell RNA sequencing (scRNA-seq) on TCs [CXCR6$^-$ RORγt(Venus)$^+$MHCII$^+$] isolated from hepatic, small intestinal, colonic, salivary gland, lung, and skin-draining lymph nodes and PPs of *Rorc*$^{Venus\text{-}creERT2}$ reporter mice at P14. Although expression of Venus

reflects transcription of the Rorc 3′ untranslated region, shared between both *Rorc* and *Rorgt* isoforms, $Rorgt^{cre}$ fate mapping confirmed that all Venus$^+$ TCs, including TC IV, express the RORγt isoform (fig. S3A).

Differential gene expression analysis of TC cluster transcriptomes confirmed the presence of previously identified subsets TC I to TC IV and proliferating (Ki67$^+$) TCs as well as a cluster whose gene expression signature was shared with proliferating TCs, suggesting the presence of TCs at the earliest stage of differentiation (Fig. 2, A and B, and data S1). Notably, TC IV were specifically enriched in intestinal lymph nodes and gut-associated lymphoid tissue including hepatic, small intestinal, and colonic lymph nodes and PPs (Fig. 2C). TC subset transcriptomes were very stable across lymph nodes, with only 3 to 20 genes exhibiting lymph node–specific patterns of expression for each individual TC subset (fig. S3B). Among TCs, TC IV were distinguished by the highest levels of *Itgb8* expression as well as *aldh1a2*, encoding RALDH2, a critical enzyme for synthesis of retinoic acid that promotes intestinal T_{reg} cell differentiation (*22*, *23*) (Fig. 2D). Analysis of TCs from lymph nodes of P14 $Rorc^{Venus\text{-}creERT2}Itgb8^{tdtomato}$ mice by flow cytometry confirmed that the absolute number of ITGB8(tdTomato)$^+$ TCs was increased in gut and hepatic lymph nodes relative to skin-draining lymph nodes (Fig. 2, E and F).

To determine whether food-specific pT_{reg} cell induction was dependent on *Itgb8* expression by TCs, we adoptively transferred naïve OT-II cells into P14 $Rorgt^{cre}Itgb8^{fl/fl}$ mice followed by oral OVA administration. OT-II pT_{reg} cell differentiation was abolished in these mice (Fig. 2, G and H, and fig. S4A), with increased numbers and proportions of OT-II T_H1 cells (fig. S4B). We did not observe altered OT-II pT_{reg} cell generation in $Cd4^{cre}Itgb8^{fl/fl}$ mice (fig. S4C), confirming that *Itgb8* expression by TCs, but not TCRβ$^+$ cells, was required for food-specific pT_{reg} cell induction. Although TC IV are distinguished by the highest levels of *Itgb8* expression, ~20% of TC III expressed low levels of ITGB8, as determined by transcript or ITGB8(tdTomato) expression (fig. S4, D and E). Moreover, TC III express Aire (fig. S5A), and previous studies have suggested that RORγt$^+$Aire$^+$ cells [also known as RORγt$^+$ extrathymic Aire-expressing cells (eTACs)] may be the cell type responsible for pT_{reg} cell differentiation (*20*, *24*). Notably, we did not observe uptake of OVA-AF647 by Aire$^+$ TC III (Fig. 1B).

To determine the role of TC III versus TC IV in pT_{reg} cell generation, we crossed $Rorgt^{cre}$ mice with mice carrying an $Aire^{flex\text{-}dtA}$ allele to allow cre-mediated recombination and inversion of the diphtheria toxin subunit A (dtA) and thus ablation of RORγt$^+$Aire$^+$ cells (fig. S5B). Analysis of $Rorgt^{cre}Aire^{flex\text{-}dtA}$ mice at P14 confirmed complete loss of Aire$^+$ TCs, encompassing TC I and TC III, but no impairment in TC IV numbers, nor Aire$^+$ medullary thymic epithelial cell (mTEC) or cDC numbers (fig. S5, C to E). These mice showed OT-II pT_{reg} cell frequencies comparable to those of their littermate controls after adoptive transfer of OT-II T cells at P14 and after OVA feeding (Fig. 2I). Moreover, host RORγt$^+$ pT_{reg} cell numbers were not altered in these mice (Fig. 2I and fig. S5F), indicating that RORγt$^+$Aire$^+$ TCs were not required for microbiota-induced pT_{reg} cells. Together, these data exclude a role for Aire$^+$ TCs, including ITGB8$^+$ TC III, in intestinal pT_{reg} cell differentiation, implicating ITGB8$^+$ TC IV as the cell type required for pT_{reg} cell induction in early life.

Role of TCs in food-specific pT_{reg} cell differentiation from birth to adulthood

Consistent with the previously reported developmental wave of TCs in mLNs (*17*), we observed a peak in ITGB8(tdTomato)$^+$ TC IV numbers in siLNs at P14, coincident with weaning, followed by a steady decline thereafter (Fig. 2J). We wondered whether low numbers of TCs in adult mice promote food-specific pT_{reg} cells after antigen introduction in later life or whether a distinct APC induced food-specific T_{reg} cells in adulthood. To address this, we treated adult (6-week-old) or periweaning (P12) $Rorc^{Venus\text{-}creERT2}H2\text{-}Ab1^{fl/fl}$ mice with tamoxifen to temporally ablate MHCII expression in RORγt$^+$ APCs (Fig. 2K). $Rorc^{Venus\text{-}creERT2}H2\text{-}Ab1^{fl/wt}$ littermate mice were used as controls to account for any toxicity effects of tamoxifen-induced activation of creERT2. Naïve OT-II T cells were adoptively transferred into recipient mice at 8 weeks (adult) or P14 (periweaning) mice followed by oral OVA administration (Fig. 2K). Seven days later, OT-II pT_{reg} cells were almost completely absent in both young and adult $Rorc^{Venus\text{-}creERT2}H2\text{-}Ab1^{fl/fl}$ mice (Fig. 2, L and M, and fig. S6A). Notably, however, in control mice, the frequency of Foxp3$^+$ cells among OT-II T cells was ~7 fold lower in adult mice compared with periweaning mice (9.3% versus 67.5%, siLNs; Fig. 2M), demonstrating a window of opportunity for enhanced T_{reg} cell differentiation in early life. As expected, 3 weeks of tamoxifen treatment in adult mice resulted in a reduction in TC but not DC numbers (fig. S6B). This was associated with a decrease in the frequency of host pT_{reg} cells within siLNs and SI, albeit no differences in absolute cell numbers (fig. S6, C and D), indicating a minimal contribution of de novo pT_{reg} cell differentiation to the pT_{reg} cell pool of adult mice with stable diets and microbial communities. Moreover, these data suggest that antigen presentation by TCs is not required for pT_{reg} cell maintenance.

IRF8-dependent TC differentiation

Previous studies have suggested that tolerance to oral food antigens is mediated by classical DCs, primarily cDC1 (*7*, *9*). $Zbtb46^{cre}Irf8^{fl/fl}$ mice are deficient in IRF8-dependent cDC1s and exhibit impaired pT_{reg} cell differentiation and oral tolerance. Yet $Batf3^{-/-}$ and *Irf8* enhancer mutant mice, which also lack cDC1, have normal numbers of intestinal pT_{reg} cells (*25*, *26*). Given expression of Zbtb46 by TCs (*15*), we wondered whether the loss of tolerance in $Zbtb46^{cre}Irf8^{fl/fl}$ mice might be due to a role for IRF8 in TC IV differentiation or function. Our previously published paired scRNA-seq and ATAC-seq (assay for transposase-accessible chromatin using sequencing) data from RORγt$^+$ APCs demonstrated enrichment of IRF8 motif activity as well as increased expression of IRF8 among TCs (Fig. 3A). To determine the role of IRF8 in TC differentiation, we analyzed TCs from mLNs of $Rorgt^{cre}Irf8^{fl/fl}$ ($Irf8^{\Delta RORγt}$) mice at P14 and found decreased numbers of TC II, III, and IV subsets but no change in TC I or MHCII$^+$ ILC3 subsets (Fig. 3B) or cDC numbers (fig. S7A). Consistent with the reduction in TC IV, $Irf8^{\Delta RORγt}$ mice exhibited reduced numbers and proportions of food-specific pT_{reg} cells after adoptive transfer of OT-II cells at P14 and OVA feeding as well as endogenous RORγt$^+$ pT_{reg} cells (Fig. 3, C and D, and fig. S7, B and C). Thus, a role for IRF8 in TC differentiation reconciled previous findings of impaired pT_{reg} cell differentiation and oral tolerance in $Zbtb46^{cre}Irf8^{fl/fl}$ mice.

Classical DCs promote food-specific T_H1 and T_{FH} cells and maintain antigen-experienced T cells

Inflammatory CD4$^+$ T cell responses are promoted by cDC1 priming of T_H1 cells (*10*) and cDC2 regulation of T_H2, T_H17, and T follicular helper (T_{FH}) cell differentiation (*27*–*33*), suggesting potential roles for cDCs in regulating inflammatory responses to food antigens after uptake by migratory cDCs (Fig. 1, A and B). We generated mice that lack cDC1 specifically through depletion of the *Irf8* gene in cells that express Clec9a ($Irf8^{\Delta DC}$) (fig. S8, A and B). After adoptive transfer of OT-II T cells and OVA administration at P14, these mice showed comparable proportions and numbers of OT-II pT_{reg} cells to littermate control $Irf8^{fl/fl}$ mice but reduced OT-II and endogenous T_H1 cells (Fig. 4, A and B, and fig. S8, C to E) (*10*). Within the host compartment, we observed equivalent numbers of RORγt$^+$ pT_{reg} cells (fig. S8F), further excluding a role for cDC1 in pT_{reg} cell differentiation. In *Zeb2* triple enhancer mutant ($Zeb2^{\Delta 1+2+3}$) mice, which lack cDC2 (*28*), OT-II pT_{reg} cell differentiation was not affected (Fig. 4C and fig. S9A), despite an almost complete loss of cDC2s in the colonic lymph node, which served as a representative gut lymph node (fig. S9B). Rather, there was a reduction in both OT-II and endogenous T_{FH} (PD1^{hi}CXCR5$^+$) cells (Fig. 4, D and E, and fig. S9C).

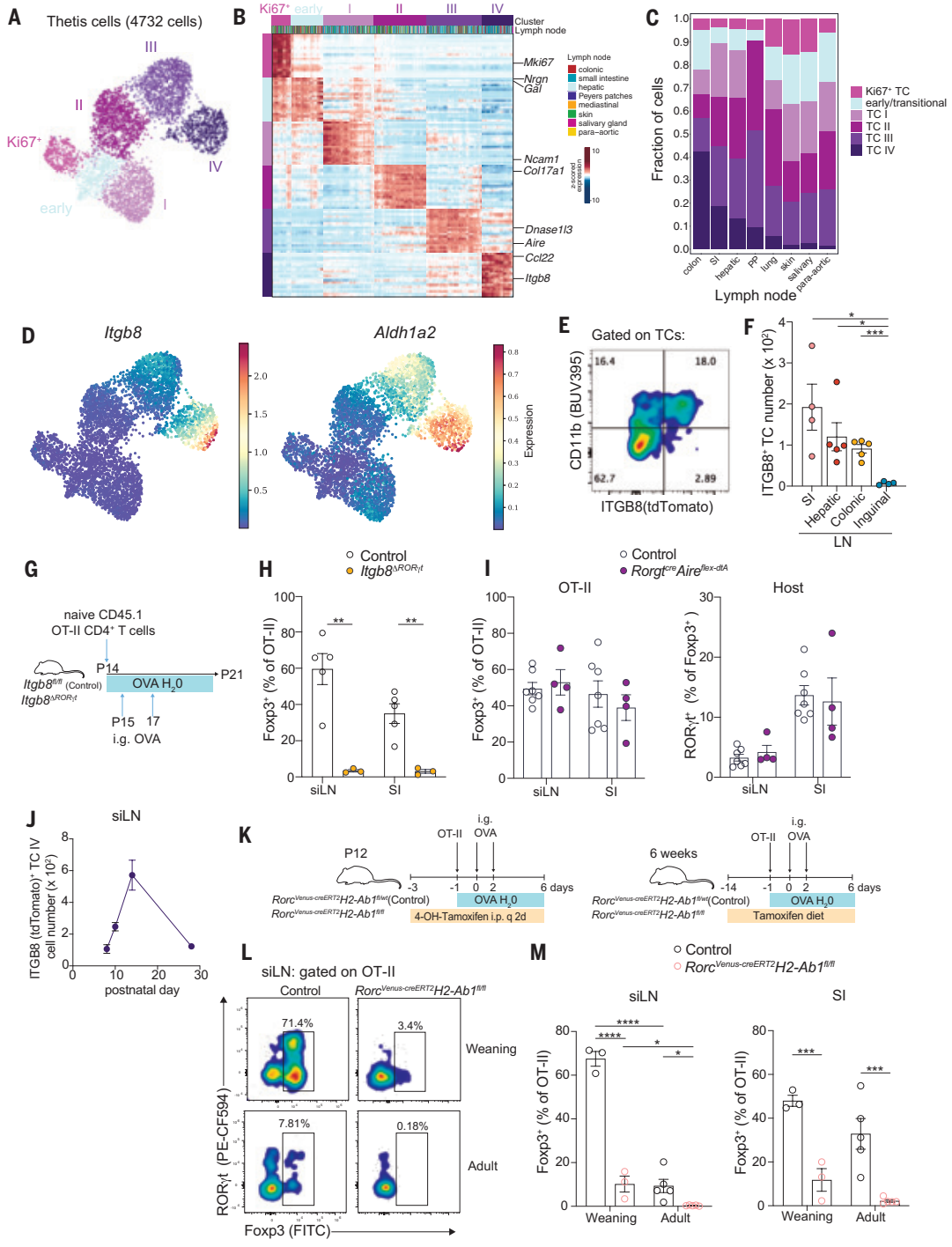

Fig. 2. Enrichment of αvβ8$^+$ TCs in early-life gut lymph nodes provides a window of opportunity for enhanced food-specific pT$_{reg}$ cell generation. (**A**) Uniform manifold approximation and projection (UMAP) of 4732 TCs from gut and nongut lymph nodes of 2-week-old (P14) *Rorc*$^{Venus\text{-}creERT2}$ mice ($n = 7$), colored by cluster identity. (**B**) Heatmap showing expression of top differentially expressed genes between TC clusters identified in (A) with lymph node of origin indicated. (**C**) Fraction of each TC subset among all TCs in each lymph node sample. (**D**) UMAP overlaid by imputed expression of *Itgb8 and Aldh1a2*. (**E**) Flow cytometry of ITGB8(tdTomato) expression in TCs isolated from mLNs of P14 *Rorc*$^{Venus\text{-}creERT2}$*Itgb8*^{tdTomato} mice and (**F**) summary graph for total number of Itgβ8$^+$ TCs in each indicated lymph node. (**G**) Experimental design. (**H**) Frequencies of OT-II pT$_{reg}$ cells in siLNs and SI in *Itgb8*$^{\Delta ROR\gamma t}$ ($n = 3$) and *Itgb8*$^{fl/fl}$ ($n = 5$) littermate control mice. (**I**) Percentage of Foxp3$^+$ pT$_{reg}$ cells among OT-II cells (left) or percentage of RORγt$^+$ pT$_{reg}$ cells among host Foxp3$^+$ cells (right) in *Rorgt*^{cre}*Aire*$^{flex\text{-}dtA}$ and littermate control (*Rorgt*^{cre} or *Aire*$^{flex\text{-}dtA}$) mice treated as shown in (G) ($n = 4$ or 7 per group). (**J**) Number of CD11b$^+$Itgβ8$^+$ TC IV in siLN of *Rorc*$^{Venus\text{-}creERT2}$*Itgb8*^{tdTomato} mice from P7 to week 4 ($n = 3$ to 5 per time point). (**K**) Schematic of tamoxifen administration, OT-II adoptive transfers, and OVA feeding in weaning (P12, left) or adult (6 weeks, right) *Rorc*$^{Venus\text{-}creERT2}$*H2-Ab1*$^{fl/fl}$ or littermate *Rorc*^{creERT2}*H2-Ab1*$^{fl/wt}$ control mice. (**L**) Flow cytometry of RORγt and Foxp3-expressing OT-II cell subsets in siLNs of mice described in (K). (**M**) Summary graphs for OT-II pT$_{reg}$ cell frequencies in siLNs and SI ($n = 3$ or 5 per group). Data in (E) and (F) are representative of two independent experiments. Data in (H) are representative of four independent experiments. Data in (I) are pooled from two independent experiments. Data in (J) are representative of three independent experiments. Data in (M) are representative of two (adult) or three (weaning) experiments. Error bars: means ± SEM. Each symbol represents an individual mouse. *P* values were calculated by two-tailed unpaired *t* test; $*P < 0.05$, $**P < 0.01$, $***P < 0.001$, $****P < 0.0001$.

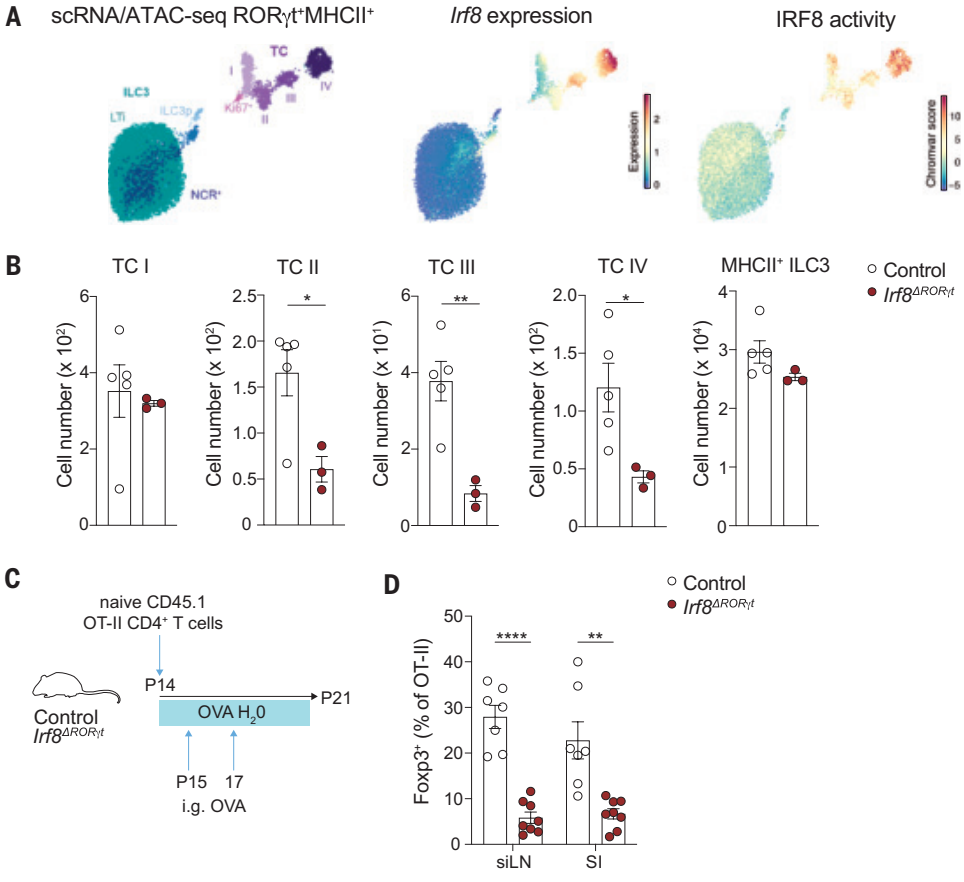

Fig. 3. IRF8 regulates TC differentiation. (**A**) UMAP visualization of publicly available scRNA/ATAC-seq of 10,145 RORγt$^+$ APCs (*17*), encompassing TCs and ILC3s, from mLNs of 2-week-old *Rorc*$^{Venus\text{-}creERT2}$ mice colored by cluster annotation (left), imputed expression of *Irf8* (middle), or chromVAR deviation IRF8 motif score (right). (**B**) Number of cells for each indicated TC or ILC3 subset in mLN of P14 *Irf8*$^{\Delta ROR\gamma t}$ ($n = 3$) and *Irf8*$^{fl/fl}$ ($n = 5$) littermate control mice. (**C**) Experimental design for OT-II adoptive transfers and OVA feeding for mice in (D). (**D**) Frequency of OT-II pT$_{reg}$ cells in siLNs and SI in *Irf8*$^{\Delta ROR\gamma t}$ ($n = 8$) and *Ifr8*$^{fl/fl}$ ($n = 7$) littermate control mice. Data in (B) are representative of four independent experiments. Data in (D) are pooled from two independent experiments. Error bars: means ± SEM. Each symbol represents an individual mouse. *P* values were calculated by two-tailed unpaired *t* test (B) or two-way ANOVA (D). $*P < 0.05$, $**P < 0.01$, $***P < 0.001$, $****P < 0.0001$.

Overall, these results suggest division of labor among TCs and DCs, whereby each subset regulates a distinct branch of the CD4 T cell response to food antigens.

Finally, to exclude potential redundancy between cDC subsets, we used *Clec9a*$^{cre/cre}$*H2-Ab1*$^{fl/fl}$ (*MHCII*$^{\Delta DC}$) mice in which both cDC1 and cDC2 cannot present antigens owing to expression of Clec9a at the common DC progenitor (CDP) stage (*34*, *35*). Analysis of *Clec9a*$^{cre/cre}$*R26*$^{lsl\text{-}tdtomato}$ fate mapping mice confirmed that by P21, almost all CCR7$^-$ and CCR7$^+$ cDC1 and ~70% of CD11b$^+$XCR1$^-$ cDC2 subsets within the mLNs were labeled (fig. S9D). We therefore adoptively transferred naïve OT-II T cells into recipient mice at P21 followed by oral OVA administration (Fig. 4F). Seven days after transfer, there were equivalent proportions of OT-II pT$_{reg}$ cells between *MHCII*$^{\Delta DC}$ and littermate control *Clec9a*$^{cre/cre}$*H2-Ab1*$^{fl/wt}$ mice (Fig. 4G), despite efficient ablation of MHCII expression on cDC1s and cDC2s (fig. S9, E and F). Among Foxp3$^-$ OT-II cells, T$_H$1 cell differentiation was impaired, consistent with our earlier finding of cDC1-dependent T$_H$1 differentiation, but the frequency of T$_H$17 cells was not affected (fig. S9G), indicating that an alternative APC subset was responsible for priming food-specific T$_H$17 cells. However, there was a global reduction in OT-II cell numbers in siLNs, but not SI, because of a deficiency of all Foxp3$^+$ and Foxp3$^-$ subsets (Fig. 4H).

Our analysis of OT-II cells was performed after 7 days of continuous OVA ingestion through drinking water. We wondered whether the reduction in numbers of antigen-experienced OT-II cells across all cell lineages in *MHCII*$^{\Delta DC}$ mice was due to a role for DCs in maintaining antigen-experienced cells through T cell receptor signaling. To distinguish the role of TCs and cDCs in induction versus maintenance of CD4 T cell differentiation, we repeated the OT-II transfer experiments in both *MHCII*$^{\Delta DC}$ and *MHCII*$^{\Delta ROR\gamma t}$ mice and analyzed OT-II cells in individual gut-draining lymph nodes, 48 hours after a single dose of i.g. OVA (Fig. 4I). At this time point, OT-II cell numbers were normal in *MHCII*$^{\Delta DC}$ mice, with equivalent proportions and numbers of Foxp3$^+$ and Foxp3$^-$ OT-II pT$_{reg}$ cells in all lymph nodes examined (Fig. 4J and fig. S9H). In contrast, OT-II T$_{reg}$ cell induction was completely abolished in *MHCII*$^{\Delta ROR\gamma t}$ mice (Fig. 4K and fig. S9I). Thus, antigen presentation by TCs but not cDCs is required for initial priming and induction of pT$_{reg}$ cell differentiation.

Moreover, we generated bone marrow chimeras with an equal mix of *Itgb8*$^{\Delta ROR\gamma t}$ and *MHCII*$^{\Delta ROR\gamma t}$ bone marrow cells—in which both cDCs and TCs can present antigen, but the same TC cannot present antigen and activate TGF-β (Fig. 4L). In these mice, OT-II pT$_{reg}$ cell induction was impaired, with an equivalent deficit in OT-II pT$_{reg}$ cells observed in *MHCII*$^{\Delta ROR\gamma t}$, *Itgb8*$^{\Delta ROR\gamma t}$, and *MHCII*$^{\Delta ROR\gamma t}$/*Itgb8*$^{\Delta ROR\gamma t}$ chimeras (Fig. 4M). These data confirm that food-induced pT$_{reg}$ cell differentiation is dependent on antigen presentation by ITGβ8-expressing TCs and exclude the possibility of redundant and compensatory functions between TCs and DCs.

Four-week-old *MHCII*$^{\Delta DC}$ mice at steady state had normal numbers of RORγt$^+$ pT$_{reg}$ cells in the intestine; however, we observed a reduction in the number of Helios$^+$ T$_{reg}$ cells, potentially reflecting nonperipherally derived thymic T$_{reg}$ cells (fig. S10A). *MHCII*$^{\Delta DC}$ mice did not exhibit any evidence of inflammation but had reduced frequencies of T$_H$1 and T$_{FH}$ cells as well as reduced numbers of all T$_H$ subsets, most notably within siLNs (fig. S10A). Twelve-week-old *MHCII*$^{\Delta DC}$ mice did not show evidence of intestinal inflammation (fig. S10, B and C), confirming that antigen presentation by cDCs is not required for intestinal tolerance, either in early life or adulthood.

To understand the role of cDCs in maintenance of food-specific CD4$^+$ T cells, we analyzed cell proliferation in transferred OT-II cells, 72 hours after a single dose of i.g. OVA. At this time point, nearly all OT-II cells were CD44^{hi}, and we did not observe differences in the proportion of CD44^{hi} cells in *MHCII*$^{\Delta DC}$ mice (fig. S11, A and B). However, OT-II cell numbers were reduced in individual gut lymph nodes in *MHCII*$^{\Delta DC}$ mice (fig. S11C). Comparison of cell proliferation revealed equivalent numbers of CD44^{hi} antigen–experienced OT-II cells among undivided cells with progressive impairment in OT-II cell numbers with subsequent cell divisions (fig. S11, D and E), suggesting that antigen presentation by DCs is required to sustain early antigen-experienced CD4^i T cells.

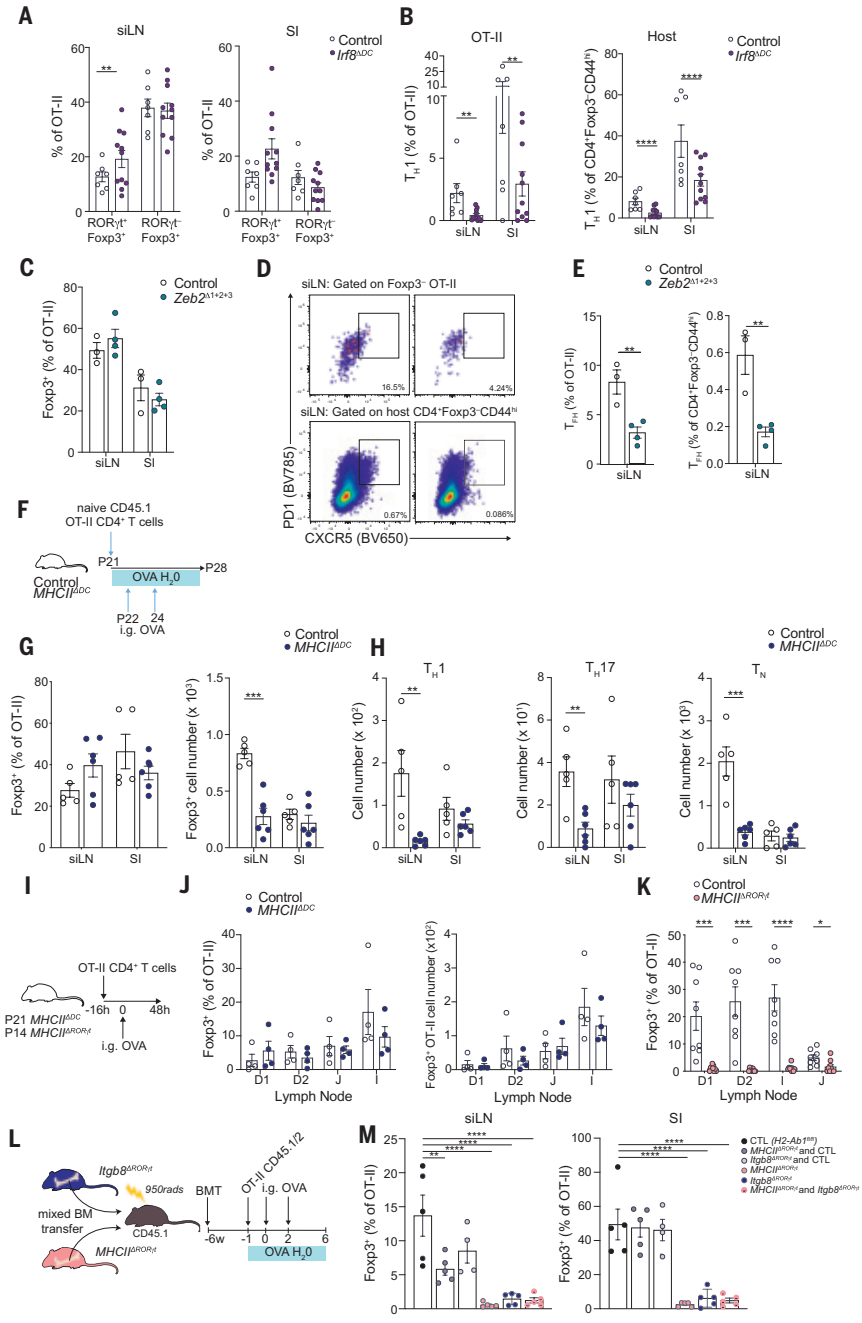

Fig. 4. Antigen presentation by classical dendritic cells promotes food-specific T_H1 and T_{FH} differentiation. (**A** and **B**) P14 *Irf8*$^{\Delta DC}$ ($n = 11$) and *Irf8*$^{fl/fl}$ ($n = 7$) littermate control mice were adoptively transferred with 20×10^3 naïve CD45.1 CD4$^+$ OT-II T cells followed by two doses of i.g. OVA on P15 and P17. Mice were maintained on OVA-supplemented drinking water and analyzed 7 days later. (A) Frequency of RORγt$^+$ and RORγt$^-$ pT_{reg} cells among OT-II cells in siLNs and SI. (B) Frequency of T_H1 cells among host CD4$^+$Foxp3$^-$CD44^{hi} T cells in siLNs and SI of mice described in (A). (**C** to **E**) *Zeb2*$^{\Delta1+2+3}$ ($n = 4$) and wild-type littermate control ($n = 3$) mice were adoptively transferred with 20×10^3 naïve CD45.1 CD4$^+$ OT-II T cells followed by two doses of i.g. OVA on P15 and P17. Mice were maintained on OVA-supplemented drinking water and analyzed 7 days later. (C) Frequency of pT_{reg} cells among OT-II cells. (D) Flow cytometry of PD1$^+$CXCR5$^+$ OT-II or host T_{FH} cells in siLNs. (E) Frequency of T_{FH} (Foxp3$^-$PD1$^+$CXCR5$^+$) cells among OT-II cells or CD4$^+$Foxp3$^-$CD44^{hi} host T cells in siLNs. (**F**) Experimental schema for OT-II adoptive transfers and OVA feeding for mice in (G). (**G**) Frequencies and numbers of OT-II pT_{reg} cells, and number of (**H**) Foxp3$^-$RORγt$^-$Tbet$^+$ T_H1, Foxp3$^-$RORγt$^+$ T_H17, and Foxp3$^-$RORγt$^-$Tbet$^-$ T lineage negative (T_N) OT-II cells in siLNs and SI of *MHCII*$^{\Delta DC}$ ($n = 6$) and *H2-Ab1*$^{fl/fl}$ ($n = 5$) littermate control mice. (**I**) Schematic of OT-II adoptive transfers, single dose of i.g. OVA at 16 hours and analysis of pT_{reg} cell induction 48 hours after i.g. OVA. (**J**) Frequency and number of OT-II pT_{reg} cells across individual gut lymph nodes of *MHCII*$^{\Delta DC}$ or control mice ($n =$ 4 mice per group). (**K**) Frequency of OT-II pT_{reg} cells in gut lymph nodes of *MHCII*$^{\Delta ROR\gamma t}$ ($n = 9$) or control ($n = 8$) mice. (**L**) Mixed bone marrow chimera mice reconstituted with *MHCII*$^{\Delta ROR\gamma t}$ and *Itgb8*$^{\Delta ROR\gamma t}$ bone marrow cells were adoptively transferred with congenic OT-II T cells before OVA administration in the drinking water and two doses of i.g. OVA. BMT, bone marrow transfer. (**M**) Frequency of Foxp3$^+$ pT_{reg} cells among OT-II cells in siLN and SI of bone marrow chimeras ($n = 5$ per group). Data in (A), (B), and (K) are pooled from two independent experiments. Data in (C) to (H) and (M) are representative of three independent experiments. Data in (J) are representative of two independent experiments. Gut lymph nodes: D1, portal; D2, distal duodenum; J, jejunum; I, ileum. Error bars: means ± SEM. Each symbol represents an individual "mouse. *P* values were calculated by two-way ANOVA in (A), (B), and (K) and by two-tailed unpaired *t* test in (C), (E), (G), (H), (J), and (M). $^*P < 0.05$, $^{**}P < 0.01$, $^{***}P < 0.001$, $^{****}P < 0.0001$.

Discussion

CD4$^+$ T cell responses to food comprise both proinflammatory T_H cells and immunosuppressive pT_{reg} cells. In our model, inflammatory CD4$^+$ T_H cell subsets represented a small proportion of the total food-specific T cell pool, but impairing pT_{reg} cell generation led to their expansion. A recent study demonstrated the importance of balance between proinflammatory and tolerogenic APCs in determining the outcome of food-specific CD4 T cell priming during concomitant enteric infection (*7*). Although cDC1 was suggested to be the tolerogenic APC subset, using precise intersectional genetic approaches to target particular cDC or TC subsets, our study defines the contribution of distinct APC types to food-specific CD4$^+$ T cell responses and establishes TC IV as the tolerogenic pT_{reg} cell–inducing subset in mice. Reconciling these findings, we found that antigen presentation by cDCs sustains TC-induced pT_{reg} cells within mLNs. In contrast to the role of TCs in microbiota-dependent RORγt$^+$ pT_{reg} cell differentiation (*15*), here we found that TCs promote the differentiation of both RORγt$^+$ and RORγt$^-$ pT_{reg} cells in response to food antigens. Whether these subsets represent transcriptionally and functionally distinct pT_{reg} cell populations is an area for future investigation.

Studies in mice and humans have established a window of opportunity for oral tolerance in early life. We found that the balance of T_{reg} to inflammatory T_H cells was skewed heavily in favor of T_{reg} cells after antigen encounter in the periweaning window. This was associated with increased abundance of tolerogenic TC IV within gut lymph nodes compared with later life. Moreover, TC IV were almost exclusively present in gut- and liver-draining lymph nodes, mirroring sites of pT_{reg} cell induction (*36*). We speculate that layered hematopoiesis ensures a preponderance of TCs and tolerance to dietary antigens during early life and contributes to the tolerogenic properties of mLNs. The paucity of TC IV in skin-draining lymph nodes may account for the increased

incidence of food allergy when food-associated antigens are encountered via the topical route in patients with altered skin barrier function, most commonly owing to eczematous inflammation (*37*, *38*).

Parallel studies confirmed the role of TCs [variably renamed tolerizing DCs (tolDCs) or RORγt$^+$ DCs] in food-specific pT$_{reg}$ cell differentiation in adulthood (*39*, *40*). Although tolDCs were suggested to represent one subset of tolerogenic APCs, these cells encompassed subsets TC II to TC IV (*40*). We show that among TCs, only the TC IV subset has the capacity to induce food-specific pT$_{reg}$ cells. The discovery that TC IV regulate tolerance to food as well as gut microbiota suggests a broad role for TC IV in intestinal tolerance to harmless foreign antigens. The presence of TCs in humans (*17*, *40*, *41*) suggests potential therapeutic value in targeting antigens to TC IV for promotion of immune tolerance in settings of food allergy and inflammatory diseases.

REFERENCES AND NOTES

1. S. W. Hong *et al.*, *Nature* **607**, 762–768 (2022).
2. T. Sujino *et al.*, *Science* **352**, 1581–1586 (2016).
3. K. S. Kim *et al.*, *Science* **351**, 858–863 (2016).
4. A. Abdel-Gadir *et al.*, *Nat. Med.* **25**, 1164–1174 (2019).
5. M. Xu *et al.*, *Nature* **554**, 373–377 (2018).
6. E. Sefik *et al.*, *Science* **349**, 993–997 (2015).
7. M. C. Campos Canesso *et al.*, *Science* **387**, eado5088 (2025).
8. V. Cerovic, O. Pabst, A. M. I. Mowat, *Nat. Rev. Immunol.* **25**, 42–56 (2025).
9. D. Esterházy *et al.*, *Nat. Immunol.* **17**, 545–555 (2016).
10. F. Ahmadi *et al.*, *J. Exp. Med.* **220**, e20221090 (2023).
11. E. V. Russler-Germain *et al.*, *Immunity* **54**, 2547–2564.e7 (2021).
12. G. Du Toit *et al.*, *N. Engl. J. Med.* **372**, 803–813 (2015).
13. G. Roberts *et al.*, *J. Allergy Clin. Immunol.* **151**, 1329–1336 (2023).
14. M. R. Perkin *et al.*, *N. Engl. J. Med.* **374**, 1733–1743 (2016).
15. H. O. Skjerven *et al.*, *Lancet* **399**, 2398–2411 (2022).
16. S. M. Jones *et al.*, *Lancet* **399**, 359–371 (2022).
17. B. Akagbosu *et al.*, *Nature* **610**, 752–760 (2022).
18. M. Lyu *et al.*, *Nature* **610**, 744–751 (2022).
19. T. Park, C. Leslie, A. Y. Rudensky, C. C. Brown, bioRxiv 2023.11.01.565227 [Preprint] (2023); https://doi.org/10.1101/2023.11.01.565227.
20. R. Kedmi *et al.*, *Nature* **610**, 737–743 (2022).
21. A. Lockhart *et al.*, *J. Exp. Med.* **220**, e20221816 (2023).
22. C. M. Sun *et al.*, *J. Exp. Med.* **204**, 1775–1785 (2007).
23. D. Mucida *et al.*, *Science* **317**, 256–260 (2007).
24. J. Abramson, J. Dobeš, M. Lyu, G. F. Sonnenberg, *Nat. Rev. Immunol.* **24**, 64–77 (2024).
25. K. Nutsch *et al.*, *Cell Rep.* **17**, 206–220 (2016).
26. E. V. Russler-Germain *et al.*, *eLife* **10**, e54792 (2021).
27. R. Tussiwand *et al.*, *Immunity* **42**, 916–928 (2015).
28. T. T. Liu *et al.*, *Nature* **607**, 142–148 (2022).
29. K. L. Lewis *et al.*, *Immunity* **35**, 780–791 (2011).
30. A. T. Satpathy *et al.*, *Nat. Immunol.* **14**, 937–948 (2013).
31. J. K. Krishnaswamy *et al.*, *Sci. Immunol.* **2**, eaam9169 (2017).
32. C. G. Briseño *et al.*, *Proc. Natl. Acad. Sci. U.S.A.* **115**, 10726–10731 (2018).
33. M. Cabeza-Cabrerizo, A. Cardoso, C. M. Minutti, M. Pereira da Costa, C. Reis e Sousa, *Annu. Rev. Immunol.* **39**, 131–166 (2021).
34. B. U. Schraml *et al.*, *Cell* **154**, 843–858 (2013).
35. N. E. Papaioannou *et al.*, *Nat. Commun.* **12**, 464 (2021).
36. J. van der Veeken *et al.*, *Immunity* **55**, 1173–1184.e7 (2022).
37. H. A. Brough *et al.*, *J. Allergy Clin. Immunol.* **135**, 164–170 (2015).
38. G. Lack, D. Fox, K. Northstone, J. Golding; Avon Longitudinal Study of Parents and Children Study Team, *N. Engl. J. Med.* **348**, 977–985 (2003).
39. P. F. Rodrigues *et al.*, *Cell* **188**, 2720–2737.e22 (2025).
40. L. Fu *et al.*, *Nature* **642**, 756–765 (2025).
41. A. Ulezko Antonova *et al.*, *Proc. Natl. Acad. Sci. U.S.A.* **120**, e2318710120 (2023).

ACKNOWLEDGMENTS

We thank the Single Cell Analysis and Innovation Lab (SAIL) at Memorial Sloan Kettering for sample processing, H. Paidassi for provision of *Itgb8*^{tdTomato} mice, S. Josefowicz for OT-II mice, and M. Li for *Irf8*$^{fl/fl}$ mice. We thank M. Canesso and D. Mucida for helpful discussions. We acknowledge the use of the Integrated Genomics Operation Core, funded by the NCI Cancer Center Support Grant (CCSG, P30 CA08748), Cycle for Survival, and the Marie-Josée and Henry R. Kravis Center for Molecular Oncology. **Funding:** This work was supported by a NIH NIAID DP2 award (DP2AI171116) (C.C.B.), NCI Cancer Center Support Grant P30 CA08748, NIH/NHGRI HG012103 (C.L.), the Mathers Foundation, a Parker Institute for Cancer Immunotherapy Senior Fellowship, a Pew Biomedical Scholar Award, a V Foundation Pediatric Scholar Award (C.C.B.), and a Josie Robertson Investigator Award (C.C.B.). V.C. is supported by the St. Baldrick's Foundation and the Kristen Ann Carr Fund. Y.A.P.I. is supported by an HHMI Gilliam Fellowship. G.S. is supported by a Kravis-WiSE Fellowship. **Author contributions:** V.C. and Y.F.P. designed the experiments, analyzed the data, and edited the manuscript. T.P. designed and performed computational analyses. B.A., Z.Z., Y.L., G.S., Y.A.P.I., and L.F. performed the experiments. C.L. supervised computational analyses. C.C.B. conceived of, designed, and supervised the research and wrote the manuscript. All authors read and approved the manuscript. **Competing interests:** The authors declare that they have no competing interests. **Data and materials availability:** All data needed to evaluate the conclusions in the paper are present in the paper or the supplementary materials. The sequencing data are available through the Gene Expression Omnibus under accession GSE294005.
License information: Copyright © 2025 the authors, some rights reserved; exclusive licensee American Association for the Advancement of Science. No claim to original US government works. https://www.science.org/about/science-licenses-journal-article-reuse

SUPPLEMENTARY MATERIALS

science.org/doi/10.1126/science.adp0535
Materials and Methods; Figs. S1 to S11; References (*42*–*52*); MDAR Reproducibility Checklist; Data S1 and S2

Submitted 9 March 2024; resubmitted 22 January 2025; accepted 30 April 2025; published online 15 May 2025

10.1126/science.adp0535

ORGANIC CHEMISTRY

Skeletal editing of pyrrolidines by nitrogen-atom insertion

Jinghao Li[1], Pengcheng Tang[1], Yang Fan[1], Hongjian Lu[1,2]*

Given the prevalence of nitrogen-containing heterocycles in bioactive molecules, inserting a nitrogen atom into a saturated ring offers a powerful yet underdeveloped scaffold-hopping strategy for expanding drug-like chemical space. In this study, we present a skeletal editing method that directly inserts a nitrogen atom into pyrrolidine rings, converting them into tetrahydropyridazine scaffolds under mild, operationally simple conditions with readily available *O*-diphenylphosphinyl hydroxylamine. This method features broad substrate scope and functional group compatibility, enabling late-stage editing of complex molecules. Furthermore, simple redox manipulation of the tetrahydropyridazines grants access to saturated piperidazines and aromatic pyridazines—nitrogen-rich scaffolds that are highly valued in medicinal chemistry but typically difficult to synthesize. Overall, this work establishes a versatile platform for nitrogen-based skeletal editing of saturated pyrrolidines, expanding the synthetic toolkit for medicinal chemistry.

Single-atom skeletal editing has gained momentum as a transformative approach for restructuring molecular frameworks—especially cyclic scaffolds—without relying on de novo synthesis (*1*–*11*). By enabling atom-level modifications of existing structures, this strategy streamlines retrosynthetic analysis, reduces synthetic burden, and grants access to previously unattainable chemical space from known compound libraries. These capabilities are particularly valuable for late-stage functionalization, offering a powerful route to accelerate the discovery and optimization of bioactive molecules (*12*, *13*).

Nitrogen-containing heterocycles (*N*-heterocycles) are among the most privileged and versatile scaffolds in medicinal chemistry, serving as critical elements for tuning molecular recognition, pharmacokinetics, and physicochemical profiles. Between 1938 and 2013, 59% of Food and Drug Administration (FDA)–approved small molecule drugs incorporated at least one *N*-heterocycle (*14*); from 2013 to 2023, this figure rose to 82%, with more than half of new drugs containing multiple nitrogenous rings (Fig. 1A) (*15*). Among the most frequently encountered frameworks are six-membered pyridine and piperidine, five-membered pyrrolidine, and diazacyclic piperazine and pyrimidine. Given their prevalence and structural diversity, the development of strategies for directly editing *N*-heterocycles is of both fundamental importance and practical relevance. In this context, atom-level skeletal editing of *N*-heterocycles offers a compelling route to construct new *N*-heterocyclic architectures (*16*–*25*). Such an approach is particularly attractive if less naturally abundant yet pharmaceutically interesting scaffolds could be rapidly accessed.

Among single-atom skeletal editing strategies, nitrogen-atom (N-atom) insertion has emerged as a particularly powerful tool (*26*, *27*), owing to the profound impact of nitrogen functionality on molecular stability, polarity, and biological activity (*28*). Recent efforts have demonstrated the feasibility of N-atom insertion into *N*-heteroaromatic systems (*29*–*33*): The Morandi (*29*), Ackermann (*30*), and Sharma (*31*) groups have independently harnessed nitrene intermediates for late-stage indole-to-quinoline conversions, and the Ghiazza (*32*) and Zheng (*33*) groups have developed photocatalytic strategies for pyridine-to-diazepine editing through aminopyridinium salts (Fig. 1B). These advances highlight how exogenous nitrogen donors can engage π systems to form transient three-membered intermediates that rearrange into new frameworks. Despite these breakthroughs, analogous transformations in saturated *N*-heterocycles remain conspicuously underdeveloped. This gap is striking given the central role of pyrrolidines and piperidines, the growing prominence of nitrogen-rich motifs such as piperazines and pyrimidines in modern drug discovery (Fig. 1A) (*14*, *15*), and the improved clinical outcomes often associated with the higher sp^3 character and increased three-dimensionality of saturated *N*-heterocycles (*34*). Although methods for N-atom deletion (*35*–*39*) and migration (*40*, *41*) in saturated rings have been reported, direct N-atom insertion into saturated azacycles to form diazacycles remains a formidable challenge. The lack of conjugated π systems precludes π-bond activation pathways (*16*–*25*, *29*–*33*), and selective cleavage and reformation of C–N or C–C σ bonds demand exceptional control over reactivity and selectivity (*42*, *43*).

Here, we report an N-atom α-insertion strategy that converts azacyclic pyrrolidines into diazacyclic tetrahydropyridazines, using commercially available *O*-diphenylphosphinyl hydroxylamine (DPPH) (*44*) (Fig. 1C). This operationally simple transformation proceeds under mild conditions and exhibits broad functional group compatibility. The resulting tetrahydropyridazines, featuring both a nucleophilic amine (NH) group and a reactive C=N bond, can be selectively reduced to saturated piperidazines or oxidized to aromatic pyridazines, providing access to versatile diazacyclohexanes across multiple redox states. Although structurally related to well-established pharmacophores such as piperazines and pyrimidines, tetrahydropyridazines and their redox congeners remain underexplored because of synthetic inaccessibility and concerns regarding the potential genotoxicity of hydrazine motifs. Nevertheless, recent advances—including the discovery of daraxonrasib, an orally active noncovalent rat sarcoma virus (RAS) (ON) inhibitor, and lydiamycin A, a natural product antibiotic, both containing hydrazine motifs, as well as drugs such as ensartinib and relugolix, which feature aromatic pyridazine scaffolds—underscore the emerging medicinal relevance of these frameworks (Fig. 1D). This strategy thus provides a concise and generalizable platform for diazacycle construction, enabling scaffold diversification and late-stage skeletal editing of drug-like molecules.

Development of N-atom insertion

To enable the skeletal transformation of pyrrolidines into diazacyclohexane motifs, we sought a suitable electrophilic nitrogen donor capable of effecting direct N-atom insertion. We selected *O*-diphenylphosphinyl hydroxylamine (DPPH) and its analogs for evaluation. Although we previously used DPPH for N-atom deletion (*39*), this reagent has been more broadly applied as an electrophilic amination reagent in synthetic chemistry (*45*). Notably, Liu and co-workers recently demonstrated its use as an N-atom source for interception of what would be Suzuki-Miyaura coupling products, thereby forming C–N–C bonds in place of C–C bonds (*46*). We selected *cis*-hexahydroisoindole hydrochloride (**1a**) as a model substrate and subjected it to reaction with DPPH under basic aqueous conditions [K_2CO_3 in tetrahydofuran (THF)/H_2O, 65°C, 12 hours; Condition I; Fig. 2A]. The desired 1,2-diazacyclic product (**1b**) was obtained in 68% yield on the basis of nuclear magnetic resonance (NMR) integration (Fig. 2A, entry 1; see table S1 for optimization details). By contrast, alternative hydroxylamine-based electrophilic nitrogen donors—such as *O*-tosylhydroxylamine and hydroxylamine-*O*-sulfonic acid—led to little or no formation of **1b** (13 and 0% yield, respectively; Fig. 2A, entries 2 to 3). Replacing K_2CO_3 with a stronger base (KOH) decreased the yield to 27% (Fig. 2A, entry 4), indicating the sensitivity of the transformation to base strength. We next explored the reaction by using proline derivative **2a** as a

[1]State Key Laboratory of Coordination Chemistry, School of Chemistry and Chemical Engineering, Nanjing University, Nanjing, Jiangsu, China. [2]School of Chemistry and Chemical Engineering, Guizhou University, Guiyang, Guizhou, China. *Corresponding author. Email: hongjianlu@nju.edu.cn

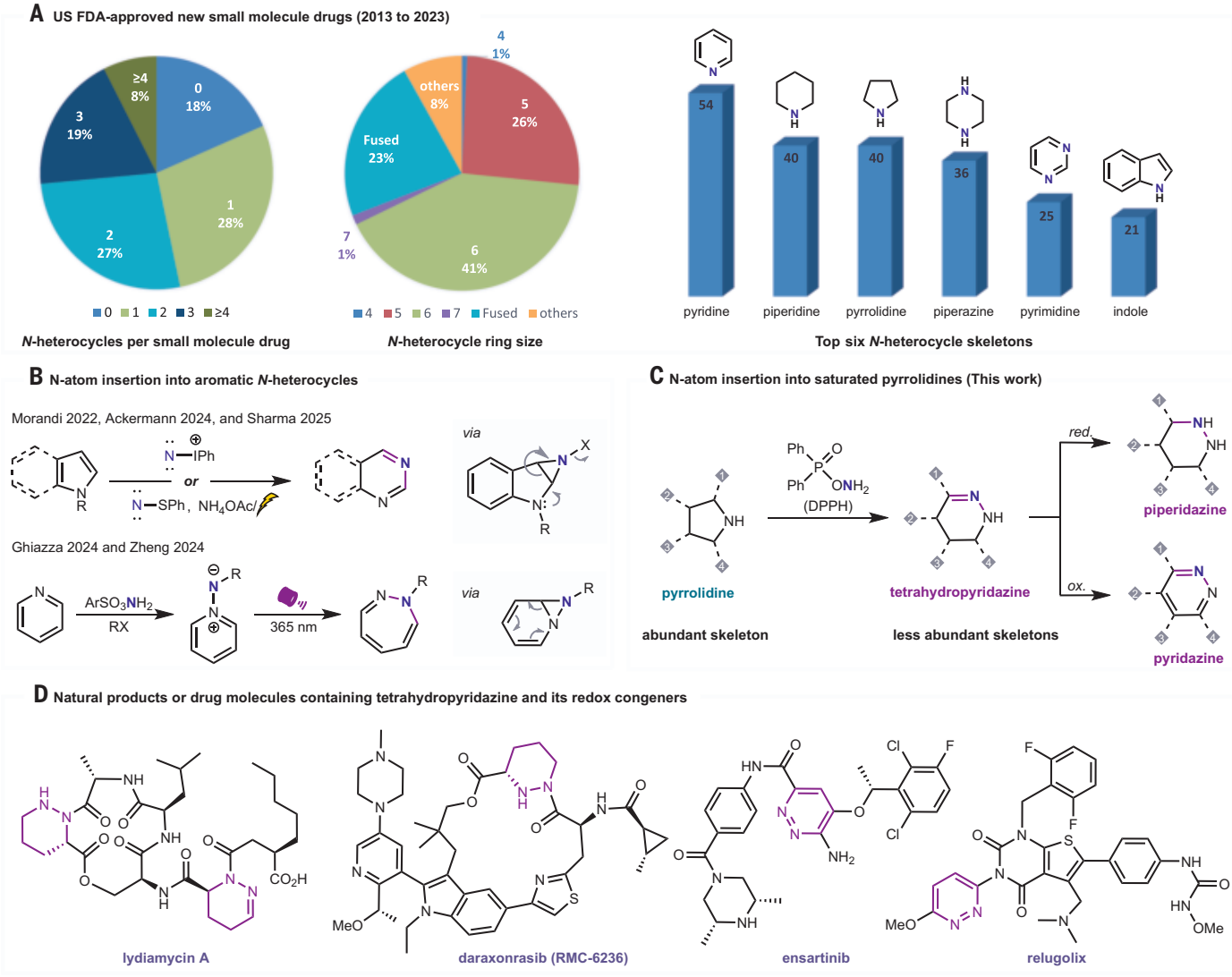

Fig. 1. N-atom insertion strategies in *N*-heterocycles. (**A**) US FDA-approved new small molecule drugs (2013 to 2023). (**B**) N-atom insertion into aromatic *N*-heterocycles (from *29*–*33*). (**C**) N-atom insertion into saturated pyrrolidines. (**D**) Natural products or drug molecules containing tetrahydropyridazine and its redox congeners.

substrate. Under the Condition II (1.0 equiv of NaOAc, DCM/MeOH, 45°C, 12 hours; Fig. 2A), the reaction proceeded smoothly to afford the N-inserted product (**2b**) in 50% NMR yield (Fig. 2A, entry 6; see table S2 for optimization details). Omitting the base resulted in only trace product formation (Fig. 2A, entry 7), whereas the use of pyridine completely suppressed the reaction (Fig. 2A, entry 8). A stronger base, such as NaOMe, modestly improved the yield to 37%, which was still inferior to that obtained under optimized conditions. Cross-conditions—applying Condition I to **2a** or Condition II to **1a**—were largely ineffective, leading to poor or negligible yields (Fig. 2A, entries 5 and 10), indicating the substrate-specific nature of the optimized conditions.

To gain insight into the mechanism of this transformation, a series of mechanistic experiments were conducted (Fig. 2B). High-resolution mass spectrometry analysis of a low-temperature, short-time reaction of **1a** revealed a triazenium intermediate (**1a'**) (Fig. 2B, Eq. 1). A hydrazine substrate (**3a'**) also furnished the N-atom insertion product (**3b**) in 72% yield (Fig. 2B, Eq. 2), suggesting that both hydrazine and triazenium species participate as intermediates. Analysis of the crude mixture from the reaction of **1a** revealed a small amount of tetrazene byproduct (**1d**) (Fig. 2B, Eq. 3). When the base was changed from K_2CO_3 to the stronger base KOH, the yield of **1d** increased to 45% (Fig. 2B, Eq. 4). This observation suggests the formation of an isodiazene (1,1-diazene) intermediate, the fate of which is strongly influenced by the pH of the reaction medium—either inducing N-atom insertion or formation of the tetrazene byproduct. The formation of an isodiazene intermediate is proposed in Step 1 of Fig. 2C. The sequential reactions of pyrrolidine **a** with two equivalents of DPPH generates a triazenium species, which spontaneously rearranges to form intermediate isodiazene (**A**) (*39*). Then, **A** may proceed via one of two mechanistic pathways, as shown in Step 2 of Fig. 2C (*47*). In Path I, **A** undergoes a 1,2-σ migration to afford diazene intermediate **B**, followed by a 1,3-hydrogen shift to deliver the N-atom inserted products (**b** and **b'**). Because the two nitrogen atoms in **B** are equivalent, the exogenous nitrogen could be incorporated into either the C=N (**b**) or C–N (**b'**) bond of the products. To probe this possibility, a reaction using ^{15}N-labeled DPPH was performed with **1a** (Fig. 2D, Eq. 5). The resulting product analysis revealed exclusive incorporation of the ^{15}N-atom label into the C=N bond (**^{15}N-1b**), with no detectable formation of the isomeric product bearing ^{15}N in the C–N bond (**^{15}N-1b'**), as confirmed by NMR analysis (details provided in supplementary materials). This result rules out Path I and the intermediacy of diazene (**B**). Alternatively, in Path II, **A** undergoes a 1,3-hydrogen shift to generate the

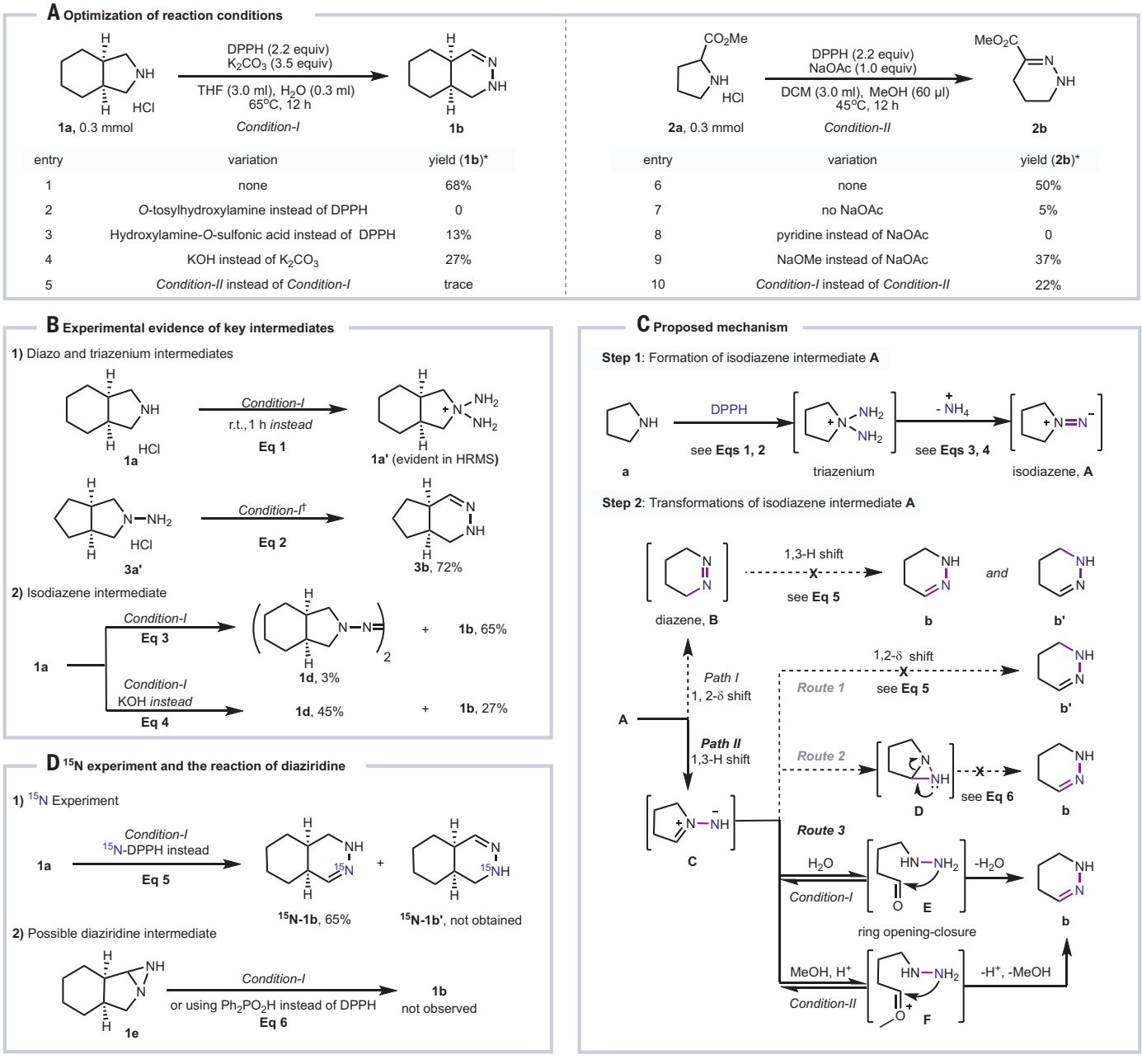

Fig. 2. Optimization of reaction conditions and mechanistic studies. (**A**) Optimization of reaction conditions. (**B**) Experimental evidence of key intermediates. (**C**) Proposed mechanism. (**D**) ^{15}N experiment and the reaction of diaziridine. *Crude NMR yield with CH_2Br_2 as internal standard. †THF (0.3 ml) instead of THF (3.0 ml). THF, tetrahydrofuran; DCM, dichloromethane; r.t., room temperature; HRMS, high-resolution mass spectrometry.

1,3-dipolar intermediate **C**, which could follow one of three possible routes. In Route 1, **C** undergoes direct 1,2-σ migration to form **b'**, which would place the exogenous nitrogen in the C–N bond—contradicting the ^{15}N-labeling results (Fig. 2D, Eq. 5)—thus excluding this pathway. In Route 2, **C** undergoes intramolecular cyclization to form a diaziridine intermediate (**D**), which may rearrange to the final product (**b**). To evaluate this possibility, we synthesized diaziridine (**1e**) and subjected it to standard conditions (Fig. 2D, Eq. 6), in the presence and absence of diphenyl phosphate (a major byproduct of the standard reaction). In both cases, no N-atom insertion product (**1b**) was observed, ruling out Route 2. Thus, the most plausible mechanism is Route 3, in which **C** undergoes ring opening to generate a hydrazine-aldehyde species (**E**) (Condition I) or hydrazine-oxonium species (**F**) (Condition II), which rapidly cyclizes to form the N-atom insertion product (**b**). This mechanism not only accounts for the observed intermediates but is also fully consistent with the exclusive incorporation of the DPPH-derived nitrogen atom into the C=N bond, as demonstrated by the ^{15}N-labeling experiment.

Reaction scope and applications

We explored the substrate scope by first evaluating the N-atom insertion reaction of simple pyrrolidine (**4a**) under a slightly modified version of Condition I [Standard Condition-A (***S.C.-A***), Fig. 3]. The resulting tetrahydropyridazine exhibited high polarity and water solubility, rendering purification challenging. To circumvent this issue, the crude product was subjected to benzoyl (Bz) protection, enabling the isolation of

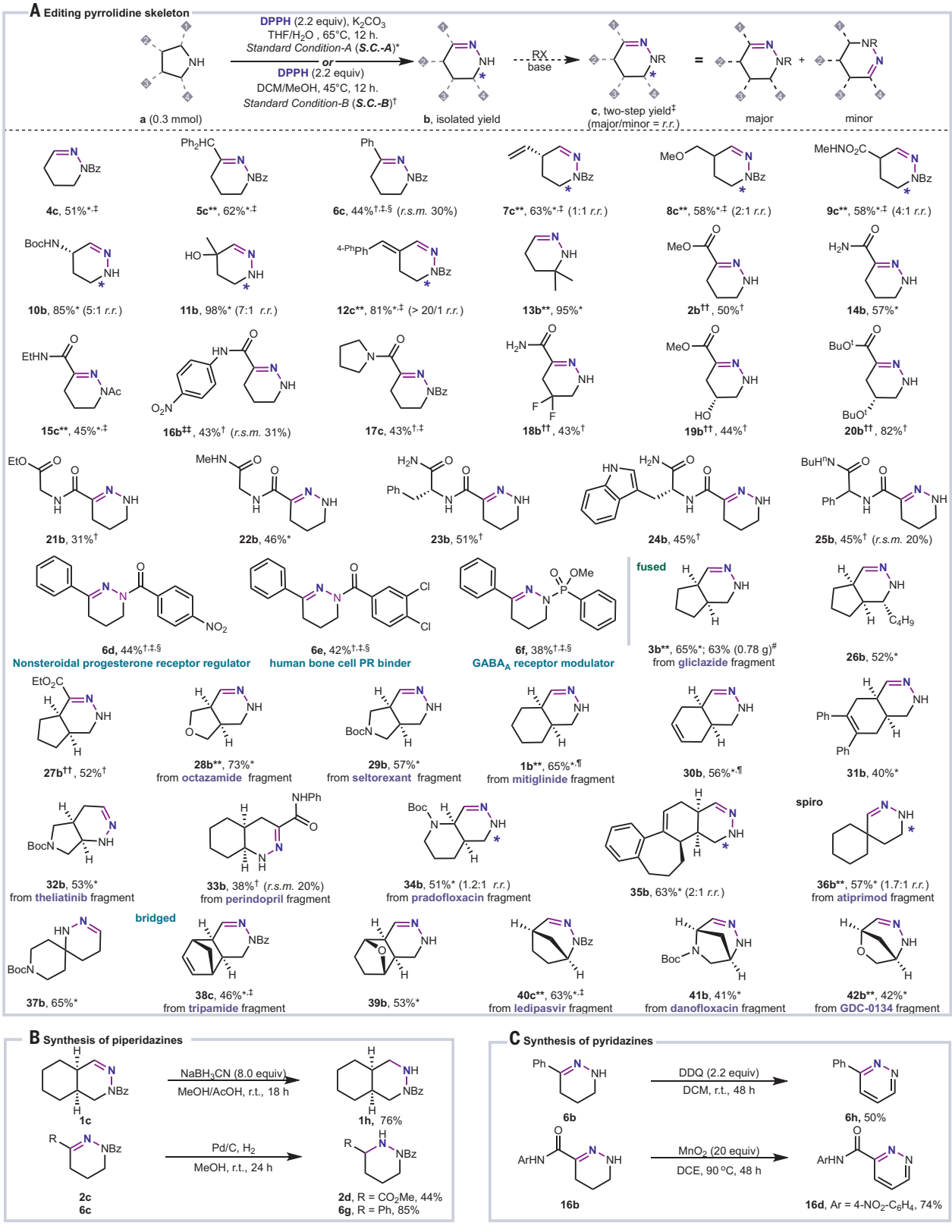

Fig. 3. Editing pyrrolidine skeleton and transformations of tetrahydropyridazines. (**A**) Editing pyrrolidine skeleton. (**B**) Synthesis of piperidazines. (**C**) Synthesis of pyridazines. *Standard Condition-A: amine (0.3 mmol), DPPH (2.2 equiv), K_2CO_3 (3.0 equiv), THF (0.3 ml), H_2O (0.3 ml), 65°C, 12 hours, isolated yield. †Standard Condition-B: amine (0.3 mmol), DPPH (2.2 equiv), DCM (3.0 ml), MeOH (60 μl), 45°C, 12 hours, isolated yield. ‡Two-step yield of N-atom insertion and acyl protection. §Pyridine (1.0 equiv). ¶THF (3.0 ml) instead of THF (0.3 ml). #Gram-scale reaction. **Amine•HCl/K_2CO_3 (3.5 equiv) instead of amine/K_2CO_3(3.0 equiv). ††Amine•HCl instead of amine; NaOAc (1.0 equiv). ‡‡Proline•TFA instead of proline; NaOAc (1.0 equiv). *r.r.* (regioselective ratio) based on isolated products. *r.s.m.*, residual starting material. All substrates are commercially available except compounds **12a**, **24a**, **25a**, **26a**, **31a**, **33a**, and **35a**. Structures of drug molecules mentioned are provided in fig. S1. r.t., room temperature.

protected tetrahydropyridazine (**4c**) in 51% overall yield over two steps. For α-substituted pyrrolidines bearing diphenylmethyl or phenyl groups, the corresponding insertion products (**5c** and **6c**) were isolated in good yields. By contrast, β-substituted pyrrolidines posed regioselectivity challenges owing to the spatial separation between the β-substituent and the reactive site, typically yielding mixtures of regioisomers. For substrates bearing vinyl or methoxymethyl groups at the β-position, regioisomeric ratios (*r.r.*s) of 1:1 and 2:1, respectively, were observed (**7c** and **8c**). When electron-withdrawing groups such as amide (**9c**), Boc-protected amino (**10b**), or hydroxyl (**11b**) were introduced, regioselectivity improved markedly (up to 7:1 *r.r.*), favoring insertion at the more electron-deficient C–N bond. These observations are consistent with a reaction pathway involving a 1,3-hydrogen shift intermediate. In the presence of a vinyl group at the β-position, selective cleavage of the weaker allylic C–N bond afforded a conjugated diene product (**12c**) in high yield. Furthermore, the method proved highly efficient for sterically hindered substrates: Pyrrolidines bearing tertiary α-substituents reacted smoothly to afford the corresponding diazacycles, as exemplified by **13b**, obtained in 95% yield. Proline-derived compounds—representing a privileged class of pyrrolidine-based scaffolds—also proved to be excellent substrates. Both proline esters and their derivatives underwent N-atom insertion to generate piperazic acid analogs (**2b**, **14b** to **16b**, and **17c**) in moderate yields. Application of our N-insertion protocol to difluoro-substituted proline and hydroxylated proline provided direct access to tetrahydropiperazine frameworks amenable to further derivatization (**18b** to **20b**). The method also demonstrated broad functional group compatibility with respect to dipeptides containing proline residues with a variety of amino acid partners, furnishing N-inserted products (**21b** to **25b**) in synthetically useful yields. Notably, even structurally simple analogs—such as *N*-acylated-2-phenyl tetrahydropyridazines (**6d** to **6f**), readily accessed from 2-phenylpyrrolidines—have demonstrated promising biological activity (*48*), further underscoring the potential of this scaffold in medicinal chemistry.

Beyond monocyclic systems, polycyclic pyrrolidine scaffolds—including fused, spirocyclic, and bridged architectures—are prevalent in natural products and pharmaceuticals. Many of these structurally complex pyrrolidines are commercially available and serve as valuable building blocks in drug discovery, as exemplified by substrates **1a**, **3a**, **28a**, **29a**, **32a** to **34a**, **36a**, **38a**, and **40a** to **42a** in Fig. 3. Given their structural rigidity and three-dimensional complexity, direct skeletal editing of polycyclic frameworks provides a highly efficient strategy for accessing novel chemical space, offering considerable advantages in step economy and synthetic tractability. For example, 3-azabicyclo[3.3.0]octane, a bicyclic structure formed by fusion of a pyrrolidine and a five-membered carbocycle, serves as a core motif in the antidiabetic drug gliclazide. Using this scaffold and its derivatives, our method delivered N-atom inserted products (**3b**, **26b**, and **27b**), all bearing a 3,4-diazabicyclo[4.3.0]nonene core. Regioselectivity was dictated by electronic and steric effects: Alkyl substitution favored insertion at the less-hindered site (**26b**), whereas electron-withdrawing esters directed insertion into the more electron-deficient C–N bond (**27b**), demonstrating precise control over site selectivity. The transformation was further extended to heteroatom-rich fused systems such as 7-oxa-3-azabicyclo[3.3.0]octane (**28a**) and 3,7-azabicyclo[3.3.0]octane (**29a**), which underwent smooth nitrogen-atom insertion. Six-membered fused systems—both saturated and unsaturated—were also compatible, affording products such as **1b**, **30b**, and **31b** in moderate yields. In scaffolds fused at the α,β-position of pyrrolidine, including 2,7-azabicyclo[3.3.0]octane (**32a**) and 2-azabicyclo[3.3.0]octane (**33a**), the reaction proceeded with high regioselectivity. In a complex system where the fused ring contains a nitrogen atom positioned distal to the reaction center (**34b**), regioselectivity was diminished. Tetracyclic framework **35a**, incorporating pyrrolidine core, also proved amenable to skeletal editing, delivering new polycyclic architecture **35b** through efficient N-atom insertion. Likewise, spirocyclic pyrrolidines (**36a** and **37a**) underwent smooth conversion to nitrogen-enriched spiro products (**36b** and **37b**). Bridged pyrrolidines represent a particularly challenging class of substrates as a result of inherent ring strain and the difficulty of cleaving conformationally constrained C–N bonds. Notably, a variety of commercially available bridged systems (**38a** to **42a**) successfully underwent N-atom insertion. Even in the presence of additional heteroatoms (**39a**, **41a**, and **42a**), the transformation proceeded efficiently, underscoring the robustness of the method. The gram-scale reaction of **3a** proceeded smoothly under standard conditions, delivering the desired product (**3b**) in 63% yield, comparable to the 65% yield obtained on the milligram scale, thereby highlighting the practicality of the method. ***S.C.-B*** is particularly suitable for proline-derived substrates, whereas ***S.C.-A*** is generally preferred for other pyrrolidines, including monocyclic, fused, spirocyclic, and bridged scaffolds. Collectively, these results demonstrate the exceptional versatility of this N-atom insertion strategy. Most substrates examined—whether monocyclic, fused, spirocyclic, or bridged—are readily available pharmaceutical fragments. The resulting products unlock previously inaccessible structural motifs and offer a powerful platform for the development of next-generation bioactive compounds.

To highlight the synthetic utility of this transformation, we investigated downstream derivatizations of the tetrahydropyridazine products into structurally privileged heterocycles (Fig. 3, B and C). Reduction of tetrahydropyridazines furnishes fully saturated piperidazines—a class of 1,2-diazacycles that, despite their structural relevance, remain largely underexplored in medicinal chemistry compared with their 1,4-diazacyclic counterpart, piperazine. Both $NaBH_3CN$-mediated reduction and Pd-catalyzed hydrogenation proceeded efficiently, affording piperidazines (**1h** and **6g**) and piperazine acid derivative (**2d**) (Fig. 3B). In parallel, oxidative aromatization of tetrahydropyridazines may offer direct access to pyridazines, electron-deficient aromatic heterocycles with emerging importance in drug discovery (*49*). Marketed drugs featuring pyridazine cores, such as ensartinib and relugolix (Fig. 1D), underscore their therapeutic potential. However, synthetic challenges have limited their representation in commercial libraries and pharmaceutical pipelines (*14*, *15*). To address this issue, we used mild oxidants such as DDQ or MnO_2 to achieve pyridazine derivatives (**6h** and **16d**) under operationally simple conditions (Fig. 3C). These results provide a modular and operationally simple route to access diverse diazacyclic frameworks.

To further highlight the versatility of this N-atom insertion strategy, we applied it to the direct skeletal editing of complex natural products and drug-like molecules (Fig. 4A). Representative substrates included (±)-nornicotine (**43a**), a major metabolite of nicotine bearing a pyridine ring; simpinicline (**44a**), a nicotinic acetylcholine receptor agonist featuring both pyrimidine and alkene moieties; the endogenous tripeptide MIF-1 (melanostatin, **45a**), an allosteric modulator of dopamine receptors; and a key fragment of seltorexant (**46a**). Each underwent smooth N-atom insertion to afford the corresponding tetrahydrodiazine derivatives in good yields (**43b** to **46b**). Further oxidative aromatization of a peptide-derived compound (**45b**) using MnO_2 yielded a pyridazine-containing dipeptide (**45d**), showcasing the method's utility for constructing nitrogen-rich heteroarenes in peptide settings. In addition, tetrahydroisoquinoline scaffold—common in natural products—is compatible with the transformation (*50*). Application to tetrahydropapaverine (**47a**) resulted in a seven-membered diazacycle (**47b**), demonstrating that the strategy can accommodate diverse ring systems (Fig. 4B). To explore the method's adaptability to more elaborate architectures, we synthesized hybrid molecules by conjugating fragments of natural products and drugs (Fig. 4C). Successful examples included seltorexant-lithocholic acid (**48a**), danofloxacin-indomethacin (**49a**), fosinopril-alogliptin (**50a**), and gliclazide-fluvoxamine (**51a**) hybrids, all of which underwent N-atom insertion smoothly (**48b** to **51b**). The incorporation of stable isotopes into organic

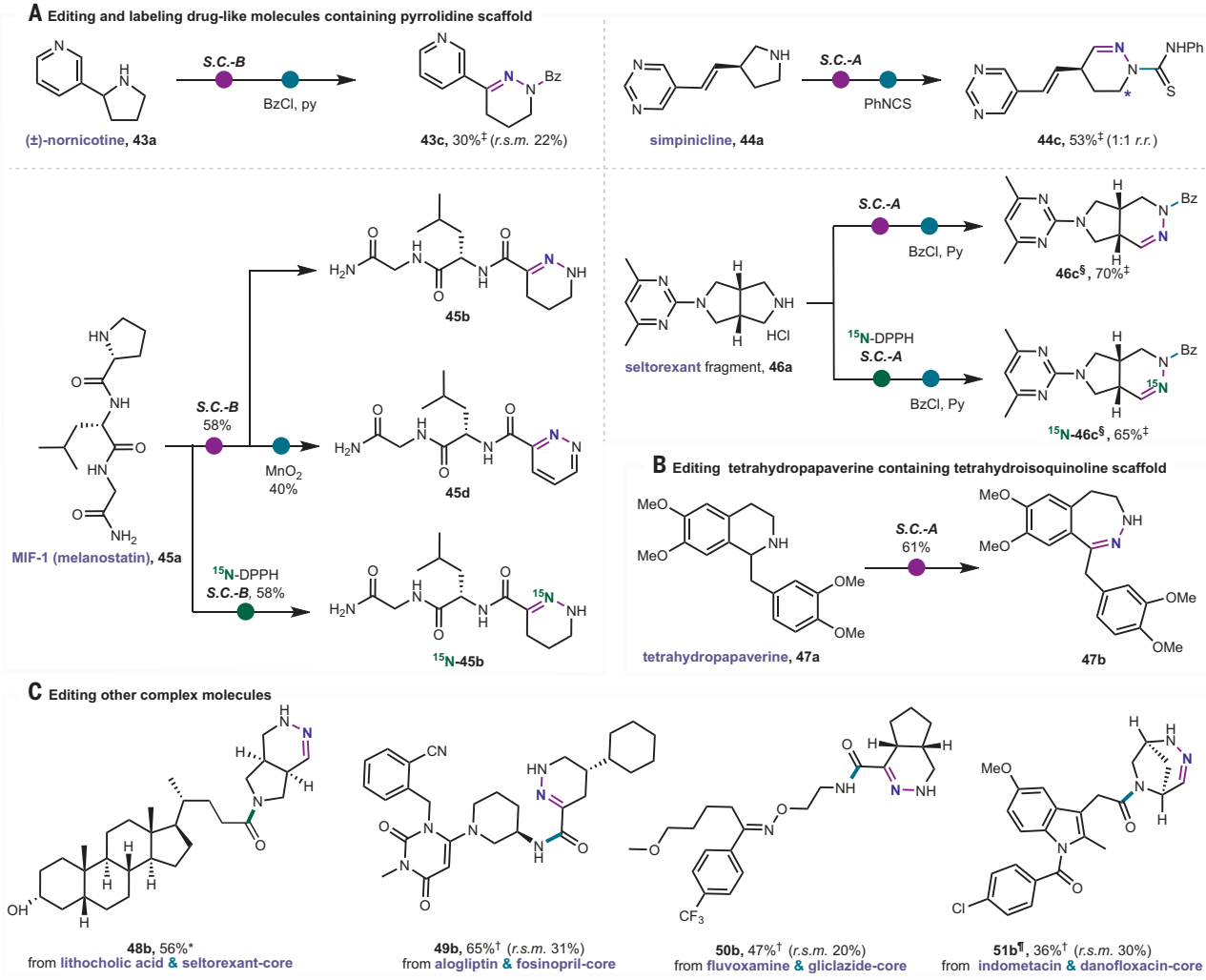

Fig. 4. Editing and labeling bioactive compounds. (**A**) Editing and labeling drug-like molecules containing pyrrolidine scaffold. (**B**) Editing tetrahydropapaverine containing tetrahydroisoquinoline scaffold. (**C**) Editing other complex molecules. *Standard Condition-A (***S.C.-A***): amine (0.3 mmol), DPPH (2.2 equiv), K_2CO_3 (3.0 equiv), THF (0.3 ml), H_2O (0.3 ml), 65°C, 12 hours, isolated yield. †Standard Condition-B (***S.C.-B***): amine (0.3 mmol), DPPH (2.2 equiv), DCM (3.0 ml), MeOH (60 μl), 45°C, 12 hours, isolated yield. ‡Two-step yield of N-atom insertion and acyl protection. §Amine•HCl/K_2CO_3(3.5 equiv) instead of amine/K_2CO_3(3.0 equiv). ¶Amine•HCl instead of amine; NaOAc (1.0 equiv). *r.r.* (regioselective ratio) based on isolated products. *r.s.m.*, residual starting material.

frameworks is vital across scientific disciplines, particularly in pharmaceutical and agrochemical research. Despite substantial progress, efficient methods for late-stage isotopic labeling remain in high demand. As shown in the supplementary materials, ^{15}N-labeled DPPH was synthesized from commercially available diphenylphosphinic chloride and $^{15}NH_2OH$. Leveraging ^{15}N-DPPH as an N-atom insertion reagent, we accessed ^{15}N-labeled analogs of MIF-1 (**^{15}N-45b**) and a key seltorexant fragment (**^{15}N-46c**) (Fig. 4A), highlighting the broad utility of this approach for synthesizing ^{15}N-labeled bioactive compounds. These results underscore the method's broad functional group compatibility—including hydroxyl, amide, ester, alkene, and heteroaromatic motifs—establishing it as a powerful platform for late-stage skeletal editing of structurally complex, bioactive molecules and for the synthesis of ^{15}N-labeled drug-like compounds.

Substrate scope evaluation reveals that our current method is limited to unsubstituted pyrrolidine scaffolds (Figs. 3 and 4). However, in many bioactive molecules containing a pyrrolidine motif, the nitrogen in pyrrolidine is substituted with a side chain. Given the accessibility of C–N bond formation, pharmaceutical syntheses often rely on coupling side-chain synthons with the unsubstituted pyrrolidine core. To overcome the limitation of this method in the editing of substituted pyrrolidines, we converted the unsubstituted pyrrolidine cores into tetrahydropyrazine-based synthons. These intermediates retain a nucleophilic NH group, enabling subsequent coupling with side-chain synthons to access N-atom inserted drug analogs (Fig. 5). For example, in the synthesis of the analgesic octazamide, a key step involves direct acylation of commercially available 7-oxa-3-azabicyclo[3.3.0]octane (**28a**) (Fig. 5A). N-Atom insertion into synthon **28a**, followed by benzoylation, delivered an N-atom expanded analog of octazamide (**28c**). A similar approach was used to modify the antidiabetic drug mitiglinide (Fig. 5B). Notably, N-atom insertion disrupts the molecular symmetry of the starting material (**1a**), and the presence of a stereogenic center in the side chain introduces challenges in both diastereo- and regioselectivity. Nevertheless, we successfully isolated the major diastereomer—an enantiomerically enriched mitiglinide analog (**1j**)—in acceptable yield using column chromatography. The synthesis of gliclazide was achieved through N-nitrosation followed by reduction of commercially available bicyclic pyrrolidine (**3a**), furnishing a hydrazine intermediate that reacted with a urea derivative (Fig. 5C). Alternatively, direct N-atom insertion into synthon **3a**, followed by side-chain installation

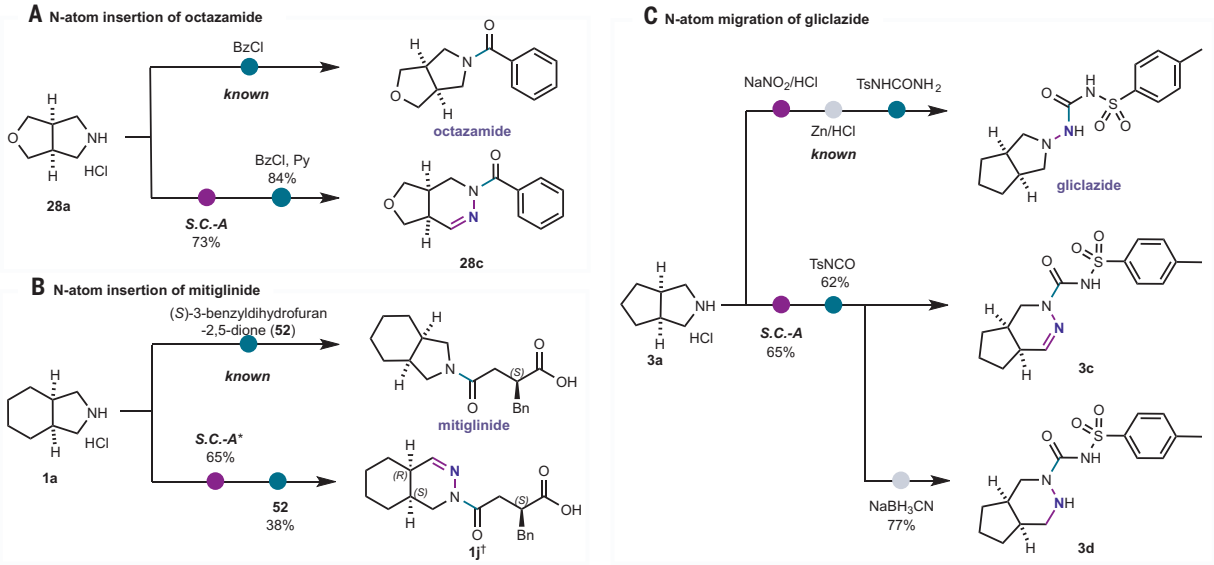

Fig. 5. Indirect editing bioactive compounds. (**A**) N-atom insertion of octazamide. (**B**) N-atom insertion of mitiglinide. (**C**) N-atom migration of gliclazide. Standard Condition-A (***S.C.-A***): amine•HCl (0.3 mmol), DPPH (2.2 equiv), K_2CO_3 (3.5 equiv), THF (0.3 ml), H_2O (0.3 ml), 65°C, 12 hours. *Using THF (3.0 ml) instead of THF (0.3 ml). †The absolute configuration was assessed with the DP4+ probabilistic tool (details provided in supplementary materials).

with *p*-toluenesulfonyl isocyanate (TsNCO), yielded N-atom–rearranged gliclazide analogs (**3c**) bearing a tetrahydropyrazine core. Incorporation of a reduction step furnished a hexahydropyrazine derivative (**3d**), representing an N-atom migrated isomer of gliclazide. This N-atom insertion platform enables access to structurally diverse drug analogs without altering the overall synthetic route, offering a powerful strategy for drug discovery and structure-activity relationship exploration.

By enabling atom-level skeletal remodeling without perturbing substitution patterns, the late-stage skeletal editing method presented here offers a powerful platform for scaffold hopping and the diversification of drug-like molecules.

REFERENCES AND NOTES

1. D. C. Blakemore *et al.*, *Nat. Chem.* **10**, 383–394 (2018).
2. K. R. Campos *et al.*, *Science* **363**, eaat0805 (2019).
3. J. Jurczyk *et al.*, *Nat. Synth.* **1**, 352–364 (2022).
4. M. Peplow, *Nature* **618**, 21–24 (2023).
5. B. W. Joynson, L. T. Ball, *Helv. Chim. Acta* **106**, e202200182 (2023).
6. Z. Liu, X. Zhang, P. Sivaguru, X. Bi, *Acc. Chem. Res.* **58**, 130–149 (2025).
7. F.-P. Wu, J. L. Tyler, F. Glorius, *Acc. Chem. Res.* **58**, 893–906 (2025).
8. P. Xu, A. Studer, *Acc. Chem. Res.* **58**, 647–658 (2025).
9. B. Huang, H. Lu, *Acc. Chem. Res.* **58**, 919–932 (2025).
10. H. Fujimoto, M. Tobisu, *Acc. Chem. Res.* **58**, 1168–1180 (2025).
11. H. Lu, J. Chang, H. Wei, *Acc. Chem. Res.* **58**, 933–946 (2025).
12. E.-Q. Li, C. W. Lindsley, J. Chang, B. Yu, *J. Med. Chem.* **67**, 13509–13511 (2024).
13. G. L. Bartholomew *et al.*, *J. Med. Chem.* **68**, 6027–6040 (2025).
14. E. Vitaku, D. T. Smith, J. T. Njardarson, *J. Med. Chem.* **57**, 10257–10274 (2014).
15. C. M. Marshall, J. G. Federice, C. N. Bell, P. B. Cox, J. T. Njardarson, *J. Med. Chem.* **67**, 11622–11655 (2024).
16. J. Woo *et al.*, *Science* **376**, 527–532 (2022).
17. S. C. Patel, N. Z. Burns, *J. Am. Chem. Soc.* **144**, 17797–17802 (2022).
18. J. Woo, C. Stein, A. H. Christian, M. D. Levin, *Nature* **623**, 77–82 (2023).
19. H. Li *et al.*, *J. Am. Chem. Soc.* **145**, 17570–17576 (2023).
20. T. J. Pearson *et al.*, *Science* **381**, 1474–1479 (2023).
21. G. L. Bartholomew *et al.*, *J. Am. Chem. Soc.* **146**, 2950–2958 (2024).
22. A. Conboy, M. F. Greaney, *Chem* **10**, 1940–1949 (2024).
23. A.-S. K. Paschke *et al.*, ChemRxiv [Preprint] (2024). https://doi.org/10.26434/chemrxiv-2024-prwm8.
24. Z. Wang, P. Xu, S. Guo, C. G. Daniliuc, A. Studer, ChemRxiv [Preprint] (2024). https://doi.org/10.26434/chemrxiv-2024-vtg73.
25. D. Kim *et al.*, *Science* **386**, 99–105 (2024).
26. X. Li, J. Xu, Z.-G. Xu, *Org. Chem. Front.* **11**, 4041–4053 (2024).
27. A. Gupta, P. Bhatti, J. K. Laha, S. Manna, *Chemistry* **30**, e202401993 (2024).
28. L. D. Pennington, D. T. Moustakas, *J. Med. Chem.* **60**, 3552–3579 (2017).
29. J. C. Reisenbauer, O. Green, A. Franchino, P. Finkelstein, B. Morandi, *Science* **377**, 1104–1109 (2022).
30. B.-S. Zhang *et al.*, *Angew. Chem. Int. Ed.* **63**, e202407384 (2024).
31. B. Ghosh *et al.*, *Science* **387**, 102–107 (2025).
32. E. Boudry, F. Bourdreux, J. Marrot, X. Moreau, C. Ghiazza, *J. Am. Chem. Soc.* **146**, 2845–2854 (2024).
33. J. Luo, Q. Zhou, Z. Xu, K. N. Houk, K. Zheng, *J. Am. Chem. Soc.* **146**, 21389–21400 (2024).
34. F. Lovering, J. Bikker, C. Humblet, *J. Med. Chem.* **52**, 6752–6756 (2009).
35. S. H. Kennedy, B. D. Dherange, K. J. Berger, M. D. Levin, *Nature* **593**, 223–227 (2021).
36. X. Zou, J. Zou, L. Yang, G. Li, H. Lu, *J. Org. Chem.* **82**, 4677–4688 (2017).
37. H. Qin *et al.*, *Angew. Chem. Int. Ed.* **60**, 20678–20683 (2021).
38. C. Hui, L. Brieger, C. Strohmann, A. P. Antonchick, *J. Am. Chem. Soc.* **143**, 18864–18870 (2021).
39. T. Guo, J. Li, Z. Cui, Z. Wang, H. Lu, *Nat. Synth.* **3**, 913–921 (2024).
40. J. Jurczyk *et al.*, *Science* **373**, 1004–1012 (2021).
41. S. F. Kim *et al.*, *J. Am. Chem. Soc.* **147**, 1851–1866 (2025).
42. L. Wu *et al.*, *Nat. Chem.* **16**, 1951–1959 (2024).
43. H. Qin, T. Guo, K. Lin, G. Li, H. Lu, *Nat. Commun.* **14**, 7307 (2023).
44. W. Klötzer, J. Stadlwieser, J. Raneburger, *Org. Synth.* **64**, 96 (1986).
45. V. C. M. Gasser, S. Makai, B. Morandi, *Chem. Commun.* **58**, 9991–10003 (2022).
46. P. Onnuch, K. Ramagonolla, R. Y. Liu, *Science* **383**, 1019–1024 (2024).
47. D. M. Lemal, F. Menger, E. Coats, *J. Am. Chem. Soc.* **86**, 2395–2401 (1964).
48. P. J. Rybczynski, D. W. Combs, K. Jacobs, R. P. Shank, B. Dubinsky, *J. Med. Chem.* **42**, 2403–2408 (1999).
49. Z.-X. He, Y.-P. Gong, X. Zhang, L.-Y. Ma, W. Zhao, *Eur. J. Med. Chem.* **209**, 112946 (2021).
50. J. D. Scott, R. M. Williams, *Chem. Rev.* **102**, 1669–1730 (2002).

ACKNOWLEDGMENTS

Funding: Financial support for this work was provided by the National Natural Science Foundation of China (22271148) and the Natural Science Foundation of Jiangsu Province (BK20231400). We are grateful to the High-Performance Computing Center of Nanjing University for doing the numerical calculations in this paper on its blade cluster system. **Author contributions:** J. L. and H. L. designed the experiments. J. L., P. T., and Y. F. performed the experiments and analyzed the data. All authors participated in writing the manuscript. H. L. conceived and supervised the project. **Competing interests:** The authors declare that they have no competing interests. **Data and materials availability:** All data are available in the main text or the supplementary materials.

License information: Copyright © 2025 the authors, some rights reserved; exclusive licensee American Association for the Advancement of Science. No claim to original US government works. https://www.science.org/about/science-licenses-journal-article-reuse

SUPPLEMENTARY MATERIALS

science.org/doi/10.1126/science.adl4755
Materials and Methods; Supplementary Text; Figs. S1 to S14; Tables S1 to S6; NMR Spectra; References (*51*–*77*)

Submitted 15 April 2025; accepted 27 May 2025

10.1126/science.adl4755

NEUROSCIENCE

Midline assembloids reveal regulators of human axon guidance

Massimo M. Onesto[1,2,3]†, Neal D. Amin[2,3]†, Chenjie Pan[4], Xiaoyu Chen[2,3], Ji-il Kim[2,3], Noah Reis[2,3], Sabina Kanton[2,3], Alfredo M. Valencia[2,3], Zuzana Hudacova[2,3], James P. McQueen[2,3], Marc Tessier-Lavigne[4], Sergiu P. Pașca[2,3]*

Organizers orchestrate cell patterning and axon guidance in the developing nervous system. Although nonhuman models have led to fundamental discoveries about floor plate (FP)–mediated midline organization, an experimental model of the human FP would enable insights into human neurodevelopment and midline connectivity. Here, we developed organoids resembling human FP (hFpOs) and assembled them with human spinal cord organoids (hSpOs) to generate midline assembloids (hMAs). We demonstrate that hFpOs promote ventral patterning, commissural axon guidance, and bilateral connectivity. To investigate midline regulators, we profiled the hFpO secretome, identifying 27 human-enriched genes compared with mouse. In an arrayed CRISPR screen of hMAs, we discovered that loss of *GALNT2* and *PLD3* impaired FP–mediated guidance of axons. This platform holds promise for revealing aspects of human-specific neurobiology and disease.

Organizers serve as neurodevelopmental guideposts that regulate the spatial patterning of neural tissues and guide axons across long distances to their targets (*1*–*4*). The floor plate (FP) organizer, located ventrally along the neural tube midline, comprises specialized neuroepithelial cells that secrete morphogens and axon guidance cues in gradients along the dorsoventral axis. This drives spinal cord patterning and midline axon crossing to establish bilateral connectivity, which governs locomotive and sensory function (*5*–*10*).

Although nonhuman models have provided fundamental insights, their organizer conservation and potential functional divergence in human midline development remain less understood. Therefore, developing human models could uncover mechanisms of axon guidance and pathways relevant to neurodevelopmental disorders.

Stem cell–derived neural organoids and assembloids can be used to study complex cellular interactions, including cell migration and axonal projections, in human brain development (*11*–*13*). Previous studies have derived and analyzed human FP cells, but their contribution to cell specification and axon guidance remains unexplored (*14*). FP formation has been demonstrated in mouse neural tube organoids (*15*, *16*), but human models of midline organizers and axonal crossing are lacking. Here, we developed a protocol to generate functional human FP organoids (hFpOs) and investigated their influence on patterning and axon guidance using assembloids.

We separately generated hFpOs and human spinal cord organoids (hSpOs) (*17*) and assembled them to form human midline assembloids (hMAs). The integration of hFpOs with early-stage hSpOs induced ventral progenitor patterning, whereas late-stage hSpO assembly enabled modeling of commissural axon guidance by the FP. We expanded this system to a three-part hMA to model midline exit and bilateral connectivity. We comprehensively profiled the hFpO secretome through liquid chromatography mass spectrometry (LC-MS) and the primary human FP transcriptome with single-cell RNA sequencing (scRNA-seq), identifying several human-enriched genes. Using an arrayed CRISPR screen in hMAs, we identified which of these factors can regulate human FP-dependent axon guidance. Together, these experiments introduce a human cellular model for investigating the functions of the FP and its role in midline development.

Generation and characterization of hFpOs and hSpOs

To generate human FP cells from human induced pluripotent stem (hiPS) cells, we exposed early neural organoids to a combination of growth factors and small molecules, mimicking notochord-driven FP induction (Fig. 1, A and B). We first enzymatically dissociated hiPS cells into single cells and aggregated ~2000 cells in ultra-low-attachment, round-bottom 96-well plates. Neuralization was initiated with dual SMAD inhibitors, dorsomorphin (DM) and SB-431542 (SB), followed by smoothened agonist (SAG), FGF2, the WNT activator CHIR 99021, and retinoic acid (fig. S1A). Immunocytochemistry of organoids at day 8 revealed a very high proportion (~85%) of FOXA2$^+$ nuclei (Fig. 1, C and D). In parallel, we generated early-stage hSpOs using an established approach (*17*) but removing Sonic Hedgehog (SHH)–pathway activators to avoid ventralization (Fig. 1B and fig. S1A). Our hFpOs displayed rosette-like structures that were surrounded by the basement membrane protein collagen IV (COL4A1/COL4A2) (fig. S1B). Reverse transcription–quantitative polymerase chain reaction (RT-qPCR) showed higher expression of the ventral transcription factors *FOXA2* and *NKX2-2*, the morphogen *SHH*, and the guidance molecule *NTN1* in hFpOs compared with hSpOs (Fig. 1E). Moreover, hSpOs showed no FOXA2 protein expression by immunocytochemistry and had higher expression of the dorsal transcription factors *PAX6* and *PAX3* (Fig. 1, D and E). We next examined secreted morphogens and guidance molecules by collecting conditioned media (CM) from hFpOs and hSpOs. Western blots detected SHH in hFpO cell lysates but not CM, whereas NTN1 was present in both. (Fig. 1F and fig. S1C). β-Actin was only detected in cell lysates, suggesting secretion rather than cell lysis–related release (fig. S1D). To test CM bioactivity, we treated mouse dorsal spinal explants embedded in collagen with hFpO or hSpO conditioned media for 40 hours. Explants exposed to hFpO CM exhibited increased axon outgrowth compared with hSpO CM (Fig. 1, G to I).

To study cell diversity in hFpOs, we performed droplet-based scRNA-seq analysis at day 8 of differentiation (Fig. 1J). We found that cells were generally homogeneous in their gene expression signature, with high expression of the known caudal FP markers *FOXA2*, *ALCAM*, *SPON1*, and *NTN1* (Fig. 1, K and L). Using Seurat label transfer to a developing spinal cord atlas (CS12-CS19), we found that hFpO cells mapped predominantly (up to ~90%) to the ventral FP/p3 domains (Fig. 1, M and N, and fig. S2, A and B). VoxHunt confirmed similarity to embryonic day 11 (E11) mouse hindbrain FP (fig. S2C). These results suggest that three-dimensional (3D) cultures resembling the early-stage human FP can be reliably and efficiently generated from stem cells.

Generation of hMAs to model patterning

To model FP influence on ventral spinal cord patterning, we created assembloids using hFpOs derived from a fluorescent hiPS cell line and hSpOs from a nonfluorescent line of the same background. We placed a day 8 hFpO and a day 8 hSpO in proximity in an ultra-low-attachment, round-bottom well, where they assembled within 24 hours (Fig. 2A). This time point was selected because hSpOs at this stage are largely unpatterned, allowing hFpOs to drive ventralization. We collected assembloids at 3 and 7 days after fusion (d.a.f.) and assessed ventral identity using immunocytochemistry. We observed graded expression of the ventral transcription factors FOXA2, NKX2.2, and NKX6.1 at the hFpO-hSpO boundary, which is suggestive of FP-induced ventral patterning (Fig. 2, B and C, and fig. S3A). Cyclopamine treatment during fusion, which inhibits SHH signaling, abolished ventral marker expression in

[1]Neurosciences Graduate Program, Stanford University, Stanford, CA, USA. [2]Department of Psychiatry and Behavioral Sciences, Stanford University School of Medicine, Stanford, CA, USA. [3]Stanford Brain Organogenesis, Wu Tsai Neurosciences Institute, Stanford University, Stanford, CA, USA. [4]Department of Biology, Stanford University, Stanford, CA, USA. ***Corresponding author. Email: spasca@stanford.edu** †These authors contributed equally to this work.

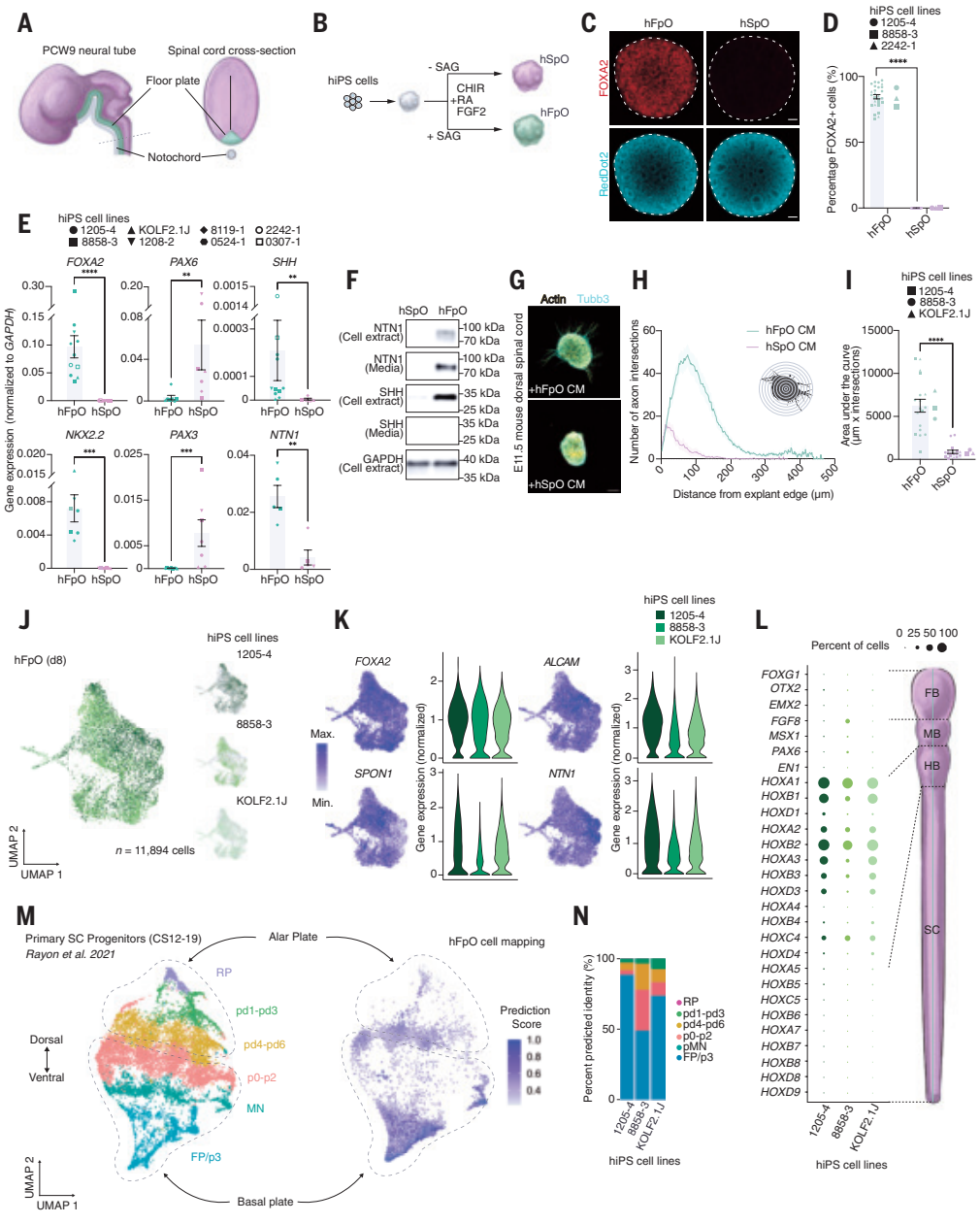

Fig. 1. Generation and characterization of hFpOs and hSpOs. (**A**) Schematic illustrating a developing human neural tube (purple) and location of the FP (green). (**B**) Schematic illustrating the generation of hFpOs (green) and hSpOs (purple). (**C**) Representative immunocytochemistry images of FOXA2 expression and RedDot2 (nuclear stain) at day 8 of differentiation in cleared hFpOs and hSpOs. Scale bar, 100 μm. (**D**) Quantification of FOXA2^{+} nuclei from immunocytochemistry images of individual hFpOs and hSpOs ($n = 27$ hFpOs and $n = 11$ hSpOs in one to three differentiation experiments from three hiPS cell lines; $^{****}P < 0.0001$, two-tailed t test). Bar plot indicates individual organoids and the larger points indicate individual hiPS cell lines. Data are presented as mean ± SEM. (**E**) Gene expression analysis (by RT-qPCR) of *FOXA2, NKX2.2, PAX6, PAX3, SHH*, and *NTN1* in hFpOs and hSpOs at day 8 of in vitro differentiation. For *FOXA2*: $n = 11$ hFpOs and $n = 8$ hSpOs from eight and six hiPS cell lines, respectively; $^{****}P < 0.0001$, two-tailed Mann-Whitney test. For *NKX2.2*: $n = 7$ hFpOs and $n = 7$ hSpOs from five hiPS cell lines; $^{***}P = 0.0006$. For *PAX6*: $n = 7$ hFpOs and $n = 7$ hSpOs from five hiPS cell lines; $^{**}P = 0.0023$. For *PAX3*: $n = 7$ hFpOs and $n = 7$ hSpOs from five hiPS cell lines; $^{***}P = 0.0006$. For *SHH*: $n = 11$ hFpOs and $n = 5$ hSpOs from eight and five hiPS cell lines, respectively; $^{**}P = 0.0018$. For *NTN1*: $n = 5$ hFpOs and $n = 5$ hSpOs from four hiPS cell lines; $^{**}P = 0.0019$. Points indicate organoid samples from different differentiation experiments. (**F**) Western blot of SHH and NTN1 (cell extract and CM) collected from hFpOs and hSpOs. Immunoblotting of GAPDH was used as loading control. (**G**) Representative z-projected confocal images of E11.5 mouse dorsal spinal explants cultured for 40 hours in CM collected from hFpOs and hSpOs. Explants were stained for Tubb3 and phalloidin (actin stain) to visualize axons. Scale bar, 100 μm. (**H**) Sholl analysis of axon outgrowth from hFpO or hSpO CM-treated E11.5 mouse dorsal spinal explants from three hiPS cell lines ($n = 17$ for hSpO-treated and $n = 18$ for hFpO-treated explants dissected from two to three embryos). (**I**) Area under the curve quantification from Sholl analysis in (H). $^{****}P < 0.0001$, two-tailed Mann-Whitney test. Bars indicate individual explants, and larger points indicate individual hiPS cell lines. (**J**) Uniform manifold approximation and projection (UMAP) visualization of single-cell gene expression of hFpOs at day 8, separately colored by individual cell lines (shades of green) ($n = 11,894$ cells from three hiPS cell lines). (**K**) UMAP and violin plots showing gene expression of selected FP markers across three hiPS cell lines (shades of green). Color scale indicates normalized gene expression abundance. (**L**) Dot plots showing the expression of rostral-caudal defining genes expressed in hFpO cells. The size of the circle represents the percentage of cells expressing each gene in three hiPS cell lines (shades of green). (**M**) UMAP visualization of subsetted primary human spinal progenitor clusters (left, CS12-19) and hFpO cells (day 8) mapped onto the primary atlas (right, color scale indicates prediction score of mapped hFpO cells, and light gray points indicate reference atlas cells). (**N**) Bar plot displaying the proportion of predicted domains of hFpO cells from mapping onto a primary spinal progenitor atlas in each of the three hiPS cell lines.

hSpOs and reduced FOXA2 in hFpOs (Fig. 2, B and C, and fig. S3, A, D, and E). To test whether SHH signaling was required in hSpO ventralization independently of its effects on hFpOs, we used a multiguide CRISPR approach to specifically target *SMO* in hSpOs only (fig. S4D). We validated editing by Sanger sequencing, and subsequent Western blot experiments confirmed a strong reduction in SMO protein in edited hSpOs compared with controls (unedited hSpOs; fig. S4, A to C). Edited hSpOs showed reduced NKX2.2, NKX6.1, and FOXA2 expression (fig. S4, E, F, and I), whereas hFpO expression of FOXA2 remained unaffected (fig. S4J). These markers were absent in unassembled, stage-matched controls (fig. S4, G to I). Fusion between two hSpOs had no effect, further confirming the specific inductive role of hFpOs (fig. S3, B to D). We next performed scRNA-seq on fluorescent hSpOs assembled with hFpOs and on stage-matched unassembled hSpOs (Fig. 2D and fig. S5A). Transcriptomic clustering showed separation of unassembled hSpOs expressing dorsal transcription factors (*LMX1A*, *PAX7*, and *PAX3*) and assembled hSpOs expressing ventral transcription factors (*NKX6.2*, *OLIG2*, *NKX2.2*, and *FOXA2*; Fig. 2, E and F). Differential gene expression

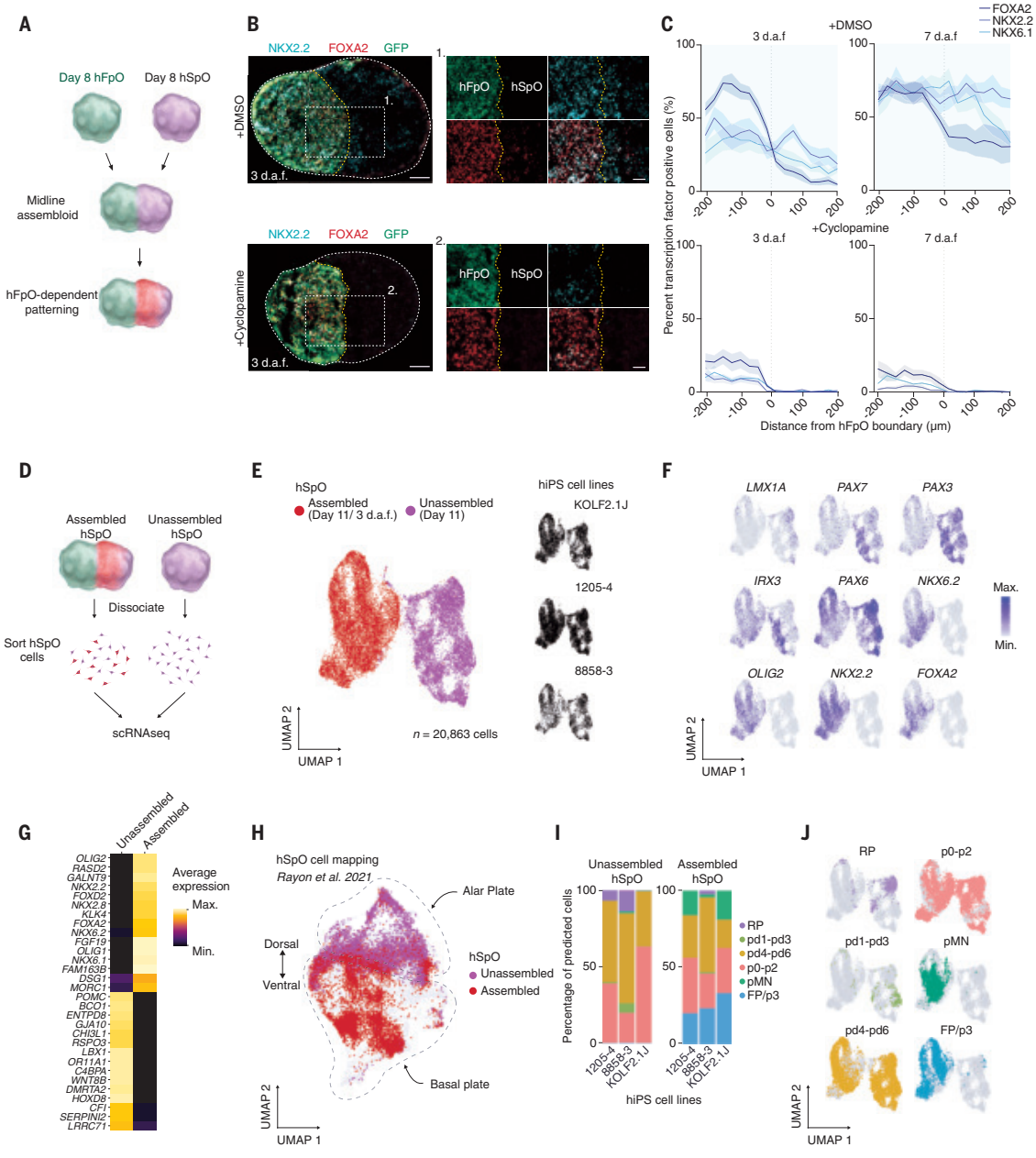

Fig. 2. Generation and characterization of hMAs for assessing hFpO-dependent ventral patterning. (**A**) Schematic illustrating the assembly of day 8 hFpOs (green) and hSpOs (purple) to form hMAs for modeling hFpO-dependent patterning. (**B**) Representative wide-field images of sectioned hMAs treated with dimethylsulfoxide (DMSO) (top) or with cyclopamine (bottom) at 3 d.a.f. Sections were immunostained for NKX2.2 and FOXA2, and an endogenously fluorescent hiPS cell line was used to label hFpOs. Scale bar, 100 μm; inset scale bar, 50 μm. (**C**) Binned plot profiles of the percentage of positive cells for ventral transcription factors from the hFpO-hSpO boundary (dotted line) 3 to 7 d.a.f. in hMAs cultured in the presence of DMSO or cyclopamine. Data are presented as mean ± SEM. For FOXA2 (dark blue), NKX2.2 (medium blue), and NKX6.1 (light blue), $n = 7$ to 9 assembloids per condition from three differentiation experiments from one hiPS cell line. (**D**) Schematic illustrating the process of collecting either unassembled hSpOs or hFpO-assembled hSpO cells for scRNA-seq analysis. (**E**) UMAP visualization of single-cell gene expression of cells collected from unassembled hSpOs (purple) and hFpO-assembled hSpOs (red) ($n = 20{,}863$ cells from three hiPS cell lines). (**F**) UMAP visualization of selected dorsal and ventral spinal progenitor gene expression in unassembled and hFpO-assembled hSpO. Color scale indicates normalized gene expression. (**G**) Heatmap visualization of the top differentially expressed genes from pseudobulked unassembled (left, $n =$ 4 samples) and hFpO-assembled (right, $n = 4$ samples) hSpOs from three hiPS cell lines. Color scale indicates average gene expression. (**H**) UMAP visualization of unassembled hSpOs (purple) and hFpO-assembled hSpOs (red) projected onto a primary human spinal progenitor atlas (light gray). (**I**) Bar plots of the proportion of unassembled ($n = 4$ samples) and hFpO-assembled ($n = 4$ samples) hSpO predicted progenitor cell domain identity from a human spinal progenitor atlas from three hiPS cell lines. (**J**) UMAP visualization of assembled and unassembled hSpOs, with highlighted points corresponding to the label-transferred progenitor cell domains predicted from primary human spinal cord atlas mapping in (H).

confirmed ventral identity in the assembled group (Fig. 2G and table S1), with no shift in anterior-posterior markers (fig. S5E). *GLI1* (expressed upon SHH pathway activation) was enriched in assembled hSpOs, whereas *GLI3* (repressed upon SHH pathway activation) was enriched in unassembled hSpOs (fig. S5B). The expression of ventral transcription factors correlated positively with *GLI1* and inversely with *GLI3*; the opposite pattern was observed for dorsal transcription factors (fig. S5C). Mapping to a primary spinal cord atlas revealed that unassembled hSpOs resembled dorsal spinal cord domains, whereas hFpO-assembled hSpOs resembled ventral progenitors (Fig. 2, H to J, and fig. S5D). The gene expression profile within these mapped cells strongly correlated with canonical regional markers (fig. S5, F to H). Overall, these findings demonstrate that hFpOs have organizer-like properties and induce ventral spinal cord fates in assembloids.

Generation of hMAs to model axon guidance

To model axon guidance in hMAs, we first verified the presence of spinal commissural neurons in hSpOs. This required patterning hSpOs at a later stage without SHH agonists to produce dorsal spinal interneurons (fig. S6A) (*17*, *18*). Single-cell profiling of hSpOs at day 35 revealed clusters of cells expressing dI1, dI2, dI3, dI4, and dI5 interneuron markers (Fig. 3, B and C). One cluster showed enriched expression of *ROBO3*, *CNTN2*,

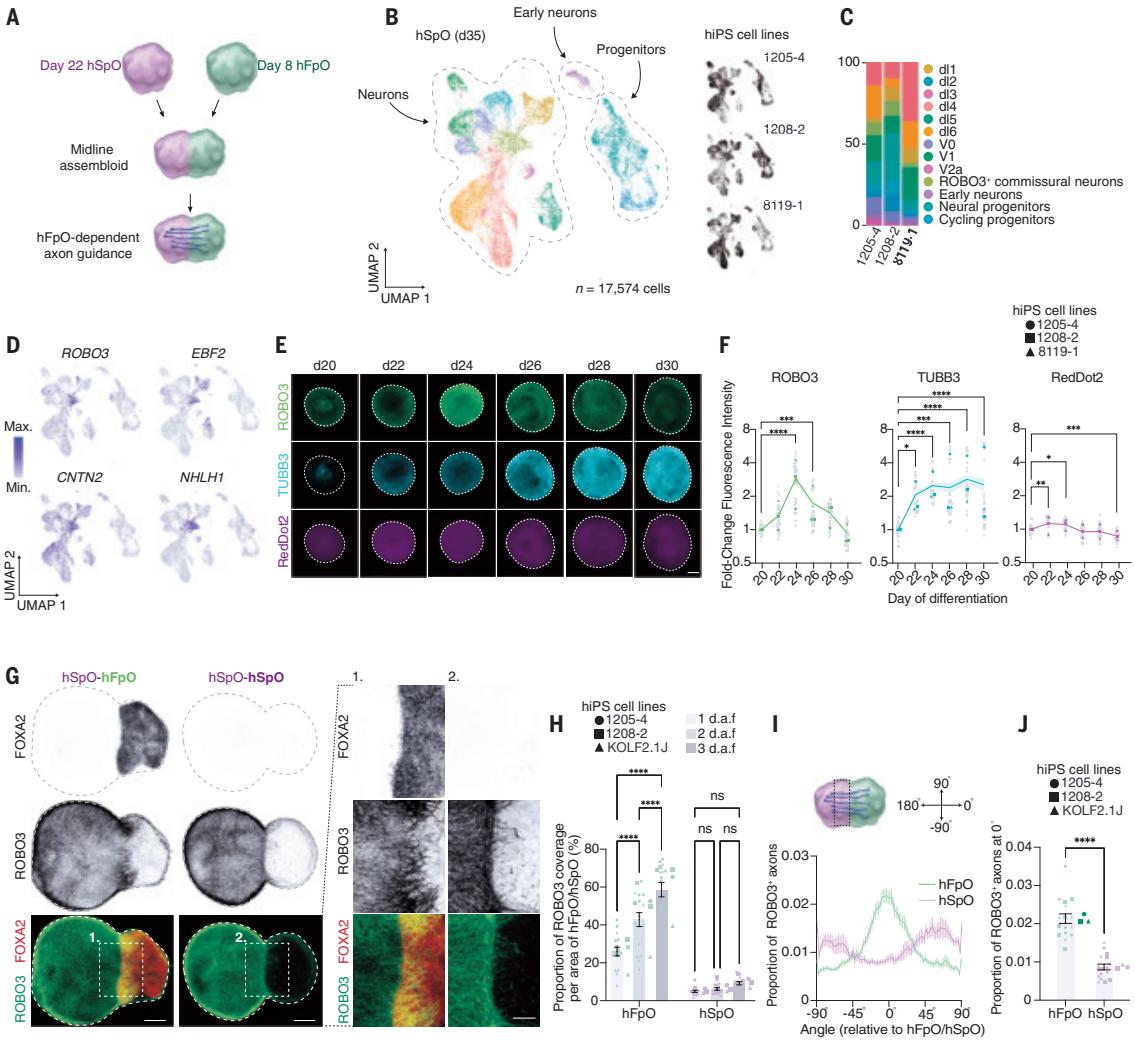

Fig. 3. Generation and characterization of hMAs for assessing hFpO-dependent axon guidance. (**A**) Schematic illustrating the assembly of day 8 hFpOs (green) and day 22 hSpOs (purple) to form hMAs for modeling hFpO-dependent axon guidance. (**B**) UMAP visualization of single-cell gene expression of cells collected from day 35 (d35) hSpOs ($n = 17{,}574$ cells from three hiPS cell lines). (**C**) Bar plots of the proportion of annotated d35 hSpO cell clusters across three hiPS cell lines. (**D**) UMAP visualization of single-cell gene expression of markers enriched in spinal commissural neuron populations, *ROBO3, EBF2, CNTN2,* and *NHLH1*. Color scale indicates normalized gene expression. (**E**) Representative z-projected immunocytochemistry images of cleared hSpOs showing expression of ROBO3 and TUBB3 with RedDot2 nuclear stain from days 20 to 30 of differentiation. Scale bar, 200 μm. (**F**) Quantification of fold-change in ROBO3, TUBB3, and Reddot2 fluorescence relative to day 20 of differentiation (n = 22 to 32 organoids per time point from three hiPS cell lines). Individual organoids are shown as gray points, and the averages per hiPS cell lines are shown as colored points. Line indicates overall mean, and shaded area represents SEM. Data are plotted on a $\log_2$-scaled axis. For ROBO3: $F_{(5,161)} = 39.26$, $P < 0.0001$; ***$P = 0.0003$, ****$P < 0.0001$. For TUBB3: $F_{(5,161)} = 6.864$, $P < 0.0001$; *$P = 0.0164$, ***$P = 0.0005$, ****$P < 0.0001$. For Reddot2: $F_{(5,161)} = 17.81$, $P < 0.0001$; **$P = 0.0036$, *$P = 0.0171$, ***$P = 0.0008$. One-way ANOVA followed by Dunnett's multiple-comparison tests was used. (**G**) Representative z-projected immunocytochemistry images of ROBO3 and FOXA2 expression in cleared hMA at 2 d.a.f. Scale bar, 200 μm; inset scale bar, 100 μm. (**H**) Quantification of the proportion of ROBO3$^+$ axon coverage normalized to the area of assembled hFpOs (green) or hSpOs (purple) over time. Bar plots indicate individual assembloids at 1 d.a.f. (light gray), 2 d.a.f. (medium gray), and 3 d.a.f. (dark gray) (n = 14 to 17 assembloids per condition/day from three hiPS cell lines), and larger points indicate individual hiPS cell lines. Comparison of the effects across time points in each condition: $F_{(2,91)} = 27.92$, $P < 0.0001$; ****$P < 0.0001$, two-way ANOVA and Tukey's test for multiple comparisons. (**I**) Directionality quantification of ROBO3$^+$ axons in hSpOs relative to either an assembled hSpO or hFpO at 2 d.a.f. (n = 17 assembloids per condition from three hiPS cell lines). Zero degrees indicates projection directly toward, and ±90° indicates away from the assembled hFpO/hSpO. The analyzed region of interest is indicated by the dotted box on the hMA schematic. $F_{(89,2880)} = 6.398$, $P < 0.0001$, two-way ANOVA. (**J**) Bar plot representing the proportion of ROBO3$^+$ axons oriented directly at 0° from (I). Data are presented as mean ± SEM. Bar plots indicate individual assembloids, and larger points indicate individual hiPS cell lines. ****$P < 0.0001$, Mann-Whitney test.

EBF2, and *NHLH1*, which are markers of projecting commissural interneurons (Fig. 3, B and D, and fig. S6, B and C) (*19*–*22*). Additionally, this cluster showed enriched expression of the major Netrin receptor *DCC* (fig. S6, D and E). Immunocytochemistry for ROBO3 showed temporally regulated expression consistent with prior reports (*23*). By contrast, TUBB3 showed a steady increase across this period (Fig. 3, E and F). To assess whether hiPS cell–derived commissural neurons project from hSpOs to hFpOs, we assembled hSpOs at day 22 with day 8 hFpOs (Fig. 3, A and G). We observed progressive and directed axonal projections and fasciculations invading the hFpOs (Fig. 3, G and H). To determine whether these projections depended on hFpOs, we assembled hSpOs (at day 22) with day 8 hSpOs, which lack FP cells, and found only rare projecting ROBO3$^+$ commissural axons with a defasciculated appearance (Fig. 3, G and H). Quantification of hSpO axon projection directionality showed

more ROBO3$^+$ axons oriented toward hFpOs, confirming hFpO-dependent commissural axon guidance (Fig. 3, I and J).

Generation of three-part hMAs to model bilateral connectivity

To investigate midline crossing and FP exiting of commissural axons in hMAs, we developed an in vitro midline-like structure by assembling multiple hFpOs. We then generated three-part assembloids by incorporating this hFpO between two hSpOs at day 22 (Fig. 4, A and B). The assembly rate was 95.65% (fig. S7, A and B). As a control, we also derived three-part assembloids without FP cells by creating a midline-like structure out of day 8 hSpOs (Fig. 4C). To track axons, we transduced one hSpO with LV-hSYN1::eYFP before assembly (movie S1). Imaging over 5 days revealed axonal crossing and contralateral exiting, which was minimal without hFpOs (Fig. 4D). Immunostaining for ROBO3 and FOXA2 revealed that hFpOs in hMAs maintained abundant FOXA2$^+$ cells and bilateral fasciculated ROBO3$^+$ axons, which colocalized with hSYN1::eYFP-labeled projections (Fig. 4E). These results indicate that hFpOs promote axon crossing and contralateral projection and therefore model aspects of midline entry and exit.

To assess bilateral connectivity, we expressed hSYN1::GCaMP8s (*24*) in both hSpO before assembly. Seven days after fusion, confocal imaging revealed synchronous calcium bursts in bilateral hSpOs. Scaled correlation analysis confirmed substantial synchrony (movie S2), whereas unassembled hSpOs exhibited asynchronous activity (Fig. 4, F to H, and movie S3). To manipulate this activity, we expressed channelrhodopsin 2 fused to enhanced yellow fluorescent protein (eYFP) under the hSYN1 promoter (hSYN1::ChR2-eYFP) in one hSpO and performed extracellular recordings (fig. S8, A and B). Ten days after fusion, axonal projections were evident in hFpO-containing assembloids but nearly absent in hSpO-midline controls (Fig. 4I). Optogenetic stimulation with 480-nm light induced robust contralateral activation in hMAs with hFpOs, whereas responses were reduced in hMAs lacking FP cells (Fig. 4, J and K). This reduction was specific to the receiving hSpOs, with no difference in the ChR2-expressing hSpOs, indicating consistent stimulation (fig. S8, C and D). Incubation with NBQX and APV (50 μM each) abolished responses in the receiving hSpO (fig. S8, E and F). Activity also decreased in the ChR2-expressing hSpO, suggesting reciprocal connectivity (fig. S8, G and H). These results demonstrate that three-part hMAs can be used to model FP entry, crossing, exit, and early bilateral connectivity.

Identification of human-enriched FP genes

We leveraged our hFpO system to generate large quantities of FP cells for proteomic analysis of membrane and secreted proteins enriched in the human FP compared with mouse. We collected CM from hFpOs (~30 million cells) and performed LC-MS, capturing 1876 proteins (table S2). To identify which of these proteins were selectively enriched in FP cells, we selected genes detected in primary human FP. We retained genes enriched in FP versus other spinal progenitors and present in at least 30% of primary FP cells, yielding 415 FP-enriched genes (table S2). Of these, 326 encoded membrane and secreted proteins, and of which 68 were essential for cell survival (fig. S9A and table S2).

We next investigated whether homologous genes are differentially expressed between species. We analyzed conservation and divergence of expression in human versus mouse FP using prior cross-species analysis methods (table S3) (*25*). We found that 10.5% of nonessential genes displayed a >10-fold divergence in expression (Fig. 5A, fig. S9B, and table S4). Three of these genes showed human-specific FP expression: *EFEMP1*, *TTR*, and *CLSTN3* (Fig. 5A and fig. S9C). Overall, these proteomic and transcriptomic experiments identified membrane and secreted proteins that were enriched in or specific to the human FP compared with mouse.

Arrayed CRISPR screen of membrane and secreted factors reveals regulators of human FP-dependent axon guidance

To investigate the role of human-enriched membrane and secreted proteins in commissural axon guidance to the FP, we designed an arrayed CRISPR screen leveraging the accessibility of hMAs for genetic manipulation and multiple functional readouts of FP-dependent axon guidance (Fig. 5B). We used guides targeting 27 human FP genes with the highest divergence in expression compared with mouse FP, three conserved genes (*NTN1*, *SPON1*, and *NRP2*) implicated in FP-dependent axon guidance (*26*–*28*), and nontargeting controls (NTCs) (table S5). We individually screened knockout (KO) hiPS cell pools for editing efficiency using ICE analysis and KO score, with ~90% showing >75% efficiency (fig. S10, A and B) (*29*). We generated hFpOs from these KO pools and assembled them at day 8 with unedited day 22 hSpOs. Three days after fusion, we fixed, immunostained for ROBO3 and FOXA2, and cleared assembloids to assess commissural axon projections (Fig. 5B). We imaged the hFpO region and quantified ROBO3 fluorescence within 150 μm of the FOXA2 boundary, normalized to pre-hFpO ROBO3 intensity (Fig. 5, C to E, and fig. S10F). Assembly and processing were reliable, with a 93.75% success rate (fig. S10G). Loss of *NTN1* and *SPON1* reduced ROBO3$^+$ axon projection into hFpOs, consistent with their known roles in commissural axon guidance in nonhuman models (Fig. 5, C to E, and fig. S10F) (*20*, *26*, *27*). In contrast to rodent studies (*28*), *NRP2* loss had no detectable effect on human commissural axon guidance (Fig. 5, C to E, and fig. S10, C and F).

We identified two human-enriched FP genes that reduced commissural axon projection: *GALNT2* and *PLD3* (Fig. 5, C to E, and fig. S10F). *GALNT2* encodes an enzyme that initiates O-linked glycosylation by transferring *N*-acetylgalactosamine, and *PLD3* encodes a lysosomal protein that hydrolyzes phospholipids. *GALNT2* KO reduced *FOXA2* expression at the transcript and protein levels, suggesting a role in FP specification (fig. S10, D and E), whereas *PLD3* did not affect FP identity. For validation, we generated isogenic *NTN1*, *SPON1, PLD3,* and *GALNT2* homozygous KO hiPS cell lines and generated hMAs (Fig. 5F and fig. S11A). Isogenic KO was confirmed by Sanger sequencing and Western blot for target proteins in lysates and CM from hFpOs (fig. S11, A to C). Isogenic KO hFpOs showed reduced ROBO3$^+$ commissural axon projection in hMAs compared with NTCs (Fig. 5, G and H). To validate consistent ROBO3 expression, we measured ROBO3 fluorescence intensity in the hSpO portion of the hMAs and found no effect in hMAs containing isogenic KO hFpO (fig. S12B). Next, we assessed whether reduced projection reflected loss of ROBO3 postentry into mutant hFpOs. We expressed hSYN1::eYFP in hSpOs before hMA assembly to track axons crossing into hFpOs. We found reduced eYFP$^+$ axon outgrowth into hFpOs across CRISPR mutants compared with NTCs (fig. S12, C and D). To determine whether these eYFP$^+$ axons were also ROBO3$^+$, we counterstained for ROBO3 and observed colocalization and correlated fluorescence in axons extending beyond the hFpO boundary (fig. S12, E and F). These findings suggest that axon guidance defects are likely due to reduced outgrowth, and that most projecting axons are ROBO3$^+$.

GALNT2 homozygous KO reduced FOXA2$^+$, NKX2.2$^+$, and NKX6.1$^+$ cells while not affecting SOX2$^+$ cell numbers in hFpOs (fig. S13, A to H). We also observed decreased *FOXA2* and increased *PAX6* expression; however, *NKX2.2* transcript abundance was not affected (fig. S13I). These results suggest that hMAs can be used to identify functionally important human-enriched FP genes.

Discussion

Neural organoids can recapitulate cellular diversity across regions of the nervous system. The integration of multiple organoids in assembloids can model cell-cell interactions essential to circuit assembly. Our previous work, along with studies from other groups, modeled migration and long-range projections with assembloids (*17*, *30*–*39*). Here, we used assembloids to explore organizer patterning and axon guidance at the midline.

We developed hMAs that model commissural axon guidance to the FP, an essential step for bilateral neural connectivity. First, we generated hFpOs and defined their transcriptome and secretome profiles. Second, we developed a modular assembloid system to capture distinct phases of midline development. Integrating hFpOs with early-stage, unpatterned

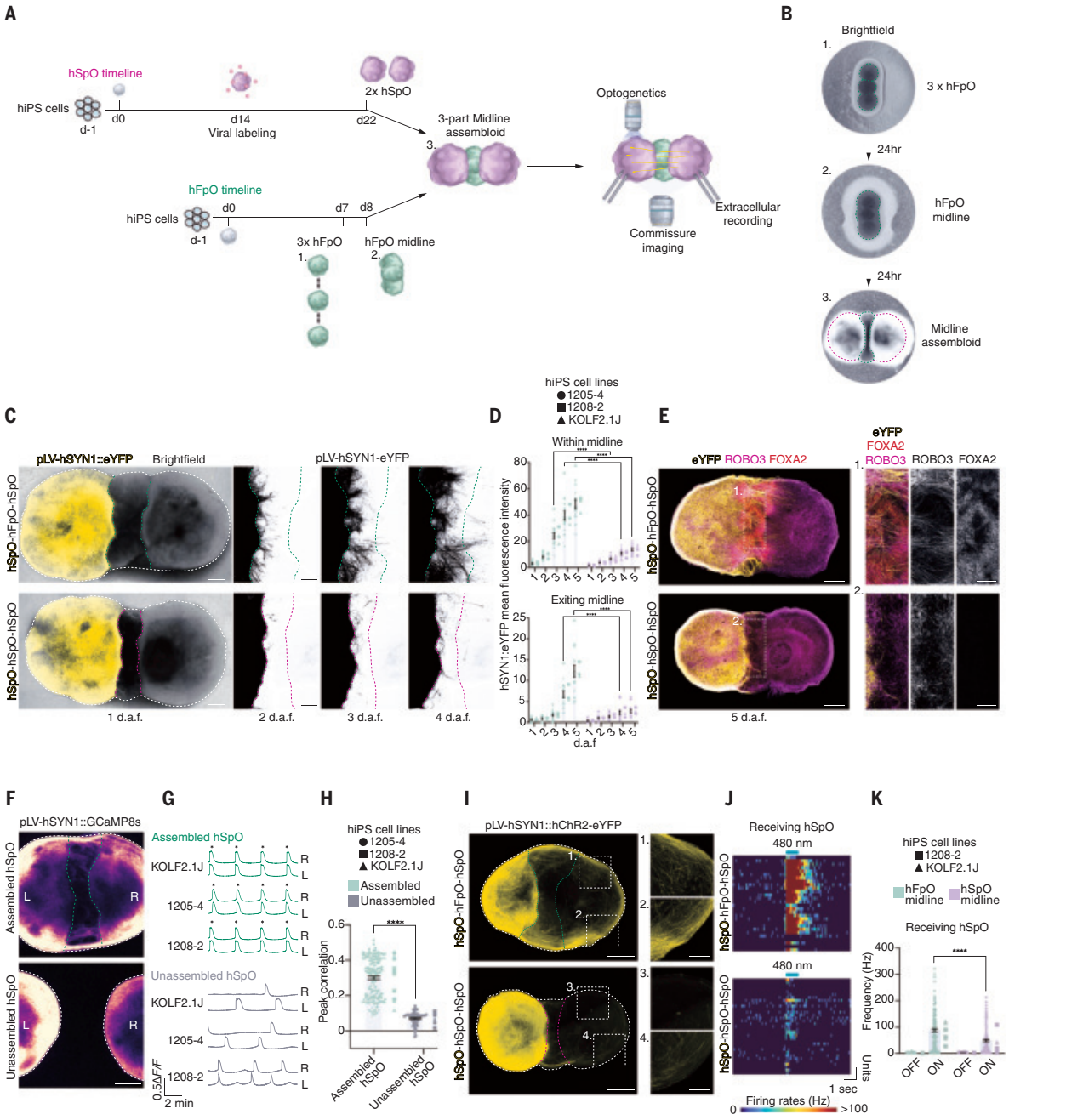

Fig. 4. Generation and characterization of three-part hMAs for modeling midline crossing and circuitry. (**A**) Schematic illustrating the generation of hFpO midline and three-part hMAs to model bilateral circuit formation. (**B**) Bright-field images of hFpO assembly to form the hFpO midline component of the hMAs. (**C**) Bright-field images of three-part hMA overlayed with z-projections of hSYN1::eYFP expression in one hSpO (left; scale bar, 200 μm) and time-lapse imaging of $eYFP^+$ axons crossing the midline (right; scale bar, 100 μm). Dotted green line represents hFpO-midline boundary, and dotted purple line represents the hSpO-midline boundary. (**D**) Quantification of hSYN1::eYFP fluorescence within (top) or 100 μm beyond (bottom) the hFpO (green symbols, $n = 15$ assembloids) or hSpO (purple symbols, $n = 14$ assembloids) midline in three-part hMA at 1 to 5 d.a.f. in three hiPS cell lines. Bar plots indicate individual assembloids, and larger points indicate individual hiPS cell lines at each time point. Data are presented as mean ± SEM. For within midline: two-way ANOVA, $F_{(1,135)} = 217.9$, $P < 0.0001$, after Sidak's multiple-comparisons test, ****$P < 0.0001$. For exiting midline: two-way ANOVA, $F_{(1,135)} = 57.40$, $P < 0.0001$, after Sidak's multiple-comparison tests, ****$P < 0.0001$. (**E**) Representative z-projected immunocytochemistry images of eYFP, ROBO3, and FOXA2 expression in cleared three-part hMAs from (C) at 5 d.a.f. Scale bar, 200 μm; inset scale bar, 100 μm. (**F**) Representative images of jGCaMP8s expression in assembled (hMA; top) and unassembled hSpO (bottom). Scale bar, 200 μm. (**G**) Example $\Delta F/F_{base}$ traces of jGCaMP8s in right (R) and left (L) assembled (hMA; top) and unassembled (bottom) hSpO in three hiPS cell lines. Spontaneous activity was monitored for 10 min. (**H**) Scaled correlation values averaged per cell for assembled (hMA; green) and unassembled (gray) hSpO (assembled, $n = 150$ cells from 15 hMAs; unassembled, $n = 70$ cells from seven nonassembled organoid pairs, three hiPS cell lines in one differentiation; ****$P < 0.0001$, two-tailed Mann-Whitney test). Bars indicate individual cells, and larger points indicate individual assembloids. (**I**) Representative z-projected images of hSYN1::hChR2-eYFP expression in cleared hMAs containing hFpO- (top) or hSpO- (bottom) midline at 10 d.a.f.. Scale bar, 200 μm; inset scale bar, 100 μm. (**J**) Representative heatmaps of extracellular recording from projection-receiving hSpOs in response to optogenetic stimulation of hSYN1::hChR2-eYFP expressing hSpOs in hMA with hFpO- (top) or hSpO- (bottom) midline at 10 d.a.f. Color scale indicates firing rate (in hertz). (**K**) Quantification of unit frequency from extracellular recordings in (J) before and after 480-nm light stimulation (hFpO-midline, $n = 141$ units; hSpO-midline, $n = 136$ units; six assembloids per condition, two hiPS cell lines in one differentiation; ****$P < 0.0001$, two-tailed Mann-Whitney test).

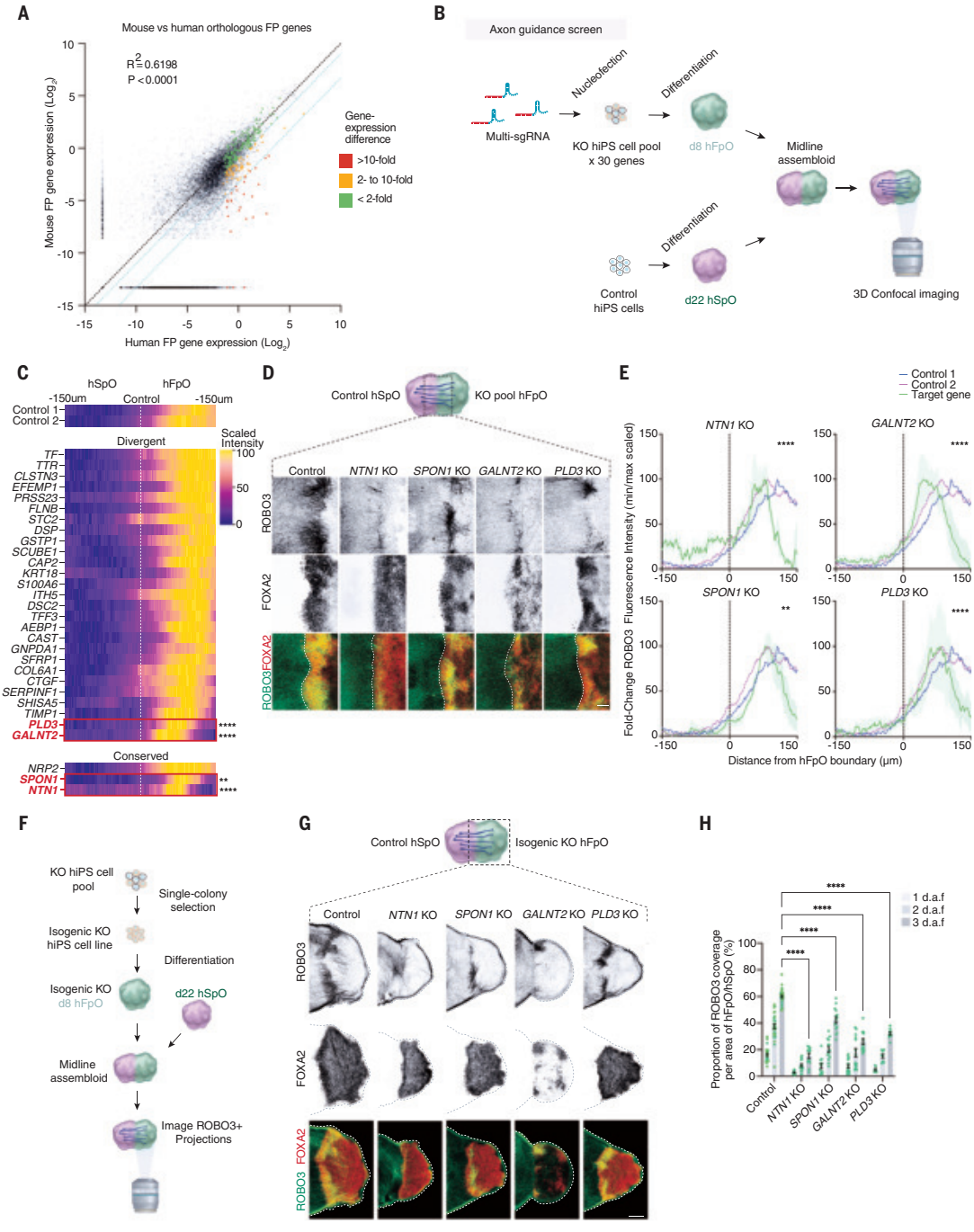

Fig. 5. hFpO-based screen for human-enriched axon guidance regulators. (**A**) Comparison of gene expression abundance of 14,852 orthologous genes (gray points) between mouse (E9 to E14) and human (CS12-19) FP cells. Black dotted line indicates 1:1 gene expression, and the blue dotted lines indicate 2- and 10-fold human enrichment. Colored points indicate membrane and secreted FP-enriched genes and indicate degree of gene expression divergence between human and mouse as indicated. Data are plotted on a $\log_2$-scaled axis. (**B**) Schematic of workflow for generating hFpOs from KO hiPS cell pools and subsequently assembling with day 22 hSpOs to form hMAs in an arrayed format. At 3 d.a.f., the assembloids were cleared and confocal imaged to visualize commissural axons guiding toward hFpOs. (**C**) Heatmap displaying min/max scaled fold-change ROBO3 fluorescence intensity of hSpO axons 150 μm pre- and 150 μm postcrossing into the hFpO, relative to the precrossing mean ($n = 2$ to 3 assembloids per gene). Two-way ANOVA was performed on measurements in the most distal 50 μm of heatmap; $F_{(31,1972)} = 10.05$, $P < 0.0001$, after Dunnett's multiple-comparisons test comparing Control 1 with all other conditions: ****$P < 0.0001$ for Control 1 versus *GALNT2*, ****$P < 0.0001$ for Control 1 versus *PLD3*, ****$P < 0.0001$ for Control 1 versus *NTN1*, and **$P = 0.0025$ for Control 1 versus *SPON1*. (**D**) Representative z-projected immunocytochemistry images of control and pooled KO hMAs expressing ROBO3 and FOXA2 to visualize ROBO3$^+$ axons projecting across the hFpO boundary. Scale bar, 100 μm. (**E**) Plot profiles of min/max scaled fold-change ROBO3 fluorescence intensity of KO pool hFpO hMA 150 μm pre- and 150 μm postcrossing into hFpOs from (C). Dotted lines indicate the nontargeting control groups, and solid lines indicate the target gene group. Data are presented as mean ± SEM. Gray-shaded region indicates the 50-μm bin where ROBO3 expression as a measure of axon guidance was assessed for statistical significance. (**F**) Schematic outlining the method for generating isogenic KO hiPS cell lines from the axon guidance screen candidates and subsequent isogenic validation of phenotypes identified in the axon guidance screen. (**G**) Representative z-projected immunocytochemistry images of control and isogenic KO hMAs expressing ROBO3 and FOXA2 at 3 d.a.f. Scale bar, 200 μm. (**H**) Bar plot showing the proportion of ROBO3$^+$ coverage relative to the area hFpOs from 1 to 3 d.a.f. (shades of gray; $n = 7$ to 29 assembloids per condition/d.a.f.). Two-way ANOVA, $F_{(4,213)} = 134.8$, $P < 0.0001$, after Tukey's multiple-comparisons test, ****$P < 0.0001$.

hSpOs captured SHH-dependent progenitor ventralization. Prior studies relied on ectopic overexpression of a single morphogen, missing the full complement of factors governing midline development (*40*, *41*). Integrating hFpOs with hSpOs containing ROBO3$^+$ commissural neurons enabled modeling of midline axon guidance, recapitulating contributions of NTN1 and SPON1. Three-part hMAs further modeled midline exit and bilateral connectivity. Third, we used hMAs to identify genes controlling midline axon guidance in human. We identified 27 nonessential human FP-enriched genes and performed an arrayed CRISPR KO screen.

Our results revealed an important role for GALNT2 in FP generation and commissural axon guidance, which may be related to changes in ventral specification. This may be mediated by GALNT2-dependent glycosylation of SHH components, a mechanism suggested for GALNT1 (*42*). Whereas patient phenotypes and animal models highlight the broader

impact of *GALNT2* on cognitive, behavioral, and neurodevelopmental outcomes, our model captures early pathway-specific disruptions, including midline crossing, that may underlie some of these phenotypes (*43*).

We observed that *PLD3* KO disrupts FP-dependent axon guidance in hMAs. Unlike *GALNT2* KO, *PLD3* KO does not alter FP specification. Given its role in vesicle trafficking and lysosomal localization, PLD3 may regulate secretory processes in FP cells (*44*, *45*). Future studies could investigate this mechanism and determine whether mis-secretion of certain factors perturbs midline axon guidance.

The human cellular model presented here holds potential for additional applications. hFpOs and hMAs can be used to investigate secreted versus cell-contact-dependent mechanisms in ventral patterning (*46*) and axon guidance (*2*, *47*, *48*). The system's modularity could clarify ventricular zone versus FP-derived Netrin-1 in midline axon guidance and allow investigation of growth cone responsivity at intermediate targets (*2*, *4*). Future studies should explore whether hFpOs can trigger receptor switches after crossing. Finally, comparing primate and human FpOs may further reveal conserved and divergent mechanisms underlying midline development.

There are several limitations to this model. The current assembloid does not capture postcrossing axonal events such as rostrocaudal turning. This could be addressed by adding another organizer-like organoid to establish a Wnt gradient, thus guiding anterior-posterior axon extension. Such a system could model spinal commissural projections to the thalamus. Studies of later hMA stages are limited by the shift to neurogenesis-promoting medium, which may deplete FP cells. Future work should optimize hMA media to promote hSpO neurogenesis without altering hFpO fate, enabling longer culture and facilitating studies of midline circuit maturation.

Expanding beyond the spinal cord, assembloids can model midline function in other brain regions such as the corpus callosum, which are often disrupted in neurodevelopmental disorders (*49*). This is important because current models lack glial wedge–generated guidance cues (*50*). Organoids mimicking roof plate and isthmic organizers could enable studies of dorsal and anterior-posterior patterning. Ultimately, organizer organoids offer a versatile toolset to advance our knowledge of human cell specification, axon guidance, and evolution, which are crucial to understanding human neurodevelopment and the impact of neurodevelopmental disorders.

REFERENCES AND NOTES

1. T. M. Jessell, *Nat. Rev. Genet.* **1**, 20–29 (2000).
2. J. D. Comer, S. Alvarez, S. J. Butler, J. A. Kaltschmidt, *Neural Dev.* **14**, 9 (2019).
3. S. A. Colamarino, M. Tessier-Lavigne, *Annu. Rev. Neurosci.* **18**, 497–529 (1995).
4. A. Chédotal, *Nat. Rev. Neurosci.* **20**, 380–396 (2019).
5. T. Yamada, M. Placzek, H. Tanaka, J. Dodd, T. M. Jessell, *Cell* **64**, 635–647 (1991).
6. H. Roelink *et al.*, *Cell* **81**, 445–455 (1995).
7. E. Schnapp, M. Kragl, L. Rubin, E. M. Tanaka, *Development* **132**, 3243–3253 (2005).
8. M. Tessier-Lavigne, M. Placzek, A. G. Lumsden, J. Dodd, T. M. Jessell, *Nature* **336**, 775–778 (1988).
9. T. E. Kennedy, T. Serafini, J. R. de la Torre, M. Tessier-Lavigne, *Cell* **78**, 425–435 (1994).
10. F. Charron, E. Stein, J. Jeong, A. P. McMahon, M. Tessier-Lavigne, *Cell* **113**, 11–23 (2003).
11. M. M. Onesto, J. I. Kim, S. P. Pasca, *Cell Stem Cell* **31**, 1563–1573 (2024).
12. Z. Zhang, X. Wang, S. Park, H. Song, G. L. Ming, *Biol. Psychiatry* **93**, 594–605 (2023).
13. I. Chiaradia, M. A. Lancaster, *Nat. Neurosci.* **23**, 1496–1508 (2020).
14. S. Kriks *et al.*, *Nature* **480**, 547–551 (2011).
15. T. Krammer *et al.*, *Dev. Cell* **59**, 1940–1953.e10 (2024).
16. A. Meinhardt *et al.*, *Stem Cell Reports* **3**, 987–999 (2014).
17. J. Andersen *et al.*, *Cell* **183**, 1913–1929.e26 (2020).
18. J. I. Kim *et al.*, *Nature* **642**, 143–153 (2025).
19. C. Sabatier *et al.*, *Cell* **117**, 157–169 (2004).
20. T. Serafini *et al.*, *Cell* **87**, 1001–1014 (1996).
21. A. Corradi *et al.*, *Development* **130**, 401–410 (2003).
22. K. Theodorakis, K. Kyriakopoulou, M. Wassef, D. Karagogeos, *Mech. Dev.* **119** (suppl. 1), S103–S106 (2002).
23. F. Friocourt *et al.*, *J. Comp. Neurol.* **527**, 2009–2029 (2019).
24. Y. Zhang *et al.*, *Nature* **615**, 884–891 (2023).
25. R. D. Hodge *et al.*, *Nature* **573**, 61–68 (2019).
26. T. Serafini *et al.*, *Cell* **78**, 409–424 (1994).
27. T. Burstyn-Cohen *et al.*, *Neuron* **23**, 233–246 (1999).
28. B. Hernandez-Enriquez *et al.*, *Genes Dev.* **29**, 2617–2632 (2015).
29. D. Conant *et al.*, *CRISPR J.* **5**, 123–130 (2022).
30. Y. Miura *et al.*, *Nat. Biotechnol.* **38**, 1421–1430 (2020).
31. J. I. Kim *et al.*, *Neuron* **112**, 4048–4059.e7 (2024).
32. X. Meng *et al.*, *Nature* **622**, 359–366 (2023).
33. X. Chen *et al.*, *Nature* **628**, 818–825 (2024).
34. F. Birey *et al.*, *Cell Stem Cell* **29**, 248–264.e7 (2022).
35. F. Birey *et al.*, *Nature* **545**, 54–59 (2017).
36. Y. Xiang *et al.*, *Cell Stem Cell* **24**, 487–497.e7 (2019).
37. D. Reumann *et al.*, *Nat. Methods* **20**, 2034–2047 (2023).
38. M. H. Patton, *Cell Rep.* **43**, 114503 (2024).
39. G. Goldberg *et al.*, *Mol. Psychiatry* **29**, 566–579 (2024).
40. R. De Santis, F. Etoc, E. A. Rosado-Olivieri, A. H. Brivanlou, *Nat. Commun.* **12**, 6768 (2021).
41. G. Y. Cederquist *et al.*, *Nat. Biotechnol.* **37**, 436–444 (2019).
42. C. Li *et al.*, *Cancer Res.* **76**, 1273–1283 (2016).
43. M. Zilmer *et al.*, *Brain* **143**, 1114–1126 (2020).
44. A. C. Gonzalez *et al.*, *Cell Rep.* **22**, 1040–1053 (2018).
45. A. S. Mukadam, S. Y. Breusegem, M. N. J. Seaman, *Cell. Mol. Life Sci.* **75**, 2613–2625 (2018).
46. P. Li *et al.*, *Science* **360**, 543–548 (2018).
47. J. A. Moreno-Bravo, S. Roig Puiggros, P. Mehlen, A. Chédotal, *Neuron* **101**, 625–634.e3 (2019).
48. Z. Wu *et al.*, *Neuron* **101**, 635–647.e4 (2019).
49. A. A. Nugent, A. L. Kolpak, E. C. Engle, *Curr. Opin. Neurobiol.* **22**, 837–843 (2012).
50. C. Martins-Costa *et al.*, *Cell Stem Cell* **31**, 866–885.e14 (2024).

ACKNOWLEDGMENTS

We thank members of the Rohatgi lab for generously providing the SMO antibody; Tyroma Analytical for mass spectrometry services and support with proteomic data analysis; the Stanford Shared FACS Facility for flow cytometry and cell sorting; and R. Levy, M. Avar, K. Kelley, N. Thom, M. Hynes, and members of the Hynes lab, as well as members of the Tessier-Lavigne lab, for their valuable input on experiments and the manuscript. **Author contributions:** M.O., N.A., M.T.L., and S.P.P. conceived the project and designed the experiments. M.O. and N.A. developed the hFpO differentiation and characterized these cultures. M.O. conducted all differentiation, sample collection, mouse embryo dissection and culture, and scRNA-seq analysis. M.O. analyzed the human-enriched FP genes and generated the list of genes used in the screen. S.K. contributed to scRNA-seq analysis. M.O. edited all CRISPR KO hiPS lines (with support from A.V. and X.C.), generated hMA and performed clearing and imaging of all samples during the screen. M.O., X.C., A.V., and Z.H. performed genotyping of hFpO cell pools during the screen. M.O. and X.C. performed FACS of hMA. N.R. and J.P.M. performed RT-qPCR for hFpO and hSpO. J.K. performed and analyzed optogenetic and extracellular recording experiments. M.O. performed calcium imaging. J.K. and N.R. performed calcium imaging analysis. N.R. performed imaging analysis for the screen. C.P. performed Western blotting, maintained mouse colonies, and provided timed mouse embryos. M.O. and S.P.P. wrote the manuscript with input from all authors. S.P.P. supervised all aspects of this study. **Funding:** This work was supported by National Institute of Neurological Disorders and Stroke of the National Institutes of Health (NINDS) grants R01-NS136675 (S.P.P.) and K08-NS123544-01 (N.D.A.), the Brain and Behavior Research Foundation (N.D.A.), Foundations of the National Institutes of Health Deeda Blair Research Initiative (N.D.A.), the Stanford Brain Organogenesis Program in the Wu Tsai Neuroscience Institute and Bio-X (S.P.P.), Kwan Funds (S.P.P.), Senkut Funds (S.P.P.), the Ludwig Foundation (S.P.P.), the Mann Foundation (S.P.P.), the New York Stem Cell Foundation (NYSCF) (S.P.P.), the Nurturing Next-generation Researchers Program from the National Research Foundation of Korea (J.K.), the Stanford Science Fellows Program (A.M.V.), the Ford Foundation (postdoctoral fellowship to A.M.V.), the EMBO postdoctoral fellowship ALTF- 321-2021 (S.K.), and Stanford University (M.T.-L.). S.P.P. is a Chan Zuckerberg Initiative (CZI) Ben Barres Investigator and a CZ BioHub Investigator. **Competing interests:** Stanford University holds patents for the generation of spinal cord organoids titled "Functional cortico-spinal-muscle assembled spheroids" listing S.P.P. as an inventor (US Patent 12,110,510) and a provisional patent application for the generation of hFpO and hMA titled "Generation of neural organizer organoids and midline assembloids from human pluripotent stem cells" listing S.P.P., M.O., and N.A. as inventors (US Patent application number 18/726,382). S.P.P. is a consultant for STEMCELL Technologies. M.T.L. is the chairman and CEO of Xiara Therapeutics and director of Denali Therapeutics; N.D.A. is the CEO of Scuplta Inc. **Data and materials availability:** Data generated for the analyses presented in this work are available in the Gene Expression Omnibus (accession number GSE268918; token: ofkbkkyidvwtjod). Datasets from the DepMap Portal (https://depmap.org/portal/) were used. The scRNA-seq data from primary fetal spinal cells were generated by Rayon *et al*. (*56*) and were downloaded from the Gene Expression Omnibus (accession number GSE171892). Source data are provided in the supplementary materials.

License information: Copyright © 2025 the authors, some rights reserved; exclusive licensee American Association for the Advancement of Science. No claim to original US government works. https://www.science.org/about/science-licenses-journal-article-reuse

SUPPLEMENTARY MATERIALS

science.org/doi/10.1126/science.adq7934
Materials and Methods; Figs. S1 to S13; References (*51*–*62*); Tables S1 to S7; Movies S1 to S3; Data S1 to S6; MDAR Reproducibility Checklist

Submitted 3 June 2024; resubmitted 8 March 2025; accepted 15 May 2025
10.1126/science.adq7934

MATERIALS SCIENCE

Dome-celled aerogels with ultrahigh-temperature superelasticity over 2273 K

Kai Pang[1]†, Yuxing Xia[1]†, Xiaoting Liu[1]†, Wenhao Tong[2]†, Xiaotong Li[1], Chenyang Li[1], Wenbo Zhao[1], Yan Chen[2], Huasong Qin[2], Wenzhang Fang[1], Li Peng[1], Yilun Liu[2], Weiwei Gao[1], Zhen Xu[1]*, Yingjun Liu[1]*, Chao Gao[1]*

Aerogels are known for their high porosity and very low density and can be made from a range of materials, but are limited by structural instability under extreme thermomechanical conditions. We report on 194 types of dome-celled ultralight aerogels that maintain superior elasticity spanning from 4.2 kelvin (K) to 2273 K, realized by a two-dimensional channel–confined chemistry method. Such aerogels exhibit superelasticity under 99% strain for 20,000 cycles and thermal shock resistance at 2273 K over 100 cycles. The high-entropy carbide aerogel achieves a thermal conductivity of 53.4 $mW{\cdot}m^{-1}{\cdot}K^{-1}$ at 1273 K and 171.1 $mW{\cdot}m^{-1}{\cdot}K^{-1}$ at 2273 K. The combination of temperature-invariant elasticity and chemical diversity makes such aerogels highly promising for extreme thermomechanics, from heat-insulated industries to deep space exploration.

Aerogels have emerged as an important family of materials that feature high porosity and low density, which enables a wide range of applications in space exploration, sensing, thermal management, and chemical catalysis (*1*–*4*). Various aerogels have been progressively synthesized using the conventional sol-gel method, spanning metals, oxides, chalcogenides, carbides, carbons, organics, and multinary compounds (*4*–*13*) (table S1). However, most sol-gel aerogels tend to exhibit mechanical brittleness and poor elasticity due to their intrinsic weak zero-dimensional granular connections (*4*, *5*).

To overcome the intrinsic weakness of aerogels, a geometrical design of structures has been developed to achieve outstanding mechanical elasticity at high porosity, typically through intertwining one-dimensional fibers or nanotubes (*14*–*20*), and assembling two-dimensional (2D) nanosheets to honeycomb and arched cell structures, as well as the formation of macroscopic hyperbolic meta-patterns (*21*–*26*) (table S2). Despite these advances, aerogels still face challenges in maintaining thermomechanical stability under extreme thermal and mechanical conditions due to unstable crystalline structure at high temperatures and the structural fragility under large mechanical deformation (*4*, *27*).

The flexible amorphous domain is a crucial component for maintaining the elasticity of ceramic aerogels at normal conditions, but its presence considerably lowers their thermal stability compared with bulk crystalline ceramics. Previous efforts to improve thermal stability of elastic ceramic aerogels have primarily focused on restricting the migration of amorphous domains, which achieved a maximum working temperature of 1973 K (*27*). Although graphene materials exhibit melting points exceeding 3000 K, their mechanical softening temperature is limited to below 2273 K (*28*), precluding stable thermomechanical performance under such extreme conditions.

Aerogel fabrication

We report a general 2D channel–confined chemistry method to synthesize a series of ultralight dome-celled aerogels across hundreds material species, covering 121 oxide, 38 carbide, and 35 metal species, with compositions tunable to high-entropy states containing up to 30 elements. We propose a dome microstructure with two nonzero principal curvatures (κ_1 and κ_2, fig. S1) as basic cells, introducing curvature as an alternative structural parameter for aerogel design. The dome structure, commonly found in biology and architectural engineering, is well known for its excellent load-bearing capacity and mechanical stability (fig. S2). Finite element analysis reveals that a dome exhibits a capability for storing elastic strain energy that is at least 10 times greater than that of conventional honeycomb and arch structures (fig. S3). This becomes more pronounced for aerogels with thinner cell walls, as it generates richly recoverable wrinkles to store elastic energy (fig. S4), due to its undevelopable surface characteristics. This comparative analysis demonstrates that the dome structure is a preferable geometric design for ultralight aerogels, potentially enabling superior elasticity under large deformation.

Experimentally, we used a general 2D channel–confined chemistry method to prepare dome-celled aerogels, starting from macroscopic assembled graphene oxide (GO) films. The method is continuously processed by three steps: ion capturing, bubbling, and heat conversion (Fig. 1A). GO was chosen as a 2D channel precursor because of its abundant chemical moieties, atomic thickness, and large-scale commercial availability (*29*), exhibiting high compatibility for fabricating dome-celled aerogels. Water easily penetrates into GO interlayer channels, forming a 2D confined nanospace with distance (d) from 0.97 to 2.14 nm (fig. S6A). When immersed in salt solutions (single or multiple ion species up to 30 kinds), the diffused ions are captured into GO interlayer channels by chelation interaction with oxygen functional groups (*29*) and the 2D barrier effect allows avoidance leakage of ions (*30*), forming confined precursor hybrids. The GO-ion hybrid exhibited an atomic uniformity in hybridization, as shown by x-ray diffraction (XRD) (single peak at 6.2°; fig. S6B) and homogeneous elemental distribution in interlamination, whether single or multiple ions (figs. S7 and S8).

Decomposing gas from the foaming reagent generates bubbles in the GO interlayer gallery (*31*), forming cells with a dome shape that contribute to the flexibility of GO-ion laminates. The dome cells inherit the non-Euclidean curvature of spherical bubbles, distinct from the regular polyhedral cell formed by the conventional ice templating method (*16*, *23*–*26*). By controlling the pressure by bubbling time, the average curvature (K_a) of dome cells is tuned from 0.045 to 0.122 μm^{-1} (fig. S9). Our hybrid aerogels were prepared by direct drying in air, avoiding the complex and costly freeze or supercritical drying methods (*4*).

We thermally treated the hybrid aerogels at 600°C for 4 hours with air to remove GO and yield neat oxide aerogels with dome-celled microstructures, extending from unary to high-entropy constituents. We used XRD, x-ray photoelectron spectroscopy, energy dispersive spectroscopy, special aberration correlated transmission electron microscopy (AC-TEM), and atomic mapping to demonstrate the confined formation mechanism that preserves the dome shape (figs. S6 to S8). Taking the Al_2O_3 aerogel as an example, atomically dispersed Al^{3+} ions in 2D confined channels gradually transform into polycrystalline oxide lamella by forming interconnected nanocrystals (fig. S10), instead of large-sized crystallite aggregates without confinement (*32*). For complex combinations of elements, local confined ions (such as Al, Ti, Cr, Co, and Ni) form polycrystalline oxide lamellae with high mixing homogeneity across a micrometer scale at minimum (fig. S11). By contrast, annealing ions only absorbed on GO surface forms coarse oxide

[1]MOE Key Laboratory of Macromolecular Synthesis and Functionalization, International Research Center for X Polymers, Zhejiang Key Laboratory of Advanced Organic Materials and Technologies, Research Center for Advanced Fibers, Department of Polymer Science and Engineering, Zhejiang University, Hangzhou, China. [2]Laboratory for Multiscale Mechanics and Medical Science, SV LAB, School of Aerospace, Xi'an Jiaotong University, Xi'an, China. ***Corresponding author. Email: zhenxu@zju.edu.cn (Z.X.); yingjunliu@zju.edu.cn (Yin.L.) chaogao@zju.edu.cn (C.G.)** †These authors contributed equally to this work.

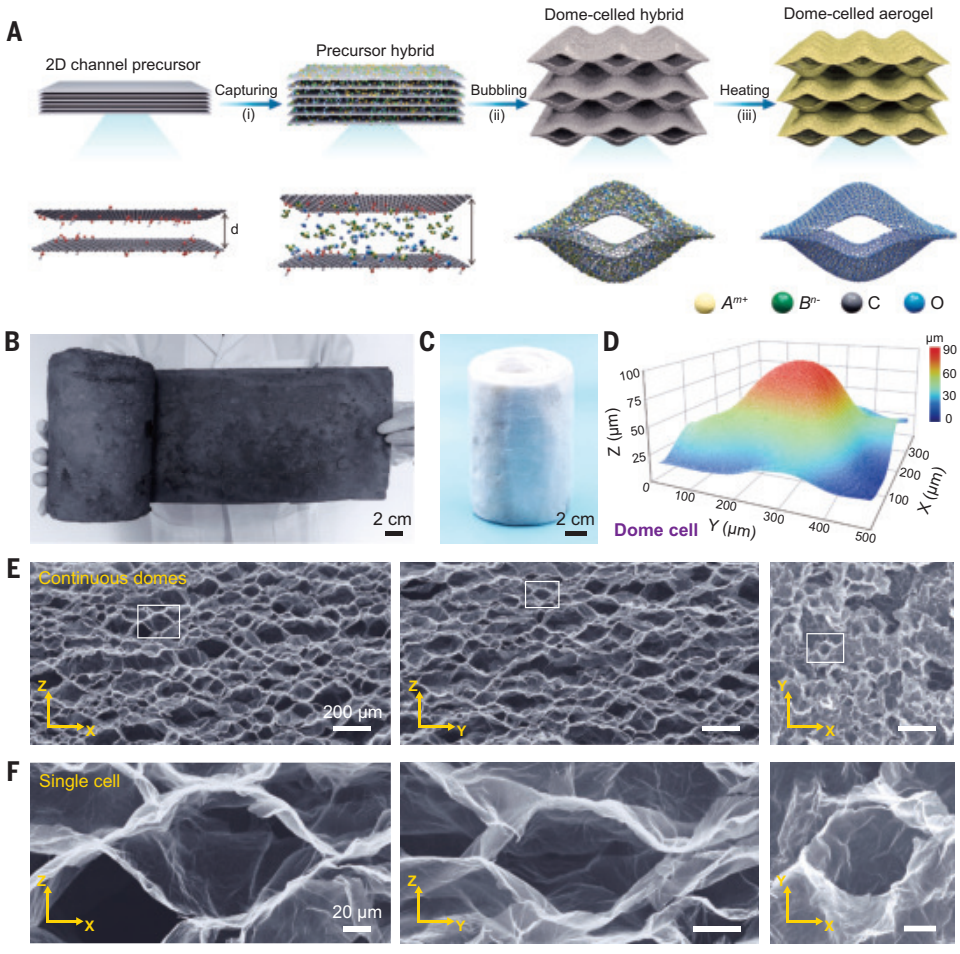

Fig. 1. Graphene-based 2D channel–confined chemistry for dome-celled aerogels. (**A**) Preparation of aerogels from the 2D channel precursor in three steps: (i) Salt ions are captured by the tunable GO channels; (ii) the solvent bubbling with foaming agent is adopted to fabricate a dome-celled hybrid; and (iii) the heat conversion process is conducted at 600°C in air for 4 hours, 2000°C in an argon atmosphere for 2 hours, or 450°C in a hydrogen atmosphere for 1 hour, to fabricate oxide, carbide, or metal aerogels, respectively. (**B** and **C**) Digital photos of as-prepared carbide plate and oxide roll aerogels. (**D**) 3D optical image of a dome cell model made by bubbling an ultrathin GO film (~500-nm thickness). (**E** and **F**) SEM analysis of dome-celled aerogel from slicing images in three directions (the X-Z, Y-Z, and X-Y planes).

crystallites, leading to the collapse of dome cells (fig. S12). By pairing species and controlling proportion of captured ions, we obtained high-entropy oxide aerogels (fig. S13 and table S3). Subsequently, the oxide aerogels were thermally reduced into metal ones by hydrogen at 450°C for 2 hours. Additionally, thermal annealing of second-step hybrid aerogels at 2000°C for 2 hours in argon activated the reaction between oxide and graphene, resulting in carbide aerogels. Alternatively, the graphene framework can be retained in these aforementioned aerogels by controlling the GO/ion ratio and heating atmosphere.

Based on the GO films, we prepared aerogel bricks of oxide, carbide, and metal members. To meet more practical application demands, other macroscopic aerogel forms of large-scale plates (~50×20×0.5 cm^3) and continuous rolls (>2 m) (Fig. 1, B and C, and fig. S14), were obtained.

We performed 3D optical profilometer and x-ray nano-computed tomography (nano-CT) to validate the dome shape of the cells. A representative cell unit was extracted to illustrate the geometrical nature of the dome shape. The dome vertex has two orthometric positive Gaussian curvatures, interconnected by saddle-shaped edges (Fig. 1D, fig. S15, and movie S1). After heat treatment, the dome-celled aerogels maintained seamless contact between structural cells (fig. S16), ensuring their structural stability and integrity. When extended to the macroscale (Fig. 1, E and F), vertical (X-Z and Y-Z planes) and horizontal (X-Y plane) slicing of aerogel using both scanning electron microscope (SEM) and nano-CT confirmed the dome shape of cells. Dome cell sizes range from tens to hundreds of microns. Layer-by-layer nano-CT slicing further reveals that the interconnected dome cells are homogeneous across the millimeter scale (movie S2).

Broad chemical diversity

We synthesized hundreds of dome-celled aerogels (194 types) with broad chemical diversity, encompassing oxide, metal and carbide components, and involving more than 30 elements (Fig. 2A). The aerogels are sufficiently diverse to form a comprehensive library, including 20 unary, 30 binary, 30 ternary, and 41 high-entropy oxides; 8 unary, 10 binary, 10 ternary, and 10 high-entropy carbides; and 5 unary, 10 binary, 10 ternary, and 10 high-entropy metals (figs. S17 to S22). These aerogels feature ultralow density (ρ), ranging from 0.35 to 13.78 mg·cm^{-3}, irrespective of elemental composition. In the density spectrum, most of our aerogels fall within the extralight (ρ < 1.29 mg·cm^{-3} of air) and ultralight (ρ < 10 mg·cm^{-3}) ranges (fig. S23).

Figure 2, B to F shows representative oxide, carbide, metal, and high-entropy aerogels with hydrolytic stability (fig. S24), which can float on flower buds as a result of their lightness. All aerogels possess dome-celled structures, comprising 2D curved walls and micro-sized pores (70 to 140 μm; fig. S25), as observed in SEM vertical sections. The thin walls are composed of planar interconnected nanosized crystal grains (AC-TEM) and have a thickness <10 nm (fig. S26) resulting from the confined growth of the crystals (*33*). The ultrathin wall thickness contributes to the ultralow density of our aerogels. Detailed examinations reveal that oxide, carbide, and metal aerogels generally exhibit structural and compositional uniformity (figs. S27 to S34). To confirm the atomic-scale homogeneity in high-entropy cases, we used high-angle annular dark-field (HAADF) imaging and atomic mapping, finding that up to 30 arbitrary elements were thoroughly mixed at the atomic scale (figs. S21, S22, and S35 to S37). In these high-entropy aerogels (figs. S38 to S40), three similar elements at minimum were preferentially chosen to minimize the mixing enthalpy, and other additional elements were incorporated to further increase the mixing entropy (*34*, *35*).

Extreme thermomechanics

All aerogels in the library exhibited exceptional elasticity, regardless of chemical species, elemental compositions, and density. We first investigated the mechanical elasticity of our aerogels under quasistatic compression. Intuitively, a stack of oxide, carbide, and metal aerogels with ~30% retained graphene—ranging from unary to high-entropy components—was compressed at an extreme strain of 99% and fully

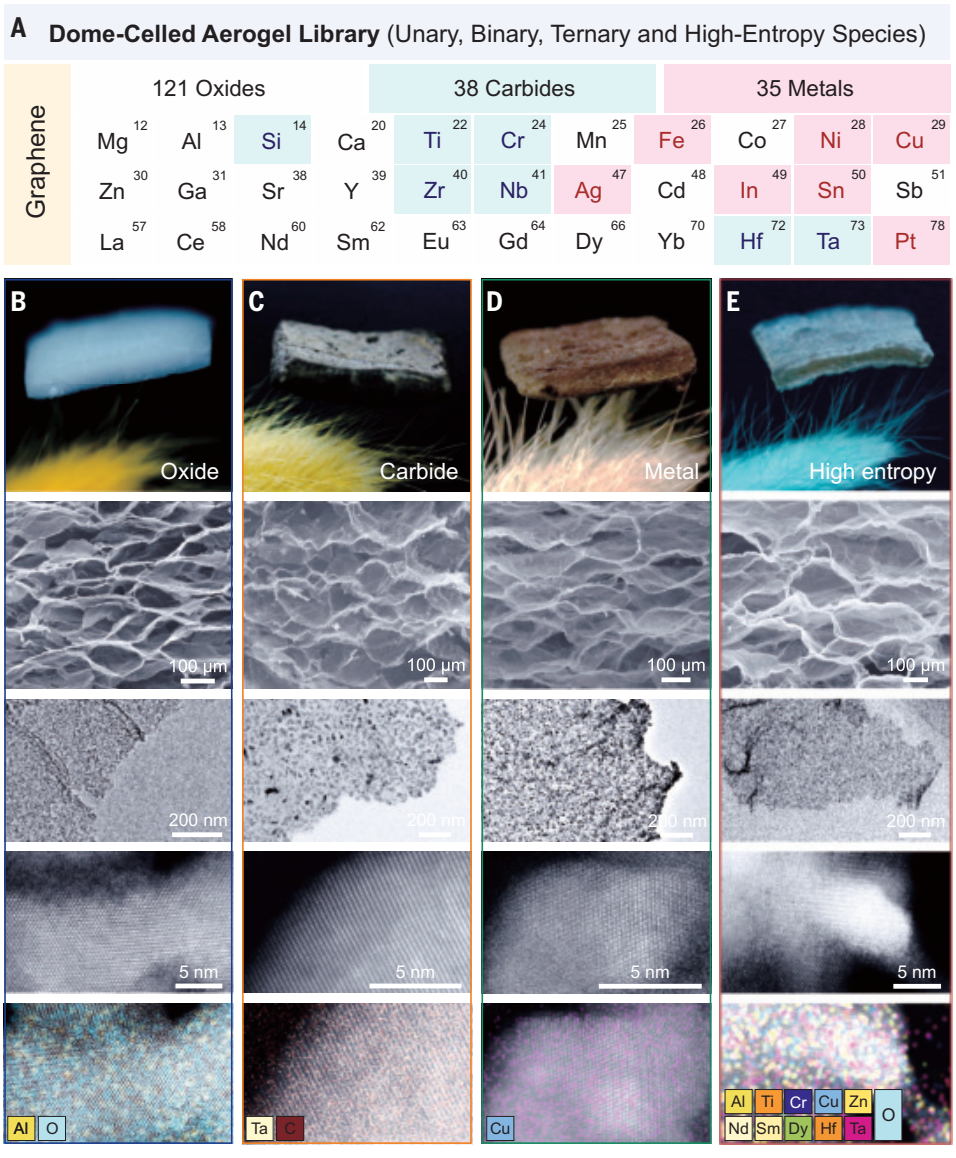

Fig. 2. Chemical diversity of dome-celled aerogels and their multiscale structures. (**A**) Elemental overview of the aerogel library for oxides (highlighted in yellow, except for Ag and Pt), carbides (highlighted in blue), and metals (highlighted in red). (**B** to **E**) Optical images of unary aluminum oxide (Al_2O_3), tantalum carbide (TaC), copper (Cu), and high-entropy denary AlTiCrCuZnNdSmDyHfTa oxide aerogels (from left), and their corresponding structure characterizations by SEM, AC-TEM, and HAADF atomic elemental mapping.

recovered to the original height after the pressure was released (Fig. 3A and movie S3). These aerogels could be repeatedly compressed at 99% strain for 20,000 cycles with nearly unchanged sample height (residual strain <3%) and minimal stress degradation (<20%). Extralight oxide aerogels (ρ of 0.35 to 1.24 mg·cm^{-3}) with compositions (Y_2O_3 and InSn, AlCrYLaCe, and MgAlCrMnFeCoNiCuSrYIn oxides) exhibiting stable elasticity and little strain degradation (<8%) at 80% strain up to 10,000 cycles (figs. S41 and S42 and movie S4), indicating excellent fatigue resistance.

We investigated the deformation behavior of the dome cell by in situ compression experiments. Under a 3D optical profilometer, the dome cell underwent doubly curved deformation in two principal directions (fig. S43), demonstrating the typical undevelopable surface nature of dome structures (fig. S1). In situ SEM observation shows that massive fine wrinkles emerged at higher strain (80%), which avoids the smooth and compact contact between nanowalls and favors the elastic recovery (Fig. 3B and movie S5). These experimental results validate the design rationale behind the dome cell as the expected aerogel structure for achieving high elasticity at ultralow density. By contrast, the flat walls of the honeycomb aerogel control sample were deformed along the longitudinal direction to form a smooth compact contact, resulting in its limited resilience (fig. S44, A to D). When scaled up, these dome cells became interconnected through a surface contact (Fig. 1 and fig. S15), efficiently transferring the load across the network (*31*) and enhancing the macroscopic elasticity of our aerogels, regardless of material components or heat treatment processes (fig. S44, E and F). By controlling cell curvature, we detected that larger curvature generates better mechanical resilience (fig. S45). When plotted on the elasticity-density map of aerogels (Fig. 3C and table S2), our aerogels not only exhibit exceptional mechanical recoverability under large strains (99%) but also break through the limits of elasticity at extreme lightness (*4*, *16*–*19*, *22*–*26*, *36*–*43*).

We investigated the crystalline structure of dome-celled carbide aerogels. On the dome wall, the carbide sheet nanograins are tightly inserted into graphene planar sheets in a mosaic pattern, (figs. S46 and S47). Below a carbide content of 88 weight percent (wt%), the carbide mosaic grains maintain a planar shape with lateral size increasing from the nanoscale (~5 nm) to the microscale (~50 nm), exhibiting confinement by graphene. Further mechanical tests (fig. S48, A to D) demonstrated dome-celled carbide aerogel with a carbide content <88 wt% displayed excellent mechanical recoverability under compressive strain of 90% in the vertical direction, surpassing its performance in the horizontal direction (fig. S49). By contrast, the freeze-dried honeycomb carbide aerogel (63 wt% carbide content) failed to recover to its original height at 90% strain after 10 cycles (fig. S48E), further highlighting the mechanical superiority of the dome-celled structure.

Under extreme thermomechanical working conditions, the carbide dome-celled aerogel demonstrated superelasticity across an ultrawide temperature range, spanning from 4.2 to 2273 K. We stacked six carbide aerogel plates (average density $\bar{\rho}$, 9.24 mg·cm^{-3}) and tested their compressive elasticity at 99% strain under liquid helium (4.2 K) (Fig. 3D and movie S6). The stack exhibited nearly identical compressive curves at both the 1st and 100th cycles, with no change in height. To explore the elasticity under extreme heat conditions, we transferred the same aerogel stack to an ultrahigh-temperature furnace and performed cycling compression tests in a vacuum. At 2273 K, the stack—compressed to 99% strain—recovered to its original state for 100 cycles (~2 hours). The coincident stress-strain curves at the 1st and 100th cycles confirmed the superior recoverability of our aerogels at ultrahigh temperature (Fig. 3E and movie S7) and excellent structural

stability (fig. S50). By contrast, neat graphene aerogels exhibited substantial plastic deformation at 2273 K (fig. S48F) due to the softening effect of graphene sheets at such high temperatures (*28*).

Our carbide aerogels demonstrate superelasticity at both extremely high temperatures and ultralow densities (<10 mg·cm^{-3}). We further evaluated the elasticity of these aerogels by exposing them to bilateral butane blowtorch flames in air (over 1573 K) and observed no apparent structural collapse (movie S8). The nearly coincident compressive curves at different strains (20 to 99%) and 100 repeated cycles (99% strain) confirm their excellent ablative-resisting and superelasticity (Fig. 3F and fig. S51).

Thermal superinsulation at ultrahigh temperatures

The chemical diversity of our aerogels also imparts a broad spectrum of functions (figs. S52 to S56). With their excellent high-temperature stability, our carbide aerogels offer attractive thermal superinsulation under extreme conditions. A peak anisotropic ratio ($\lambda_{horizontal}/\lambda_{vertical}$) of thermal conductivity (λ) was found at ~70% carbide content, enabling the lowest λ in the vertical direction (fig. S57). This trend can be attributed to the anisotropy of 2D topology of ultrathin walls, which facilitates the heat transport along the vertical direction and retards the thermal transport in the other horizontal direction. Our carbide aerogels presented the low λ from 173 to 2273 K (Fig. 4A) due to the

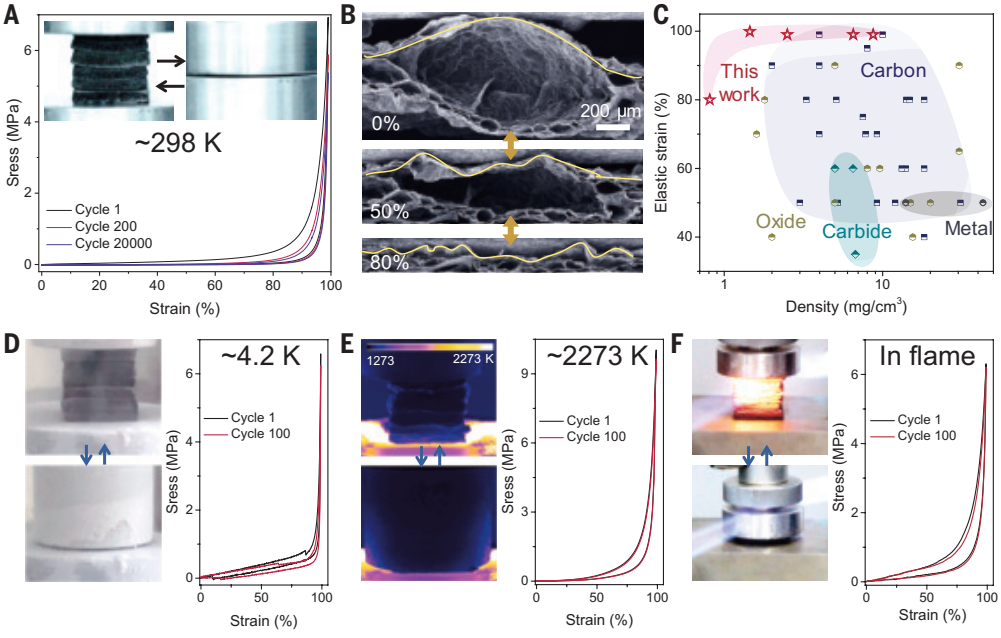

Fig. 3 Mechanical properties of dome-celled aerogels. (**A**) Compressive stress-strain curves of a stack of representative dome-celled aerogels subjected to 99% strain for 20,000 cycles at room temperature (298 K). The stacked aerogels include Al_2O_3, TaC, Cu, (TiZr)C, (AlTiCrCoNi)O, and (AlTiCrCuZnNdSmDyHfTa)O (from top), each containing ~30% graphene. (**B**) In situ SEM observations showing the vertical section of a dome cell during compression. (**C**) Plot of the maximum recoverable strain versus apparent density of dome-celled aerogels, compared with previously reported aerogels. (**D** and **E**) Compressive stress-strain curves of a stack of carbide aerogels subjected to 99% strain for 100 cycles at 4.2 K and 2273 K. (**F**) Compressive stress-strain curves of a stack of carbide aerogels subjected to 99% strain for 100 cycles in the bilateral flame of a butane blowtorch. (Inset) Experimental snapshots taken during the cycles. All stacked carbide aerogels include ZrC, TaC, TiC, (TiZr)C, (TiCrTa)C, and (ZrTiHfNbTa)C (from top).

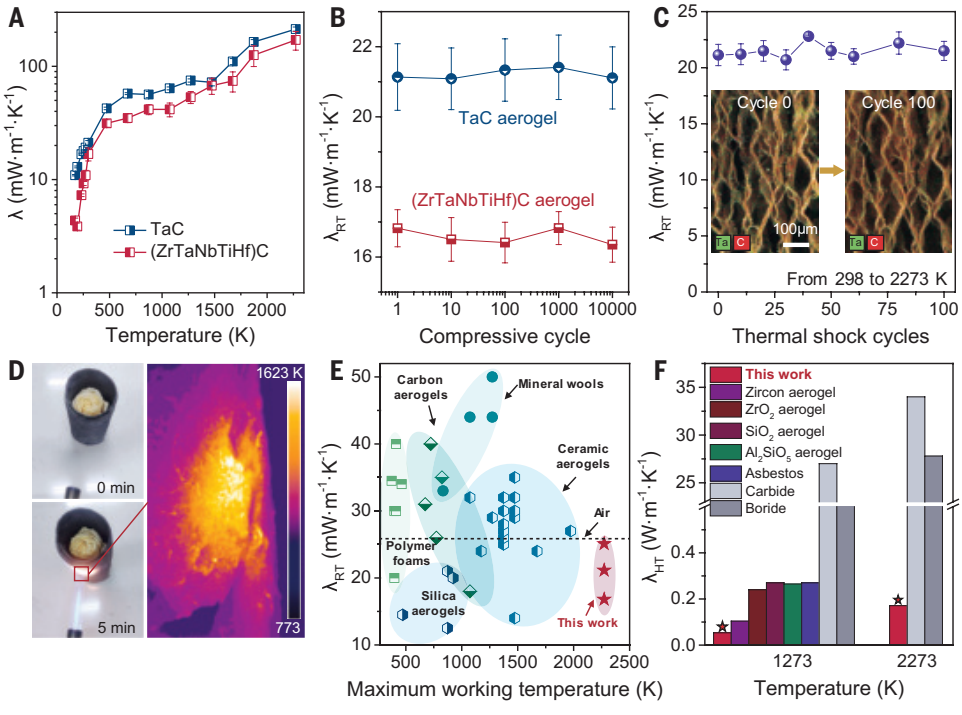

Fig. 4. Thermal superinsulation of carbide aerogels. (**A**) Thermal conductivity of TaC and high-entropy (ZrTaNbTiHf)C aerogels measured from 173 to 2273 K. (**B**) Room-temperature thermal conductivity of TaC and high-entropy (ZrTaNbTiHf)C aerogels during compression at 99% strain for 10,000 cycles. (**C**) Thermal conductivity variation of TaC aerogel during thermal shock at 2273 K (500 K s^{-1} below 1773 K and 100 K s^{-1} from 1773 to 2273 K) for 100 cycles. (Inset) Structure and elemental distribution of TaC aerogels. (**D**) Photographs illustrating the thermal protection provided by TaC aerogels and the corresponding thermal imaging map. (**E**) Comparative diagram of maximum working temperature versus room-temperature (RT) thermal conductivity (λ_{RT}) for typical insulators and our carbide aerogels (including TaC, ZrC, and high-entropy ZrTaNbTiHf carbide aerogels). (**F**) High-temperature (HT) thermal conductivity (λ_{HT}) at 1273 K and 2273 K for our carbide aerogel compared with previously reported representative ceramics.

diluted solid transport (ultralow density and nanograin boundaries), restrained gas transport with nanopores (~30 nm), and 2D anisotropy effect (figs. S58 and S59). Additionally, we found that the high-entropy (ZrTaNbTiHf)C aerogel possessed a lower λ than that of unary, binary, and ternary carbide aerogel (fig. S58D), with values of 53.4 $mW{\cdot}m^{-1}{\cdot}K^{-1}$ at 1273 K and 171.1 $mW{\cdot}m^{-1}{\cdot}K^{-1}$ at 2273 K. This high-entropy effect (*44*–*46*) was also shown by dome-celled oxide aerogels, which exhibited ultralow thermal conductivity (λ~13.4 $mW{\cdot}m^{-1}K^{-1}$) of (YTiLaCeNdSmGdDyEuHf oxide) in the vertical direction (fig. S52, C and D), surpassing benchmark silica aerogel and most reported insulating aerogels (*4*, *16*, *38*, *39*, *47*).

We further demonstrated that our carbide aerogels exhibit high mechanical and thermal stability. Even after mechanical fatigue tests for 10,000 cycles at room temperature and 100 cycles at 2273 K, the λ of these insulating aerogels remained stable at the ultralow level (Fig. 4B and fig. S60A), demonstrating the excellent structural stability and resistance to deformation. At 1573 K, our aerogel showed a much smaller thermal expansion coefficient (TEC) of ~1.8×10^{-6} K^{-1}, compared with a neat ceramic bulk (TEC~12.4×10^{-6} K^{-1}) (fig. S60B), further indicating the high-temperature structural stability. We then measured its thermal stability under rapid thermal shocks at an ultrahigh temperature (2273 K) using a pulse-heating furnace. The sample retained its original morphology after 100 thermal shock cycles, with nearly unchanged thermal conductivity (Fig. 4C). As a demonstration, an 8-mm-thick plate of carbide aerogel effectively protected a fresh rose when exposed to butane blowtorch flames for 5 min at temperatures exceeding 1573 K (Fig. 4D and movie S9). The mass retention ratio of carbide aerogels was ~97% after exposure to air for four hours (fig. S60C). Compared with reported high-temperature ceramic aerogels (*25*, *42*, *48*), our synthesized aerogels present a much lower λ at elevated operating temperatures up to 2273 K (Fig. 4E). The λ of carbide aerogel at high temperature is far below other aerogels and conventional insulators (Fig. 4F) (*18*, *49*, *50*), demonstrating exceptional high-temperature thermal insulating performance and reliability in extreme service environments.

In conclusion, a general graphene-based 2D channel-confined chemistry is demonstrated to fabricate a library of ultralight superelastic aerogels (194 species) with diverse materials, 35 elements, and arbitrary elemental combinations. The dome-celled microstructure imparts superelasticity even at apparent densities lower than that of air, allowing the aerogels to withstand more than 20,000 fatigue cycles at 99% strain. This ultralight aerogel library achieves both superior mechanical elasticity and ultralow thermal conductivity in a wide temperature range from 4.2 to 2273 K, considerably extending space of aerogels for extreme thermomechanics. The broad chemical diversity enables substantial design flexibility, facilitating the integration of optical, thermal, electrical, and magnetic properties.

REFERENCES AND NOTES

1. R. Wordsworth, L. Kerber, C. Cockell, *Nat. Astron.* **3**, 898–903 (2019).
2. M. Zhang *et al.*, *Science* **309**, 1215–1219 (2005).
3. S. Bag, A. F. Gaudette, M. E. Bussell, M. G. Kanatzidis, *Nat. Chem.* **1**, 217–224 (2009).
4. X. Xu *et al.*, *Mater. Today* **42**, 162–177 (2020).
5. S. S. Kistler, *Nature* **127**, 741 (1931).
6. X. Jiang, R. Du, R. Hübner, Y. Hu, A. Eychmüller, *Matter* **4**, 54–94 (2021).
7. *Aerogels Handbook*. M. A. Aegerter, N. Leventis, M. M. Koebel, Eds. (Springer, 2011).
8. N. Hüsing, U. Schubert, *Angew. Chem. Int. Ed.* **37**, 22–45 (1998).
9. J. L. Mohanan, I. U. Arachchige, S. L. Brock, *Science* **307**, 397–400 (2005).
10. W. Ma *et al.*, *Scr. Mater.* **235**, 115596 (2023).
11. L. Han *et al.*, *J. Am. Ceram. Soc.* **106**, 841–847 (2023).
12. J. T. Cahill *et al.*, *Chem. Mater.* **31**, 3700–3704 (2019).
13. N. Leventis, A. Sadekar, N. Chandrasekaran, C. Sotiriou-Leventis, *Chem. Mater.* **22**, 2790–2803 (2010).
14. M. A. Worsley, S. O. Kucheyev, J. H. Satcher Jr., A. V. Hamza, T. F. Baumann, *Appl. Phys. Lett.* **94**, 073115 (2009).
15. M. B. Bryning *et al.*, *Adv. Mater.* **19**, 661–664 (2007).
16. F. Wu, Y. Liu, Y. Si, J. Yu, B. Ding, *Nano Today* **44**, 101455 (2022).
17. L. Li *et al.*, *Nat. Commun.* **14**, 5410 (2023).
18. J. Guo *et al.*, *Nature* **606**, 909–916 (2022).
19. T. A. Schaedler *et al.*, *Science* **334**, 962–965 (2011).
20. L. R. Meza, S. Das, J. R. Greer, *Science* **345**, 1322–1326 (2014).
21. M. A. Worsley *et al.*, *J. Am. Chem. Soc.* **132**, 14067–14069 (2010).
22. Z. Xu, Y. Zhang, P. Li, C. Gao, *ACS Nano* **6**, 7103–7113 (2012).
23. M. Wu *et al.*, *Nat. Commun.* **13**, 4561 (2022).
24. L. Qiu, Z. He, D. Li, *Adv. Mater.* **30**, 1704850 (2018).
25. X. Xu *et al.*, *Science* **363**, 723–727 (2019).
26. H. L. Gao *et al.*, *Nat. Commun.* **7**, 12920 (2016).
27. Z. Xu *et al.*, *Adv. Mater.* **36**, e2401299 (2024).
28. S. Sato, H. Awaji, H. Akuzawa, *Carbon* **16**, 95–102 (1978).
29. D. Chang *et al.*, *Science* **372**, 614–617 (2021).
30. T. Mouterde *et al.*, *Nature* **567**, 87–90 (2019).
31. K. Pang *et al.*, *Sci. Adv.* **6**, eabd4045 (2020).
32. X. Bai *et al.*, *Nat. Mater.* **23**, 747–754 (2024).
33. J. Zhao *et al.*, *Science* **343**, 1228–1232 (2014).
34. Y. Yao *et al.*, *Science* **376**, eabn3103 (2022).
35. C. Oses, C. Toher, S. Curtarolo, *Nat. Rev. Mater.* **5**, 295–309 (2020).
36. Q. Zhang *et al.*, *Adv. Mater.* **29**, 1605506 (2017).
37. H. Guo *et al.*, *Adv. Mater.* **35**, e2301418 (2023).
38. C. Zhu *et al.*, *Nat. Commun.* **6**, 6962 (2015).
39. X. Cheng, Y. T. Liu, Y. Si, J. Yu, B. Ding, *Nat. Commun.* **13**, 2637 (2022).
40. L. Li *et al.*, *Mater. Today* **54**, 72–82 (2022).
41. Y. Si, X. Wang, L. Dou, J. Yu, B. Ding, *Sci. Adv.* **4**, eaas8925 (2018).
42. L. Su *et al.*, *Sci. Adv.* **6**, eaay6689 (2020).
43. S. Vinod *et al.*, *Nat. Commun.* **5**, 4541 (2014).
44. L. Gibson, M. Ashby, *Cellular Solids: Structure and Properties* (Cambridge Univ., 1997), pp. 283–307.
45. B. Notario *et al.*, *Polymer* **56**, 57–67 (2015).
46. F. Hu, S. Wu, Y. Sun, *Adv. Mater.* **31**, e1801001 (2019).
47. S. Zhao *et al.*, *Nature* **584**, 387–392 (2020).
48. L. Han *et al.*, *Nat. Commun.* **15**, 6959 (2024).
49. E. C. Schwind, M. J. Reece, E. Castle, W. G. Fahrenholtz, G. E. Hilmas, *J. Am. Ceram. Soc.* **105**, 4426–4434 (2022).
50. R. Mitra *et al.*, *J. Mater. Res.* **38**, 2122–2136 (2023).

ACKNOWLEDGMENTS

We thank G. Zhu and Y. Zeng of the Center of Electron Microscopy of Zhejiang University for assistance with performing the AC-TEM measurements. **Funding:** This work is funded by the National Natural Science Foundation of China (grants 52090031, 52090030, 52122301, 52272046, 12325204, and 12472108); National Key Research and Development Program of China (2022YFA1205300 and 2022YFA1205301); "Pioneer" and "Leading Goose" R&D Program of Zhejiang (2023C01190); Natural Science Foundation of Zhejiang Province (grant LR23E020003); and the Fundamental Research Funds for the Central Universities (grants 226-2024-00074 and 226-2024-00172). **Author contributions:** Conceptualization: K.P., Z.X., Yin.L., and C.G. Methodology: K.P., X.T.L., Z.X., Yin.L., and C.G. Investigation: K.P., Y.X., Y.X.X., X.T.L., W.H.T., X.T.L., C.Y.L., W.B.Z., Y.C., H.S.Q., W.Z.F., and L.P. Visualization: K.P., Z.X., Yin.L., Yil.L., and C.G. Funding acquisition: Z.X., Yin.L., W.W.G., H.S.Q., Yil.Li., and C.G. Project administration: Z.X. and C.G. Supervision: Z.X., Yin.L., and C.G. Writing – original draft: K.P., Z.X., and C.G. Writing – review & editing: K.P., Y.X., X.T.L., W.H.T., Z.X., Yin.L., and C.G. **Competing interests:** C.G. and K.P. are listed as inventors on a China National Intellectual Property Administration patent application filed under the Patent Cooperation Treaty (PCT/CN2025/076908, pending), which covers a preparation method for ceramic aerogels and their applications. All other authors declare no competing interests. **Data and materials availability:** All data are available in the main text or the supplementary materials.
License information: Copyright © 2025 the authors, some rights reserved; exclusive licensee American Association for the Advancement of Science. No claim to original US government works. https://www.science.org/content/page/science-licenses-journal-article-reuse

SUPPLEMENTARY MATERIALS

science.org/doi/10.1126/science.adw5777
Materials and Methods; Supplementary Text; Figs. S1 to S60; Tables S1 to S3; References (*51*–*59*); Movies S1 to S9

Submitted 7 February 2025; accepted 23 May 2025

10.1126/science.adw5777

ORGANIC CHEMISTRY

Bridging the pyridine-pyridazine synthesis gap by skeletal editing

Mikus Puriņš, Hikaru Nakahara, Mark D. Levin*

Pairs of heterocycles differing by a single constitutive ring atom can exhibit stark differences in the retrosynthetic disconnections available for their preparation. Such a synthesis gap is exemplified by pyridine and pyridazine. Pyridine (a six-membered C_5N ring) has risen to prominence in discovery chemistry, its ease of assembly spurring further synthetic development. Despite a host of favorable properties, pyridazine (an analogous C_4N_2 ring) has comparatively lagged behind—a discrepancy attributable to its often-challenging preparation, which arises from an electronically dissonant heteroatom arrangement. In this work, we achieve a single-atom skeletal edit that produces pyridazines from pyridines by direct carbon-to-nitrogen atom replacement: Azide introduction at the ortho position enables a photoinitiated rearrangement of *N*-amino-2-azidopyridinium cations. This transformation links the two heterocycles such that the richness of pyridine retrosynthesis becomes available to pyridazines.

Functional molecules, including medicines, are optimized through iterative synthesis campaigns (*1*), wherein subtle changes to the lead structure, such as skeletal C-to-N replacement (*2*), can markedly affect the physiochemical properties of a drug candidate. However, such campaigns do not sample chemical space (*3*) uniformly in every direction because each new structure requires a new, often disparate synthesis. Chemists will naturally be biased toward compound families with well-established syntheses and functionalization protocols (Fig. 1A); other, less-studied compound classes consequently are at risk of being overlooked owing to this synthesis gap, which could result in missed opportunities during lead optimization (*4*). Skeletal editing reactions (*5*) offer an opportunity to address synthesis gaps by leveraging well-trodden synthetic routes of easily assembled compounds with an appropriate modification to provide access to orphaned core structures. By linking the different scaffolds retrosynthetically with a single chemical transformation, syntheses of the former become applicable to the latter scaffold. This study discusses such a transformation—linking privileged pyridines to underutilized pyridazines.

Pyridazine is a six-membered aromatic heterocycle with two adjacent nitrogen atoms that lead to specific properties (*6*–*9*). Chemically, it will exhibit similar hydrogen-bonding affinity to that of pyridine (pK_{BHX}, 1.7 versus 1.9), but its lower basicity (pK_{BH}, 2.0 versus 5.2) extends this capacity to more acidic environments. In addition, the pyridazine ring has substantially decreased lipophilicity (cLogP, −0.51 versus 0.84) and increased dipole [μ(D), 4.2 versus 2.2], which imparts increased water solubility to pyridazine-containing drugs. It is therefore surprising that although pyridine is the most popular heterocycle in Food and Drug Administration (FDA)–approved drugs in the past decade (*10*, *11*), pyridazine is present in only six such therapeutics (Fig. 1B). Some recent examples of approved medicines containing pyridazines include glutaminase ALK/MET inhibitor ensartinib (approved in 2024) (*12*) and TYK2 inhibitor deucravacitinib (approved in 2022) (*13*). On the basis of the above analysis, we posit that this discrepancy between the two heterocycles is due to a synthesis gap. Whereas pyridine syntheses have been the subject of several books (*14*–*16*), pyridazine synthesis is far less well developed. Pyridine can be traced to consonant (*17*) starting materials, such as 1,3- or 1,5-dicarbonyl compounds. By contrast, pyridazines are usually synthesized from dissonant starting materials, such as 1,4-dicarbonyls/hydrazine (*18*) or 1,2,4,5-tetrazines (*19*). In the retrosynthetic sense, atom transmutation can flip the polarity of one of the nitrogen atoms and thus is the most simplifying skeletal edit. Considering the wide availability of pyridines, a synthetic method that achieves the direct pyridine C(2)-to-N replacement would facilitate the evaluation of pyridazines in discovery chemistry settings.

Department of Chemistry, University of Chicago, Chicago, IL, USA. *Corresponding author. Email: marklevin@uchicago.edu

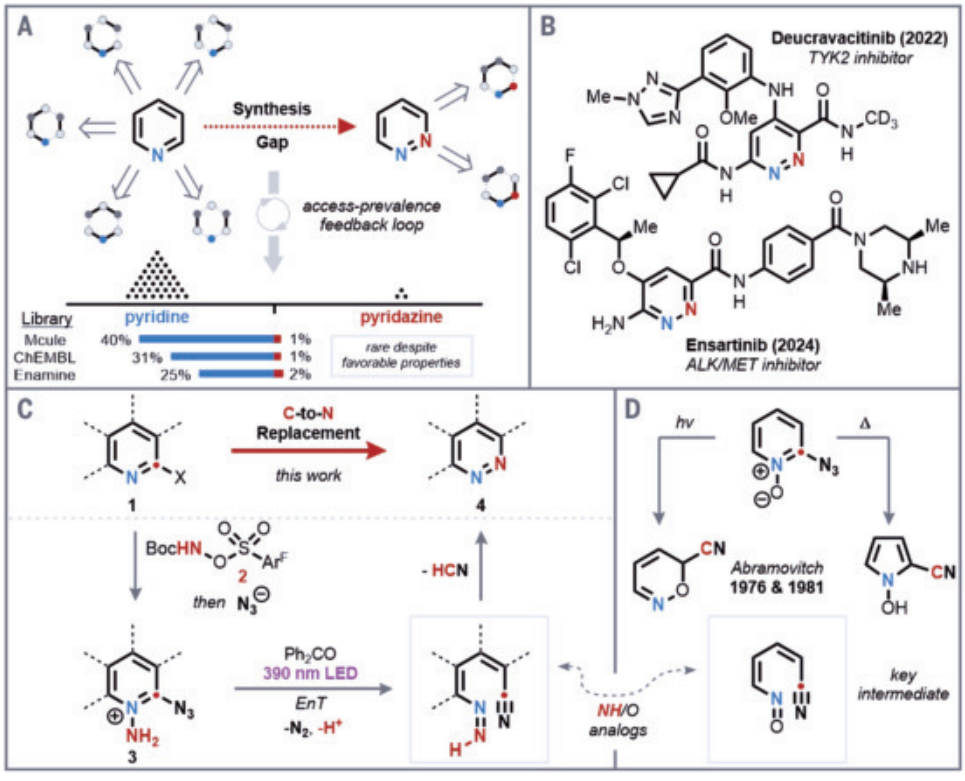

Fig. 1. Rationale and reaction conception. (**A**) Synthesis gap between pyridine and pyridazine. Filled atoms represent nucleophilic centers, and faded atoms represent electrophilic centers. Library composition was reproduced from the literature (*49*). (**B**) Examples of recently approved pyridazine pharmaceuticals. (**C**) Pyridine C(2)-to-N atom replacement reported in this work. (**D**) Relevant precedents of thermal and photochemical rearrangements of 2-azidopyridine *N*-oxides. Ar^F, 3,5-$(CF_3)_2C_6H_3$; Me, methyl; X, halogen; Boc, *tert*-butyloxycarbonyl; Ph, phenyl; EnT, energy transfer.

The toolbox of available C-to-N transmutations is limited in ways that prevent application to the pyridine C(2) position. For example, quinoline C(2)-to-N(2) (*20*) and C(3)-to-N(3) (*21*) transmutation relies heavily on the photochemistry of quinoline *N*-oxides through benzoxazepine intermediates; the analogous photorearrangements of pyridine *N*-oxides do not afford isolable oxazepines owing to parasitic secondary photo-processes (*22*). The recently reported benzenoid to pyridine nitrene internalization (*23*) is not applicable to 2-azidopyridines owing to the azide-tetrazole tautomerism, which necessitates the use of high-energy light for photochemical activation (*24*). Moreover, putative diazepines formed by this method would require a challenging N-N bond-forming C(2) deletion to form pyridazines. Pyridine-to-pyridazine reactivity has only previously been observed in trace amounts by oxidization of *N*-aminopyridines (*25*) or of tetraaryl substituted *N*-aminopyridones (*26*).

We were drawn to a study indicating that 2-azidopyridine *N*-oxides generate cyanooxazines under irradiation with 350-nm light (Fig. 1D) (*27*, *28*). The product is proposed to form through the formation of an acyclic nitrosodiene that is formed by concomitant N_2 elimination and C-N cleavage (a heterocyclic aza-Zbiral fragmentation) (*29*). We postulated that by irradiation of the related 2-azido *N*-aminopyridines, the analogous cyanodiazine would be formed, perfectly positioned for electrocyclization followed by cyanide elimination to form the desired pyridazine. In this work, we report the successful implementation of this concept (Fig. 1C).

Reaction development

The key 2-azido-*N*-aminopyridinium intermediates cannot be accessed by electrophilic amination of azidopyridines because the azide-tetrazole equilibrium (*30*) masks the pyridine while also introducing other potentially nucleophilic nitrogen sites. To circumvent these issues, we instead opted to perform an electrophilic amination directly on 2-chloropyridines **1**. 2-Halopyridines are notoriously weak nucleophiles (*31*–*33*), but the desired *N*-amination could be achieved with the use of our recently disclosed hydroxylamine reagent **2** (*34*), which serves as a highly reactive in situ generated source of $^{+}NH_2$. The installation of the *N*-amino moiety activates the pyridine ring toward S_NAr, enabling reaction with sodium azide at room temperature (*35*). Both the 2-chloro-*N*-aminopyridiniums and 2-azido-*N*-aminopyridiniums are base sensitive, such that superior yields were observed in the presence of a buffering pyridinium *p*-toluenesulfonate (PPTS) additive. Finally, irradiation of the 2-azido-*N*-aminopyridines **3** with 390-nm light-emitting diodes (LEDs) delivers the corresponding pyridazines **4**, and this process is accelerated by the addition of benzophenone as a triplet sensitizer (vide infra). Critically, this whole protocol can be telescoped into a sequence that requires no purification of the intermediates.

Several aspects of the optimized procedure merit discussion from a safety perspective. First, the combination of PPTS buffer and sodium azide has the potential to produce toxic and explosive hydrazoic acid (though this is somewhat alleviated by pyridine's higher basicity compared with azide) (*36*). Second, the C(2) is extruded in the form of cyanide, which requires effective ventilation and quenching procedures. Finally, both reagent **2** and intermediate ***3*** have the potential for exothermic decomposition, which limits the scale at which the reaction can be conducted. Nevertheless, by taking appropriate precautions, the reaction is practicable on the small scales typically used in discovery chemistry.

The reaction proceeds in synthetically useful yields when at least one electron-withdrawing group is present on the starting pyridine (Fig. 2A). For example, a pyridine bearing a trifluoromethyl group in the 4-position gives 4-trifluoromethyl pyridazine (**4a**), which was assayed by nuclear magnetic resonance (NMR) because of its volatility. Notably,

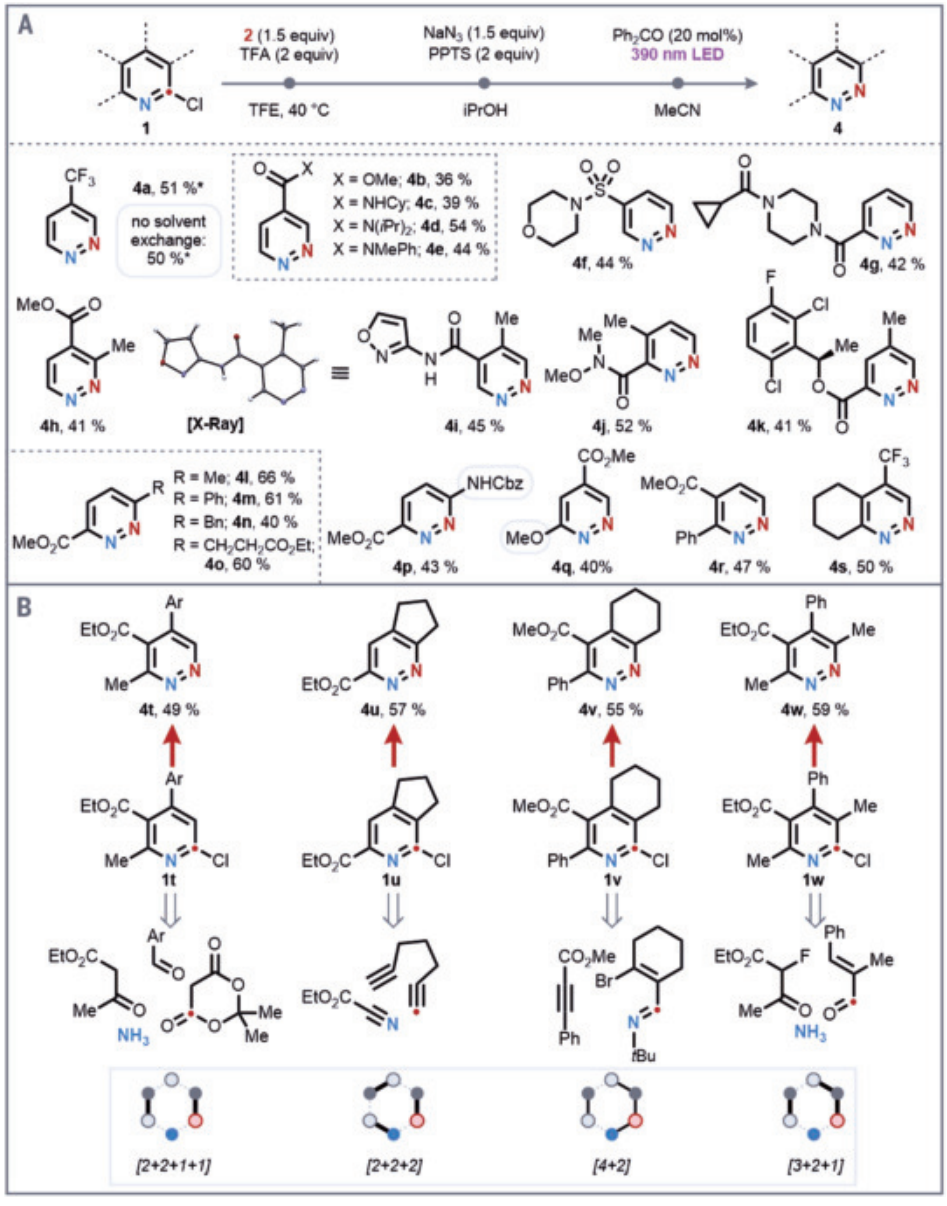

Fig. 2. Scope addressing the synthesis gap. (**A**) Functional group and substitution pattern tolerance. (**B**) Examples of pyridine syntheses mapping onto pyridazines; shaded box below the precursors represents the disconnection pattern used in ring synthesis. Isolated yields unless otherwise noted, 0.3-mmol scale. Amination, 16 hours; azidation, 2 hours; photolysis, 20 hours; temperature, 22°C unless otherwise noted. See the supplementary materials for detailed conditions. *NMR yield. TFA, trifluoroacetic acid; TFE, 2,2,2-trifluoroethanol; PPTS, pyridinium *para*-toluenesulfonate; Cy, cyclohexyl; Pr, propyl; Et, ethyl; Bn, benzyl; Cbz, benzyloxycarbonyl; Ar, 4-*tert*-butyl-C_6H_4.

the sequence could be also performed without solvent exchanges (see the supplementary materials) to give pyridazine **4a** with only a slight decrease in yield. Other electron-withdrawing groups, such as esters and amides, were also compatible to give products **4b** to **4e**. In addition, morpholine sulfonamide and substituted piperazinyl amide could also be placed in the 5- or 6-position to give **4f** and **4g**, respectively; however, substrates bearing an ester in the 3-position did not provide pyridazine upon irradiation (for other scope limitations, see fig. S2). Our subsequent investigations determined that this requirement for electron-withdrawing substituents could be offset by electron-donating substituents to a substantial extent. Alkyl substituents could be introduced at each remaining position, notably giving pyridazines bearing a 3-alkyl substituent (**4h**), an isoxazole (**4i**), a Weinreb amide (**4j**), and a functionalized benzyl ester (**4k**). 3,6-Disubstitution proved to be the most effective, giving the corresponding pyridazine **4l** in 66% yield. Further investigation of the 3,6-disusbtitution pattern revealed that phenyl, benzyl, and propanoate substituents as well as, notably, a carbamate-protected nitrogen were all compatible, affording products **4m** to **4p**. This latter amino pyridazine product is a particularly important substance class in medicinal chemistry (compare ensartinib and deucravacitinib, above). In addition, other di- and trisubstituted pyridazines **4q** to **4s** could be obtained, each requiring only a single electron-withdrawing group.

To explicitly demonstrate the bridging of the pyridine-pyridazine synthesis gap addressed by our method, we performed several classic pyridine syntheses, each of which represents a distinct ring disconnection pattern (Fig. 2B). These were followed by installation of the 2-chloro substituent and then the title method. For example, using Meldrum's acid and ethyl acetoacetate, a [2+1+2+1] cyclization (*37*) could be used to access chloropyridine **1t**, which was converted to the trisubstituted pyridazine **4t** in 49% yield. Alternatively, Ru-catalyzed [2+2+2] of a bis-alkyne and ethyl cyanoformate provides pyridine **1u** bearing a fused ring (*38*), which, after atom replacement, gave the pyridazine **4u** in 57% yield. Pd-catalyzed [4+2] cycloaddition of an alkynoate and bromo-tert-butylimine (*39*) provided pyridine **1v**, which could be converted to tetrasubstituted pyridazine **4v** in 55% yield. Finally, we performed a [3+2+1] condensation of ethyl trifluoroacetoacetate, NH_4OAc, and a substituted cinnamaldehyde (*40*) to afford fully substituted pyridine **1w**, which then could be converted into the tetrasubstituted pyridazine **4w** in 59% yield.

Mechanism

Our mechanistic evidence is most consistent with a proposed sequence from 2-azido-*N*-aminopyridinium ***3*** to pyridazine ***4*** consisting of five key steps: (i) formation of a triplet nitrene, (ii) C-C bond cleavage forming a diazatriene concomitant with intersystem crossing back to the singlet surface, (iii) proton transfer, (iv) electrocyclization, and (v) cyanide extrusion (retro-Reissert reaction) (*41*). The intermediacy of triplet states is supported by observable luminescence of isolable intermediate **3a**, which is quenched by exposure to air. In addition, benzophenone, a known triplet sensitizer (*42*), accelerates the reaction, and comparison of the phosphorescence energies of the two species suggests that an energy-matched sensitization is possible. Alternative mechanisms of photocatalysis (electron transfer or hydrogen atom transfer) are unlikely given that the

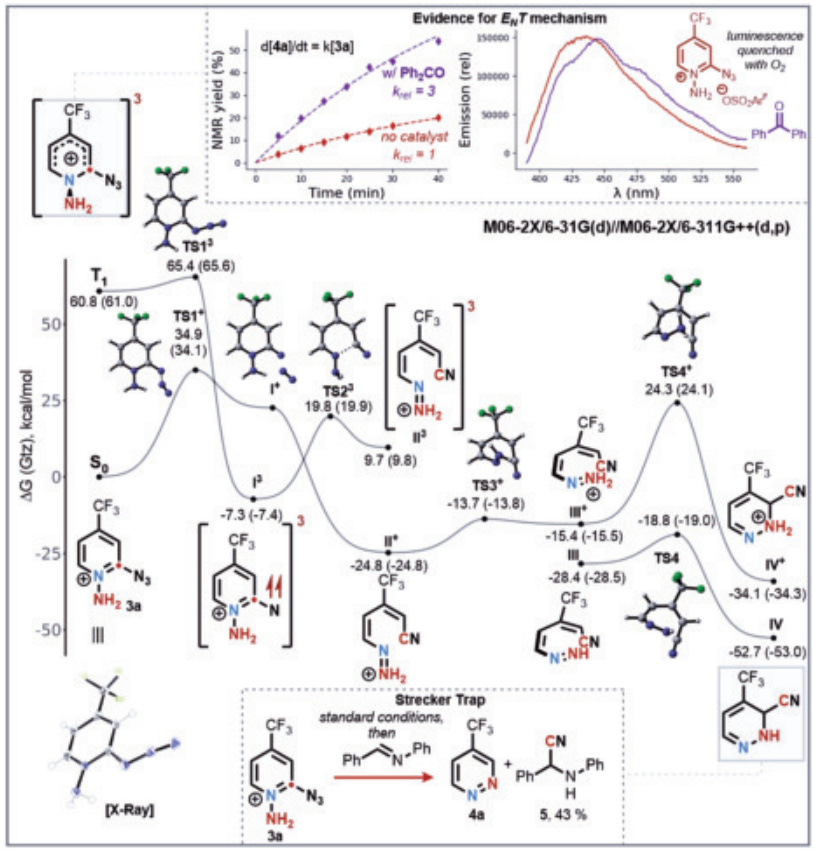

Fig. 3. Computational and experimental mechanistic analysis. Kinetic data fit numerically to first-order kinetic model by least squares. Energy diagram was created using EveRplot (*50*).

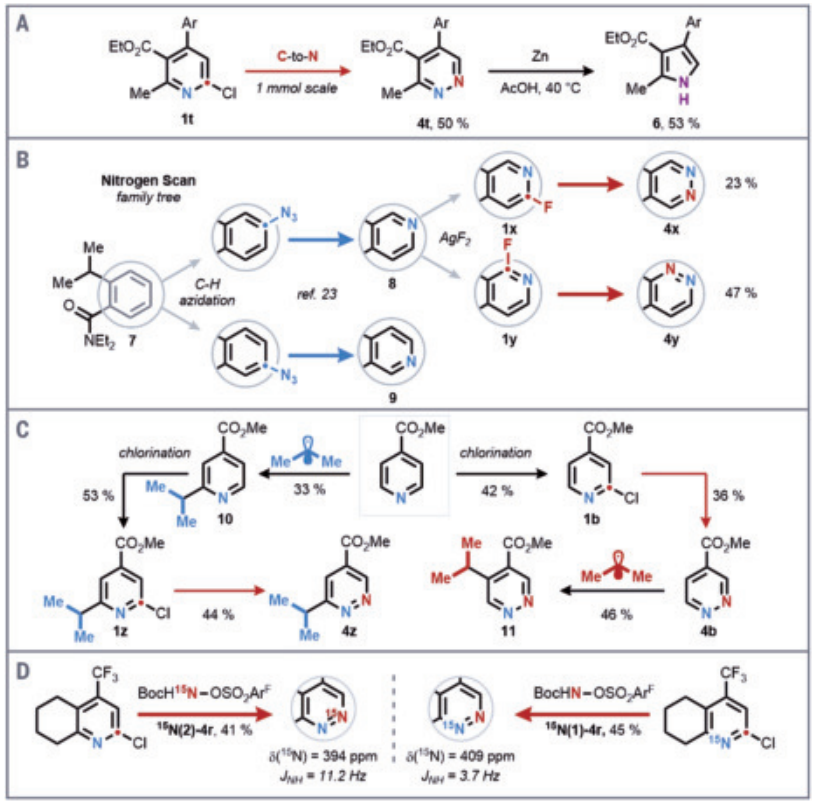

Fig. 4. Applications. (**A**) A 1-mmol scale reaction and net formal C(2) deletion. (**B**) Nitrogen scan family tree. (**C**) Capitalizing on selectivity; chlorination conditions: (i) *meta*-chloroperoxybenzoic acid and (ii) $POCl_3$. Minisci conditions: isobutyric acid, $AgNO_3$, Selectfluor. (**D**) Selective ^{15}N monolabeling.

reaction proceeds in the absence of a photocatalyst, and the observed product distributions (side-products originating from reduction of the azide and oxidation of **IV**) are similar in the catalyzed and uncatalyzed processes (see the supplementary materials for details).

Computationally (Fig. 3), we have found that the ground-state surface has a prohibitively high barrier (**TS1**$^{+}$) for N_2 extrusion, which is substantially reduced in the triplet excited state (**TS1**^{3}). However, subsequent ring opening of the triplet nitrene **I**^{3} is similarly prohibitive; by contrast, the corresponding singlet species (**I**$^{+}$) is not bound, exhibiting barrierless ring opening. This indicates that the triplet nitrene may undergo intersystem crossing to the singlet surface to give ring-opened diazatriene intermediate **II**$^{+}$. This cationic intermediate cannot energetically proceed with electrocyclization (**TS4**$^{+}$); however, the electrocyclization is energetically accessible for the neutral species, through **TS4**. Thus, we posit that a proton transfer between the cationic species and a sulfonate anion (either from the aminating reagent or PPTS buffer) is necessary. Finally, a cyanide elimination provides the final pyridazine. This final step is experimentally supported by a cyanide trapping experiment, where treatment of the crude photolysate with *N*-benzylidene aniline provides an isolable Strecker adduct ***5*** (*43*).

Synthetic applications

Several further demonstrations of the application of this protocol were undertaken (Fig. 4). First, we performed the pyridine C(2)-to-N reaction on a 1-mmol scale to provide pyridazine **4t** in 50% yield (Fig. 4A). A Boger-type nitrogen deletion reaction (*44*) afforded pyrrole **6** in 53% yield, resulting in a net C(2) deletion starting from pyridine **1t**. Next, we examined the title reaction's use in a nitrogen scan. Previously, our group has reported the C-to-N conversion of benzene to pyridine (*23*), which, when combined with C-H azidation, enabled a prototypical direct nitrogen scan of a simple benzene substrate **7** to give pyridines **8** and **9** (Fig. 4B). This sequence was extended using AgF_2-mediated pyridine fluorination chemistry (*45*), affording two separable isomeric 2-fluoropyridines **1x** and **1y**. Each of these was converted regiospecifically into the corresponding pyridazines **4x** and **4y** using our developed reaction conditions. This sequence highlights the synergy of our method both with advances in C-H functionalization and with other skeletal editing methods; continued developments in each will extend and improve the ability for such direct nitrogen-scan trees to be conducted. Next, we capitalized on the differing symmetry and selectivity of pyridine and pyridazine in C-H functionalization. By changing the order of functionalization and atom replacement steps, we can access multiple isomers of a disubstituted pyridazine selectively (Fig. 4C). Specifically, Minisci reactions proceed preferably at the 2-position for pyridines and at the 3-position for pyridazines (*46*). Therefore, starting from methyl isonicotinate, a Minisci reaction provides pyridine **10** (*47*), and 2-chlorination, followed by atom replacement, gives pyridazine **4z** with the added radical in the 6-position. Alternatively, by conducting the chlorination and atom replacement first, followed by Minisci alkylation, the alkyl radical is incorporated into the 5-position of pyridazine **11**. Finally, our method differs critically from classical hydrazine-based pyridazine syntheses in the differentiated origin of the two ring nitrogens. By using a labeled aminating reagent, preparation of nonsymmetrically ^{15}N-monolabeled pyridazine ^{15}**N(2)-4r** is possible (Fig. 4D). By contrast, an ^{15}N-labeled starting material and nonlabeled reagent afford the other ^{15}N-isotopomer ^{15}**N(1)-4r** with full control of the selectivity. These results are notable because even if a selectively monolabeled hydrazine were prepared (*48*), control of regioselectivity in a condensation reaction (not to mention separation) would likely be impossible.

REFERENCES AND NOTES

1. D. C. Blakemore *et al.*, *Nat. Chem.* **10**, 383–394 (2018).
2. L. D. Pennington, P. N. Collier, E. Comer, *Med. Chem. Res.* **32**, 1278–1293 (2023).
3. T. Hoffmann, M. Gastreich, *Drug Discov. Today* **24**, 1148–1156 (2019).
4. J. Krieger, D. Li, D. Papanikolaou, *Rev. Financ. Stud.* **35**, 636–679 (2022).
5. J. Jurczyk *et al.*, *Nat. Synth.* **1**, 352–364 (2022).
6. Z.-Q. Liu *et al.*, *Bioorg. Med. Chem.* **111**, 117847 (2024).
7. N. A. Meanwell, *Med. Chem. Res.* **32**, 1853–1921 (2023).
8. C. G. Wermuth, *MedChemComm* **2**, 935–941 (2011).
9. C. Lamberth, *J. Heterocycl. Chem.* **54**, 2974–2984 (2017).
10. C. M. Marshall, J. G. Federice, C. N. Bell, P. B. Cox, J. T. Njardarson, *J. Med. Chem.* **67**, 11622–11655 (2024).
11. A. R. Dwivedi *et al.*, *RSC Med. Chem.* **16**, 12–36 (2024).
12. L. Horn *et al.*, *Clin. Cancer Res.* **24**, 2771–2779 (2018).
13. S. T. Wrobleski *et al.*, *J. Med. Chem.* **62**, 8973–8995 (2019).
14. X.-F. Wu, *Transition Metal-Catalyzed Pyridine Synthesis* (Elsevier, 2016), pp. i–iii.
15. P. Singh, Ed., *Recent Developments in the Synthesis and Applications of Pyridines* (Elsevier, 2022).
16. E. Scriven, Ed., *Pyridines: From Lab to Production* (Elsevier, 2013).
17. D. A. Evans, G. C. Andrews, *Acc. Chem. Res.* **7**, 147–155 (1974).
18. J. A. Joule, K. Mills, *Heterocyclic Chemistry* (Wiley, ed. 5, 2010).
19. J. Zhang, V. Shukla, D. L. Boger, *J. Org. Chem.* **84**, 9397–9445 (2019).
20. J. Woo *et al.*, *Science* **376**, 527–532 (2022).
21. J. Woo, C. Stein, A. H. Christian, M. D. Levin, *Nature* **623**, 77–82 (2023).
22. H. Weber, T. Rohn, *Z. Naturforsch. B* **45**, 701–706 (1990).
23. T. J. Pearson *et al.*, *Science* **381**, 1474–1479 (2023).
24. A. Reisinger, R. Koch, P. V. Bernhardt, C. Wentrup, *Org. Biomol. Chem.* **2**, 1227–1238 (2004).
25. T. Okamoto, M. Hirobe, *J. Synth. Org. Chem. Jpn.* **26**, 746–757 (1968).
26. C. W. Rees, M. Yelland, *J. Chem. Soc. Perkin Trans. 1* **1972**, 77–82 (1972).
27. R. A. Abramovitch, C. Dupuy, *J. Chem. Soc. Chem. Commun.* **1981**, 36–37 (1981).
28. R. A. Abramovitch, B. W. Cue Jr., *J. Am. Chem. Soc.* **98**, 1478–1486 (1976).
29. J. Schweng, E. Zbiral, *Justus Liebigs Ann. Chem.* **1978**, 1089–1095 (1978).
30. P. Cmoch, H. Korczak, L. Stefaniak, G. A. Webb, *J. Phys. Org. Chem.* **12**, 470–478 (1999).
31. E. M. Arnett, R. Reich, *J. Am. Chem. Soc.* **102**, 5892–5902 (1980).
32. T. Kiguchi, J. L. Schuppiser, J. C. Schwaller, J. Streith, *J. Org. Chem.* **45**, 5095–5100 (1980).
33. T. Eichenberger, H. Balli, *Helv. Chim. Acta* **69**, 1521–1530 (1986).
34. A. Fanourakis *et al.*, *Nature* **641**, 646–652 (2025).
35. T. B. Phan, H. Mayr, *J. Phys. Org. Chem.* **19**, 706–713 (2006).
36. D. S. Treitler, S. Leung, *J. Org. Chem.* **87**, 11293–11295 (2022).
37. H. R. Memarian, M. Kalantari, *J. Iran. Chem. Soc.* **14**, 143–155 (2017).
38. Y. Yamamoto *et al.*, *J. Am. Chem. Soc.* **127**, 605–613 (2005).
39. K. R. Roesch, H. Zhang, R. C. Larock, *J. Org. Chem.* **66**, 8042–8051 (2001).
40. Z. Song, X. Huang, W. Yi, W. Zhang, *Org. Lett.* **18**, 5640–5643 (2016).
41. S. Wang *et al.*, *Tetrahedron Lett.* **57**, 3067–3070 (2016).
42. F. Strieth-Kalthoff, F. Glorius, *Chem* **6**, 1888–1903 (2020).
43. M. Köckinger, C. A. Hone, C. O. Kappe, *Org. Lett.* **21**, 5326–5330 (2019).
44. D. L. Boger, R. S. Coleman, J. S. Panek, D. Yohannes, *J. Org. Chem.* **49**, 4405–4409 (1984).
45. P. S. Fier, J. F. Hartwig, *Science* **342**, 956–960 (2013).
46. F. O'Hara, D. G. Blackmond, P. S. Baran, *J. Am. Chem. Soc.* **135**, 12122–12134 (2013).
47. J. D. Galloway, D. N. Mai, R. D. Baxter, *Org. Lett.* **19**, 5772–5775 (2017).
48. J. P. Jacobsen, O. Snerling, E. J. Pedersen, J. Tormod Nielsen, K. Schaumburg, *J. Magn. Reson.* **1969**, 130–138 (1973).
49. G. L. Bartholomew *et al.*, *J. Med. Chem.* **68**, 6027–6040 (2025).
50. M. K. Bogdos, B. Morandi, *J. Chem. Educ.* **100**, 3641–3644 (2023).

ACKNOWLEDGMENTS

We thank A. Bracken for assistance with x ray diffractometry, L. McNamara for assistance with luminescence experiments, A. Crolais for assistance with thermal analysis, D. Stroila for experimental assistance, and S. Li for helpful discussions. **Funding:** The research reported in this work was supported by the National Institutes of Health (R35 GM142768). The University of Chicago Research Computing Center (RCC) is thanked for computational resources. M.P. was supported by a SNSF Postdoctoral Fellowship (P500PN_217911). H.N. was supported by the JSPS Overseas Challenge Program for Young Researchers. **Author contributions:** M.P. and M.D.L. conceived of the work. M.P. and H.N. designed and conducted synthetic experiments, including purification and characterization. M.P. conducted computational studies. M.D.L. and M.P. prepared the manuscript with input from all authors. M.D.L. directed the research. **Competing interests:** The authors declare no competing interests. **Data and materials availability:** Crystallographic data are freely available from the Cambridge Crystallographic Data Centre under CCDC 2431452 and 2431454. All other data are provided in the supplementary materials. **License information:** Copyright © 2025 the authors, some rights reserved; exclusive licensee American Association for the Advancement of Science. No claim to original US government works. https://www.science.org/about/science-licenses-journal-article-reuse

SUPPLEMENTARY MATERIALS

science.org/doi/10.1126/science.adx4762
Supplementary Text; Figs. S1 to S39; Tables S1 to S4; NMR Spectra; References (*51–63*); Reproducibility Checklist

Submitted 15 March 2025; accepted 13 May 2025

10.1126/science.adx4762

ELECTRONIC MATERIALS

Two-dimensional indium selenide wafers for integrated electronics

Biao Qin[1,2]†, Jianfeng Jiang[3]*†, Lu Wang[4], Quanlin Guo[1,5], Chenxi Zhang[3], Lin Xu[3], Xing Ni[4], Peng Yin[2], Lian-Mao Peng[3], Enge Wang[6,7], Feng Ding[8], Chenguang Qiu[3]*, Can Liu[2]*, Kaihui Liu[1,6,9]*

Two-dimensional (2D) indium selenide, with its low effective mass, high thermal velocity, and exceptional electronic mobility, is a promising semiconductor for surpassing silicon electronics, but grown films have not achieved performance comparable with that of exfoliated micrometer-scale flakes. We report a solid–liquid–solid strategy that converts amorphous indium selenide films into pure-phase, high-crystallinity indium selenide wafers by creating an indium-rich liquid interface and maintaining a strict 1:1 stoichiometric ratio of indium to selenium. The as-obtained indium selenide films exhibit exceptional uniformity, a pure phase, and a high crystallinity across an entire ~5-centimeter wafer. Transistor arrays based on the produced indium selenide wafers demonstrate outstanding electronic performance surpassing that of all 2D film-based devices, including an extremely high mobility (averaging as high as 287 square centimeters per volt-second) and a near-Boltzmann-limit subthreshold swing (averaging as low as 67 millivolts per decade) at room temperature.

Advancements in artificial intelligence and Internet of Things technologies have imposed substantial demands on computational power (*1*). However, silicon-based transistor technology is approaching its intrinsic physical limits at sub–10-nm nodes, restricting further improvements in the chip performance, power efficiency, and integration density (*2*, *3*). New semiconductor channel materials that can overcome the limitations of silicon, thereby sustaining further growth in the transistor density for future integrated circuit nodes, are needed (*4*–*7*).

Two-dimensional (2D) atomically thin semiconductors—such as molybdenum disulfide (MoS_2), tungsten disulfide (WS_2), tungsten diselenide (WSe_2), black phosphorus, bismuth oxyselenide (Bi_2O_2Se), and indium selenide (InSe)—are candidates for sub–3-nm technology nodes (*8*–*17*). Among them, InSe is a 2D semiconductor that theoretically could surpass silicon limits because of its low effective mass [$0.14m_0$, compared with $0.19m_0$ for silicon and 0.3 to $0.6m_0$ for transition-metal dichalcogenides (TMDs), where m_0 is the electron mass], high thermal velocity (>1.3 cm/s, compared with 1.2 cm/s for silicon and <0.8 cm/s for TMDs), theoretically high mobility (1000 $cm^2/V{\cdot}s$ at room temperature), and appropriate bandgap (>1.26 eV, compared with 1.12 eV for silicon) (*17*, *18*). This exceptional performance has recently been demonstrated for exfoliated microscale InSe flakes (*19*), but the scalability of integrated electronics based on a vast number of devices ultimately relies on large-scale, high-quality InSe wafers.

Currently, wafer-scale InSe films are primarily produced through various thin-film deposition techniques, such as metal-organic chemical vapor deposition and molecular beam epitaxy, but the performance of the grown films is decreased so that they underperform compared with 2D TMD semiconductors (*20*–*23*). The main challenge in high-quality InSe film growth arises for two main reasons. First, the phase diversity within the In-Se system is complex because there are at least four stable phases (InSe, In_2Se_3, In_4Se_3, and In_6Se_7). Even slight compositional variations can trigger unwanted phase transitions that lead to considerable performance deviation and degradation (*22*). Second, the crystallinity of InSe films is poor because of the difficulty in maintaining a stoichiometric balance between In and Se because the vapor pressure of Se is approximately seven orders of magnitude greater than that of In at a growth temperature of ~500°C (*24*). Achieving a pure-phase, high-crystallinity film is a critical prerequisite for unlocking the full potential of InSe wafers in large-scale integrated electronics.

Design and growth

To prevent the formation of other phases, we maintained a strict 1:1 stoichiometric ratio of In to Se by sealing a predeposited amorphous InSe wafer. A high-purity InSe target was used in magnetron sputtering to uniformly deposit the amorphous InSe film onto a ~5-cm sapphire substrate (Fig. 1A and fig. S1). This amorphous InSe wafer was placed into a custom steel groove, covered with fused silica, and sealed at the edges with liquid In (with a melting point of ~157°C). This configuration created a sealed space that prevented atomic loss during growth at a high temperature of ~550°C and maintained the stoichiometric ratio of In to Se in the InSe film [Fig. 1B and supplementary materials (SM) materials and methods].

High crystallinity was achieved with a solid–liquid–solid (SLS) growth mechanism, in which recrystallization of amorphous InSe occurred at an In-rich liquid interface. Trace amounts of additional In atoms were introduced by the surrounding liquid In and the saturated In vapor in the reactor to facilitate the formation of a liquid In-rich interface (Fig. 1C and fig. S2) (*25*). Our density functional theory calculations showed that the formation energy of amorphous InSe was ~0.38 eV/atom greater than that of the crystalline InSe, so the transformation from amorphous to crystalline InSe would be energetically preferred (fig. S3). With a liquid In-rich interface, the In and Se atoms of the amorphous InSe quickly dissolved into the liquid interface and then precipitated out on the crystalline InSe side, which kinetically promoted the structural transformation (Fig. 1D and fig. S4). To verify the SLS mechanism, we carefully examined the interface between amorphous and crystalline InSe. The In-rich interface was clearly visualized in the cross-sectional scanning transmission electron microscopy (STEM) images and further confirmed with corresponding fast Fourier transform (FFT) patterns (Fig. 1E).

High crystallinity of InSe wafers

We experimentally prepared ~5-cm high-quality InSe wafers on sapphire substrates through the proposed strategy (Fig. 2A). The thickness of the InSe films was nearly linearly dependent on the sputtering time, with a slope of ~0.28 layers per second (fig. S5). In our current experimental configuration, the minimum achievable thickness was ~2.5 nm (three layers), which was mainly constrained by the limitations of the magnetron sputtering technique (fig. S6). When the film thickness reaches ≥30 nm, the vertical penetration of liquid In becomes insufficient to achieve full crystallization of the InSe layers (fig. S7). The crystallization of the InSe film was evident from the reduction in the surface roughness from ~415 pm in the amorphous state to only ~37 pm in the crystalline state (Fig. 2B and fig. S8). In addition, the uniform contrast in the optical

[1]State Key Laboratory for Mesoscopic Physics, Frontiers Science Centre for Nano-optoelectronics, School of Physics, Peking University, Beijing, China. [2]Key Laboratory of Quantum State Construction and Manipulation (Ministry of Education), School of Physics, Renmin University of China, Beijing, China. [3]Key Laboratory for the Physics and Chemistry of Nanodevices and Center for Carbon-based Electronics, School of Electronics, Peking University, Beijing, China. [4]Institute of Functional Nano & Soft Materials (FUNSOM) and Jiangsu Key Laboratory of Advanced Negative Carbon Technologies, Soochow University, Suzhou, China. [5]Interdisciplinary Institute of Light-Element Quantum Materials and Research Centre for Light-Element Advanced Materials, Peking University, Beijing, China. [6]International Centre for Quantum Materials, Collaborative Innovation Centre of Quantum Matter, Peking University, Beijing, China. [7]Tsientang Institute for Advanced Study, Hangzhou, China. [8]Suzhou Laboratory, Suzhou, China. [9]Songshan Lake Materials Laboratory, Dongguan, China. ***Corresponding author. Email: canliu@ruc.edu.cn (C.L.); jjf19950926@gmail.com (J.J.); chenguangqiu@pku.edu.cn (C.Q.); khliu@pku.edu.cn (K.L.)** †These authors contributed equally to this work.

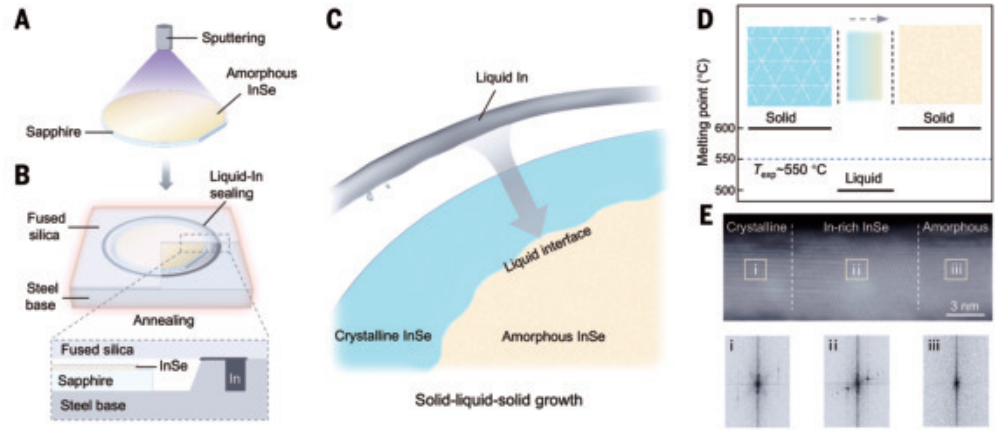

Fig. 1. Design of the SLS strategy for InSe wafer growth. (**A**) Amorphous InSe films are deposited on a single-crystal sapphire substrate by means of magnetron sputtering. (**B**) Schematic of the annealing device designed to hold a ~5-cm wafer. In the main structure, the central groove in the steel base holds the wafer, whereas the surrounding groove (1 mm deep) contains liquid In. A fused silica plate was placed on top of the steel base. Liquid In was used to seal InSe wafers. (**C**) Zoomed-in diagram of the SLS growth in (B). Liquid In evaporated to create an In-rich interface between amorphous and crystalline InSe. At this interface, the amorphous solid continuously transformed into a crystalline InSe film. (**D**) Schematic of SLS evolution. At the experimental temperature (T_{exp} ~ 550°C), only the In-rich interface is in liquid state, promoting recrystallization by enhancing atomic diffusion and lowering the formation energy. (**E**) Cross-sectional STEM image and corresponding FFT patterns, showing the presence of the In-rich interface between amorphous and crystalline InSe regions.

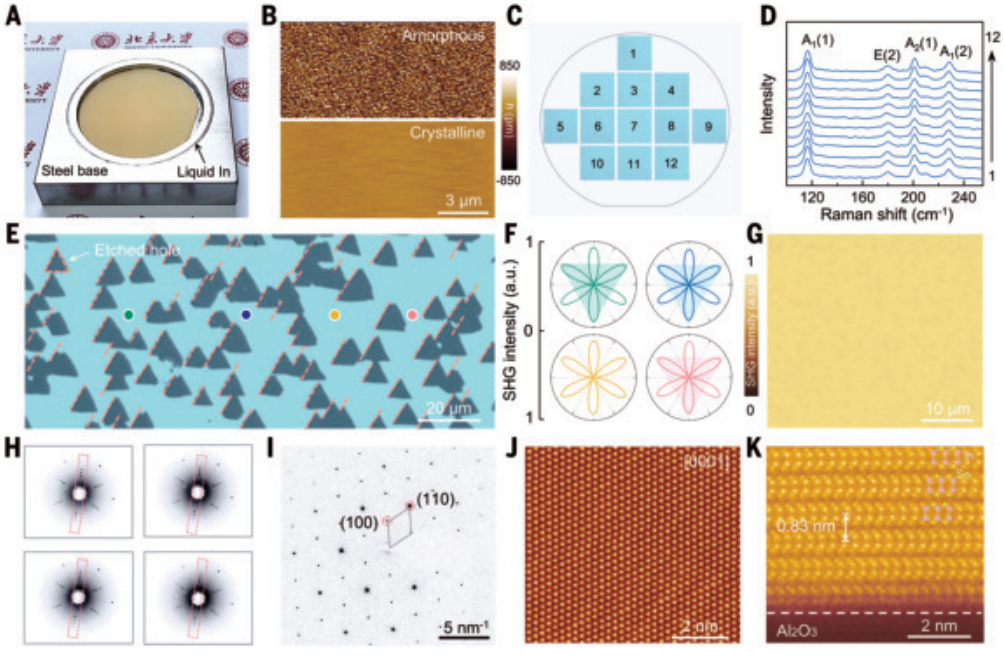

Fig. 2. Characterizations of InSe films. (**A**) Photograph of an as-grown 10-nm-thick InSe film on a ~5-cm sapphire substrate positioned in the steel base. (**B**) Atomic force microscopy roughness (standard deviation of the height, *h*) images of (top) amorphous and (bottom) crystalline InSe. (**C**) Optical images of an as-grown InSe film collected from 12 representative areas on a ~5-cm wafer. All the images are of the same size (150 by 150 μm). (**D**) Raman spectra of InSe collected at the corresponding areas in (C), indicating the uniformity of the as-grown InSe film. (**E**) Optical images of InSe films after H_2 etching. The etched holes all had triangular shapes and the same orientation. (**F**) Polarization-dependent SHG patterns of InSe in the corresponding areas marked in (E). (**G**) SHG mapping of the InSe film. (**H**) LXD patterns of an InSe film at four different positions. The size of the x-ray spot was ~0.2 mm. (**I**) SAED patterns of the InSe film. (**J**) HAADF-STEM image of the InSe film. (**K**) Cross-sectional HAADF-STEM image of as-grown InSe on sapphire substrate, revealing the ABC stacking order.

images and nearly identical Raman spectra collected from 12 representative areas evenly distributed across the ~5-cm InSe wafer consistently demonstrated its large-area uniformity (Fig. 2, C and D). Our methodology is fundamentally scalable for the production of large InSe wafers, as demonstrated by the highly uniform ~10-cm wafer (fig. S9).

To evaluate the crystallinity of the grown InSe film, we used H_2 etching to visualize its crystallographic orientation. Because of the threefold symmetry (C_{3v}) of InSe, triangular holes with a uniform orientation consistently appeared, providing strong evidence of the single-crystal structure of the film across a large area (Fig. 2E and fig. S10). Additionally, the highly consistent polarization-dependent second-harmonic generation (SHG) patterns, along with the uniform intensity distribution in the SHG mapping, further validated the monocrystalline nature of the InSe film (Fig. 2, F and G). Furthermore, Laue x-ray diffraction (LXD) patterns (x-ray spot of ~0.2 mm) measured at four different positions across a 1- by 1-cm region revealed sharp and consistently arranged spots, confirming the high crystallinity on a large scale (Fig. 2H).

The detailed atomic structures of the InSe films were characterized by using selected-area electron diffraction (SAED) and high-angle annular dark-field STEM (HAADF-STEM). The SAED pattern with an incident zone axis of ⟨001⟩ clearly showed the intensities of representative diffraction spots (Fig. 2I), revealing the high crystallinity of the InSe lattice. Specifically, the lattice spacings of InSe are 0.34 and 0.21 nm, corresponding to the (100) and (110) planes, respectively, as reported in a previous study of single-crystal flakes (*26*). The triangular lattice of InSe was clearly visualized through the in-plane HAADF-STEM image, in which each atomic column represents a series of stacked In_2 + Se_2 (Fig. 2J and fig. S11). The out-of-plane view revealed a well-defined atomic structure with a layer spacing of 0.83 nm, in which each InSe layer is aligned in the same direction and followed a rhombohedral (ABC) stacking order (Fig. 2K and fig. S12). These results demonstrate that the InSe film had high crystallinity and quality.

Electronic performance of wafer-scale InSe transistor arrays

To further evaluate the crystalline quality of the InSe films, we fabricated large-scale integrated arrays of field-effect transistors (FETs) directly on sapphire substrates using the as-obtained 5-nm-thick InSe wafers for reliable statistical analysis of the electrical performance. A schematic of the devices is shown in Fig. 3A. To avoid the Fermi-level pinning effect, we used rare-earth yttrium (Y) doping in the contact metallization layer to achieve robust ohmic contact in wafer-scale InSe device arrays (*19*). Additionally, ultrathin 2.6-nm hafnium oxide (HfO_2) was

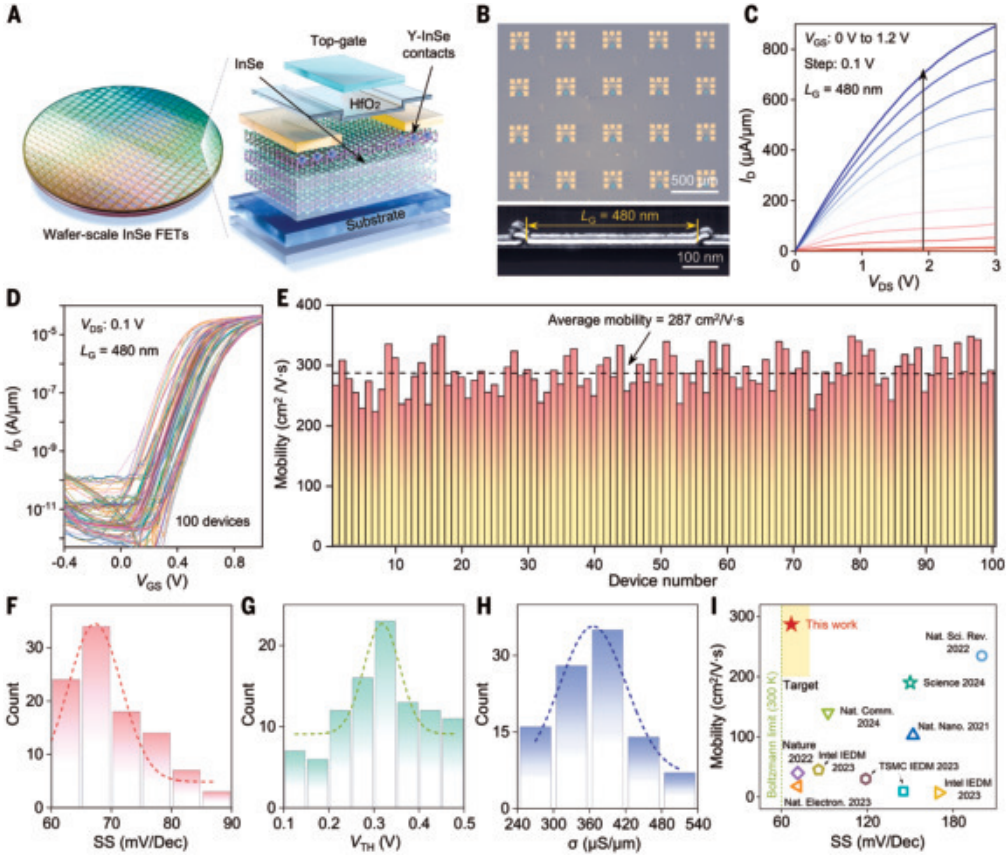

Fig. 3. Wafer-scale fabrication and statistics of the electrical performance of 2D InSe FETs. (**A**) Schematic diagram of wafer-scale InSe FETs with Y-doping–induced contact metallization. The purple, green, and blue spheres indicate In, Se, and Y atoms, respectively. (**B**) (Top) False-color SEM image and (bottom) typical cross-sectional STEM image of the top-gate InSe FET arrays on sapphire. (**C**) Typical output characteristic curve of the InSe FET with gate length L_G of 480 nm. (**D**) Transfer characteristics of 100 individual fabricated 2D InSe FET devices. (**E**) Statistical histogram of the field-effect mobility values from 100 individual 2D InSe FET devices. (**F** to **H**) Statistical distributions of the (F) SS, (G) threshold voltage V_{TH}, and (H) electric conductance σ of 100 individual 2D InSe FETs, revealing mean values of 67.3 mV per decade, 0.31 V, and 369 μS/μm, respectively. The dashed lines are Gaussian fitting curves. (**I**) Comparison of the mobility versus SS plots of our wafer-scale 2D InSe FETs (red star) with those of other reported film-based 2D counterparts (open symbols) (SM materials and methods, section S1.5, and references therein).

used as the top dielectric layer (SM materials and methods). In Fig. 3B, we show a false-colored scanning electron microscopy (SEM) image of the 2D InSe FET integrated array and a cross-sectional STEM image of a typical top-gate device with a gate length of 480 nm. Under a source-drain voltage (V_{DS}) of 3 V, with a gate-source voltage (V_{GS}) of 1.2 V, the corresponding saturation current density reached 892 μA/μm, which far exceeds that of any reported similarly sized 2D semiconductor devices for grown films (Fig. 3C).

The transfer characteristics of 100 individual InSe transistors at V_{DS} of 0.1 V are shown in Fig. 3D, and the field-effect mobility distribution is illustrated in Fig. 3E. The average field-effect mobility was 287 cm^2/V·s, with a peak mobility as high as 347 cm^2/V·s, which is higher than those of all other reported film-based 2D devices (figs. S13 and S14) (*27*, *28*). Additionally, these values meet the International Roadmap for Devices and Systems (IRDS) requirements for channel mobility in very-large-scale integration (*2*). Statistical histograms of the subthreshold swing, threshold voltage (V_{TH}), and electrical conductance (σ) are presented in Fig. 3, F to H, showing that the mean values of SS, V_{TH}, and σ are 67.3 mV per decade, 0.31 V, and 369 μS/μm, respectively. In Fig. 3I, the benchmark plot of the mobility versus the SS demonstrates the advantage of our InSe devices in both the switching speed and mobility compared with those of other reported devices.

Ballistic transport performance of 10-nm InSe transistors

The ballistic transport performance in ultrashort-channel 2D devices offers another robust assessment measure beyond the mobility to evaluate the wafer quality in advanced technology nodes below 10 nm. We fabricated ballistic InSe transistors with a channel length of 10 nm (Fig. 4A) using Y-doping contacts and a dual-gate structure to enhance gate efficiency by transferring the films from sapphire to Si substrates (fig. S15 and SM materials and methods). The cross-sectional structure and elemental distribution of the devices were determined by using STEM and electron energy-loss spectroscopy (EELS) (Fig. 4B). The back-gate length was 10 nm, whereas the top-gate length was 5 nm, with the channel comprising three layers of InSe. Both the top- and back-gate dielectrics were composed of ~2.6-nm-thick HfO_2.

The transfer characteristics of a representative ballistic InSe transistor are shown in Fig. 4C, demonstrating nearly ideal switching behavior, with an SS as low as 79 mV per decade and a switching current ratio exceeding 10^7, which meets the stringent requirements for advanced logic circuits. Additionally, the device operates at an ultralow voltage of 0.5 V, with its off-state current satisfying the IRDS requirements for high-performance and high-density applications. The on/off ratio versus the drain current (I_D) illustrates that the comprehensive switching characteristics of our device surpassed those of other 2D counterparts by at least two orders of magnitude (Fig. 4D) (*29*–*31*).

The output characteristics of a representative 10-nm InSe transistor are presented in Fig. 4E, which displays a saturation current density of up to 1.2 mA/μm at 0.8-V V_{DS} and 1.0-V V_{GS}, and a standard current density of 1 mA/μm was achieved at an ultralow V_{DS} of 0.46 V. Because of the high-quality InSe channel material, Y-doped metallic ohmic contacts, and efficient dual-gate architecture, our ballistic InSe device exhibited superior comprehensive electrical characteristics across six key parameters—operating voltage, gate length, drain-induced barrier lowering (DIBL), effective mass, on/off ratio, and ballistic ratio—compared with Intel 3 technology nodes and state-of-the-art film-based 2D transistors (Fig. 4F) (*32*–*35*). Its overlap-free intrinsic gate delay was as low as 0.39 ps, and its energy-delay product (EDP) reached a particularly low value of 5.27×10^{-29} J·s/μm, exceeding the predicted limits for silicon-based technologies outlined in the IRDS until 2037 (Fig. 4G) (*2*).

Discussion and outlook

We have developed a SLS strategy to produce high-quality InSe films at the wafer scale. These films exhibit exceptional uniformity and crystallinity, which enables outstanding transistor array performance, including a record high mobility and a near-Boltzmann-limit

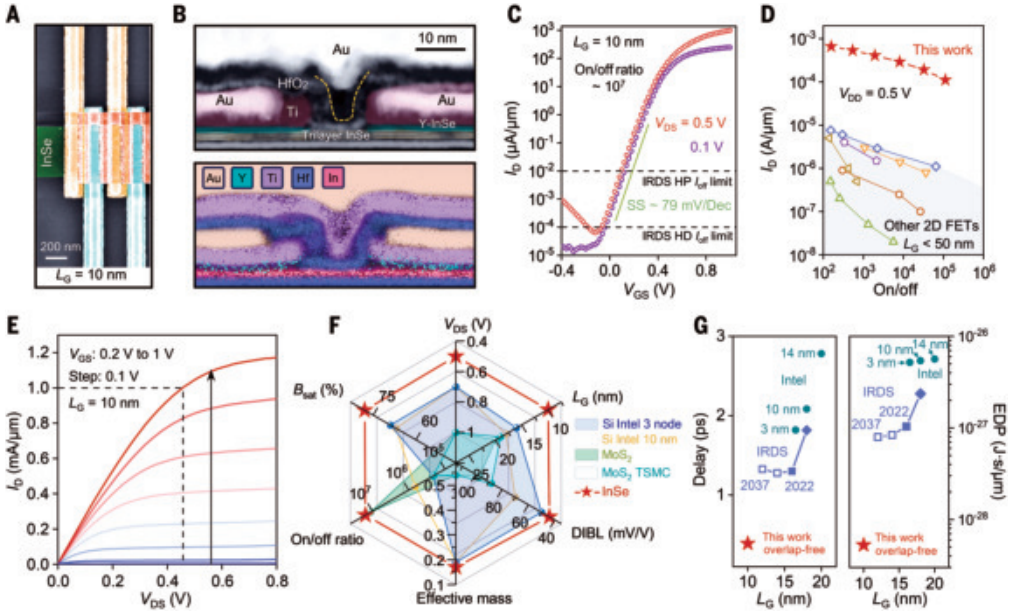

Fig. 4. Short-channel electrical performance and benchmarking of InSe FETs. (**A**) Top-view SEM image of a typical fabricated ballistic 2D trilayer InSe FET with a 10-nm gate length. (**B**) (Top) Cross-sectional STEM image of a ballistic trilayer InSe FET featuring a highly efficient dual-gate structure. (Bottom) The EELS maps illustrate the spatial distributions of gold (Au), Y, titanium (Ti), hafnium (Hf), and In, confirming the locations of the 2D InSe channel, electrode, and gate stack. (**C**) Transfer characteristics of a typical ballistic double-gate InSe FET with a 10-nm gate length. (**D**) Comparison of the on-state current (I_D) versus the on/off ratio of our typical ballistic trilayer double-gate InSe FETs (red stars) with that of other short-channel ($L_G < 50$ nm) 2D counterparts (light blue shaded area). The I_D and corresponding on/off ratio are defined within a 0.5-V window along each transfer curve. (**E**) Output characteristic curves of the ballistic 2D InSe FET with L_G of 10 nm. (**F**) Radar plot of the electrical performance of our InSe FETs versus other reported short-channel FETs, including key parameters such as V_{DS} (reaching a standard saturation current density of >1 mA/μm), L_G, DIBL, effective mass, on/off ratio, and ballistic ratio (B_{sat}). TSMC, Taiwan Semiconductor Manufacturing Company. (**G**) Scaling trends of (left) intrinsic gate delay and (right) EDP of our ballistic 2D InSe FETs with an overlap-free architecture compared with those of silicon.

SS for large-scale 2D devices. Ultrashort-channel (10-nm) InSe transistors demonstrate key parameters—including the operating voltage, gate length, DIBL, effective mass, on/off ratio, and ballistic ratio—that exceed those of the current state-of-the-art Intel 3-nm-node technology. The delay and EDP of the device fall below the 2037 IRDS predicted limits for silicon technology. We anticipate that integrated electronics produced from 2D InSe wafers will drive the development of advanced transistors, offering a more flexible, low-power, high-performance solution for next-generation computing and communication technologies.

REFERENCES AND NOTES

1. T. N. Theis, H. S. P. Wong, *Comput. Sci. Eng.* **19**, 41–50 (2017).
2. IEEE International Roadmap for Devices and Systems 2023 Update; https://irds.ieee.org/editions/2023.
3. W. Cao *et al.*, *Nature* **620**, 501–515 (2023).
4. D. Akinwande *et al.*, *Nature* **573**, 507–518 (2019).
5. Y. Liu *et al.*, *Nature* **591**, 43–53 (2021).
6. M. Chhowalla *et al.*, *Nat. Chem.* **5**, 263–275 (2013).
7. A. D. Franklin, M. C. Hersam, H. P. Wong, *Science* **378**, 726–732 (2022).
8. L. Li *et al.*, *Nat. Nanotechnol.* **9**, 372–377 (2014).
9. M. Y. Li, S. K. Su, H. P. Wong, L. J. Li, *Nature* **567**, 169–170 (2019).
10. T. Li *et al.*, *Nat. Nanotechnol.* **16**, 1201–1207 (2021).
11. K. C. Zhu *et al.*, *Nat. Electron.* **4**, 775–785 (2021).
12. J. Wang *et al.*, *Nat. Nanotechnol.* **17**, 33–38 (2022).
13. R. Wu *et al.*, *Nat. Electron.* **5**, 497–504 (2022).
14. J. H. Fu *et al.*, *Nat. Nanotechnol.* **18**, 1289–1294 (2023).
15. K. P. O'Brien *et al.*, *Nat. Commun.* **14**, 6400 (2023).
16. C. Tan *et al.*, *Nature* **616**, 66–72 (2023).
17. D. A. Bandurin *et al.*, *Nat. Nanotechnol.* **12**, 223–227 (2017).
18. E. G. Marin, D. Marian, G. Iannaccone, G. Fiori, *IEEE Electron Device Lett.* **39**, 626–629 (2018).
19. J. Jiang, L. Xu, C. Qiu, L. M. Peng, *Nature* **616**, 470–475 (2023).
20. Z. Yang *et al.*, *ACS Nano* **11**, 4225–4236 (2017).
21. J. Kang *et al.*, *Adv. Mater.* **30**, e1802990 (2018).
22. S. Song *et al.*, *Matter* **6**, 3483–3498 (2023).
23. H.-C. Chang *et al.*, *Small* **14**, e1802351 (2018).
24. C. H. Wu *et al.*, *Nanomaterials* **12**, 2435 (2022).
25. H. Bergeron *et al.*, *Appl. Phys. Rev.* **7**, 041402 (2020).
26. J. F. Jiang *et al.*, *Small Methods* **4**, 2000238 (2020).
27. G. Xue *et al.*, *Chem. Rev.* **124**, 9785–9865 (2024).
28. L. Liu *et al.*, *Nature* **605**, 69–75 (2022).
29. C. S. Pang, P. Wu, J. Appenzeller, Z. Chen, in *2020 IEEE International Electron Devices Meeting (IEDM)* (IEEE, 2020), pp. 3.4.1–3.4.4.
30. A. Nourbakhsh *et al.*, *Nano Lett.* **16**, 7798–7806 (2016).
31. S. B. Desai *et al.*, *Science* **354**, 99–102 (2016).
32. W. Li *et al.*, *Nature* **613**, 274–279 (2023).
33. W. C. Wu *et al.*, in *2024 IEEE Symposium on VLSI Technology and Circuits* (IEEE, 2024), pp. 1–2.
34. W. Hafez *et al.*, in *2024 IEEE Symposium on VLSI Technology and Circuits* (IEEE, 2024), pp. 1–2.
35. C. Auth *et al.*, in *2017 IEEE International Electron Devices Meeting (IEDM)* (IEEE, 2017), pp. 29.1.1–29.1.4.

ACKNOWLEDGMENTS

Funding: This work was supported by the National Natural Science Foundation of China (52025023, 52322205, 12274456, 52250398, T2188101, 51991342, 92163206, 11888101 62122006, and 92477201), National Key R&D Program of China (2022YFA1403500, 2022YFA1405600, 2021YFA1400502, and 2021YFA0717400), Guangdong Major Project of Basic and Applied Basic Research (2021B0301030002), Beijing Municipal Science and Technology Project (Z221100005822003), and Strategic Priority Research Program of Chinese Academy of Sciences (XDB3300000). This work has been supported by the New Cornerstone Science Foundation through the XPLORER PRIZE and Hangzhou Tsientang Education Foundation. **Author contributions:** K.L., C.L., and C.Q. supervised the project. K.L., C.L., C.Q., J.J., and B.Q. conceived the experiments. B.Q., X.N., L.W., C.L., F.D., and K.L. developed the growth mechanism. B.Q. conducted the growth experiments. J.J., C.Z., L.X., and C.Q. fabricated InSe devices and performed the electrical measurements and VS model simulation. B.Q., Q.G., C.Z., and P.Y. performed the SHG, Raman, PL, LXD, STEM, SEM, magnetron sputtering, and XRD experiments. B.Q., J.J., C.L., C.Q., and K.L. wrote the article. C.Q., K.L., L. P., and E.W. revised the manuscript. All the authors discussed the results and revised the paper. **Competing interests:** A Chinese patent application (no. 202510419972.2) related to this article was submitted by Peking University (K.L., C.L., and B.Q.). All other authors declare that they have no competing interests. **Data and materials availability:** All data are available in the main text or the supplementary materials.

License information: Copyright © 2025 the authors, some rights reserved; exclusive licensee American Association for the Advancement of Science. No claim to original US government works. https://www.science.org/about/science-licenses-journal-article-reuse

SUPPLEMENTARY MATERIALS

science.org/doi/10.1126/science.adu3803
Materials and Methods; Figs. S1 to S15; References (*36*–*53*)

Submitted 8 November 2024; accepted 14 May 2025

10.1126/science.adu3803

MICROBIOTA

Controlled colonization of the human gut with a genetically engineered microbial therapeutic

Weston R. Whitaker[1,2]*, Zachary N. Russ[1], Elizabeth Stanley Shepherd[1]†, Lauren M. Popov[1], Alexander Louie[1], Kathy Lam[1], David M. Zong[1], Clare C. C. Gill[1], Jeanette L. Gehrig[1], Harneet S. Rishi[1], Jessica A. Tan[1], Areta Buness[1], Janeth Godoy[1], Domenique Banta[1], Sonia Jaidka[1], Katheryne Wilson[1], Jake Flood[1], Polina Bukshpun[1], Richard Yocum[1], David N. Cook[1], Tariq Warsi[1], Lachy McLean[1]‡, Justin L. Sonnenburg[2,3,4], William C. DeLoache[1]

Precision microbiome programming for therapeutic applications is limited by challenges in achieving reproducible colonic colonization. Previously, we created an exclusive niche that we used to engraft engineered bacteria into diverse microbiota in mice by using a porphyran prebiotic. Building on this approach, we have now engineered conditional attenuation into a porphyran-utilizing strain of *Phocaeicola vulgatus* by replacing native essential gene regulation with a porphyran-inducible promoter to allow reversible engraftment. Engineering a five-gene oxalate degradation pathway into the reversibly engrafting strain resulted in a therapeutic candidate that reduced hyperoxaluria, a cause of kidney stones, in preclinical models. Our phase 1/2a clinical trial demonstrated porphyran dose–dependent abundance and reversible engraftment in humans, reduction of oxalate in the urine, and characterized genetic stability challenges to achievinglong-term treatment.

The lower gastrointestinal tract has evolved to harness diverse functions from its resident microbiota, thereby providing a compartmentalized yet biologically meaningful site to target engineered cell therapies. Pioneering efforts have tended to take a direct approach by delivering the maximally tolerated dose of auxotrophic bacteria engineered to express therapeutic activities while transiently inhabiting the gut (*1*–*8*). Despite showing efficacy in animals and a good safety profile in humans, these therapeutics have struggled to show clinical efficacy. A colonizing strategy may enable therapeutic concentrations high enough to drive the activity necessary for efficacy.

We approached the challenge of stably colonizing the gut with bacteria engineered to robustly perform a therapeutic function by focusing on *Phocaeicola vulgatus*, a *Bacteroidaceae* family member abundant in the gut microbiota of industrialized peoples (*9*–*14*). Previously, our group engineered a *Bacteroidaceae* strain by adding genes that encode utilization of the seaweed-derived polysaccharide porphyran to enable colonization levels that are tunable with porphyran concentration (*15*). We chose porphyran as a candidate for creating an exclusive niche for our engineered bacteria because only 2% of Western individuals appear to harbor a native porphyran-utilizing microbe (*16*). In mice, our engineered *Bacteroidaceae* overcomes colonization resistance, even from established isogenic strains lacking the capacity for porphyran consumption (*15*, *17*). Although a robust engraftment technology is necessary, for therapeutic purposes, it must be reversible, and we have addressed this in the present work.

We applied our strategy to developing a therapeutic for addressing enteric hyperoxaluria (EH), a disease with unmet clinical need and mechanistic links to the gastrointestinal tract, by engineering a high-flux oxalate degradation pathway in *P. vulgatus*. We developed a candidate microbial therapeutic and showed controlled colonization of healthy human volunteers in phase 1. However, phase 2a clinical trials revealed that horizontal gene transfer (HGT) occurred specifically in the microbiota of EH patients, which we characterized.

Results

Engineered microbe reduces rat urine oxalate

EH is a disease caused by pathological overabsorption of dietary oxalate, often leading to recurrent calcium oxalate kidney stones (*18*). Reduced prevalence of colonic oxalate-degrading bacteria due to antibiotic use has been associated with EH (*19*). No natural oxalate-consuming *Bacteroidaceae* have been described previously. To engineer oxalate consumption into *P. vulgatus*, we introduced an oxalate:formate transporter, as well as a pathway for the conversion of oxalate to formate (Fig. 1A). We screened 92 enzymes in permutated combinations for optimized expression of several five- to seven-gene metabolic pathways using an iterative approach (see the supplementary materials) to create strains able to rapidly degrade oxalate into formate. We achieved conversion rates of up to 15 mM per hour at bacterial densities of 10^{10} colony-forming units (CFUs)/g expected in the gut (fig. S1, A to C). We observed a trade-off between oxalate degradation and bacterial growth rates in vitro, which we did not observe in growth conditions lacking oxalate. We selected a pathway to advance (sZR0310) with a 9 mM per hour conversion rate and modest oxalate-dependent fitness defect (fig. S1, C and D).

In a dietary EH rat model, high-density engraftment (7.2×10^8 to 2.6×10^{10} CFUs/ml) with porphyran-utilizing *P. vulgatus* containing the oxalate-degradation pathway reduced urine oxalate by 47% compared with the control strain lacking the pathway (Fig. 1B). Separately, when porphyran concentration was gradually increased, the corresponding colonization level and urine oxalate reduction both increased (fig. S2). Gastric bypass surgery is clinically associated with EH onset in humans (*18*), and we further showed that our therapeutic strain reduced urine oxalate in a rat Roux-en-Y gastric bypass (RYGB) surgical model. RYGB surgery resulted in a 51% increase in the urine oxalate in rats colonized by the control strain, an increase that was completely eliminated in animals harboring the oxalate-degrading strain (Fig. 1C).

Essential gene regulation enables reversible engraftment

If microbial cell therapies are to be widely adopted, then reversible engraftment is essential (*2*, *5*, *20*, *21*). Dietary porphyran can create an exclusive niche for porphyran-utilizing strains to enable predictable colonization of diverse microbiotas (*15*, *17*). However, the persistence of porphyran-utilizing strains after porphyran removal is difficult to predict because of the complexity of the ecosystem and the broad range of nutrients that *Bacteroidaceae* can consume.

To improve strain clearance without complicating treatment dosing, we engineered our strain to have additional dependence upon porphyran by replacing the native regulation of the essential gene *arginyl-tRNA synthetase* (*argS*) with a porphyran-inducible promoter (Fig. 2A). A 115-nucleotide sequence from the porphyran polysaccharide utilization locus (PUL) (*22*) with a 500-fold induction was identified and used to replace the *argS* promoter (fig. S3A). Replacing the promoter and tuning the ribosome-binding site of essential genes ensures that growth becomes dependent on the presence of porphyran even in rich media, where other carbon sources are available (fig. S3). This conditional attenuation resists complementation by cross-feeding, because charged transfer RNAs (tRNAs) are not readily imported. It also resists simple loss-of-function mutations, because inactivation of the porphyran

[1]Novome Biotechnologies, South San Francisco, CA, USA. [2]Department of Microbiology and Immunology, Stanford University School of Medicine, Stanford, CA, USA. [3]Chan Zuckerberg Biohub, San Francisco, CA, USA. [4]Center for Human Microbiome Studies, Stanford University School of Medicine, Stanford, CA, USA. ***Corresponding author. Email: wrw@stanford.edu †Present address: North Seattle College, Seattle, WA, USA. ‡Present address: Parexel International, San Diego, CA, USA.**

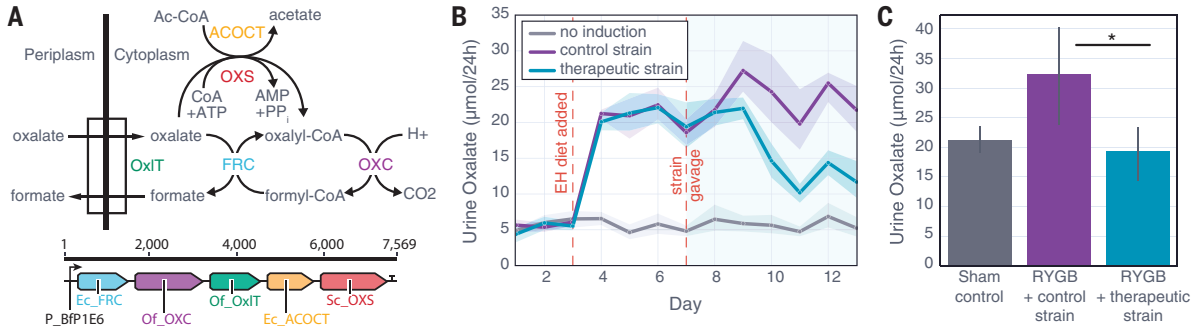

Fig. 1. *Bacteroidaceae* with engineered oxalate degradation reduce urine oxalate in rat EH models. (**A**) Oxalate degradation was engineered into a *P. vulgatus* strain by introducing genes encoding oxalate transport (*OxlT*) and four enzymatic activities (*OXS*, *ACOCT*, *FRC*, and *OXC*). (**B**) High urine oxalate was induced (first vertical dashed red line) in rats by incorporating spinach into their diet on day 3 (blue and purple). Strains with (blue) or without (purple) an oxalate-degrading pathway were gavaged on day 7 (second vertical dashed red line). After 24 hours, urine was collected for each rat and the average total urine oxalate (µmol/24 h) and 95% confidence interval (shaded area) were plotted. (**C**) Urine oxalate (mean per animal, days 6 to 10 after gavage) was elevated in rats that underwent RYGB and were colonized with the control strain (purple) compared with sham-operated rats (gray). Colonization with the oxalate-degrading strain (blue) abrogated this RYGB-induced increase. Data are shown as mean ± 95% confidence interval for days 6 to 10. $P < 0.05$, two-tailed unpaired Student's *t* test.

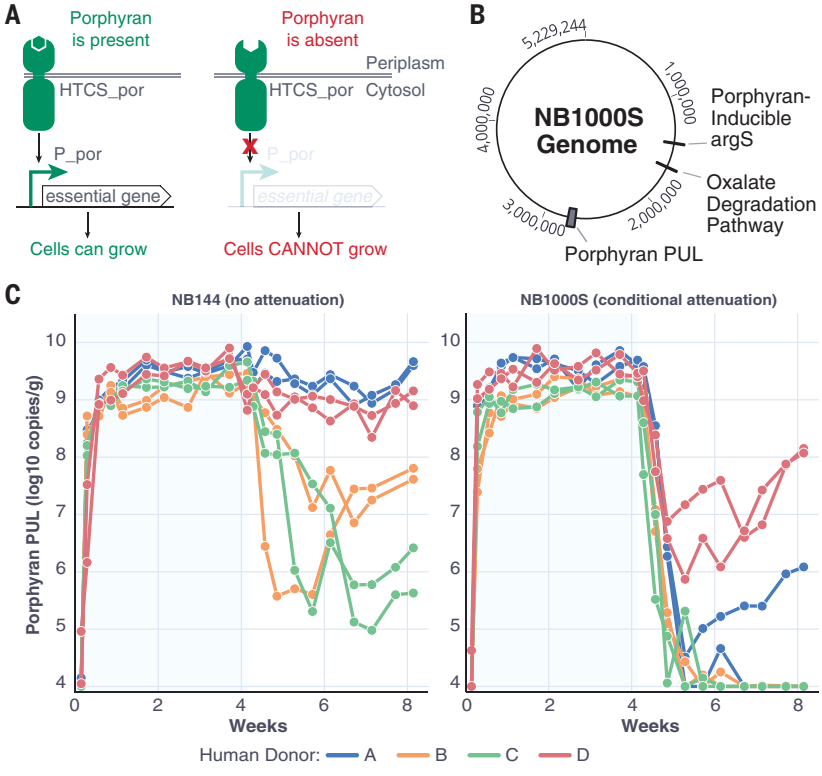

Fig. 2. Combining porphyran utilization and essential gene regulation enables reversible engraftment. (**A**) Conditional attenuation strategy uses a porphyran-sensing HTCS to drive an essential gene. (**B**) Diagram of the NB1000S therapeutic strain containing conditional attenuation, an oxalate-degradation pathway, and a porphyran PUL. (**C**) Gnotobiotic mice harboring one of four human donor microbiotas were gavaged on day 1 with NB144, a strain containing a porphyran PUL (left), or NB1000S, a therapeutic strain bearing a porphyran PUL and porphyran-dependent expression of *argS* (right). Porphyran was supplied in the diet for the first 28 days (green). Copies of the porphyran PUL per gram of feces are plotted for individual mice. Colonization dropped to the LOD, 10^4 copies/g, in five of the eight NB1000S-gavaged mice after porphyran was removed.

sensor, promoter, or essential gene prevents growth. Additionally, this strategy imposes a minimal fitness burden and uses a rare, nonabsorbable, and safe dietary control molecule.

We added this conditional attenuation module to our oxalate-degrading, porphyran-utilizing *P. vulgatus* strain to make the therapeutic strain NB1000S (Fig. 2B). We administered NB1000S or a control strain carrying the porphyran polysaccharide utilization locus (PUL^+) alone but lacking conditional attenuation and the oxalate pathway (NB144) to formerly germ-free mice harboring different healthy human donor gut microbiotas and fed a porphyran-containing diet. After 4 weeks, removing dietary porphyran resulted in variable colonization levels of unattenuated PUL^+ *P. vulgatus* (10^5 to 10^{10} copies/g; Fig. 2C, left panel). Porphyran removal from the NB1000S-colonized mice resulted in clearance to below the limit of detection (LOD) of the strain from five of eight mice (Fig. 2C, right panel). The remaining three mice in which NB1000S persisted showed reduced abundance when porphyran was removed before subsequently rebounding. Sequencing NB1000S isolates from donor D mice, both of which exhibited rebounding colonization (Fig. 2C, right panel), revealed a single point mutation (S811L) in the porphyran hybrid two-component system (HTCS), likely driving constitutive essential gene expression.

To test the long-term genetic stability of NB1000S in the presence of porphyran, we colonized conventional mice and periodically phenotyped bacterial isolates for oxalate degradation and growth restriction in rich media lacking porphyran. After 421 days, 52% of isolates lost oxalate degradation, but no conditional attenuation escapes occurred (fig. S6).

Because human microbiomes reconstituted in gnotobiotic mice are likely to contain less diversity than the original human community, we sought to test whether this conditional attenuation, which did not fully prevent persistence in humanized mice, would be sufficient for clearance in a native human gut. Despite the possibility

of mutational escape, testing NB1000S in humans carries minimal risk because oxalate is not required for human physiological function, and the natural oxalate-degrading bacteria and the genes used here often exist in the gut microbiome of healthy individuals.

Engineered microbe controllably colonizes healthy volunteers

To test the safety, tolerability, and colonization performance of NB1000S in humans, we designed and ran study NOV-001-CL01, an adaptive phase 1/2a clinical trial conducted in the US and Canada (figs. S7 to S10 and tables S3 and S4) (*23*). In phase 1, a total of 39 healthy volunteer subjects were randomized to seven study arms. On day 1, participants received the antacid Alka Seltzer Gold and NB1000S (one or two doses of 10^9 CFUs as frozen glycerol stocks) or placebo administered orally. Individuals received 0 to 20 g of porphyran daily for 14 days upon strain or placebo dosing, with groups receiving different daily porphyran doses: Group 1 received 0.5 g, group 2 received 10 g, group 3 received 2.5 g, and group 2X received two 10-g doses. NB1000S abundance in the fecal samples of individuals was measured regularly through quantitative polymerase chain reaction (qPCR) of the porphyran PUL and oxalate-degradation sequences immediately before, during, and for at least 8 weeks after cessation of porphyran dosing (Fig. 3A).

In the first two groups dosed with NB1000S (groups 1 and 2), colonization was variable, with engraftment failing in half of the individuals (engraftment was defined by NB1000S being detected in the stool at a level of $\geq 10^7$ copies/g in the last sample collected during porphyran dosing) (fig. S11B). To enhance bacterial survival through the stomach, a 40-mg dose of extended-release omeprazole (a proton pump inhibitor) was administered before dosing NB1000S (fig. S11C). With this intervention, colonization improved, with seven of eight individuals becoming engrafted in group 3 (Fig. 3B) and four of four individuals becoming engrafted in group 2X (fig. S11). When comparing engrafted individuals across all groups, strain colonization density showed dose responsiveness to porphyran, with an ~10-fold increase in NB1000S for each fivefold increase in porphyran (Fig. 3C).

Upon cessation of porphyran administration, NB1000S fecal abundance dropped below the LOD in 15 of 19 engrafted subjects in the four groups dosed with NB1000S (fig. S11). To test whether the strain could rebound upon porphyran reintroduction, we readministered NB1000P or porphyran in amounts that might be encountered in the diet and monitored NB1000S levels in the stool. Six subjects who showed NB1000S measurements below the LOD participated in a porphyran rechallenge after 56 to 98 days of no porphyran ("washout") by consuming either 10 g of porphyran or 5.2 g of seaweed snacks (which contain porphyran) daily for 7 days. In all six subjects, the levels of NB1000S in the stool remained undetectable on porphyran rechallenge, indicating that clearance of the strain was achieved.

NB1000S remained detectable in the stool of four subjects 56 days after cessation of porphyran administration. These individuals were treated with a 7-day course of oral antibiotics, which failed to clear NB1000S in most patients (fig. S13) despite the strain's sensitivity to the antibiotics in vitro (table S2).

In the four persistently colonized subjects, genomic sequencing of fecal NB1000S isolates revealed distinct genomic mutations disrupting porphyran responsiveness. In two cases, the HTCS contained point mutations that resulted in constitutive HTCS activity, consistent with the escape mechanisms observed in our humanized mouse study. In the other two subjects, genome rearrangements were present that placed other promoters immediately upstream of the essential gene.

Adverse events (AEs) were mostly mild and transient, with a predominance of gastrointestinal AEs such as diarrhea and flatulence (tables S5 and S6). There were no severe or serious AEs attributable to NB1000S. There was also no apparent relationship between product dose, engraftment, or persistent fecal shedding by NB1000S and the incidence or severity of AEs. Consistent with the synthetic metabolic niche engraftment approach in mice (*15*, *17*), metagenomic profiling of human subject feces before, during, and after treatment revealed no discernible change in the diversity of the native microbiota (fig. S12).

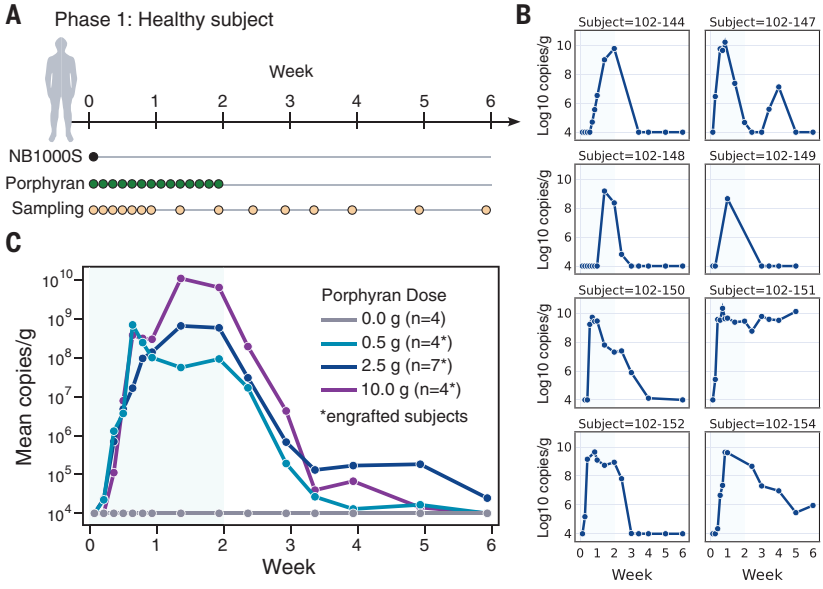

Fig. 3. Porphyran-dose–dependent colonization of healthy volunteers by therapeutic strain NB1000S. (**A**) Volunteers were administered a single dose of NB1000S on day 1 and administered porphyran daily for 2 weeks, with periodic sampling to assess colonization. (**B**) Copies of NB1000S per gram of feces for all eight individuals in the 2.5-g porphyran cohort. The period of porphyran dosing is highlighted in green. (**C**) For engrafted subjects, defined as those who were colonized above 10^7 copies/g on the last collected sample during porphyran dosing (all data are shown in fig. S11), mean NB1000S copies per gram of feces for all collected samples are shown for the four cohorts given different daily doses of porphyran.

Redundancy prevents conditional attenuation escape mutants

In light of the observed mutants that escape conditional attenuation in humanized mice and healthy volunteer individuals in our clinical trial, we investigated the mechanism of escape to develop prevention strategies. We inoculated a conditionally attenuated strain into a chemostat initially containing porphyran. After 2 days of washout with media lacking porphyran, we observed a large drop in abundance, followed by takeover by conditional attenuation escapes (Fig. 4A). Whole-genome sequencing (WGS) of 385 escape mutants revealed that 95% were driven by point mutations resulting in constitutive activation of the HTCS (fig. S14A). The remaining 5% of mutants revealed genomic rearrangements or transposon insertion immediately upstream of *argS*, likely inserting an alternative promoter to drive this gene. These escape mechanisms were consistent with those observed in humanized mice and humans.

Because all observed escape strains appear to be the result of rare gain-of-activity mutations to the HTCS or rearrangements specific to the essential gene promoter, we attempted to improve our conditional attenuation strategy such that multiple independent rare mutations would be required for escape. We hypothesized that engineering the porphyran sensor domain to drive three

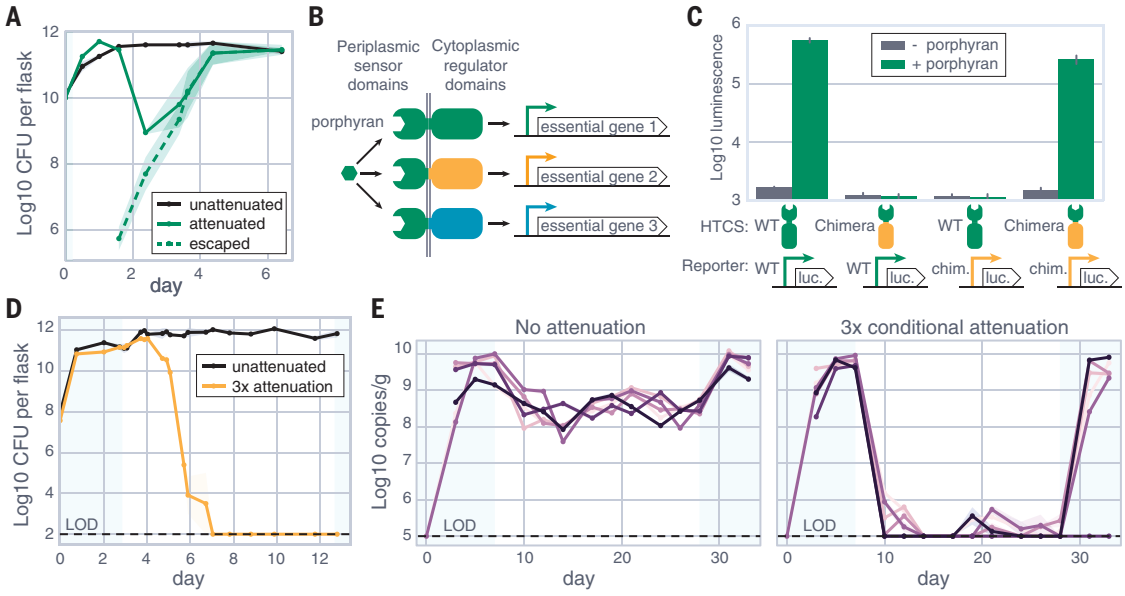

Fig. 4. Additional layers of conditional attenuation through chimeric porphyran sensors improve attenuation. (**A**) Chemostats initially containing porphyran were inoculated with a strain with either no conditional attenuation (black) or one layer of conditional attenuation (green) and then continuously diluted by media lacking porphyran. The mean CFUs per chemostat on porphyran-containing (solid line) or porphyran-lacking (dashed line), associated with conditional attenuation escape, plates are shown. (**B**) Heterologous regulator domains and corresponding promoters were used to create chimera HTCSs capable of independently driving porphyran-dependent expression of three essential genes. (**C**) The wild type (WT) and a chimeric $HTCS_{PorReg17150\text{-}v2}$ show more than a 100-fold induction in response to porphyran (green) only in their corresponding promoter, with no observed cross-talk. (**D**) Chemostats were switched from dilution with porphyran-containing media (green background) to media without porphyran on day 3, and average CFUs on porphyran containing plates are plotted for nonattenuated (black) or three-layered conditional attenuation (orange) strains. (**E**) Strain abundance was monitored for conventionally raised mice colonized with porphyran PUL–containing strains without attenuation (left) or after three-layered conditional attenuation (right). Abundance in individual mice is plotted. Porphyran was supplied in the diet in the periods highlighted in green.

different essential genes with three unrelated orthogonal promoters (Fig. 4B) would provide a system requiring three independent rare mutations to achieve escape, resulting in a vanishingly small probability of mutational escape. We generated chimeric HTCSs (*24*) using porphyran sensors (*16*, *22*) and regulatory domain and promoter pairs from the PULDB database (*25*) that were rarely found in other *Bacteroidaceae*, yielding functional but weak (two- to 15-fold) porphyran-activated chimeras (fig. S14C). Additional tuning of the HTCS expression and mutagenesis of the chimeric HTCS at the fusion point resulted in the orthogonal chimeras $HTCS_{PorReg17150\text{-}v3}$ and $HTCS_{PorReg17106\text{-}v2}$ with 100-fold porphyran induction (Fig. 4C and fig. S14). These chimeras were used to create a strain bearing three conditional attenuation mechanisms, which were cleared from a chemostat upon porphyran depletion and showed no rebound in growth, as shown by optical density (OD_{600nm}) upon reintroduction of porphyran for an additional week (Fig. 4D).

We tested the three-layered conditional attenuation strain for clearance in conventionally raised mice, and when porphyran was removed, a strain lacking conditional attenuation decreased in density by ~1 to 2 logs, whereas the strains containing three conditional attenuation mechanisms decreased 4 logs to the LOD (Fig. 4E). After 3 porphyran-free weeks, the numbers of conditionally attenuated strains in the feces were undetectable in most mice, but five of six mice rebounded upon porphyran reintroduction (Fig. 4E). The conditionally attenuated strains isolated from the persistently colonized animals showed no mutations by WGS, and phenotypically behaved as if there were no escapes in vitro (fig. S15A). In mice colonized with permissive human-derived microbiotas, removal of porphyran led to a greater reduction in the strain when bearing three-layered conditional attenuation compared with a single layer, but neither strain was fully cleared (fig. S15B). Recreating and testing two-layered conditional attenuation in three other *Bacteroidaceae* species also resulted in persistence without mutation (fig. S15C). We ran >100 experiments to determine the non-mutational means of persistence in the absence of porphyran, including RNA sequencing in gnotobiotic mice and transposon-sequencing screens (fig. S15, D and E), but genetic escapes were not evident, and the mechanism of in vivo persistence of the strains bearing three-layered conditional attenuation remains undetermined.

Genetic exchange was evident in phase 2

In parallel to our efforts to improve conditional attenuation, and after demonstrating successful and safe engraftment in healthy human volunteers, in phase 2 of the study, NB1000S was tested in individuals with EH secondary to RYGB or to biliopancreatic diversion with duodenal switch (BPD-DS) bariatric surgical procedures. Nine EH individuals received omeprazole followed by NB1000S (two doses of 10^9 CFUs orally) and 10 g of porphyran daily for 28 days; three individuals received placebo (Fig. 5A and fig. S7). NB1000S engraftment was less consistent and reached a lower density in individuals compared with healthy volunteers (fig. S16), possibly related to the strain's fitness defect observed only in the presence of high oxalate in vitro (fig. S1D) or, in the case of individual 103-203, due to prior colonization with a porphyran-utilizing strain (fig. S17A).

As with healthy volunteers, NB1000S abundance was tracked in patients using qPCR of both unique porphyran PUL and oxalate pathway sequences. However, unlike healthy volunteers, in whom the oxalate pathway and porphyran PUL sequences were very closely correlated, many phase 2 human samples showed substantially higher PUL copy number than the oxalate pathway (Fig. 5B). This discrepancy appeared before strain dosing (individual 103-203), during porphyran treatment (individual 125-202) or shortly after porphyran was removed (individuals 121-212, 110-204, 117-201, and 125-204) (Fig. 5C and

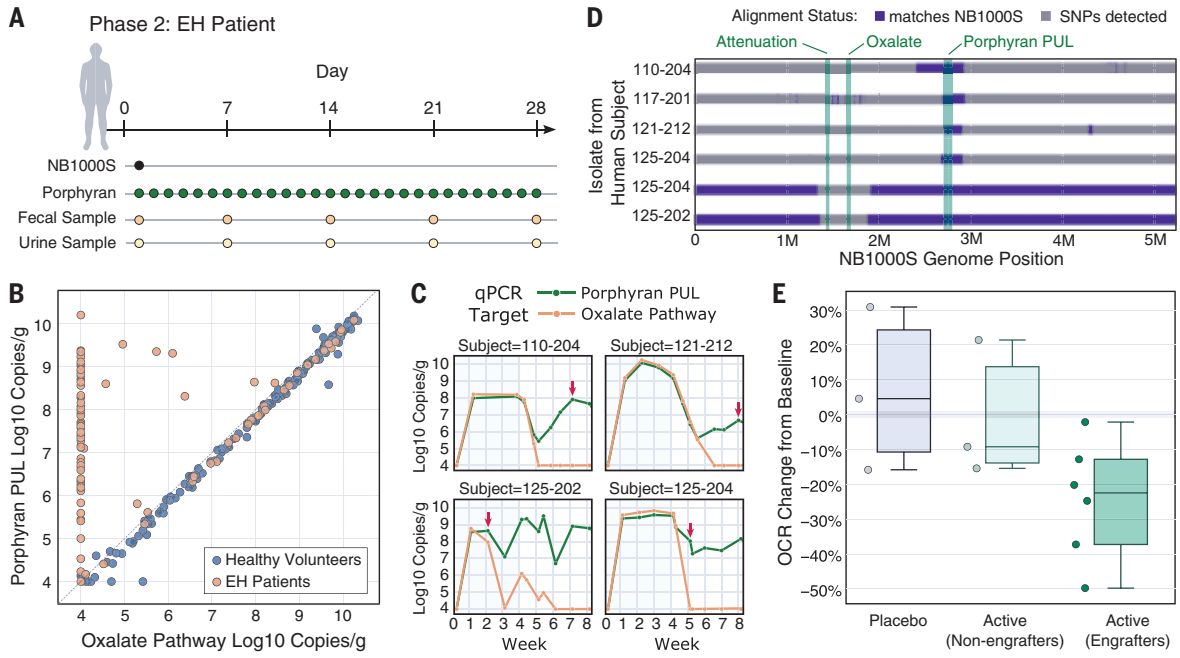

Fig. 5. Large HGT events are found in EH patients but not in healthy volunteers. (**A**) In phase 2, EH patients that had prior RYBG or BPD-DS treatment and exhibited high levels of urine oxalate were administered NB1000S on day 1 and porphyran daily. Once per week fecal and 24-hour urine samples were taken. (**B**) Copies of the porphyran PUL and the oxalate degradation pathway per gram of feces plotted for the healthy volunteers in phase 1 (blue) and the EH patients in phase 2 (orange) who were negative for porphyranase during screening. Dashed line indicates equal abundance. (**C**) Copies of the oxalate pathway (orange) and porphyran PUL (green) are plotted for representative patients. Daily porphyran dosing period is highlighted in light green. Red arrows indicate point of strain isolation. (**D**) Genomes of strains isolated from phase 2 patients compared with the original NB1000S strain (matches are shown in blue). Genetically modified regions of NB1000S are highlighted in green. Regions with elevated levels of single-nucleotide polymorphisms and deletions relative to NB1000S, suggesting origin from another strain, are shown in gray. (**E**) Percentage change in baseline urine oxalate to creatinine ratio (OCR) is shown for placebo (gray), nonengrafted patients falling below 10^7 oxalate pathway copies/g on last porphyran day (light green), and the remaining engrafted patients (dark green). $P = 0.08$ versus placebo, two-tailed Welch's t test.

fig. S17A). Two individuals (103-201 and 121-216) showed no discrepancy. To determine the reason for this discrepancy, six strains bearing the porphyran PUL were isolated from five different individuals (time points are indicated in fig. S17) and underwent WGS. Comparative sequence analysis revealed that two NB1000S strains had incoming 667- and 724-kb HGT that fully replaced the oxalate pathway and conditional attenuation module (Fig. 5D). The other three strains were native *Phocaeicola* (table S9) that took up the porphyran PUL from NB1000S through HGT events ranging from 216 to 561 kb. We also isolated the native *Phocaeicola* strains before they acquired the porphyran PUL. Comparative analysis (fig. S17) revealed DNA sequences in the post-HGT strain that were absent from both its original parent strain and NB1000S. Among these was an integrative and conjugative element (ICE) that may have promoted outgoing HGT (*26*). We experimentally introduced an ICE element into NB1000S, which significantly increased the rate of outgoing HGT in vitro (fig. S18A). Using this strain in vitro, we showed that splitting two essential porphyran-utilization genes, a glycoside hydrolase and a sulfatase, by 200 kb on the chromosome reduced HGT frequency by >10,000-fold compared with when they were adjacent (fig. S18B).

All predefined urine oxalate analyses (table S1) showed small, statistically insignificant improvements over placebo. Post hoc analysis of the urine oxalate-to-creatinine ratio showed a 27% reduction comparing all treated individuals with placebo ($P = 0.13$; fig. S19D) or comparing engrafted individuals with placebo or nonengrafted individuals ($P = 0.03$; fig. S19H). In both phases of trial NOV-001-CL01, there were no serious product-related adverse events, and no individuals left the study or required dose adjustment because of safety or tolerability issues (tables S5 to S8).

Discussion

In this study of the effectiveness of controllably colonizing therapeutic bacteria in humans, we tested an oxalate-degrading clinical candidate strain coupled with porphyran polysaccharide ingestion in healthy subjects and individuals with EH. We showed that it is possible to colonize humans with an engineered gut commensal for a sustained period at high levels. A single dose of the strain was sufficient for colonization if the subject was provided proper gastric protection, and even at high doses of porphyran, the treatment was safe and well tolerated.

Because the human gut is a highly competitive environment, it was unclear whether conditional attenuation would be required for strain clearance. Our data showed that although NB1000S cleared from most subjects, a single conditional attenuation layer was not sufficient to prevent persistent colonization in healthy volunteers through mutations of the HTCS or the essential gene promoter seen in preclinical models. Adding two additional layers of conditional attenuation successfully prevented the emergence of escape mutations, but for unknown reasons, although attenuated, the strain bearing three-layered conditional attenuation could persist in vivo.

Unlike healthy volunteers, in individuals diagnosed with EH, our strain colonized at more variable levels. We observed large HGT events in five of the seven patients in whom NB1000S lost its oxalate degradation pathway and conditional attenuation or other gut bacteria acquired the porphyran PUL. Without exclusive access to porphyran, NB1000S may be outcompeted by more fit strains, reducing treatment durability (*27*). Individuals with EH were selected based on high urine oxalate and RYGB history as a proxy for elevated intestinal oxalate, which imposes a fitness burden on NB1000S and may explain the

observed HGT prevalence, although the altered gut environment associated with RYGB could also play a role.

Despite conditional attenuation escape and genetic stability issues limiting the potential effectiveness of NB1000S, we saw promising, although inconclusive, directional reductions in urine oxalate levels. Reducing the oxalate-associated fitness burden in a future probiotic strain may improve colonization and genetic stability. Additionally, although clearance is currently imperfect, we did not observe escape using the single-layer conditional attenuation of NB1000S in colonized mice after 421 days on a porphyran diet. An improved conditional attenuation could be used to periodically clear and replace any strains with defective therapeutic activity. Moving beyond porphyran, an even more exclusive synthetic polysaccharide could enable greater control, which may be particularly important in populations with higher porphyran consumption and associated porphyran-utilizing microbes, as seen in parts of Asia (*16*).

Limitations of this study highlight key challenges for clinical implementation. Enhancing biosafety will require further improvements in conditional attenuation and HGT prevention, as well as strategies to reduce the fitness burden of therapeutic activity, which may improve colonization in the target population. Although our approach appeared safe and did not broadly disrupt microbiome diversity, specific ecological and metabolic impacts, including potential consequences of *P. vulgatus* expansion (*28*) and oxalate-to-formate conversion (*29*, *30*), merit further study.

As causal molecular mechanisms underlying associations between the gut microbiota and human disease become clearer, our platform and data offer a tool to deliver defined therapeutic activities to the human colon. Combining multiple activities into a single therapeutic strain to better treat complex diseases may be possible without substantially increasing the complexity of manufacturing, trial design, and other downstream activities.

REFERENCES AND NOTES

1. L. Steidler *et al.*, *Science* **289**, 1352–1355 (2000).
2. L. Steidler *et al.*, *Nat. Biotechnol.* **21**, 785–789 (2003).
3. H. Braat *et al.*, *Clin. Gastroenterol. Hepatol.* **4**, 754–759 (2006).
4. K. Vandenbroucke *et al.*, *Mucosal Immunol.* **3**, 49–56 (2010).
5. V. M. Isabella *et al.*, *Nat. Biotechnol.* **36**, 857–864 (2018).
6. C. B. Kurtz *et al.*, *Sci. Transl. Med.* **11**, eaau7975 (2019).
7. M. K. Puurunen *et al.*, *Nat. Metab.* **3**, 1125–1132 (2021).
8. J. Vockley *et al.*, *Nat. Metab.* **5**, 1685–1690 (2023).
9. Human Microbiome Project Consortium, *Nature* **486**, 207–214 (2012).
10. J. Xu *et al.*, *Science* **299**, 2074–2076 (2003).
11. A. G. Wexler, A. L. Goodman, *Nat. Microbiol.* **2**, 17026 (2017).
12. M. Mimee, A. C. Tucker, C. A. Voigt, T. K. Lu, *Cell Syst.* **1**, 62–71 (2015).
13. B. Lim, M. Zimmermann, N. A. Barry, A. L. Goodman, *Cell* **169**, 547–558.e15 (2017).
14. W. R. Whitaker, E. S. Shepherd, J. L. Sonnenburg, *Cell* **169**, 538–546.e12 (2017).
15. E. S. Shepherd, W. C. DeLoache, K. M. Pruss, W. R. Whitaker, J. L. Sonnenburg, *Nature* **557**, 434–438 (2018).
16. N. A. Pudlo *et al.*, *Cell Host Microbe* **30**, 314–328.e11 (2022).
17. S. M. Kearney, S. M. Gibbons, S. E. Erdman, E. J. Alm, *Cell Rep.* **24**, 1842–1851 (2018).
18. C. Witting *et al.*, *Clin. J. Am. Soc. Nephrol.* **16**, 487–495 (2021).
19. L. Nazzal, M. J. Blaser, *J. Am. Soc. Nephrol.* **29**, 1590–1592 (2018).
20. J. D. Hillman, J. Mo, E. McDonell, D. Cvitkovitch, C. H. Hillman, *J. Appl. Microbiol.* **102**, 1209–1219 (2007).
21. J. W. Lee, C. T. Y. Chan, S. Slomovic, J. J. Collins, *Nat. Chem. Biol.* **14**, 530–537 (2018).
22. J. H. Hehemann, A. G. Kelly, N. A. Pudlo, E. C. Martens, A. B. Boraston, *Proc. Natl. Acad. Sci. U.S.A.* **109**, 19786–19791 (2012).
23. Novome Biotechnologies, "Safety, tolerability, and pharmacodynamics of NOV-001 in adult subjects" (ClinicalTrials.gov identifier: NCT04909723, 2023); https://clinicaltrials.gov/study/NCT04909723.
24. J. B. Lynch, J. L. Sonnenburg, *Mol. Microbiol.* **85**, 478–491 (2012).
25. N. Terrapon *et al.*, *Nucleic Acids Res.* **46**, D677–D683 (2018).
26. M. J. Coyne, N. L. Zitomersky, A. M. McGuire, A. M. Earl, L. E. Comstock, *mBio* **5**, e01305-14 (2014).
27. M. R. Charbonneau, V. M. Isabella, N. Li, C. B. Kurtz, *Nat. Commun.* **11**, 1738 (2020).
28. T. Zhang *et al.*, *Nat. Microbiol.* **10**, 348–361 (2025).
29. G. Hawkins-van der Cingel, S. B. Walsh, K. U. Eckardt, F. Knauf, *Mayo Clin. Proc.* **99**, 1149–1161 (2024).
30. D. Ternes *et al.*, *Nat. Metab.* **4**, 458–475 (2022).

ACKNOWLEDGMENTS

We thank A. Huang, S. Kim, L. Piette, L. Ramirez, R. Robinson, Z. Basham, T. Kao, A. Cho, K. Rodriguez, K. Sharma, A. Chazin-Gray, L. Waldburger, C. Chaplin, Q. Knight, H. Ling Mak, H. Kim, E. Yu, M. Kindle, G. Kerney, J. Guzman, K. Sapasap, and M. J. Madrigal-Moeller for assistance in setting up experiments; K. Jensen for clinical administration assistance; M. Olm for analysis assistance; and J. Dueber, M. Lee, P. Spanogiannopoulos, V. Ridaura, L. Weaver, B. Bond-Watts, C. Gillis, J. De Leon, K. Roelofs, A. Pao, and E. Martens for providing input on experimental design. J.L.S. is a Chan-Zuckerberg SF Biohub investigator. Institutional review board (IRB) approval for this study was obtained from Advarra (IORG number: 0000635, protocol: Pro00050374, approval date: 25 March 2021). Advarra's IRB is registered with the US Food and Drug Administration and the Office for Human Research Protections of the US Department of Health and Human Services (IRB registration number 00000971, FWA number 00023875). **Funding:** This study was funded by Novome Biotechnologies Inc. and supported by the National Science Foundation (NSF) through Small Business Innovation Research (SBIR) award numbers 1648230 (phase 1) and 1831185 (phase 2), and the National Institutes of Health R01DK085025 to J.L.S. **Author contributions:** W.R.W., Z.N.R., E.S.S., L.M.P., A.L., K.L., D.M.Z., J.L.G., H.S.R., J.A.T., K.W., J.F., P.B., R.Y., D.N.C., T.W., L.M., J.L.S., and W.C.D. conceived of the project or developed study plans. W.R.W., Z.N.R., E.S.S., L.M.P., A.L., K.L., D.M.Z., C.C.C.G., J.L.G., H.S.R., J.A.T., A.B., J.G., D.B., S.J., K.W., J.F., P.B., L.M., J.L.S., and W.C.D. were all involved with data acquisition and/or interpretation. W.R.W., Z.N.R., E.S.S., L.M.P., K.L., C.C.C.G., S.J., K.W., J.F., P.B., T.W., L.M., and W.C.D. were involved in supervision and administration. W.R.W. wrote the manuscript with input from all authors. **Competing interests:** Novome Biotechnologies is no longer operational. W.R.W., Z.R.N., E.S.S., J.L.S., and W.C.D. may receive future financial benefits from the licensing of intellectual property related to this work. W.R.W., E.S.S., and J.L.S. are inventors on US patent 11766461B2 held by Stanford University that covers gene expression. W.R.W., E.S.S., J.L.S., and W.C.D. are inventors on US patent 11566238B2 held by Stanford University that covers porphyran use for colonization. W.R.W., Z.N.R., E.S.S., J.L.S., and W.C.D. are inventors on World Intellectual Property Organization (WIPO) patent application WO2020123483A1 submitted by Novome Biotechnologies that covers EH treatment. W.R.W., Z.N.R., E.S.S., L.M.P., J.L.S., and W.C.D. are inventors on WIPO patent application WO2020252370A1 submitted by Novome Biotechnologies that covers conditional attenuation. D.N.C. serves as a consultant and board member to Novome Biotechnologies. J.G. is affiliated with Natera, Inc. D.C. is affiliated with Edgewood Oncology, Inc. J.L.S. has additional funding provided by National Institutes of Health grant R01DK085025. **Data and materials availability:** The NB1000S genome sequence (GenBank accession number CP179925) and additional isolated strains (table S9) have been deposited in GenBank as part of BioProject PRJNA1211572. All plasmids (table S10) used in constructing the strains (table S1) are available under BankIt submission 2918352 (see table S10 for individual plasmid accession numbers). All nonclinical research materials in this paper are available upon request. Clinical-grade investigational products (NB1000S and NB1000P) are no longer available. Metagenomic data are available under BioProject PRJNA1224809. Additional experimental data are provided in the supplementary materials.
License information: Copyright © 2025 the authors, some rights reserved; exclusive licensee American Association for the Advancement of Science. No claim to original US government works. https://www.science.org/about/science-licenses-journal-article-reuse

SUPPLEMENTARY MATERIALS

science.org/doi/10.1126/science.adu8000
Materials and Methods; Supplementary Text; Figs. S1 to S19; Tables S1 to S12; References (*31*–*47*); Data Tables S1 to S6; MDAR Reproducibility Checklist

Submitted 22 November 2024; accepted 16 May 2025

10.1126/science.adu8000

MOLECULAR BIOLOGY

ASB7 is a negative regulator of H3K9me3 homeostasis

Liwen Zhou[1]*†, Zhenxuan Chen[1]†, Yezi Zou[2]†, Xia Zhang[1], Zifeng Wang[1], Hongwen Zhu[3], Jiahui Lin[1], Ziyao Huang[1], Lisi Zheng[1], Jiali Chen[1], Miner Xie[4], Meifang Zhang[1], Ruhua Zhang[1], Minglu Zhu[5], Ziwen Wang[1], Hu Zhou[3], Song Gao[1], Yuxin Yin[5], Yuanzhong Wu[1]*, Tiebang Kang[1]*

The maintenance of histone H3 lysine 9 trimethylation (H3K9me3) involves the recognition of preexisting modifications by heterochromatin protein 1 (HP1), which recruits the methyltransferase suppressor of variegation 3-9 homolog 1 (SUV39H1) to methylate the adjacent newly incorporated histones, establishing a positive feedback loop. However, how this positive feedback is restricted to maintain H3K9me3 homeostasis remains largely unknown. We performed an unbiased genome-scale CRISPR-Cas9 screen and identified $CUL5^{ASB7}$ E3 ubiquitin ligase as a negative regulator of H3K9me3. ASB7 is recruited to heterochromatin by HP1 and promotes SUV39H1 degradation. During mitosis, cyclin-dependent kinase 1 (CDK1) phosphorylates ASB7, preventing its interaction with SUV39H1, leading to SUV39H1 stabilization and H3K9me3 restoration. Our findings reveal a dynamic circuit involving HP1, SUV39H1, and ASB7 that governs H3K9me3 homeostasis, ensuring faithful epigenetic inheritance and preventing excessive heterochromatin formation.

Heterochromatin plays a fundamental role in transcription repression and genome stability (*1*–*4*). Histone modifications are essential for heterochromatin formation, with histone H3 lysine 9 trimethylation (H3K9me3) being one of the key modifications (*4*–*8*). After DNA replication, histone marks are diluted owing to the newly incorporated unmodified histones (*9*–*11*). Heterochromatin protein 1 (HP1) recognizes the preexisting H3K9me3 and serves as a platform to recruit H3K9me3-writer suppressor of variegation 3-9 homolog 1 (SUV39H1) to modify the adjacent newly incorporated histones, thus forming a positive feedback loop (*7*, *12*–*16*). This mechanism ensures the propagation and restoration of H3K9me3 to the parental level. However, this positive feedback must be tightly regulated to prevent excessive H3K9me3 modification and deleterious over-heterochromatinization. In fission yeast *Schizosaccharomyces pombe*, autoinhibition of Clr4 (the ortholog of human SUV39H1/2) serves to restrain its methyltransferase activity (*17*). However, the precise regulation of H3K9me3 homeostasis in mammalian cells remains unclear.

$CUL5^{ASB7}$ restricts H3K9me3 modification

The KDM4 demethylase family has been reported to remove H3K9me3 modification (*18*–*22*). However, after triple depletion of *KDM4A/B/C* followed by multiple rounds of cell division, H3K9me3 levels failed to increase (fig. S1, A and B). This result suggests the existence of unknown mechanisms beyond KDM4 that precisely restrict H3K9me3 during the cell cycle. To identify the potential regulators, we performed a genome-scale CRISPR-Cas9 knockout screen and used fluorescence-activated cell sorting (FACS) to quantitatively assess H3K9me3 immunostaining intensity as a readout (Fig. 1A). H3K9me3 levels oscillate throughout the cell cycle. After the incorporation of unmodified new histones in the S phase, H3K9me3 levels are reduced by half and gradually return to the parental levels by the next G_1 phase (*9*, *11*, *23*). To mitigate bias resulting from gene deletion–induced cell cycle disruptions, we conducted two independent screens, one in untreated cells and one in cells treated with hydroxyurea, which arrests the cell cycle at the S phase checkpoint. The results of these two screens showed strong correlation (Fig. 1B; fig. S1, C and D; and table S1). Among the depleted single guide RNA (sgRNA) hits, we found known H3K9 methyltransferases, including the H3K9me1/2 methyltransferases *EHMT1* and *-2*, the H3K9me2/3 methyltransferases *SUV39H1* and *-2*, *SETDB1*, and the SETDB1 nuclear cofactor *ATF7IP* (Fig. 1B and fig. S1C) (*1*, *4*, *24*–*28*), which validated our approach. Consistent with the data in fig. S1B, the screens showed that deletion of the *KDM4* family members had a marginal effect on H3K9me3 levels (Fig. 1B and fig. S1C). ASB7, which is encoded by *ankyrin repeat and SOCS box containing 7*, was among the enriched sgRNA hits (Fig. 1B and fig. S1C). ASB7 is a substrate adaptor for the CUL5-Elongin B (encoded by *TCEB2*)–Elongin C (encoded by *TCEB1*) E3 ubiquitin ligase (Fig. 1C) (*29*, *30*), indicating that $CUL5^{ASB7}$ E3 ubiquitin ligase may play a critical role in restricting H3K9me3 levels.

We sought to validate the effects of ASB7 on H3K9me3. In cells with *ASB7* deletion, CUT&RUN (cleavage under targets and release using nuclease) sequencing revealed a substantial increase in H3K9me3 signals across the genome, including strengthened, spread, and de novo regions (Fig. 1, D to F). The elevated H3K9me3 signals were enriched in both repetitive elements (71.72%) and nonrepetitive elements (28.28%) (Fig. 1G), such as long interspersed nuclear elements (LINEs), satellite repeats, and imprinted genes (fig. S1, E to G). Western blot and immunofluorescent staining further confirmed that *ASB7* deletion up-regulated H3K9me3 levels (Fig. 1, H to J). By contrast, *ASB7* overexpression (OE) resulted in a substantial reduction in H3K9me3 levels (fig. S1, H to M). According to the Genotype Tissue Expression (GTEx) database, *ASB7* is widely expressed across various tissues (fig. S2A). We observed elevated H3K9me3 levels after *ASB7* depletion in multiple cell lines of different tissue origins (fig. S2B). These findings collectively underscore the general role of ASB7 in restricting H3K9me3 levels.

HP1 recruits ASB7 to heterochromatin

Next, we examined the intracellular distribution of ASB7. Cell fractionation revealed that ASB7 was enriched in chromatin and colocalized with H3K9me3 (Fig. 2, A and B), indicating that ASB7 is a heterochromatin-associated protein. To investigate how ASB7 is recruited to heterochromatin, we used a TurboID-based proximity labeling assay to biotinylate ASB7-interacting proteins (*31*), followed by streptavidin pull-down and mass spectrometry analysis (fig. S3A). The enriched hits included components of the $CUL5^{ASB7}$ E3 ubiquitin ligase complex, such as CUL5 and Elongin B/C, validating our assay (Fig. 2C and table S2). Furthermore, we identified several well-established heterochromatin-associated proteins, including H3K9 methyltransferases SUV39H1, EHMT1 and -2, and SETDB1 (Fig. 2C). Members of the HP1 family—HP1α, HP1β, and HP1γ—were also enriched (Fig. 2C). HP1, a heterochromatin scaffold protein, binds to H3K9me2/3 through its amino-terminal chromodomain (CD) and forms dimers through the carboxy-terminal chromo shadow domain (CSD) (fig. S3B) (*12*, *32*). The intrinsically disordered middle region of HP1 contributes to low-affinity, multivalent interactions (*33*, *34*). By combining stoichiometric and nonstoichiometric interactions, HP1 acts as a platform to recruit various heterochromatin regulators, including SUV39H1, HDACs, and the nucleosome remodeling and deacetylase (NuRD) complex (*35*–*38*).

To determine whether HP1 facilitates the recruitment of ASB7 to heterochromatin, we performed a series of assays. Fluorescence imaging

[1]Sun Yat-sen University Cancer Center, State Key Laboratory of Oncology in South China, Guangdong Provincial Clinical Research Center for Cancer, Guangzhou, China. [2]School of Medicine, Shenzhen Campus of Sun Yat-Sen University, Shenzhen, China. [3]Department of Analytical Chemistry, State Key Laboratory of Drug Research, Shanghai Institute of Materia Medica Chinese Academy of Sciences, Shanghai, China. [4]Department of Hematology, Guangzhou First People's Hospital, South China University of Technology, Guangzhou, China. [5]Department of Pathology, Institute of Systems Biomedicine, School of Basic Medical Sciences, Beijing Key Laboratory of Tumor Systems Biology, Peking University Health Science Center, Beijing, China. ***Corresponding author. Email: kangtb@sysucc.org.cn; wuyzh@sysucc.org.cn; zhoulw@sysucc.org.cn** †These authors contributed equally to this work.

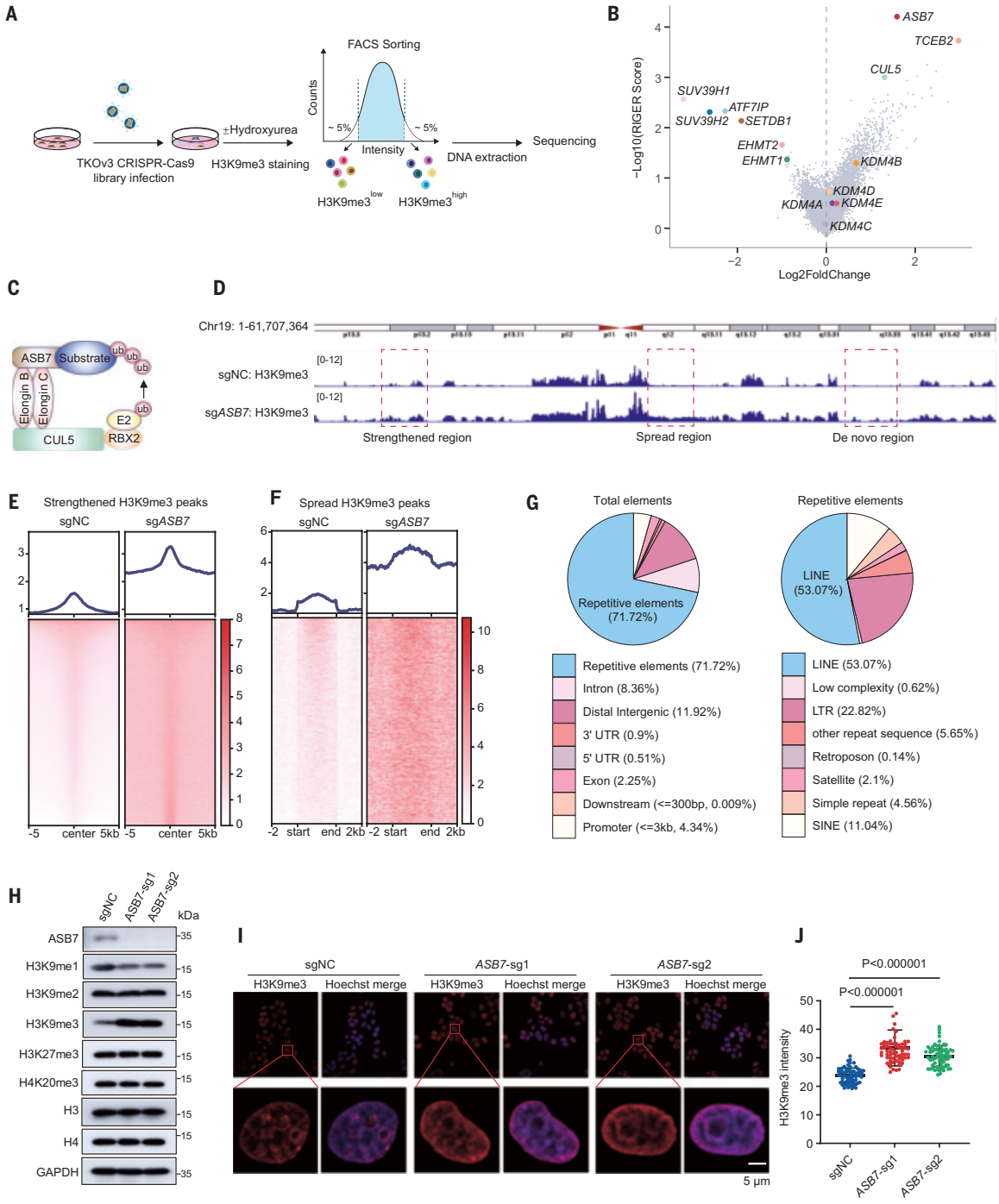

Fig. 1. CUL5^{ASB7} restricts H3K9me3 levels. (**A**) Schematic of the genome-scale CRISPR-Cas9 screen. (**B**) Plot of the screen results using RNA interference gene enrichment ranking (RIGER) analysis. (**C**) Schematic of CUL5^{ASB7} E3 ubiquitin ligase complex. (**D**) Genome browser views of H3K9me3 CUT&RUN distribution in control (sgNC) and *ASB7*-depleting (sg*ASB7*) HeLa cells. (**E**) Heatmap of the H3K9me3 signal in sgNC and sg*ASB7* HeLa cells ($n = 2$ independent experiments). (**F**) Heatmap of the spread H3K9me3 region in sg*ASB7* compared with sgNC ($n = 2$ independent experiments). (**G**) Annotation of gained H3K9me3 regions categorized by chromosome features. (**H**) Immunoblot of the two independent lentiCRISPR sgRNAs (sg1 and sg2) targeting *ASB7* in HeLa cells ($n = 3$ independent experiments). (**I**) Immunostaining of H3K9me3 in *ASB7*-depleted HeLa cells. (**J**) Quantification of the immunofluorescence intensity in (I). $n = 69$ cells in sgNC group, $n = 67$ cells in *ASB7* sg1 group, and $n = 69$ cells in *ASB7* sg2 group; *P* values were calculated by using two-tailed Student's *t* test.

and TurboID-based proximity labeling revealed that ASB7 colocalized with HP1 within heterochromatic regions (Fig. 2D and fig. S3, C to E), and HP1 silencing impaired the heterochromatin localization of ASB7 (Fig. 2E). CUT&RUN sequencing demonstrated co-occupancy of ASB7 and HP1 across the genome (Fig. 2, F and G), and HP1 depletion reduced chromatin-bound ASB7 (Fig. 2, H and I). Coimmunoprecipitation assays confirmed that ASB7 interacts with the CSD of HP1 (fig. S3, F and G), and deletion of this domain inhibited ASB7 recruitment to heterochromatin (fig. S3H). Given that the valine at position 22 (V22) in the CD of HP1α is essential for binding H3K9me3 (*35*, *39*), we found that either the HP1α V22M mutant (in which methionine replaced valine at position 22) or deletion of the CD disrupted the localization of both HP1α

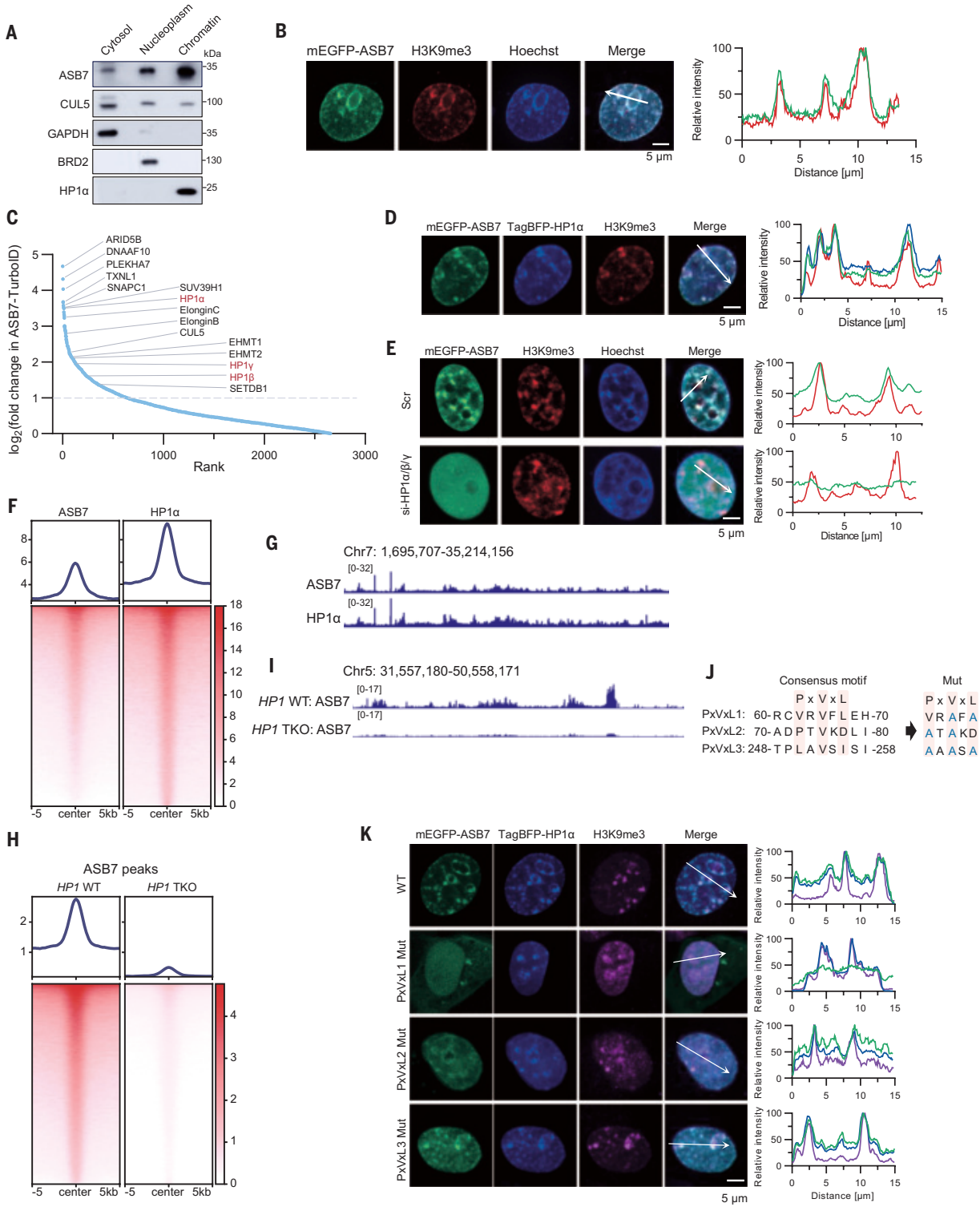

Fig. 2. HP1 recruits ASB7 to heterochromatin. (**A**) Cell fractionation and immunoblot of HeLa cells. (**B**) HeLa cells transfected with monomeric enhanced green fluorescent protein (mEGFP)–ASB7 were immunostained with H3K9me3. The relative fluorescence intensity of the indicated line scan is shown. Scale bar, 5 μm. (**C**) V5-TurboID-ASB7 identified interacting proteins in human embryonic kidney (HEK) 293T cells. The fold change represents the ratio of V5-TurboID-ASB7–identified proteins to those identified by the V5-TurboID empty vector using mass spectrometry. (**D**) Immunostaining of HeLa cells transfected with indicated plasmids and the relative intensity along the indicated line. (**E**) HeLa cells were transfected with scramble or HP1α/β/γ–targeting siRNAs and mEGFP-ASB7 construct then underwent immunostaining. The fluorescence intensity along the indicated lines are plotted on the right. (**F**) CUT&RUN sequencing and heatmap of the distribution of ASB7 and HP1α in HeLa cells ($n = 2$ independent experiments). (**G**) Genome browser views of ASB7 and HP1α CUT&RUN distribution. (**H**) Heatmap of the ASB7 CUT&RUN distribution in *HP1* WT and TKO (HP1α, HP1β, and HP1γ triple knockout) cells (**I**) Genome browser views of ASB7 CUT&RUN distribution in *HP1* WT and TKO cells ($n = 2$ independent experiments). (**J**) Sequence of the three potential PxVxL motifs and related mutants (Mut) of ASB7. (**K**) Immunostaining of HeLa cells transfected with indicated plasmids. The relative intensity along the indicated lines are plotted on the right.

and ASB7 to heterochromatin (fig. S3H). Together, these findings underscore the critical role of the ASB7-HP1 interaction in mediating ASB7 recruitment to heterochromatin.

We next mapped the interaction domain of ASB7 responsible for binding HP1. Coimmunoprecipitation revealed that the ankyrin (ANK) domain of ASB7 mediates its interaction with HP1 (fig. S4, A and B). Because the HP1 CSD dimer provides a docking platform for effector proteins that harbor a PxVxL motif (*40*–*42*), and ASB7 contains three candidate PxVxL motifs, we hypothesized that the interaction between HP1 and ASB7 is mediated by the CSD-PxVxL interface. To test this, we generated mutants for each of the three PxVxL motifs (designated PxVxL1 to PxVxL3) (Fig. 2J). Mutation of the PxVxL1 site severely impaired the ASB7-HP1 interaction and disrupted ASB7 heterochromatin localization (Fig. 2K and fig. S4, C to F). A synthetic peptide corresponding to the PxVxL1 motif directly interacted with HP1α in vitro (fig. S4G). PxVxL1 resides within the ankyrin repeat 2 (ANK2) of ASB7. Deletion of ANK2 reduced HP1α binding, whereas ANK2 alone was sufficient to interact with HP1α and to localize to heterochromatin (fig. S4, H and I). Further mutational analysis of the PxVxL1 motif revealed that leucine 67 (L67) was more critical than V65 for HP1 interaction (fig. S4, J and K). Mutation of PxVxL1 or substitution of leucine at position 67 with alanine (L67A) markedly attenuated the ability of ASB7 to restrict H3K9me3 levels (fig. S4, L and M). Together, these results illustrate that HP1 recruits ASB7 to heterochromatin through a CSD-PxVxL1 interaction, which is critical for limiting H3K9me3 levels.

ASB7 interacts with and reduces SUV39H1

Given that CUL5^{ASB7} functions as an E3 ubiquitin ligase responsible for substrate degradation, we hypothesized that ASB7 might restrict H3K9me3 levels by degrading key H3K9me3 regulators. To identify potential substrates, we performed quantitative mass spectrometry on stable cell lines with ASB7 OE compared with control (Vector) and observed a marked reduction in the abundance of H3K9me3 methyltransferase SUV39H1 (Fig. 3A). *ASB7* or *CUL5* depletion specifically increased the SUV39H1 protein levels, whereas other H3K9 methyltransferases—including SUV39H2, SETDB1, and EHMT1/2—remained unchanged (Fig. 3B and fig. S5, A to C). The increase of SUV39H1 after ASB7 depletion was validated in multiple cell lines (fig. S5D). Gene effect scores from the Cancer Dependence Map (DepMap) database revealed a strong inverse correlation between ASB7 and SUV39H1 (fig. S5E), with each being the top inverse correlated gene for the other (Fig. 3C), highlighting a functional relationship.

The above findings suggest that SUV39H1 might be a physiological substrate of ASB7. We also found that ASB7 OE not only reduced SUV39H1 levels but also partially decreased SUV39H2 and SETDB1 levels (fig. S5F). Because these three proteins are known H3K9me3 methyltransferases (fig. S5G), this likely explains the substantial reduction in global H3K9me3 levels observed after ASB7 OE (fig. S1, H to M). Nonetheless, SUV39H1 appears to be the primary physiological target. In support of this, *ASB7* deletion failed to elevate H3K9me3 levels in SUV39H1-deficient cells (fig. S5H). Considering that HP1 contributes to ASB7 localization to heterochromatin (Fig. 2), we generated *HP1* triple-knockout (TKO) cells. ASB7 deletion in *HP1* TKO cells led to only a modest increase in SUV39H1 and H3K9me3 compared with that in *HP1* wild-type cells (fig. S5I), suggesting that HP1 facilitates ASB7-mediated degradation of SUV39H1 in the heterochromatin compartment.

We next explored the interaction between ASB7 and SUV39H1. Endogenous ASB7 and SUV39H1 colocalized with HP1α (Fig. 3D). CUT&RUN profiling demonstrated co-occupancy of ASB7 and SUV39H1 on chromatin, and *ASB7* deletion resulted in elevated chromatin-bound SUV39H1 and H3K9me3 levels (Fig. 3, E to G). In vitro pull-down assays confirmed a direct interaction between ASB7 and SUV39H1 (fig. S5J). Multiple regions of SUV39H1—including the CD, Disorder region, and SET domain—were capable of binding ASB7 (fig. S5, K and L), whereas the ANK domain of ASB7 mediated the interaction with SUV39H1 (fig. S5M). Collectively, these findings establish that ASB7 interacts with SUV39H1 and negatively regulates SUV39H1 protein abundance, consequently restricting H3K9me3 levels.

CUL5^{ASB7} ubiquitinates and degrades SUV39H1

The proteasome inhibitor bortezomib, but not the lysosome inhibitor bafilomycin A1, stabilized SUV39H1 (fig. S6A), indicating that ASB7 regulates SUV39H1 through the ubiquitin-proteasome degradation pathway. *ASB7* deletion markedly extended the half-life of SUV39H1 and reduced its ubiquitylation (Fig. 3, H to J), whereas *ASB7* OE enhanced SUV39H1 ubiquitylation (fig. S6B). In vitro ubiquitination assay further demonstrated that CUL5^{ASB7} directly ubiquitinates SUV39H1 (Fig. 3K and fig. S6C). Mass spectrometry, site-directed mutagenesis, and ubiquitination assays identified lysine 138 as the predominant site of SUV39H1 ubiquitination mediated by CUL5^{ASB7} (fig. S6, D and E). Furthermore, ASB7, SUV39H1, and CUL5 were found to colocalize on heterochromatin (fig. S6F). Given that neddylation is essential for the activation of Cullin-RING E3 ligases, treatment with the neddylation inhibitor MLN4924 increased SUV39H1 abundance in control [negative-control sgRNA (sgNC)] cells but not in cells with *ASB7* deletion (fig. S6, G and H). MLN4924 also prevented the ASB7 OE–induced ubiquitylation and degradation of SUV39H1 (fig. S6, I and J). In addition, MLN4924 increased ASB7 protein levels (fig. S6G), suggesting that ASB7 itself may also be a Cullin E3 ligase substrate. An in vitro ubiquitination assay revealed that ASB7 undergoes autoubiquitination (fig. S6K), a common feature among E3 ubiquitin ligases (*43*). Moreover, we found that ASB7 forms oligomers, primarily through its C-terminal suppressor of cytokine signaling (SOCS) box domain (fig. S6, L to N). These ASB7 oligomers appear to enhance SUV39H1 ubiquitination, as shown by chemically and optogenetically inducible oligomerization systems (fig. S6, O and P). Together, these results establish that CUL5^{ASB7} promotes SUV39H1 degradation through the ubiquitin-proteasome pathway.

ASB7 represses SUV39H1 protein levels in vivo

Next, we sought to validate the role of ASB7 in regulating SUV39H1 degradation in vivo. Analysis of The Cancer Genome Atlas (TCGA) dataset revealed a recurrent R287X nonsense mutation within the SOCS domain of ASB7 (fig. S7A), leading to a premature stop and abolished its ability to degrade SUV39H1 (fig. S7B). Substitution of arginine at position 287 (R287) with a stop codon (*ASB7*$^{R287X/R287X}$) substantially increased SUV39H1 and H3K9me3 levels and extended the half-life of SUV39H1 in cells (fig. S7, C to E). Furthermore, we generated *Asb7*$^{K285X/K285X}$ mice using sgRNA to target the vicinity of the R287 codon (fig. S7, F and G). In these mutant mice, both Suv39h1 and H3K9me3 levels were markedly elevated (Fig. 3L and fig. S7H). CUT&RUN sequencing further confirmed increased H3K9me3 occupancy across the genome in *Asb7*$^{K285X/K285X}$ mice (fig. S7, I to K). Collectively, these findings establish the in vivo role of ASB7 in promoting SUV39H1 degradation and restriction of H3K9me3 levels.

CDK1 phosphorylates and inactivates ASB7

H3K9me3 undergoes a twofold dilution after DNA replication because of the incorporation of newly synthesized histones. The HP1- and SUV39H1-mediated positive feedback loop ensures the propagation and reestablishment of H3K9me3 in the subsequent cell cycle (*4*, *9*–*11*). We hypothesized that ASB7 might be regulated to secure the restoration of H3K9me3 during the cell cycle. Using double thymidine and nocodazole block-release assays, we observed that ASB7 protein levels exhibited minimal changes throughout the cell cycle, whereas SUV39H1 protein levels gradually increased from S phase to M phase and dropped upon G_1 entry (Fig. 4, A to D, and fig. S8, A and B), suggesting that SUV39H1 degradation by ASB7 may be temporally regulated.

Previous studies have reported that SUV39H1 is phosphorylated at serine 391 (S391) by cyclin-dependent kinase 2 (CDK2) (*44*). However, both S391A (serine to alanine, mimicking the unphosphorylated state) and S391D/E (serine to aspartate or glutamate, mimicking the phosphorylated state) mutants had little effect on its interaction with

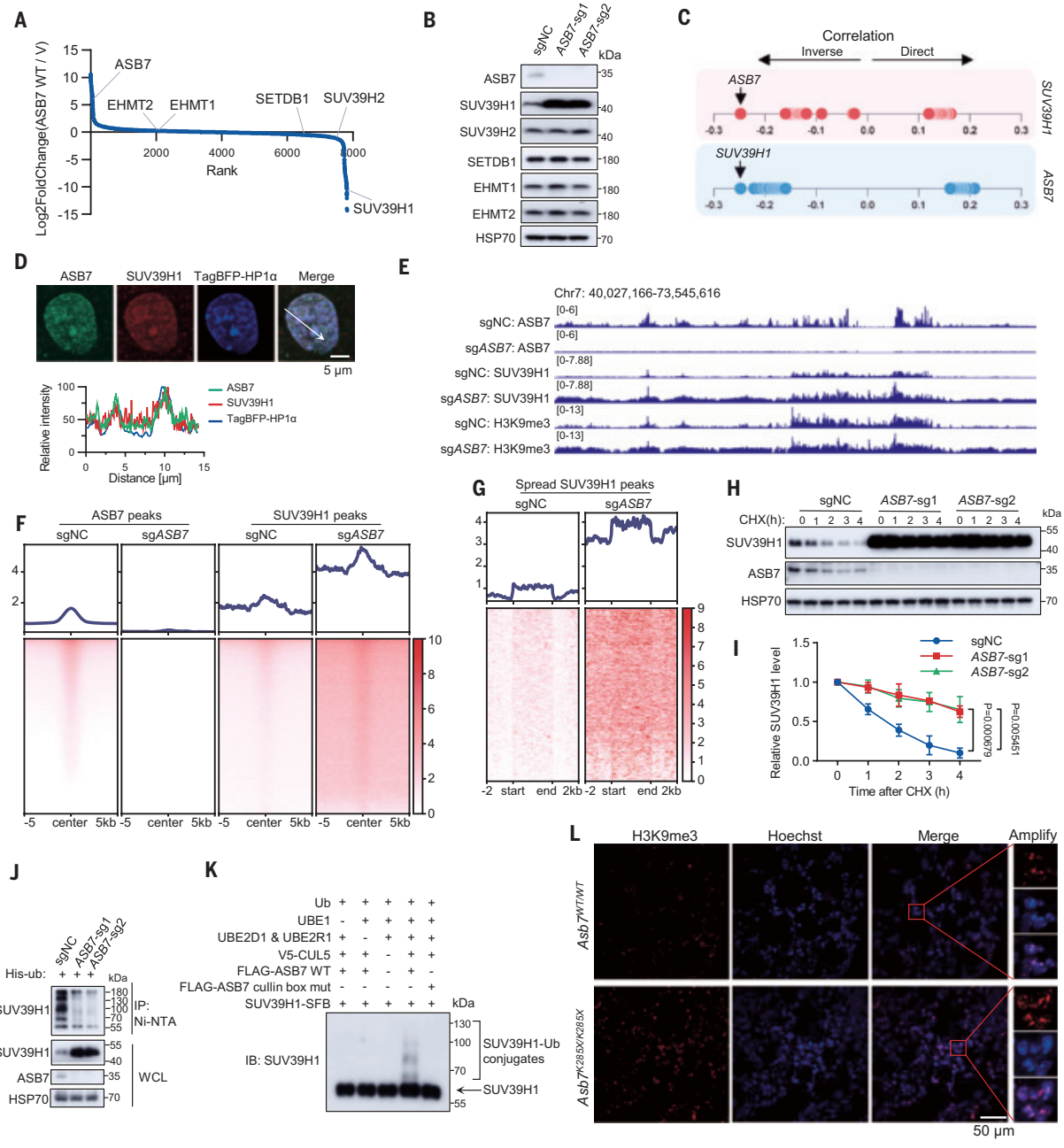

Fig. 3. CUL5^{ASB7} targets SUV39H1 for ubiquitin-proteasome degradation. (**A**) Quantitative proteomics of HeLa cells with *ASB7* OE or empty vector (V) stable expression. (**B**) Immunoblot of indicated markers in sgNC and sg*ASB7* HeLa cells. (**C**) The top 100 23Q2 precomputed associated genes for *SUV39H1* and *ASB7* in DepMap. (**D**) Immunostaining of endogenous ASB7 and SUV39H1 in HeLa cells, and plot of the relative fluorescence intensity along the indicated line. (**E**) Genome browser views of ASB7, SUV39H1, and H3K9me3 in sgNC and sg*ASB7* HeLa cells. (**F**) Heatmap of ASB7 and SUV39H1 CUT&RUN distribution in sgNC and sg*ASB7* HeLa cells ($n = 2$ independent experiments). (**G**) Heatmap of the spread SUV39H1 CUT&RUN distribution in sgNC and sg*ASB7* HeLa cells ($n = 2$ independent experiments). (**H** and **I**) Half-life and quantification of SUV39H1 in sgNC and sg*ASB7* HeLa cells treated with cycloheximide (CHX) ($n = 3$ independent experiments). *P* values were calculated by using two-tailed Student's *t* test. (**J**) Endogenous SUV39H1 ubiquitination assay in *ASB7*-deleted cells transfected with His-ub. Cell lysates were pulled down by using nickel–nitrilotriacetic acid (Ni-NTA) ($n = 3$ independent experiments). (**K**) In vitro ubiquitination assay of SUV39H1 ($n = 3$ independent experiments). (**L**) H3K9me3 immunostaining of lung tissues from *Asb7*$^{WT/WT}$ and *Asb7*$^{K285X/K285X}$ mice.

ASB7 or its protein stability (fig. S8, C to E). By contrast, we detected threonine phosphorylation in ASB7, which was strongly enhanced by the M phase–activated CDK1-Cyclin B1 complex (Fig. 4E). Inhibition of CDK1 by roscovitine led to destabilization of SUV39H1 (Fig. 4F), implying that CDK1-mediated phosphorylation may inactivate ASB7.

Sequence analysis revealed four potential CDK1 consensus motifs [threonine-proline (TP) sites] within the linkers of ASB7 ankyrin repeats (Fig. 4G). Among them, threonine 119 (T119), T152, and T216 were identified as phosphorylation sites by means of mutagenesis and mass spectrometry (Fig. 4H and fig. S8F). Simultaneous alanine substitution of these sites (T119A, T152A, and T216A, referred to as T3A) abolished ASB7 phosphorylation (Fig. 4I). To confirm endogenous ASB7 phosphorylation, we generated a phospho-specific antibody against ASB7 T216 phosphorylation (pT216) (Fig. 4J). Using this antibody, we found that pT216 fluctuated in synchrony with CDK1-Cyclin B1 activity and SUV39H1 levels during the cell cycle (Fig. 4, K and L).

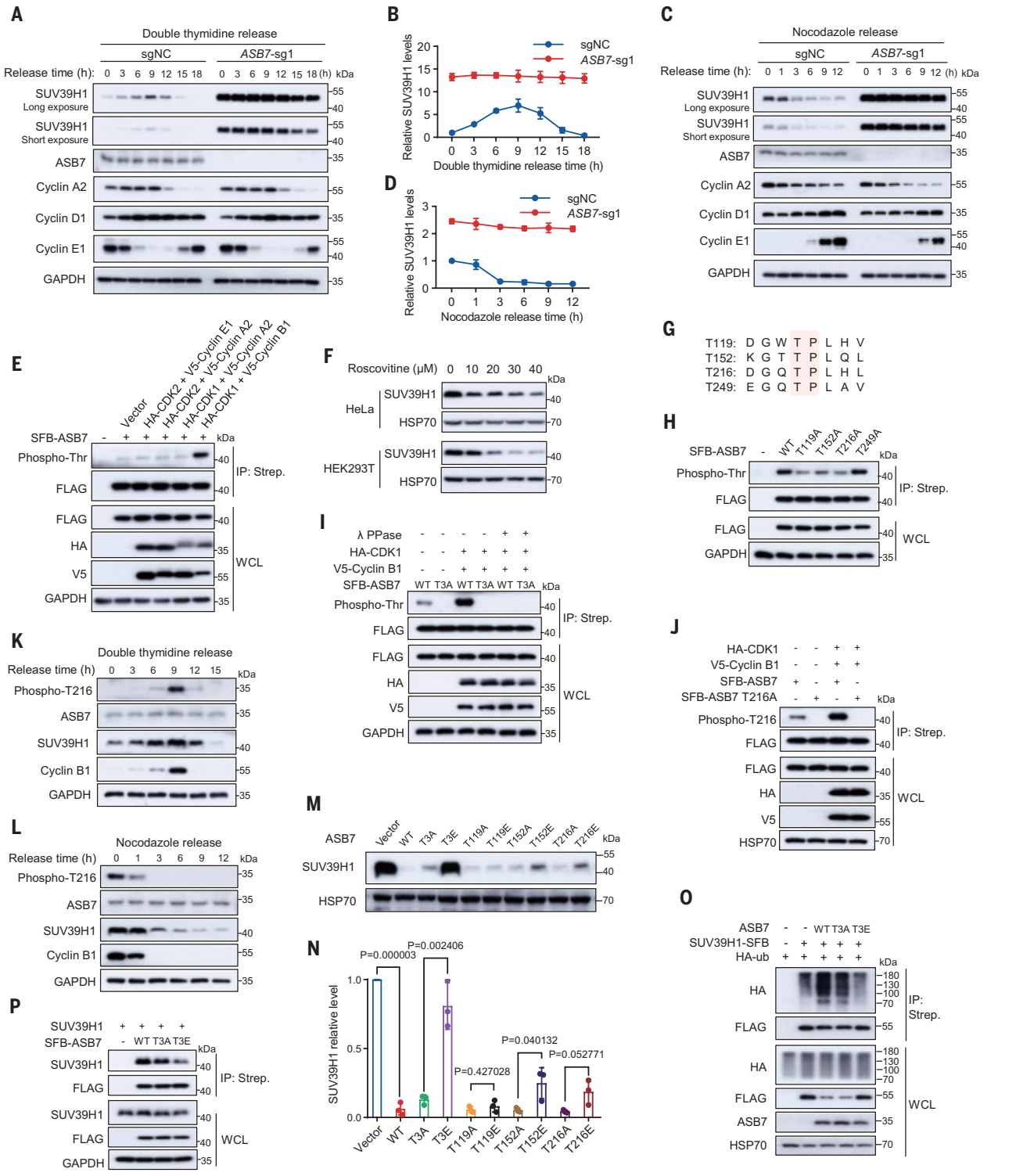

Fig. 4. CDK1 phosphorylates and inhibits ASB7 to prevent SUV39H1 degradation. (**A** to **D**) Immunoblots of cell lysates from HeLa cells synchronized in (A) G_1/S boundary or (C) M phase by means of double thymidine or nocodazole block and release. The SUV39H1 relative levels are quantified in (C) and (D) ($n = 3$ independent experiments). (**E**) HEK293T cells were transfected with indicated constructs and were lysed and pulled down for immunoblot. (**F**) Treatment of roscovitine for 24 hours at indicated concentrations in HeLa and HEK293T cells, then cell lysates were analyzed by means of immunoblot. (**G**) Amino acid sequences of the potential CDK1 substrates motif TP in ASB7 protein. (**H**) HEK293T cells were transfected with ASB7 mutants and subjected to streptavidin pull-down and immunoblot. (**I**) ASB7 phosphorylation detection with or without λ protein phosphatase (λ PPase) treatment. T3A means T119, T152, and T216 triply mutated to alanine. (**J**) Transfection and validation of ASB7 T216 phosphorylation-specific antibody. (**K** and **L**) HeLa cells were synchronized by using (K) double thymidine or (L) nocodazole then released to detect ASB7 T216 phosphorylation. (**M**) HeLa cells with stable expression of the indicated constructs were lysed and analyzed for SUV39H1 proteins expression. T3E means T119, T152, and T216 triply mutated to glutamate. (**N**) Quantification of the SUV39H1 relative intensity in (M) ($n = 3$ independent experiments). *P* values were calculated by using two-tailed Student's *t* test. (**O**) HeLa cells were transfected with indicated plasmids to detect the ubiquitination. (**P**) Immunoprecipitation analysis of the interactions between ASB7 WT, T3A, T3E, and SUV39H1 in HEK293T cells.

Functionally, the phosphomimetic T3E mutant (T119E, T152E, T216E) almost abolished the ability of ASB7 to ubiquitinate and degrade SUV39H1, whereas individual T-to-E mutations had only modest effects. By contrast, T-to-A mutations, whether individual or combined, had no impact on ASB7 function (Fig. 4, M to O, and fig. S8G). Mechanistically, the T3E showed reduced localization to heterochromatin (fig. S8H), likely owing to impaired interaction with SUV39H1 (Fig. 4P and fig. S8I), whereas its interactions with HP1 and the CUL5 complex remained unchanged (fig. S8, I and J). Taken together, these results illustrate that ASB7 is phosphorylated by CDK1-Cyclin B1 during M phase, which suppresses its interaction with SUV39H1 and thereby inhibits SUV39H1 degradation. This regulatory mechanism ensures effective H3K9me3 restoration during the cell cycle.

Repression of H3K9me3 by ASB7 sensitizes cancer cells to PARP inhibitors

Loss of H3K9me3 disrupts chromatin compaction, leading to increased susceptibility to DNA damage and genome instability (*1*, *45*–*47*). During DNA double-strand break (DSB) repair, transient induction of H3K9me3 at the break site is required for the recruitment of TIP60 and subsequent activation of ataxia-telangiectasia mutated (ATM) signaling (*48*, *49*). Analysis of TCGA showed that *ASB7* is frequently amplified in multiple cancer types, including sarcoma, ovarian, stomach, and esophageal carcinomas (Fig. 5A). We hypothesized that elevated *ASB7* expression, through repression of H3K9me3, may impair DNA repair and promote genomic instability. Doxycycline-induced expression of *ASB7* reduced homologous recombination (HR), whereas nonhomologous end joining

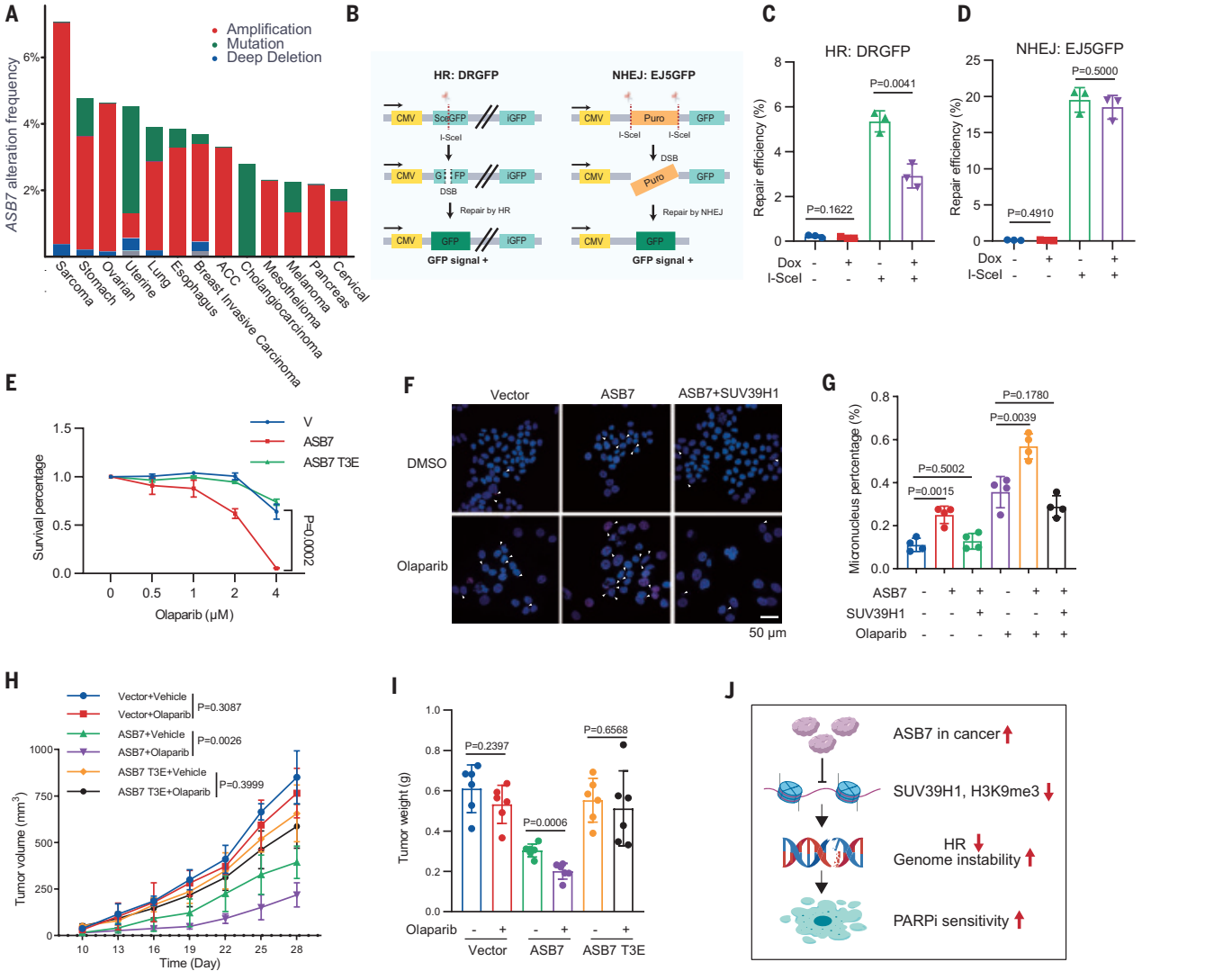

Fig. 5. High *ASB7* expression sensitizes cancer cells to PARP inhibitor. (**A**) Alteration frequency of *ASB7* in cancer patient samples from TCGA. (**B**) Schematic of HR:DRGFP and NHEJ:EJ5GFP reporters. (**C** and **D**) Doxycycline (Dox)–inducible TetOn-ASB7 stable HEK293T cells were transfected with (C) HR:DRGFP or (D) NHEJ: EJ5GFP reporters then treated with or without Dox to induce ASB7 expression. The green fluorescent protein (GFP) signal was detected by means of FACS ($n = 3$ independent experiments). (**E**) Survival assay of control (V) and ASB7 WT or T3E ectopic expressed 143B cells under the treatment of Olaparib ($n = 3$ independent experiments). (**F**) HeLa cells with empty vector, *ASB7*, and *ASB7*/*SUV39H1* double ectopic expression were treated with or without Olaparib for 48 hours, then cells were fixed and stained with γH2AX-AF594. Hoechst33342 was used to visualize nuclear. Scale bar, 50 μm. (**G**) Quantification of the percentage of micronuclei positive cells in (F) ($n = 4$ independent experiments). (**H** and **I**) Stable143B cells with *ASB7* WT or T3E ectopic expression were subcutaneously injected into nude mice and treated with Olaparib at 50 mg/kg/day. (H) Tumor volumes were measured at indicated times, and (I) tumor weights were measured after mice euthanasia ($n = 6$ mice for each group). (**J**) *ASB7* amplification in cancer cells induces SUV39H1 degradation and hypo H3K9me3, which would decrease HR ability and induce genome instability, conferring the vulnerability for cancer cells to PARP inhibitors. *P* values in (C) to (E) and (G) to (I) were calculated by using two-tailed Student's *t* test.

(NHEJ) remained unaffected (Fig. 5, B to D). Because HR deficiency is known to sensitize tumor cells to poly(ADP-ribose) polymerase (PARP) inhibitors such as Olaparib, we assessed the response to Olaparib in ASB7-overexpressing cells. We found that ectopic expression of wild-type (WT) ASB7, but not T3E mutant, increased the sensitivity to Olaparib (Fig. 5E). ASB7 OE also led to increased formation of γH2AX-positive micronuclei, a marker of genomic instability, which was rescued by coexpression of SUV39H1 (Fig. 5, F and G). In a xenograft mouse model, tumors overexpressing WT ASB7 exhibited slower growth, likely reflecting increased genomic stress, and displayed enhanced sensitivity to Olaparib compared with that of control (Vector) or T3E-expressing tumors (Fig. 5, H and I). Collectively, these findings suggest that ASB7 OE impairs HR through H3K9me3 repression, rendering cancer cells more vulnerable to PARP inhibitors. Therefore, patients with elevated ASB7 expression may represent a therapeutically responsive subgroup for PARP inhibitor–based treatment (Fig. 5J).

Discussion

This study identifies the $CUL5^{ASB7}$ E3 ubiquitin ligase as a potent negative regulator of H3K9me3 homeostasis (fig. S9). We demonstrate that H3K9me3 reader HP1 recruits ASB7 to heterochromatin, where ASB7 interacts with SUV39H1 and facilitates its ubiquitin-proteasome–mediated degradation. Given that the reestablishment of H3K9me3 after chromatin replication relies on a positive feedback loop involving HP1 and SUV39H1 (*4*, *12*, *13*, *23*), we propose the existence of a dynamic HP1-SUV39H1-ASB7 regulatory circuit. In this model, ASB7 serves as a counteracting factor that restricts excessive H3K9me3 accumulation and prevents aberrant or deleterious over-heterochromatinization. This circuit is further modulated by CDK1 activity. Specifically, during mitosis, CDK1-mediated phosphorylation of ASB7 weakens its interaction with SUV39H1, stabilizing SUV39H1 and promoting its accumulation on chromatin. This mechanism facilitates the spread of SUV39H1 and H3K9me3 on chromatin, which is in line with findings that the local concentration of chromatin-bound Clr4 is critical for heterochromatin propagation (*50*). Through this cell cycle–coupled regulation, the HP1-SUV39H1-ASB7 axis ensures accurate restoration of H3K9me3 after DNA replication and contributes to the faithful epigenetic inheritance of heterochromatin structure.

H3K9me3 is a dynamic histone modification that can be demethylated by the KDM4 family, including the somatically expressed *KDM4A*, *KDM4B*, and *KDM4C*, as well as the testis-specific *KDM4D* and *KDM4E* (*19*–*22*, *51*). Traditionally, HP1 was believed to recruit KDM4 to heterochromatin to antagonize H3K9me3 accumulation, establishing a "read-write-erase" regulatory loop (*52*). However, we found that triple deletion of *KDM4A/B/C* failed to increase H3K9me3 levels, even after multiple cell divisions (fig. S1B). This suggests that demethylation by KDM4 plays only a minor role in H3K9me3 regulation during the cell cycle, which aligns with prior observations that showed minimal turnover of H3K9me3 in mammalian cells (*9*, *10*, *53*). Therefore, regulation of SUV39H1 protein stability, rather than active demethylation, serves as the predominant mechanism to restrain H3K9me3 levels during cell proliferation.

Our study establishes the $CUL5^{ASB7}$ E3 ubiquitin ligase as a key negative regulator of H3K9me3 homeostasis, a process that is essential for epigenetic fidelity and genome integrity. Pathologically, elevated ASB7 expression in tumor cells reduces H3K9me3 levels, impairs homologous recombination, and promotes genome instability. As a result, tumors with ASB7 OE may exhibit increased sensitivity to PARP inhibitors, providing a potential therapeutic strategy for precision oncology.

REFERENCES AND NOTES

1. R. C. Allshire, H. D. Madhani, *Nat. Rev. Mol. Cell Biol.* **19**, 229–244 (2018).
2. S. I. S. Grewal, *Mol. Cell* **83**, 1767–1785 (2023).
3. A. Janssen, S. U. Colmenares, G. H. Karpen, *Annu. Rev. Cell Dev. Biol.* **34**, 265–288 (2018).
4. J. Padeken, S. P. Methot, S. M. Gasser, *Nat. Rev. Mol. Cell Biol.* **23**, 623–640 (2022).
5. J. Nakayama, J. C. Rice, B. D. Strahl, C. D. Allis, S. I. Grewal, *Science* **292**, 110–113 (2001).
6. J. S. Becker, D. Nicetto, K. S. Zaret, *Trends Genet.* **32**, 29–41 (2016).
7. S. Rea *et al.*, *Nature* **406**, 593–599 (2000).
8. D. Moazed, *Cell* **146**, 510–518 (2011).
9. C. Alabert *et al.*, *Genes Dev.* **29**, 585–590 (2015).
10. M. Xu, W. Wang, S. Chen, B. Zhu, *EMBO Rep.* **13**, 60–67 (2011).
11. A. V. Probst, E. Dunleavy, G. Almouzni, *Nat. Rev. Mol. Cell Biol.* **10**, 192–206 (2009).
12. M. Lachner, D. O'Carroll, S. Rea, K. Mechtler, T. Jenuwein, *Nature* **410**, 116–120 (2001).
13. A. J. Bannister *et al.*, *Nature* **410**, 120–124 (2001).
14. C. Maison, G. Almouzni, *Nat. Rev. Mol. Cell Biol.* **5**, 296–304 (2004).
15. W. Zeng, A. R. Ball Jr., K. Yokomori, *Epigenetics* **5**, 287–292 (2010).
16. K. Yamamoto, M. Sonoda, *Biochem. Biophys. Res. Commun.* **301**, 287–292 (2003).
17. N. Iglesias *et al.*, *Nature* **560**, 504–508 (2018).
18. J. C. Black *et al.*, *Mol. Cell* **40**, 736–748 (2010).
19. M. T. Pedersen *et al.*, *EMBO J.* **35**, 1550–1564 (2016).
20. P. A. Cloos *et al.*, *Nature* **442**, 307–311 (2006).
21. R. J. Klose *et al.*, *Nature* **442**, 312–316 (2006).
22. J. R. Whetstine *et al.*, *Cell* **125**, 467–481 (2006).
23. W. Du *et al.*, *Sci. China Life Sci.* **65**, 2162–2190 (2022).
24. R. T. Timms, I. A. Tchasovnikarova, R. Antrobus, G. Dougan, P. J. Lehner, *Cell Rep.* **17**, 653–659 (2016).
25. D. O'Carroll *et al.*, *Mol. Cell. Biol.* **20**, 9423–9433 (2000).
26. M. Tachibana, K. Sugimoto, T. Fukushima, Y. Shinkai, *J. Biol. Chem.* **276**, 25309–25317 (2001).
27. H. Ogawa, K. Ishiguro, S. Gaubatz, D. M. Livingston, Y. Nakatani, *Science* **296**, 1132–1136 (2002).
28. D. C. Schultz, K. Ayyanathan, D. Negorev, G. G. Maul, F. J. Rauscher 3rd, *Genes Dev.* **16**, 919–932 (2002).
29. K. Uematsu *et al.*, *J. Cell Biol.* **215**, 95–106 (2016).
30. J. R. Muniz *et al.*, *J. Mol. Biol.* **425**, 3166–3177 (2013).
31. T. C. Branon *et al.*, *Nat. Biotechnol.* **36**, 880–887 (2018).
32. S. G. Prasanth, Z. Shen, K. V. Prasanth, B. Stillman, *Proc. Natl. Acad. Sci. U.S.A.* **107**, 15093–15098 (2010).
33. A. G. Larson *et al.*, *Nature* **547**, 236–240 (2017).
34. A. R. Strom *et al.*, *Nature* **547**, 241–245 (2017).
35. L. Wang *et al.*, *Mol. Cell* **76**, 646–659.e6 (2019).
36. S. A. Denslow, P. A. Wade, *Oncogene* **26**, 5433–5438 (2007).
37. G. Job *et al.*, *Mol. Cell* **62**, 207–221 (2016).
38. T. Yamada, W. Fischle, T. Sugiyama, C. D. Allis, S. I. Grewal, *Mol. Cell* **20**, 173–185 (2005).
39. A. L. Nielsen *et al.*, *Mol. Cell* **7**, 729–739 (2001).
40. A. L. Nielsen *et al.*, *EMBO J.* **18**, 6385–6395 (1999).
41. J. F. Smothers, S. Henikoff, *Curr. Biol.* **10**, 27–30 (2000).
42. Y. Liu *et al.*, *J. Biol. Chem.* **292**, 5655–5664 (2017).
43. P. de Bie, A. Ciechanover, *Cell Death Differ.* **18**, 1393–1402 (2011).
44. S. H. Park, S. E. Yu, Y. G. Chai, Y. K. Jang, *Nucleic Acids Res.* **42**, 6196–6207 (2014).
45. A. H. Peters *et al.*, *Cell* **107**, 323–337 (2001).
46. J. C. Peng, G. H. Karpen, *PLOS Genet.* **5**, e1000435 (2009).
47. J. C. Peng, G. H. Karpen, *Curr. Opin. Genet. Dev.* **18**, 204–211 (2008).
48. J. Zhang *et al.*, *DNA Repair* **107**, 103206 (2021).
49. Y. Sun *et al.*, *Nat. Cell Biol.* **11**, 1376–1382 (2009).
50. A. R. Cutter DiPiazza *et al.*, *Proc. Natl. Acad. Sci. U.S.A.* **118**, e2100699118 (2021).
51. N. Iwamori, M. Zhao, M. L. Meistrich, M. M. Matzuk, *Biol. Reprod.* **84**, 1225–1234 (2011).
52. W. L. Berry, R. Janknecht, *Cancer Res.* **73**, 2936–2942 (2013).
53. B. M. Zee, R. S. Levin, P. A. DiMaggio, B. A. Garcia, *Epigenetics Chromatin* **3**, 22 (2010).

ACKNOWLEDGMENTS

We appreciate the assistance from the members of the Kang laboratory who were actively involved in this work. We used ChatGPT-4o to assist with grammatical revisions, mainly to suggest synonyms and check clarity. **Funding:** Grants supporting this project are from the National Key Research and Development Program of China (2021YFA1300601), National Natural Science Foundation of China grants (82341015, 82321003, 82273048, 82372591, 82030090, and 82172939), and the Cancer Innovative Research Program of Sun Yat-sen University Cancer Center (CIRP-SYSUCC-0015). **Author contributions:** Conceptualization: L. Zhou, Y.W., T.K. Methodology: M.X., M.Zha., R.Z., Z.H., M. Zhu., Ziw.W., H. Zhou, Y.Y., S.G. Investigation: L. Zhou, Z.C., Y.Z., X.Z., Zif.W., J.L., H. Zhu, J.C., L.Zhe., Visualization: L. Zhou, Z.C., Y.Z. Funding acquisition: L. Zhou, Y.W., T.K. Project administration: Y.W., T.K. Supervision: Y.W., T.K. Writing – original draft: L. Zhou, Y.W. Writing – review & editing: Y.W., T.K. **Competing interests:** The authors declare that they have no competing interests. **Data and materials availability:** Sequencing data that support the findings of this study has been deposited into the Genome Sequence Archive for Humans (cell lines: HRA010290; tissues: CRA022676). Mass spectrometry data has been deposited into the ProteomeXchange Consortium through the iProX partner repository (PXD053445). All other data are available in the main text or the supplementary materials.

License information: Copyright © 2025 the authors, some rights reserved; exclusive licensee American Association for the Advancement of Science. No claim to original US government works. https://www.science.org/about/science-licenses-journal-article-reuse

SUPPLEMENTARY MATERIALS

science.org/doi/10.1126/science.adq7408
Materials and Methods; Figs. S1 to S9; Table S1 to S3; References (*54*–*76*);
MDAR Reproducibility Checklist

Submitted 30 May 2024; resubmitted 5 February 2025; accepted 12 May 2025;
published online 29 May 2025

10.1126/science.adq7408

ARE YOU THE KIND WHO WORKS TO HELP ALL HUMANKIND?

Find your next job at ScienceCareers.org

For anyone who's looking to get ahead in—or just plain get into—science, there's no better, more trusted resource or authority on the subject than *Science* Careers. Here you'll find opportunities and savvy advice across all disciplines and levels. There's no shortage of global problems today that science can't solve. Be part of the solution.

ScienceCareers

FROM THE JOURNAL SCIENCE AAAS

ScienceCareers.org

ScienceCareers

Stigma did not kill my dream

Juan Carlos Cambronero-Heinrichs

I was less than a year into my Ph.D. when I learned my scholarship had been canceled. I was heartbroken. Studying in Germany was meant to be a fresh start, a chance to escape the stigma I'd faced back home in Costa Rica since testing positive for HIV. After years of struggle, I finally felt my dream of a scientific career was back on track. But securing medical insurance for my treatment had proved difficult, which eventually led the scholarship organization to cancel my funding. I was forced to return home.

I'd always wanted to be a scientist. As a child, I spent hours catching insects in the garden and watching nature documentaries. I made it into a prestigious science-focused high school in the capital, and then into an undergraduate microbiology program.

But something else was unfolding beneath the surface. I'd long known I was gay, and at university I found a community and came out. I dated and explored my identity. But in my final year, I started to lose weight and developed a swollen lymph node. My doctor told me it could be cancer or HIV. I was terrified. A part of me even hoped it was cancer, because society tends to view cancer survivors as brave, whereas HIV-positive people are still heavily stigmatized.

Eventually, the diagnosis came: I was HIV positive.

The response from many of my colleagues was deeply hurtful. Some said that, as a microbiologist, I should have known how HIV spreads and been more careful. At the time, I was a student in a bacteriology lab located in the same hospital where I was receiving treatment. The infectious disease doctor managing my case regularly visited the lab, and to see him in that context was unsettling. One day, a colleague casually mentioned they had processed my laboratory samples. I felt exposed, unsafe, and overwhelmed.

Telling my family was excruciating. My relationship with my father fell apart. Some friends disappeared, too. One said I was a burden on the health care system; another called me a bad person. The stress led to a mental health crisis and a psychotic episode, and I had to take time off from my studies to recover.

But I didn't give up. I completed my degree and began working as a research assistant, even as my mental health struggles continued. I was hospitalized again and eventually diagnosed with schizoaffective disorder. The stigma only deepened. Now, I wasn't just HIV positive, I was "crazy," too.

Eventually, I decided I needed to get away. In Costa Rica, most microbiologists work in hospitals, places I could no longer bear to be in. After years of trying, I was awarded the scholarship in Germany. It felt like a new beginning: It was a relief to simply exist, without having to talk about my diagnoses. But the private health insurance provided by the scholarship organization excluded HIV treatment—and I couldn't get public insurance without a job, which was incompatible with my study program. The organization said it could not fund me without coverage. I was devastated. I thought I'd lost everything I had worked so hard for. I felt ashamed: ashamed to explain to my supervisor why my scholarship had ended, ashamed to tell others what had happened, ashamed of having to return home. At some point, I began to believe I was simply a failure.

Fortunately, I still had people to support me. My former supervisor connected me with researchers in Italy, who offered me a Ph.D. position—this time with full insurance. From the beginning, my new supervisors knew about my HIV status, and I soon told them about my mental health. They regularly checked on my well-being, even coming with me on an initial visit to a psychiatrist. It meant the world to know that some people believed in an HIV-positive scientist with a mental health condition. I began to believe that speaking about my scars might help, that it could foster understanding, and perhaps even awaken empathy in others. If we don't talk about HIV or mental health, the stigma will never end.

I completed my Ph.D., and am now living my dream as a postdoc. My mental health is stable, and I have not had a crisis in a long time. I've been undetectable for nearly a decade. Living with stigma is hard—but life didn't end. I'm still here. □

Juan Carlos Cambronero-Heinrichs is a postdoctoral researcher at the University of Padua.

ILLUSTRATION: ROBERT NEUBECKER

NEWS FROM Science

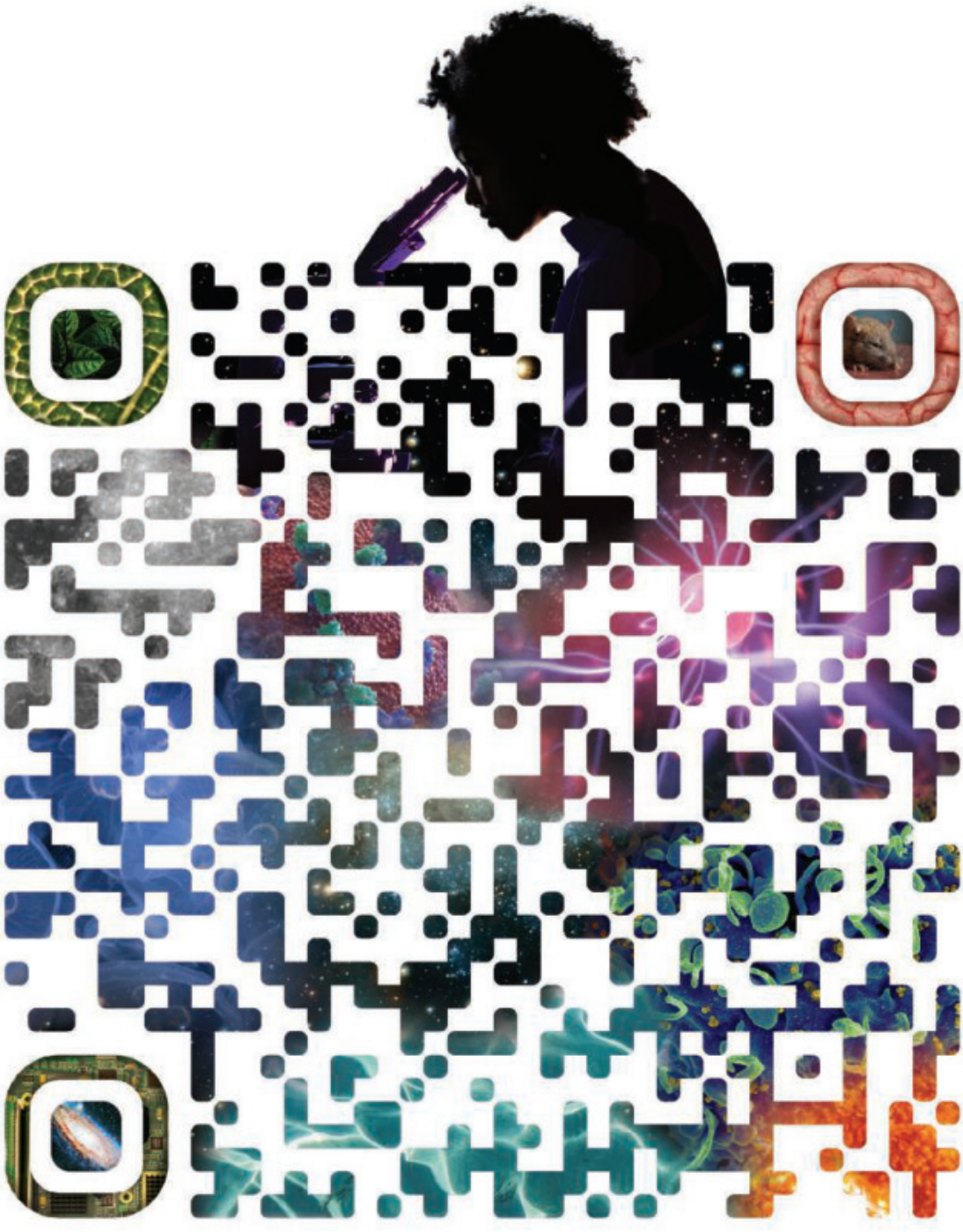

Sign up for
Science.org/News

Science
JOURNALS AAAS

Publish your research in the *Science* family of journals

The *Science* family of journals (*Science, Science Advances, Science Immunology, Science Robotics, Science Signaling*, and *Science Translational Medicine)* are among the most highly-regarded journals in the world for quality and selectivity. Our peer-reviewed journals are committed to publishing cutting-edge research, incisive scientific commentary, and insights on what's important to the scientific world at the highest standards.

Submit your research today!

Learn more at **Science.org/journals**